Nondestructive Evaluation of the Depth of Cracks in Concrete Plates Using Surface Waves

by

Yanjun Yang

A thesis
presented to the University of Waterloo
in fulfillment of the
thesis requirement for the degree of
Doctor of Philosophy
in
Civil Engineering

Waterloo, Ontario, Canada, 2009

I hereby declare that I am the sole author of this thesis. This is a true copy of the thesis, including any required final revisions, as accepted by my examiners.

I understand that my thesis may be made electronically available to the public.

Yanjun Yang

Abstract

Concrete structures can often be modeled as plates, for example, bridges, tunnel walls and pipes. Near-surface damage in concrete structures mostly takes the form of cracking. Surface-breaking cracks affect concrete properties and structural integrity; therefore, the nondestructive evaluation of crack depth is important for structural monitoring, strengthening and rehabilitation. On the other hand, material damping is a fundamental parameter for the dynamic analysis of material specimens and structures. Monitoring damping changes is useful for the assessment of material conditions and structural deterioration. The main objective of this research is to develop new methodologies for depth evaluation of surface-breaking cracks and the evaluation of damping in concrete plates.

Nondestructive techniques based on wave propagation are useful because they are non-intrusive, efficient and cost effective. Previous studies for the depth evaluation of surface-breaking cracks in concrete have used diffracted compressional waves (P-waves). However, surface waves exhibit better properties for the characterization of near surface defects, because (a) surface waves dominate the surface response, they carry 67% of the wave propagation energy, and present lower geometrical attenuation because the propagating wave front is cylindrical; and (b) the penetration depth of Rayleigh waves (R-waves) depends on their frequency. Most of the R-wave energy concentrates at a depth of one-third of their wavelengths. The transmission of R-waves through a surface-breaking crack depends on the crack depth; this depth sensitivity is the basis for the so-called Fourier transmission coefficient (FTC) method.

R-waves only exist in a half-space (one traction-free surface); whereas in the case of a plate (two traction-free surfaces), Lamb modes are generated. Fundamental Lamb modes behave like R-waves at high frequencies, because their wavelengths are small relative to the plate thickness. Lamb modes are not considered in the standard FTC method, and the FTC method is also affected by the selected spacing between receivers. The FTC calculation requires the use of an explicit time window for the identification of the arrival of surface waves, and the selection of a reliable frequency range.

This research presents theoretical, numerical and experimental results. Theoretical aspects of Lamb modes are discussed, and a theoretical transfer function is derived, which can be used to study changes of Lamb modes in the time and frequency domains as a function of distance. The maximum amplitude of the wavelet transform varies with distance because of the dispersion of Lamb modes and the participation of higher Lamb modes in the response. Numerical simulations are conducted to study the wave propagation of Lamb modes through a surface-breaking crack with different depths. The surface response is found to be dominated by the fundamental Lamb mode. Using the

2D Fourier transform, the incident, transmitted and reflected fundamental Lamb modes are extracted. A transmission ratio between the transmitted and incident modes is calculated, which is sensitive to crack depths (d) normalized to the wavelength (λ) in a range $(d/\lambda) = 0.1$ to $1/3$.

A new wavelet transmission coefficient (WTC) method for the depth evaluation of surface-breaking cracks in concrete is proposed to overcome the main limitations of the FTC method. The WTC method gives a global coefficient that is correlated with the crack depth, which does not require time windowing and the pre-selection of a frequency bandwidth. To reduce the effects of wave reflections, which are present in the FTC method because of the non-equal spacing configuration, a new equal spacing configuration is used in the WTC method. The effects of Lamb mode dispersion are also reduced. In laboratory tests, an ultrasonic transmitter with central frequency at $50kHz$ is used as a source; the $50kHz$ frequency is appropriate for the concrete plate tested (thickness $80mm$), because the fundamental Lamb modes have converged to the Rayleigh wave mode. The new method has also been used in-situ at Hanson Pipe and Precast Inc., Cambridge, Ontario, Canada, and it shows potential for practical applications.

In general, the evaluation of material damping is more difficult than the measurement of wave velocity; the dynamic response and attenuation of structural vibrations are predominantly controlled by damping, and the damping is typically evaluated using the modal analysis technique, which requires considerable efforts. The existing methods based on surface waves, use the Fourier transform to measure material damping; however, an explicit time window is required for the spectral ratio method to extract the arrival of surface wave; in addition, a slope of the spectral ratio varies for different frequency ranges, and thus a reliable frequency range needs to be determined.

This research uses the wavelet transform to measure material damping in plates, where neither an explicit time window nor the pre-selection of a frequency bandwidth are required. The measured material damping represents an average damping for a frequency range determined by source. Both numerical and experimental results show good agreement and the potential for practical applications.

Acknowledgements

First and foremost, I offer my sincerest gratitude to my supervisors: Prof. Giovanni Cascante and Prof. Maria Anna Polak whose wisdom, stimulating suggestions, and encouragement helped me all the time during this research. Without their guidance and patience, this thesis would not exist.

I would like to thank all members in our NDT group, especially Ali Nasseri Moghaddam, Zahid H. Khan, Fernando Tallavo and Simone Berube. During my study, I always had a chance to discuss technical problems with them, and their comments were of great value to my research. My great appreciations go to staff members in the department, Ken Bowman, Richard Morrison and Doug Hirst for helping me with experimental specimen preparation, especially Marguarite Knechtel who did a wonderful job as Administrative Co-ordinator of Graduate Studies.

This research has been supported by Materials Manufacturing, Ontario, Ontario Concrete Pipe Association, and the National Science and Engineering Research Council (NSERC). I wish to express my gratitude for this support. I am grateful to Hanson Pipe and Precast Inc., Cambridge, Ontario for providing concrete pipe specimens for in-situ testing.

Dedication

I am forever indebted to my parents for their understanding, endless patience and encouragement when it was most required. Finally, many thanks to my patient and loving wife, who has been a great source of strength through all this work, my two pretty daughters, who have been my primary motivation to succeed.

Contents

List of Tables

List of Figures

Nomenclature

α_x, α_t: Attenuation coefficients in space and in time $[1/m; 1/s]$.

β: Geometric attenuation constant.

$\Delta\theta$: Initial phase difference $[rad]$.

Δf: Frequency interval $[hertz]$.

Δt: Time interval $[second]$.

Δt_{crit}: Critical time increment $[second]$.

Δx: Distance interval $[meter]$.

Δx_{crit}: Critical size $[meter]$.

Δ: Dilatation or volumetric strain.

η: Modulation parameter for a Lamb source $[second]$.

η_0, η_1: Mass and stiffness damping constants.

κ: Wave number $[1/m]$.

λ: Wavelength $[meter]$.

λ_P, λ_S, λ_R: P-, S- and R-wavelength $[meter]$.

λ_{cut}: Cut-off wavelength $[meter]$.

$[\mathbf{M}]$, $[\mathbf{C}]$, $[\mathbf{K}]$: Mass, damping and stiffness matrices.

∇: Differential operator.

∇^2: Laplacian operator.

ω: Angular frequency $[rad/s]$.

ω_0: Central or resonant angular frequency $[rad/s]$.

ω_d: Damped frequency $[rad/s]$.

ω_n: Natural frequency $[rad/s]$.

$\Phi(\omega)$: Spectral amplitude of a Morlet function.

$\phi(t)$: Morlet function.

ρ: Mass density $[kg/m^3]$.

σ_{ij}: Stress $[Pa]$.

τ: Modulation parameter for a Morlet function $[second]$.

TRa: Transfer function for the acoustic port of a piezoelectric transducer.

TRe: Transfer function for the electric port of a piezoelectric transducer.

θ: Initial phase $[rad]$.

$\Theta(a,b,x)$: Phase spectrum of the wavelet transform $[rad]$.

υ: Poisson's ratio.

$\varphi(x_1,x_2)$, $\psi(x_1,x_2)$: Potential functions.

ξ: Rayleigh damping ratio.

ξ_{min}, f_{min}, ω_{min}: Minimum Rayleigh damping ratio, corresponding frequency $[hertz]$ and angular frequency $[rad/s]$.

$\{\ddot{u}\}$, $\{\dot{u}\}$, $\{u\}$, $\{f\}$: Acceleration $[m/s^2]$, velocity $[m/s]$, displacement $[m]$ and force $[N]$ vectors.

A, B, C: Constant numbers.

a: Frequency scale.

b: Time shift $[second]$.

BW: Frequency bandwidth $[hertz]$.

C_ϕ: Admission constant.

D: Damping ratio.

d: Depth of a crack [$meter$].

E: Young's modulus [Pa].

$E^{<WT>}(a,b)$: Wavelet-based energy [$kg \times m^2/s^2$].

$E^{<WT>}_{total}$: Total wavelet-based energy [$kg \times m^2/s^2$].

$E_{lower}(\omega)$: Cumulative spectral energy with a lower-bound variable in the integral [$kg \times m^2/s^2$].

E_{total}: Total spectral energy [$kg \times m^2/s^2$].

$E_{upper}(\omega)$: Cumulative spectral energy with a upper-bound variable in the integral [$kg \times m^2/s^2$].

f: Frequency [$hertz$].

f_0: Central or resonant frequency [$hertz$].

F_b: Amplitude for a Lamb source [$N \times second$].

f_{cut}: Cut-off frequency [$hertz$].

f_{max}: Maximum frequency of interest [$hertz$].

f_{nyqu}: Nyquist frequency [$hertz$].

f_{samp}: Sampling frequency [$hertz$].

$FTC(\omega)$: Fourier transmission coefficient.

G: Shear modulus [Pa].

$G(\omega,\kappa)$: 2D function in frequency and wave number domains.

$G(\omega,b)$: Short-time Fourier transform.

$G(\omega,x)$: 2D function in frequency and space domains.

$g(t)$, $G(\omega)$: Time signal, Fourier spectrum.

$g(t,x)$: 2D function in time and space domains.

$G^{<EWT>}(b)$: Extended wavelet transform.

$G^{<WT>}(a,b)$: Wavelet transform.

$G_{12}(\omega)$: Cross power spectrum.

h: Half the thickness of a plate [$meter$].

$H(\omega)$: Transfer function for a piezoelectric transmitter.

$H(\omega,x)$: Transfer function for Lamb modes.

i, n: Index numbers.

j: Imaginary unit.

K: Bulk modulus [Pa].

k: Stiffness of a spring [N/m].

$Lm(t)$: Lamb source [N].

M: Constraint modulus [Pa].

m: Mass [kg].

$m(t,x)$: Modulation function.

N: Total number of points.

N_{anti}: Number of anti-symmetric Lamb modes.

N_{sym}: Number of symmetric Lamb modes.

$q(x_1,x_2,t)$: Pressure distribution function [N/m^2].

R: Radius [$meter$].

R_A, R_B: Reflection coefficients.

Re: Reflection coefficients.

$S(\omega)$, $C(\omega)$, $R(\omega)$, $M(\omega)$: Transfer functions of source, coupling, receiver and medium.

S_1, S_2 $\cdots$: Spacings between the source and the crack [$meter$].

$S_b(t)$: Sinusoidal tone burst source [N].

t: Time [$second$].

t_d: Contact duration of time [$second$].

t_n: Transit time of an ultrasonic pulse through a piezoelectric transmitter [$second$].

t_r: Arrival time [$second$].

t_{zero}: Time delay from measurement system [$second$].

Tr: Transmission coefficients.

u_1, u_2, u_3: Displacements in three axes [$meter$].

$V_k(t)$: Output voltage of a pulser [$volt$].

V_P, V_S, V_R: P-wave, S-wave and R-wave velocities [m/s].

V_{EXT}: Velocity of the extensional vibration mode [m/s].

V_{FLX}: Velocity of the flexural vibration mode [m/s].

V_{ph}: Phase velocity [m/s].

$W(\omega, \kappa)$: 2D filter in frequency and wave number domains.

$w(t)$: Window function.

$w(x,t)$: Solution to the vertical displacements for Lamb's problem [$meter$].

w_i: Weighing factor.

$whn(t)$: Hanning window function.

WTC: Wavelet transmission coefficient.

x: Horizontal distance [$meter$].

x_1, x_2, x_3: Three mutually-perpendicular axes [$meter$].

$Y(x)$: Maximum amplitude of the wavelet transform.

z_1, z_2: Acoustic impedances [$Pa \times s/m^3$].

$[a_1, a_2]$: Frequency scale range for an extended wavelet transform.

Chapter 1

Introduction

1.1 Depth evaluation of a surface-breaking crack

Concrete structures can often be modeled as plates, for example, bridges, and tunnel walls and pipes. Near-surface damage in concrete structures mostly often takes the form of cracking (*Song* 2003); surface-breaking cracks in concrete structures are caused by:

- Exterior loading, as in the case of a structure under mechanical actions.
- Interior volume changes due to freeze or thaw.
- Environmental conditions such as the corrosion of rebars.

Surface-breaking cracks affect concrete properties and structural integrity, and they can be considered one of the indications of structural residual strength and serviceability conditions. Even small cracks can grow and eventually lead to the failure of a structure. Therefore, nondestructive evaluation of the crack depth is important for health monitoring, strengthening and rehabilitation. Nondestructive techniques based on wave propagation are commonly used because they are non-invasive, efficient and cost effective. Two main types of waves exist: body waves and surface waves. Body waves could be compressional waves or shear waves; whereas surface waves could be Rayleigh waves or Love waves. In a plate, another type of surface waves exist, which are called Lamb waves. Considerable works have been done in this area; however, there is no robust nondestructive technique that can be easily used in-situ (*Lin* 1996).

Based on the impact echo technique, *Lin* (1996) measured P-wave reflections between the surface boundary and the tip of surface-breaking cracks. The analysis of wave

reflections shown in the frequency domain is used to calculate the crack depth. However, a significant amount of energy is required from the wave reflections.

A dynamic force acting on a structure excites different vibration modes, each with a distinct natural frequency, which is altered by the presence of a defect. *Toutanji* (2003) attempted to find a quantitative relationship between the natural frequencies and the depth of a surface-breaking crack. However, the results excited are affected by different vibration modes.

Previous studies on concrete structures for the depth evaluation of surface-breaking cracks have used diffracted P-waves (*Sansalone* 1998). A vertical point loading at the surface of a medium generates P-waves that propagate spherically. The P-wave diffraction occurs at the tip of surface-breaking cracks, where a new wave source is formed. The diffracted P-waves are recorded by a receiver that is placed at surface on the other side of the crack. The arrival time or initial amplitude is measured for the calculations of the crack depth. However, surface responses in a medium are dominated by surface waves; in addition, the intensity of diffracted P-waves depends on the discontinuity at the crack tip. As a result, the selection of the P-wave arrival in time domain is difficult.

Surface waves exhibit unique properties suitable for the characterization of near surface (*Rix* 1990; *Kalinski* 1994). Two useful features for the evaluation of the depth of surface-breaking cracks are:

- Surface waves dominate the surface response. A vertical point load applied to the surface of a homogeneous half space generates Rayleigh waves, which contain 67% of the propagation energy, and present lower geometrical attenuation because the propagating wave front is cylindrical; (*Miller* and *Pursey* 1955). Shear waves and compressional waves contain 26% and 7% of the the propagation energy, respectively, their propagating wave fronts are in spherical.

- The penetration depth of surface wave depends on the frequency or wavelength.

Hevin (1998) found the Rayleigh wave energy concentrates at a depth of one-third of the wavelength. Based on the characteristics of Rayleigh waves, *Popovics* (2000) and *Song* (2003) use the Fourier transform to calculate a transmission coefficient, and they propose the so-called Fourier transmission coefficient (FTC) method for the depth evaluation of surface-breaking cracks; the numerical and experimental results of FTC is sensitive to the crack depth (d) normalized to the wavelength (λ) in a range from d/λ = 0 to $1/3$.

Although the FTC method is promising, some problems exist:

- Rayleigh waves are a non-dispersive in a half-space where only one traction-free surface is present, non-dispersion means that different frequency components propagate at a constant velocity; whereas for the case of a plate with two traction-free surfaces, different Lamb modes are generated. Lamb waves are dispersive, and the penetration depth of Lamb waves is different from the corresponding Rayleigh waves because of the different mode shapes.

- For the FTC calculations, a time window is required to extract the arrival of surface wave from the measured time signal; however, the results vary because of the subjective identification. The FTC is a function of frequency, and the determination of a reliable frequency range is difficult; thus the FTC results depend on the selected frequency range.

- A mechanical impactor is used as a source for the FTC measurement. *Popovics* (1995) indicated that the generated frequency components can be controlled by varying the impactor size and the drop height; however, in reality the control of the frequency is limited because of the inelastic and inhomogeneous properties of concrete, and the complex surface conditions at a micro scale level. High frequency components are required for the detection of a small crack. *Popovics* (1995) performed experimental tests on a Plexiglas plate using a small steel ball as an impactor; the generated wave energy is shown below $50kHz$.

- A non-equal spacing configuration is used in the FTC method, where two receivers are aligned with the source and unequally spaced from a source. Constructive and destructive interference occurs before a crack, and the variation in frequency content for the propagating waves at the two receiver locations affect the FTC results.

This research addresses the above problems by conducting the theoretical and numerical studies. The major contributions of this research are the new method for the nondestructive evaluation of the depth of surface-breaking cracks, the new theoretical transfer function for the study of Lamb modes in plates, and the new method for the evaluation of material damping using a surface array of receivers. The following works are performed:

- The Lamb wave propagation in a concrete plate is studied and a theoretical transfer function is derived. Theoretical and numerical results show that Lamb wave modes are dispersive; as a result, the frequency components of a propagating Lamb wave vary with distance. However, fundamental Lamb modes behave similar to

Rayleigh waves for high frequencies where the wavelength is small relative to the plate thickness.

- In the presence of a surface-breaking crack, the contour plot of the 2D Fourier transform of numerical results shows incident, transmitted, and reflected Lamb modes. With a 2D filter, a single Lamb mode can be extracted. Because surface responses are dominated by fundamental Lamb modes for both the transmitted and reflected waves, they can be used for the crack depth evaluation.

- The numerical models are calibrated using Lamb's problem, theoretical geometric attenuation, and 2D Fourier transform. For the case presented in this study, the fundamental Lamb mode S0 is nearly non-dispersive at low frequencies in a small frequency bandwidth; this non-dispersive behavior is used to calibrate the numerical models.

- The wavelet transform is applied to time signals measured at different distances from the source. With a fixed dilation parameter, the magnitude of the wavelet transform varies with the time shifting parameter; the magnitude is the maximum at a time corresponding to an arrival of the fundamental Lamb modes, and this magnitude information is used to calculate a newly proposed wavelet transmission coefficient (WTC), where neither a time windowing nor a reliable frequency range are needed. The WTC integrates the signal over a frequency bandwidth to give a global value that is related to the crack depth.

- An ultrasonic piezoelectric transmitter provides known frequency components in a high frequency range, and it is used on the surface of a medium as a source. The initial output force of the transmitter is modeled with a Morlet function; therefore, the generated ultrasonic pulse propagates in a medium, and the surface responses are analyzed with the wavelet transform using the same Morlet function as a wavelet.

- To eliminate the variation in the frequency spectra at two receiver locations, a new equal configuration with the two receivers placed at equal distance from the source is used. In the new equal spacing configuration, the variation between two receivers in the WTC measurement is attributed only to the presence of a surface-breaking crack.

- The WTC is correlated with the crack depth in a sensitive depth range, which is determined by the central frequency of an ultrasonic piezoelectric transmitter. The

new method has been applied in-situ at Hanson Pipe and Precast Inc., Cambridge, Ontario, Canada, and it shows potential for practical applications.

1.2 Measurement of material damping ratio

Material damping is important for the dynamic analysis of material specimens and structures. In geomaterials, the wave propagation depends strongly on the physical state and saturation conditions, for example, the wave attenuation caused by material damping in dry, saturated or frozen rocks, or cemented soil varies much more than the wave velocities for these conditions. However, the experimental measurement of material damping ratio is more difficult than the measurement of wave velocity (*Toksoz* 1979). The dynamic response of structures is predominantly controlled by damping (*Liu* 1995); therefore, monitoring variation of damping is useful for the assessment of structural health or deterioration. Moreover, the presence of a defect in a medium generates a reduction in stiffness and an increase in damping; thus damping measurements can be used to detect or locate defects, for example crack initiation and propagation in a structural element can be monitored by measuring changes in wave attenuation in given frequency range.

This research proposes a new methodology to measure material damping ratio in a medium. The medium is assumed to be represented by a single-degree-freedom system (SDOF), and a theoretical equation for the calculation of material damping ratio is derived, which uses the maximum amplitude and phase information of the propagating waves from the wavelet transform. Both the numerical and experimental results show good potential and the potential for practical applications.

1.3 Thesis organization

Chapter 2 presents a theoretical background on wave propagation in an elastic medium. The characteristics for Rayleigh waves in a half-space and Lamb waves in a plate are introduced. The dispersion curve of Lamb waves for the concrete plate used in the experiments is calculated.

In Chapter 3, basic signal processing techniques that are used for nondestructive testing, such as Fourier transform, 2D Fourier transform and wavelet transform are described.

A literature review on the use of mechanical waves for the crack depth evaluation is given in Chapter 4. The Fourier transmission coefficient (FTC) is a promising technique,

which constitutes the basis for the new WTC method.

The characteristics of surface wave propagation are studied in Chapter 5, where different wave sources are compared. A theoretical transfer function for Lamb wave propagation, and a theoretical equation for the measurement of material damping ratio are derived.

The experimental setups for the depth evaluation in a concrete plate and the damping measurement in a sand box are given in Chapter 6.

Chapter 7 introduces the basic principles for the numerical finite difference modeling. A commercial software package FLAC ^{TM} (fast Lagrangian analysis of continua) is used for the numerical simulations in this research, and numerical calibrations for the FLAC models are conducted.

The results from the numerical simulations, laboratory and in-situ tests are presented and discussed in Chapter 8.

Finally, the conclusion and recommendation are given in Chapter 9.

Chapter 2

Wave propagation background

2.1 Introduction

Nondestructive techniques based on wave propagation are important because they are non-intrusive, efficient and cost effective. Understanding the fundamentals of wave propagation in an elastic medium is helpful for the application of these techniques in practice.

Nondestructive testing using wave propagation has been practiced for many decades, and the primary purpose was the detection of defects. Waves exist as different solutions to the wave equation of motion. According to particle motions, waves could be compressional waves, shear waves or surface waves; for example, particles for compressional waves move parallel to the wave propagation, particles for shear waves move perpendicular to the wave propagation, and particles for surface waves move elliptically. When applying one traction-free boundary condition to the wave equation of motion, Rayleigh waves as one type of surface waves are solved; therefore, Rayleigh waves exist in a half space. While, Lamb waves are another type of surface waves, which are the solutions to the wave equation of motion with two traction-free boundaries used; therefore, Lamb waves exist in a plate. Lamb waves are also called "plate" waves or guided Lamb waves, because their wave propagation is guided by the finite dimensions of a plate.

This chapter provides background of theoretical equations for the wave propagation in an elastic medium. Two types of surface waves are related to this study: Rayleigh waves as a non-dispersive mode in a half space; Lamb waves as different dispersive modes in a plate. Lamb wave propagation is complicated because of the dispersion and multiple mode participation. However, the wave propagation of the fundamental Lamb modes is similar to Rayleigh waves when the wavelength is small relative to the thickness of a plate. Wave transmission through and wave reflection from an interface between two

different media are introduced, and the transmitted and reflected waves can be evaluated with the transmission and reflection coefficients. The superimposition of the reflected and incident waves before the interface varies with distance.

2.2 Wave propagation fundamentals

2.2.1 Navier's equation

In an elastic, isotropic and homogeneous medium without the presence of a body force, when waves propagate through it, the pressure changes in a small element are related to the acceleration by Newton's law:

$$\sum_{i=1}^{3} F_i = m\, a_i \tag{2.1}$$

where i indicates the elements for the three mutually-perpendicular axes x_1, x_2, and x_3, respectively.

The above equation is rewritten in terms of functions:

$$\sigma_{1i} dx_2 dx_3 + \sigma_{2i} dx_1 dx_3 + \sigma_{3i} dx_1 dx_2 = (\rho dx_1 dx_2 dx_3) \frac{\partial^2 u_i}{\partial t^2} \tag{2.2}$$

where σ_{ji} is the stress in axis x_i and act on a plane with the normal in axis x_j (i, j = 1, 2, and 3); u_i is the displacement in axis x_i; ρ is the mass density of a medium.

By dividing by the volume factor ($dx_1 dx_2 dx_3$) on the both sides of Eq. 2.2, it becomes the equation of wave motion:

$$\sum_{j=1}^{3} \frac{\partial \sigma_{ji}}{\partial x_j} = \rho \frac{\partial^2 u_i}{\partial t^2} \tag{2.3}$$

In the elastic range of an isotropic and homogenous medium, the relation between stress and displacement exist in the generalized Hooke's law:

$$\sigma_{ii} = \lambda\Delta + 2\mu\frac{\partial u_i}{\partial x_i} \tag{2.4a}$$

$$\sigma_{12} = \mu\left(\frac{\partial u_1}{\partial x_2} + \frac{\partial u_2}{\partial x_1}\right) \tag{2.4b}$$

$$\sigma_{13} = \mu\left(\frac{\partial u_1}{\partial x_3} + \frac{\partial u_3}{\partial x_1}\right) \tag{2.4c}$$

$$\sigma_{23} = \mu\left(\frac{\partial u_2}{\partial x_3} + \frac{\partial u_3}{\partial x_2}\right) \tag{2.4d}$$

where i = 1, 2, and 3; λ and μ are the Lame constants; Δ is the dilatation or volumetric strain and it is given:

$$\Delta = \frac{\partial u_1}{\partial x_1} + \frac{\partial u_2}{\partial x_2} + \frac{\partial u_3}{\partial x_3}$$

An isotropic, homogeneous and elastic medium has only two independent material constants λ and μ. For engineering purposes, some authors may use the independent constants: Young's modulus E and Poisson's ratio υ; they are related:

$$\lambda = \frac{E\upsilon}{(1+\upsilon)(1-2\upsilon)} \tag{2.5a}$$

$$\mu = \frac{E}{2(1+\upsilon)} \tag{2.5b}$$

The other three elastic constants commonly used in engineering are shear modulus G, bulk modulus K and constraint modulus M:

$$G = \mu \tag{2.6a}$$

$$K = \frac{E}{3(1-2\upsilon)} \tag{2.6b}$$

$$M = \frac{E(1-\upsilon)}{(1+\upsilon)(1-2\upsilon)} \tag{2.6c}$$

Navier's equation is obtained by substituting Eq. 2.4 into Eq. 2.3:

$$\rho\frac{\partial^2 u_i}{\partial t^2} = (\lambda+\mu)\frac{\partial\Delta}{\partial x_i} + \mu\nabla^2 u_i \tag{2.7}$$

where i = 1, 2, and 3; ∇ is the differential operator, and ∇^2 is the Laplacian operator:

$$\nabla = \frac{\partial}{\partial x_1} + \frac{\partial}{\partial x_2} + \frac{\partial}{\partial x_3}$$

$$\nabla^2 = \frac{\partial^2}{\partial x_1^2} + \frac{\partial^2}{\partial x_2^2} + \frac{\partial^2}{\partial x_3^2}$$

2.2.2 Body waves in a medium

Navier's equation is not a wave equation, but it has a plane wave solution, which is obtained by manipulating the Navier's equation (Eq. 2.7). First, applying the differential operator ∇ to the both sides of the Navier's equation results in:

$$\rho \frac{\partial^2 \Delta}{\partial t^2} = (\lambda + \mu) \frac{\partial^2 \Delta}{\partial^2 x_i} + \mu \frac{\nabla^2 \Delta}{\partial x_i^2} \tag{2.8}$$

where i = 1, 2, and 3.

Furthermore:

$$\frac{\partial^2 \Delta}{\partial t^2} = \frac{\lambda + 2\mu}{\rho} \nabla^2 \Delta \tag{2.9}$$

Then it gives:

$$V_P = \sqrt{\frac{\lambda + 2\mu}{\rho}} = \sqrt{\frac{M}{\rho}} \tag{2.10}$$

Eq. 2.9 implies a strain direction aligned with the wave propagation, and the variation in strain causes a volumetric change in compressional waves (P-waves). The velocity is determined by the constraint modulus M and mass density ρ (Eq. 2.10). The particle motion for P-wave propagation is shown in Fig. 2.1.

Secondly, the Navier's equation (Eq. 2.7) is manipulated with the curl operation on the both sides of the Navier's equation, it gives:

$$\rho \frac{\partial^2 curl(u_i)}{\partial t^2} = (\lambda + \mu)\, curl\left(\frac{\partial \Delta}{\partial x_i}\right) + \mu \nabla^2\, curl(u_i) \tag{2.11}$$

where i = 1, 2, and 3.

The "curl" operates a vector $\vec{v} = (v_1 \quad v_2 \quad v_3)$ as:

$$curl \begin{bmatrix} v_1 \\ v_2 \\ v_3 \end{bmatrix} = \left(\frac{\partial v_3}{\partial x_2} - \frac{\partial v_2}{\partial x_3}\right)\vec{n}_1 + \left(\frac{\partial v_1}{\partial x_3} - \frac{\partial v_3}{\partial x_1}\right)\vec{n}_2 + \left(\frac{\partial v_2}{\partial x_1} - \frac{\partial v_1}{\partial x_2}\right)\vec{n}_3 \tag{2.12}$$

where n_1, n_2, and n_3 are the mutual-perpendicular unit vectors for axes x_1, x_2, and x_3, respectively.

Therefore,

$$curl\left(\frac{\partial \Delta}{\partial x_1}\right) = \frac{\partial}{\partial x_2}\frac{\partial \Delta}{\partial x_3} - \frac{\partial}{\partial x_3}\frac{\partial \Delta}{\partial x_2} = 0 \tag{2.13a}$$

$$curl\left(\frac{\partial \Delta}{\partial x_2}\right) = \frac{\partial}{\partial x_3}\frac{\partial \Delta}{\partial x_1} - \frac{\partial}{\partial x_1}\frac{\partial \Delta}{\partial x_3} = 0 \tag{2.13b}$$

$$curl\left(\frac{\partial \Delta}{\partial x_3}\right) = \frac{\partial}{\partial x_1}\frac{\partial \Delta}{\partial x_2} - \frac{\partial}{\partial x_2}\frac{\partial \Delta}{\partial x_1} = 0 \tag{2.13c}$$

Eq. 2.11 reduces to:

$$\frac{\partial^2 \eta_i}{\partial t^2} = \frac{\mu}{\rho}\nabla^2 \eta_i \tag{2.14}$$

where,

$$\begin{aligned} \eta_1 &= \frac{1}{2}\left(\frac{\partial u_3}{x_2} - \frac{\partial u_2}{x_3}\right) \\ \eta_2 &= \frac{1}{2}\left(\frac{\partial u_1}{x_3} - \frac{\partial u_3}{x_1}\right) \\ \eta_3 &= \frac{1}{2}\left(\frac{\partial u_2}{x_1} - \frac{\partial u_1}{x_2}\right) \end{aligned}$$

Then it gives:

$$V_S = \sqrt{\frac{\mu}{\rho}} \tag{2.15}$$

The curl operation describes the circulations of a vector along a closed loop, which indicates the tendency to be propagating circularly and generates the shear waves (S-waves). Unlike P-waves, the strain direction caused by S-waves is perpendicular to the

wave propagation, and the variation in strain does not cause a volumetric change. The particle motion for S-wave propagation is shown in Fig. 2.2.

The ratio of P-wave to S-wave velocities is given:

$$\frac{V_P}{V_S} = \sqrt{\frac{2(1-\upsilon)}{1-2\upsilon}} \tag{2.16}$$

2.2.3 Helmholtz equation

To solve two dimensional (2D) problems of wave propagation using the Navier's equation for an elastic isotropic medium, the displacements can be represented in terms of the potential functions $\varphi(x_1,x_2)$ and $\psi(x_1,x_2)$. The horizontal component parallel to the surface of a medium is represented by axis x_1 and vertical component perpendicular to the surface by axis x_2. There is no displacement in axis x_3 ($u_3 = 0$) for a two dimensional problem.

$$u_1 = \frac{\partial\varphi(x_1,x_2)}{\partial x_1} + \frac{\partial\psi(x_1,x_2)}{\partial x_2} \tag{2.17a}$$

$$u_2 = \frac{\partial\varphi(x_1,x_2)}{\partial x_2} - \frac{\partial\psi(x_1,x_2)}{\partial x_1} \tag{2.17b}$$

As an advantage for such potential functions, the following Helmholtz equation must hold in order to satisfy Navier's equation (Eq. 2.7):

$$\frac{\partial^2\varphi(x_1,x_2)}{\partial t^2} = V_P\nabla^2\varphi(x_1,x_2) \tag{2.18a}$$

$$\frac{\partial^2\psi(x_1,x_2)}{\partial t^2} = V_S\nabla^2\psi(x_1,x_2) \tag{2.18b}$$

Substituting Eq. 2.17 into the generalized Hooke's law (Eq. 2.4) results in:

$$\sigma_{11} = \mu\left[\left(\frac{V_P}{V_S}\right)^2\nabla^2\varphi(x_1,x_2)+2\left(\frac{\partial^2\psi(x_1,x_2)}{\partial x_1x_2}-\frac{\partial^2\varphi(x_1,x_2)}{\partial x_2^2}\right)\right] \quad (2.19a)$$

$$\sigma_{22} = \mu\left[\left(\frac{V_P}{V_S}\right)^2\nabla^2\varphi(x_1,x_2)-2\left(\frac{\partial^2\psi(x_1,x_2)}{\partial x_1x_2}-\frac{\partial^2\varphi(x_1,x_2)}{\partial x_2^2}\right)\right] \quad (2.19b)$$

$$\sigma_{12} = \mu\left[2\left(\frac{\partial^2\varphi(x_1,x_2)}{\partial x_1x_2}+\frac{\partial^2\psi(x_1,x_2)}{\partial x_2^2}-\frac{\partial^2\psi(x_1,x_2)}{\partial x_1^2}\right)\right] \quad (2.19c)$$

2.3 Rayleigh waves in a half-space

The Rayleigh waves (R-waves) propagate along one traction-free surface of a half-space and decay with depth. *Rayleigh* (1885) first discovered these waves by choosing the potential functions as:

$$\varphi(x_1,x_2) = A\exp(-\alpha x_2)\exp[j(\kappa x_1-\omega t)] \quad (2.20a)$$

$$\psi(x_1,x_2) = B\exp(-\beta x_2)\exp[j(\kappa x_1-\omega t)] \quad (2.20b)$$

where,

$$\alpha^2=\kappa^2-\frac{\omega^2}{V_P^2} \qquad \beta^2=\kappa^2-\frac{\omega^2}{V_S^2} \qquad \kappa=\frac{\omega}{V_R} \quad (2.21)$$

and j is the imaginary unit; t is the time; ω is the angular frequency; κ is the wave number; V_R is the R-wave velocity; A and B are the constants; x_1 and x_2 are the horizontal and vertical axes, respectively.

The potential functions (Eq. 2.20) satisfy both the Helmholtz equation (Eq. 2.18) and Eq. 2.19 with the boundary conditions as $\sigma_{22} = \sigma_{12} = 0$ at $x_2 = 0$, which locates the traction-free surface, if the following Rayleigh-frequency equation is true:

$$\left[2-\left(\frac{V_R}{V_S}\right)^2\right]^4 = 16\left[1-\left(\frac{V_R}{V_P}\right)^2\right]\left[1-\left(\frac{V_R}{V_S}\right)^2\right] \quad (2.22)$$

The R-wave velocity (V_R) depends on the P-wave and S-wave velocities (V_P and V_S). For an isotropic, homogeneous and elastic medium, an approximate expression for the ratio of V_R to V_S is related to the Poisson's ratio υ as:

$$\frac{V_R}{V_S} = \frac{0.862 + 1.14\upsilon}{1+\upsilon} \tag{2.23}$$

Substituting the potential functions (Eq. 2.20) into Eq. 2.17 results in the horizontal displacement u_1 and the vertical displacements u_2 for the R-waves:

$$u_1 = C\kappa j\left[-\exp(-\alpha x_2) + \frac{2\alpha\beta}{\beta^2+\kappa^2}\exp(-\beta x_2)\right]\exp[j(\omega t - \kappa x_1)] \tag{2.24a}$$

$$u_2 = C\kappa\left[-\frac{\alpha}{\kappa}\exp(-\alpha x_2) + \frac{2\alpha\kappa}{\beta^2+\alpha^2}\exp(-\beta x_2)\right]\exp[j(\omega t - \kappa x_1)] \tag{2.24b}$$

where C is the constant; α and β are defined in Fig. 2.21. The particle motion for R-wave propagation is shown in Fig. 2.3.

If u_{10} and u_{20} represent the horizontal and vertical displacement amplitudes at the surface ($x_2 = 0$), respectively, by normalizing the horizontal (u_1) and vertical displacement (u_2) amplitudes at a depth in axis x_2 to the surface as u_1/u_{10} and u_2/u_{20}, and normalizing the depth to the R-wavelength (λ_R), the normalized displacement vs. normalized depth is plotted for different Poisson's ratios in Fig. 2.4. Near the subsurface, an elliptical particle motion with a retrograde rotation is generated because of positive vertical displacements ($u_2 > 0$) and negative horizontal displacements ($u_1 > 0$). This motion is reversed at greater depths where horizontal displacements become positive. This phenomenon happens earlier when Poisson's ratio is larger.

2.4 Lamb waves in a plate

2.4.1 Basic principles

In a plate, a series of reflected and mode-converted body waves (P- and S- waves) are generated. These waves interact with each other and the two parallel traction-free surfaces of a plate to form new wave modes propagating along the two surfaces in axis x_1, which are called Lamb or plate waves.

The potential functions are chosen for this case as below (*Graff* 1991), where the origin of the vertical axis ($x_2 = 0$) is defined at half the thickness of a plate.

$$\varphi(x_1,x_2) = f(x_2)\exp[j(\omega t - \kappa x_1)] \tag{2.25a}$$
$$\psi(x_1,x_2) = g(x_2)\exp[j(\omega t - \kappa x_1)] \tag{2.25b}$$

Substituting Eq. 2.25 into the Helmholtz equation (Eq. 2.18) results in the two sets of equations for functions $f(x_2)$ and $g(x_2)$:

$$f(x_2) = A\cosh(\alpha x_2) \tag{2.26a}$$
$$g(x_2) = B\sinh(\beta x_2) \tag{2.26b}$$

$$f(x_2) = C\sinh(\alpha x_2) \tag{2.27a}$$
$$g(x_2) = D\cosh(\beta x_2) \tag{2.27b}$$

where A, B, C, and D are the constants; α and β are defined in Fig. 2.21.

With the boundary conditions: $\sigma_{22} = \sigma_{12} = 0$ at two surfaces of a plate, where $x_2 = \pm h$ and h is half the plate thickness, the potential functions (Eq. 2.25) and Eqs. 2.26 and 2.27 must satisfy Eq. 2.19, which yields Rayleigh-Lamb-frequency equation:

$$\frac{\tan(\beta h)}{\tan(\alpha h)} + \left[\frac{4\kappa^2\alpha\beta}{(\beta^2-\kappa^2)^2}\right]^{\pm 1} = 0 \tag{2.28}$$

where the wave number $\kappa = \omega/V_{ph}$, V_{ph} is the phase velocity of Lamb waves; α and β are defined in Fig. 2.21; the exponent $+1$ represents the solution for the symmetric Lamb modes using Eq. 2.26; while the exponent -1 represents the solution for the anti-symmetric Lamb modes using Eq. 2.27. The symmetric Lamb modes generate waves with symmetric thickness variation with respect to a plane at the middle thickness of a plate (Fig. 2.5); while the anti-symmetric Lamb modes generate a bending deformation of the plate as it propagates.

If the frequency is sufficiently high, or equivalently the wavelength is sufficiently small, $\tan(\alpha h) \approx \tan(\beta h) \approx 1$, the Rayleigh-Lamb-frequency equation (Eq. 2.28) reduces to Rayleigh-frequency equation (Eq. 2.22). It implies that the plate thickness appears to be large for high frequency components, and they propagate as R-waves in a plate independently on the top surface without any interference from the bottom surface.

For low frequencies, the following conditions are considered approximately true (*Viktorov* 1967):

$$\tan(\alpha h) \approx \alpha h(1+\frac{1}{3}\alpha^2 h^2) \tag{2.29a}$$

$$\tan(\beta h) \approx \beta h(1+\frac{1}{3}\beta^2 h^2) \tag{2.29b}$$

By substituting the above equation into the Rayleigh-Lamb-frequency equation (Eq. 2.28), the velocities for the global vibration modes: the extensional vibration mode V_{EXT} (symmetric mode) and the flexural vibration mode V_{FLX} (anti-symmetric mode) are:

$$V_{EXT} = \sqrt{\frac{E}{\rho(1-\upsilon^2)}} \tag{2.30a}$$

$$V_{FLX} = \kappa h\sqrt{\frac{E}{3\rho(1-\upsilon^2)}} \tag{2.30b}$$

The extensional vibration mode is non-dispersive; while the flexural vibration mode remains dispersive because of the wave number κ involved in the calculation of V_{FLX}.

The Rayleigh-Lamb-frequency equation (Eq. 2.28) is governed by three parameters: P-and S-wave velocities (V_P and V_S), and half the plate thickness (h). This equation is considered as relating the frequency ω to the wave number κ, resulting in the frequency spectrum, or as relating the frequency ω to the phase velocity of Lamb waves V_{ph}, resulting in the dispersion curves. As different solutions to Eq. 2.28, Lamb modes exist, differing from one another by their dispersion curves and contribution of the displacements throughout the thickness of a plate.

By substituting the potential functions (Eq. 2.25), Eqs. 2.26 and 2.27 into Eq. 2.17, the horizontal displacement u_1 and vertical displacement u_2 are calculated.

For symmetric Lamb modes:

$$u_1 = A\kappa\left[\frac{\cosh(\alpha x_2)}{\sinh(\alpha h)} - \frac{2\alpha\beta}{\kappa^2+\beta^2}\frac{\cosh(\beta x_2)}{\sinh(\beta h)}\right]\exp[j(\kappa x_1 - \omega t - \frac{\pi}{2})] \tag{2.31a}$$

$$u_2 = -A\alpha\left[\frac{\sinh(\alpha x_2)}{\sinh(\alpha h)} - \frac{2\beta^2}{\kappa^2+\beta^2}\frac{\sinh(\beta x_2)}{\sinh(\beta h)}\right]\exp[j(\kappa x_1 - \omega t)] \tag{2.31b}$$

For anti-symmetric Lamb modes:

$$u_1 = B\kappa\left[\frac{\sinh(\alpha x_2)}{\cosh(\alpha h)} - \frac{2\alpha\beta}{\kappa^2+\beta^2}\frac{\sinh(\beta x_2)}{\cosh(\beta h)}\right]\exp[j(\kappa x_1 - \omega t - \frac{\pi}{2})] \quad (2.32a)$$

$$u_2 = -B\alpha\left[\frac{\cosh(\alpha x_2)}{\cosh(\alpha h)} - \frac{2\beta^2}{\kappa^2+\beta^2}\frac{\cosh(\beta x_2)}{\cosh(\beta h)}\right]\exp[j(\kappa x_1 - \omega t)] \quad (2.32b)$$

where A and B are the arbitrary constants. There is a phase difference of $\pi/2$ between the horizontal and vertical displacements for both the symmetric and the anti-symmetric Lamb modes.

2.4.2 Calculation of dispersion curves

For any given frequency, there are an infinite number of wave numbers that satisfy the Rayleigh-Lamb-frequency equation (Eq. 2.28), and they might be complex, for example, $\kappa = \kappa_{re} + j\kappa_{im}$, where κ_{re} and κ_{im} are the real and imaginary parts, respectively. Therefore, a harmonic time signal propagating in the horizontal axis x_1 is expressed:

$$\exp[j(\kappa x_1 - \omega t)] = \exp[j(\kappa_{re} x_1 - \omega t)]\exp(-\kappa_{im} x_1)$$

A physical interpretation is discussed for three possible cases (*Rose* 1999):

1. $\kappa_{im} < 0$: the waves grow exponentially with distance. They have not been physically observed.
2. $\kappa_{im} > 0$: the waves decay exponentially with distance. They are called evanescent waves, and disappear rapidly.
3. $\kappa_{im} = 0$: the waves propagate with no attenuation. Only real wave numbers supply the information about the propagating waves.

For the propagating Lamb waves ($\kappa_{im} = 0$), the Rayleigh-Lamb-frequency equation (Eq. 2.28) becomes the following equations, which are used for the calculation of the dispersion curves (*Rose* 1999).

For symmetric Lamb modes:

$$F_{sym}(\omega, V_{ph}) = \frac{\tan(\beta h)}{\beta} + \frac{4\frac{\omega^2}{V_{ph}^2}\alpha\tan(\alpha h)}{\left(\beta^2 - \frac{\omega^2}{V_{ph}^2}\right)^2} = 0 \tag{2.33}$$

For anti-symmetric Lamb modes:

$$F_{anti}(\omega, V_{ph}) = \tan(\beta h)\beta + \frac{\left(\beta^2 - \frac{\omega^2}{V_{ph}^2}\right)^2 \tan(\alpha h)}{4\alpha\left(\frac{\omega^2}{V_{ph}^2}\right)^2} = 0 \tag{2.34}$$

The calculation of dispersion curves for Lamb waves is implemented using the commercial software MathCAD ^{TM}, and the algorithm is described in Fig. 2.6. The frequencies and phase velocities are digitized in a range with an appropriate increment. Because the functions given in Eqs. 2.33 and 2.34 are continuous, a change of the phase velocities in sign for each frequency is accomplished by a crossing through zero. Therefore, a root exists in the interval of phase velocities where the sign changes. This interval is used in a root function to locate precisely the phase velocity, and then the root is taken as a solution to Eqs. 2.33 and 2.34 for each frequency.

For a typical concrete plate, which is assumed isotropic and homogenous, three parameters are given for the calculation of dispersion curves for Lamb waves: P-wave velocity $V_P = 4800m/s$, S-wave velocity $V_S = 2770m/s$, and half the plate thickness $h = 40mm$. Other elastic constants are calculated: Poisson's ratio $\upsilon = 0.25$, Young's modulus $E = 45GPa$, R-wave velocity $V_R = 2550m/s$, the velocity for the extensional vibration mode, $V_{EXT} = 4524m/s$, and the velocity for flexural vibration mode at frequency $500Hz$, $V_{FLX} = 572.9m/s$. The dispersion curves are shown in Fig. 2.7 for this concrete plate.

Fundamental symmetric Lamb mode S0 starts from low frequency with the highest phase velocity that is close to V_{EXT}, and then the phase velocity decreases with frequency; while fundamental anti-symmetric Lamb mode A0 starts from low frequency with the lowest phase velocity, which is close to V_{FLX} for frequency at $500Hz$, and then the phase velocity increases with frequency. Finally, the fundamental Lamb modes (S0 and A0) converge to the value of V_R at frequencies larger than $f = 60kHz$; the corresponding wavelength ($\lambda_R = 42.5mm$) is close to half the plate thickness $h = 40mm$. It indicates a non-dispersion behavior of the fundamental Lamb modes as the Rayleigh wave mode occurring at high frequencies. Higher Lamb modes (symmetric modes Si and anti-symmetric modes Ai, where $i > 0$) first appear at different frequencies that are called

critical frequencies, where the phase velocity goes to infinity, and then the corresponding phase velocity decreases to S-wave velocity V_S (*Viktorov* 1967) as the frequency goes to infinity.

2.4.3 Determination of mode numbers

The critical frequencies for higher Lamb modes are given by a factor of P- or S-wavelengths, which are related to half the plate thickness (h) as (*Viktorov* 1967):

For Symmetric Lamb modes:

$$2h = \frac{1}{2}\lambda_P, \frac{3}{2}\lambda_P, \frac{5}{2}\lambda_P \ldots \quad (2.35a)$$

$$2h = \lambda_S, 2\lambda_S, 3\lambda_S \ldots \quad (2.35b)$$

For Anti-symmetric Lamb modes:

$$2h = \lambda_P, 2\lambda_P, 3\lambda_P \ldots \quad (2.36a)$$

$$2h = \frac{1}{2}\lambda_S, \frac{3}{2}\lambda_S, \frac{5}{2}\lambda_S \ldots \quad (2.36b)$$

where λ_P and λ_S are the P- and S-wavelengths, respectively.

$$\lambda_P = 2\pi\frac{V_P}{\omega} \quad \lambda_S = 2\pi\frac{V_S}{\omega}$$

The total numbers of symmetric Lamb modes N_{sym} and anti-symmetric Lamb modes N_{anti} that are possible in a plate are given:

$$N_{sym} = 1 + round\left(\frac{2h}{\lambda_S}\right) + round\left(\frac{2h}{\lambda_P} + \frac{1}{2}\right) \quad (2.37a)$$

$$N_{anti} = 1 + round\left(\frac{2h}{\lambda_P}\right) + round\left(\frac{2h}{\lambda_S} + \frac{1}{2}\right) \quad (2.37b)$$

where the "round" function gives the nearest integer part of the number that are enclosed. For the case given in Fig. 2.7, the numbers of Lamb modes are calculated in Fig. 2.8.

2.4.4 Calculation of displacement vs. depth

The horizontal and vertical displacement amplitudes vs. depth are calculated according to Eqs. 2.31 and 2.32, where for each Lamb mode the wave number or the phase velocity is a function of frequency that is determined by the dispersion curve. For the case given in Fig. 2.7, the results of normalized displacement amplitude vs. normalized depth for frequencies at $50kHz$ and $100kHz$ are shown in Fig. 2.9 for the fundamental Lamb mode S0, and in Fig. 2.10 for the higher Lamb mode S1. The horizontal axis in the plot represents the displacement amplitude (u_1 or u_2) that is normalized to the horizontal displacement amplitude at surface, which is denoted as u_{S0} or u_{S1}; while the vertical axis (x_2) represents a depth that is normalized to the S0 or S1 wavelength (λ_{ph}). The phase velocity (V_{ph}) at a certain frequency is measured from the dispersion curves. For a comparison, the R-wave displacement amplitude is also shown. For $50kHz$, R-wave and S0 mode match well for normalized depths smaller than $1/3$; for $100kHz$, they match well up to the center of the plate (normalized depth $d/\lambda = 1.57$). However, displacements for higher Lamb mode S1 show more variations with respect to the normalized depth. Horizontal displacements of the Lamb modes are symmetric to a horizontal plane at half the thickness; while vertical displacements of the Lamb modes are anti-symmetric to a horizontal plane at half the thickness.

2.5 Wave transmission and reflection

In Fig. 2.11, a plane harmonic wave propagates in axis x_1 at a normal incidence through an interface between two media, which have the wave velocities V_1 and V_2, and mass densities ρ_1 and ρ_2, respectively. The displacements of incident (u_{in}), reflected (u_{re}) and transmitted (u_{tr}) waves are expressed:

$$u_{in}(x_1,t) = A_{in}\exp[j(\kappa_1 x_1 - \omega t)] \tag{2.38a}$$

$$u_{re}(x_1,t) = -A_{re}\exp[j(-\kappa_1 x_1 - \omega t)] \tag{2.38b}$$

$$u_{tr}(x_1,t) = A_{tr}\exp[j(\kappa_2 x_1 - \omega t)] \tag{2.38c}$$

where κ_1 and κ_2 are the wave numbers for the wave propagation in two different media; A_{in}, A_{re} and A_{tr} are the amplitudes for incident, reflected and transmitted waves, respectively.

If the displacement u_1 is the only non-zero displacement component, the plane stress σ_{11} is given from Eq. 2.4:

$$\sigma_{11} = (\lambda + 2\mu)\frac{\partial u_1}{\partial x_1} = \rho V_1^2 \frac{\partial u_1}{\partial x_1} \tag{2.39}$$

A continuity condition must hold: both the displacements and the stresses are continuous at the interface between two different elastic media, thus:

$$\begin{aligned} u_{in}(x_1,t) + u_{re}(x_1,t) &= u_{tr}(x_1,t) && \text{(2.40a)} \\ \rho_1 V_1^2 \frac{\partial u_{in}(x_1)}{\partial x_1} + \rho_1 V_1^2 \frac{\partial u_{re}(x_1)}{\partial x_1} &= \rho_2 V_2^2 \frac{\partial u_{tr}(x_1)}{\partial x_1} && \text{(2.40b)} \end{aligned}$$

By substituting Eq. 2.38 into Eq. 2.40, the following equations are true at the interface $x_1 = 0$:

$$\begin{aligned} A_{in} - A_{re} &= A_{tr} && \text{(2.41a)} \\ \rho_1 V_1^2 A_{in} + \rho_1 V_1^2 A_{re} &= \rho_2 V_2^2 A_{tr} && \text{(2.41b)} \end{aligned}$$

Solving the above equation allows the reflection coefficient Re and transmission coefficient Tr defined as:

$$\begin{aligned} Re &= \frac{A_{re}}{A_{in}} = \frac{\rho_2 V_2 - \rho_1 V_1}{\rho_2 V_2 + \rho_1 V_1} = \frac{1 - (z_1/z_2)}{1 + (z_1/z_2)} && \text{(2.42a)} \\ Tr &= \frac{A_{tr}}{A_{in}} = \frac{2\rho_1 V_1}{\rho_2 V_2 + \rho_1 V_1} = \frac{2(z_1/z_2)}{1 + (z_1/z_2)} && \text{(2.42b)} \end{aligned}$$

where,

$$z_1 = \rho_1 V_1 \quad z_2 = \rho_2 V_2 \tag{2.43}$$

and z_1 and z_2 are the acoustic impedances for the first medium and the second medium, respectively.

The reflection and transmission coefficients Re and Tr depend only on a ratio of the acoustic impedances (z_1/z_2). The relation of Re and Tr vs. the acoustic impedance ratio (z_1/z_2) is plotted in Fig. 2.12. Two coefficients are identical at $z_1/z_2 = 1/3$, where $Re = Tr = 0.54$; two media are uniform when $z_1/z_2 = 1$, resulting in $Tr = 1$ and $Re = 0$.

For a free surface, for example a solid-to-air interface, it is considered: $(z_1/z_2) \rightarrow \infty$; then it follows: $Re \rightarrow -1$, $Tr \rightarrow 2$, $A_{re} \approx -A_{in}$ and $A_{tr} \approx 2A_{in}$. The total displacement on the solid side at the interface ($x_1 = 0$) is almost double that of the incident waves:

$$u_{in}(x_1 = 0) + u_{re}(x_1 = 0) = A_{in} - A_{re} = 2A_{in} \tag{2.44}$$

The condition of the displacement continuity is satisfied because of an equal displacement amplitude ($2A_{in}$) occurred on both sides of the interface. The propagating wave is doubled when it encounters a free surface.

When a wave propagates into a rigid medium, for example, $(z_1/z_2) \rightarrow 0$ for an air-to-solid interface; then it follows: $Re \approx 1$ and $Tr \approx 0$. The total displacement at the both sides of the interface is approximately zero. Therefore, to induce waves into a medium from a transducer, the use of a coupling agent is necessary.

The presence of a surface-breaking crack provides two traction-free boundaries on the both edges of the crack, which blocks the passage of waves through the crack (the wave propagation is perpendicular to the crack). If a harmonic wave propagates as a normal incidence to the crack, the reflected wave propagates to opposite with a phase shifted by π. (Eq. 2.38). As a result, the incident and reflected waves are superimposed at locations before the crack. A ratio of the displacement amplitudes between the superimposed waves, $u_{in}(x_1,t) + u_{re}(x_1,t)$, and the incident wave, $u_{in}(x_1,t)$ is plotted in Fig. 2.13, where the horizontal axis is the distance from the crack that is normalized to half the wavelength $\lambda/2$. The two waves are in phase at distances multiple of $\lambda/2$, where the displacement amplitudes for the superimposed waves is doubled that of the incident wave, a phenomenon called constructive interference or amplification; whereas, they are out of phase at distances multiple of $\lambda/2$ plus one quarter of the wavelength $\lambda/4$, a phenomenon called destructive interference or de-amplification.

2.6 Summary

Waves are complicated because different geometries and boundary conditions of a medium can be applied to the wave equation of motion. Basically, a point load acting on the surface of a medium generates two types of waves: body waves, which propagate spherically from the source, and surface waves, which propagate cylindrically from the source. Body waves can be compressional waves or shear waves. Body waves are non-dispersive and their velocities depend only on elastic constants of the medium. As one type of surface

waves, Rayleigh waves exist in a half space where only one traction-free surface boundary is present; another type of surface waves are Lamb waves, which exist in a plate with two traction-free surface boundaries. Rayleigh waves are non-dispersive in a homogeneous medium; while Lamb waves are generally dispersive. A half-space does not exist in reality; however, when the wavelength is small compared to the thickness of a plate, the wave propagation of fundamental Lamb modes is similar to the Rayleigh wave. The dispersion curves of Lamb modes are used to find a frequency where the fundamental Lamb modes and Rayleigh wave mode can be comparable.

An interface is formed between two different media. When a wave propagates at a normal incidence through the interface, wave reflection and transmission occur. For locations before the interface, the incident and reflected waves are superimposed, causing construction and destructive interferences.

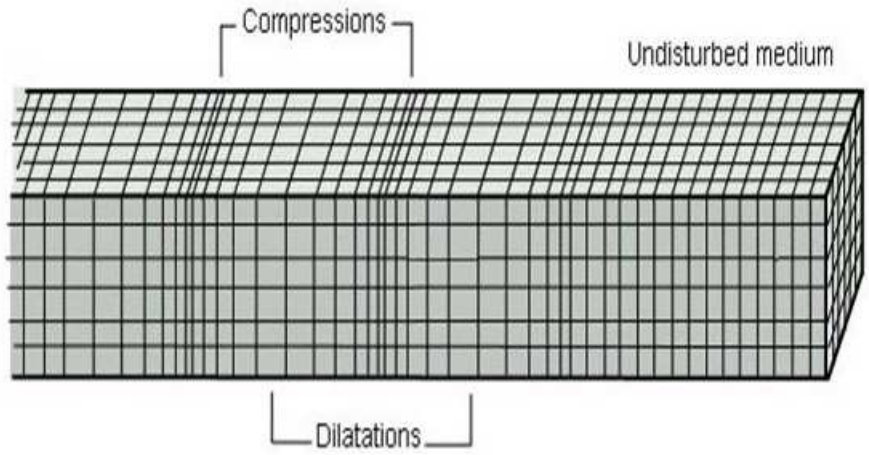

Figure 2.1: Particle motion for compressional wave (P-wave) propagation (http://www.picsearch.com).

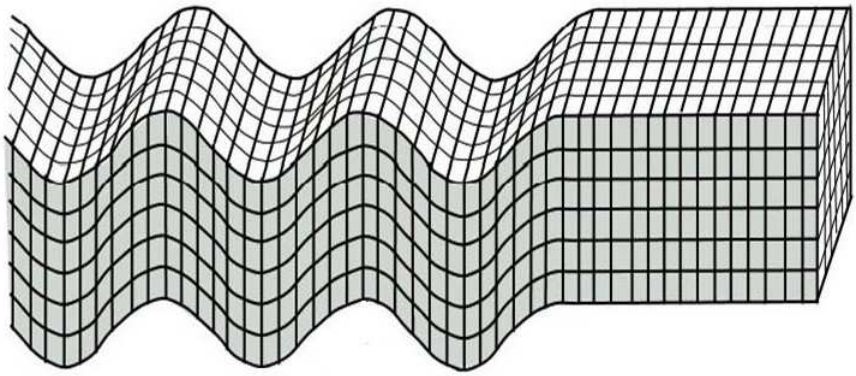

Figure 2.2: Particle motion for shear wave (S-wave) propagation (http://www.picsearch.com).

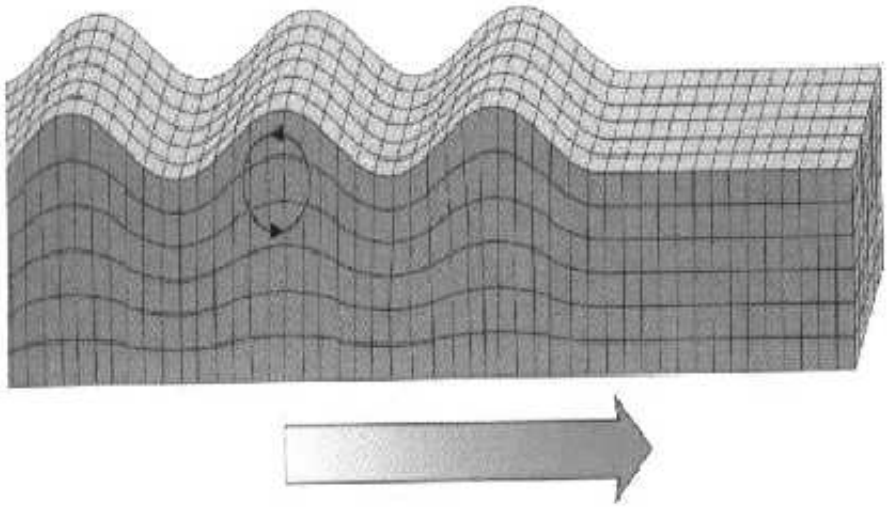

Figure 2.3: Particle motion for Rayleigh wave propagation (http://www.picsearch.com).

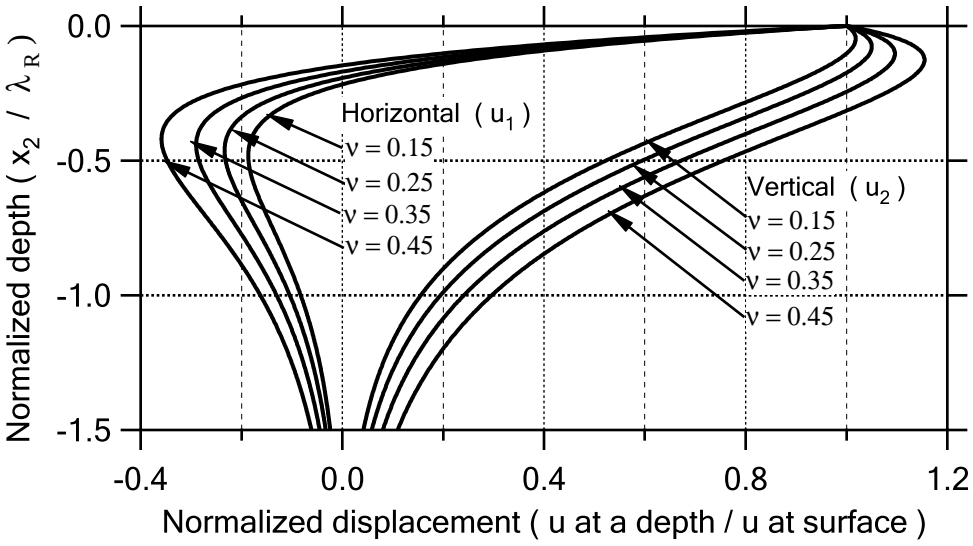

Figure 2.4: Normalized horizontal (u_1) and vertical (u_2) displacement amplitudes vs. normalized depth (x_2/λ_R) for different Poisson's ratios.

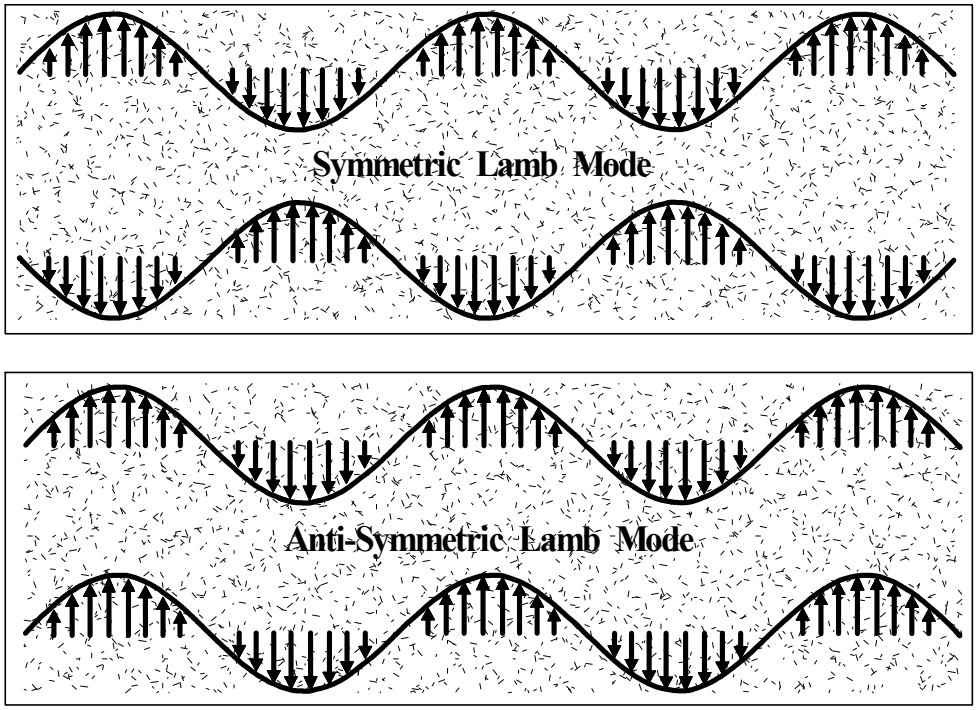

Figure 2.5: Symmetric and anti-symmetric Lamb mode variations in a plate.

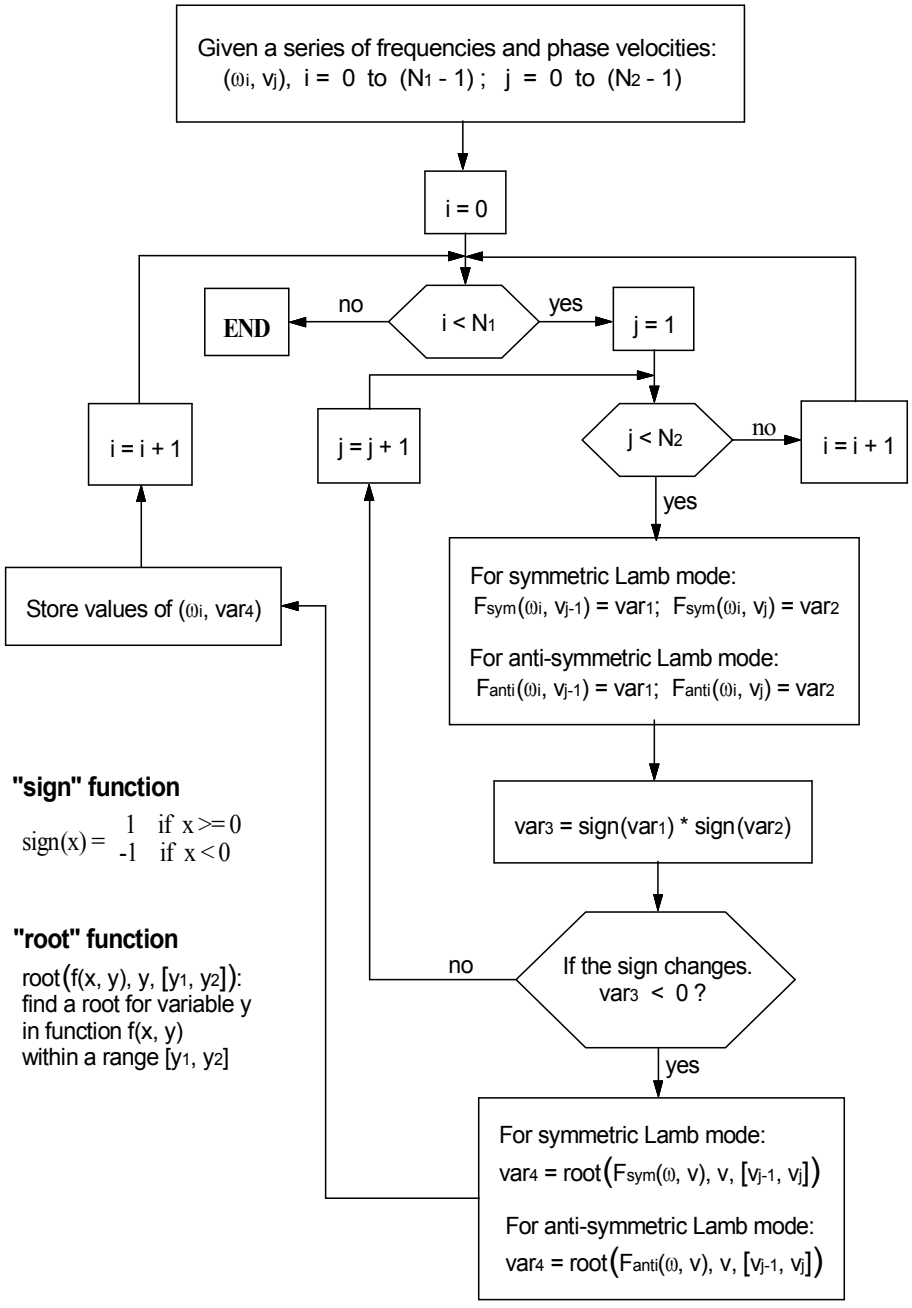

Figure 2.6: Algorithm for the calculation of the dispersion curves for Lamb waves.

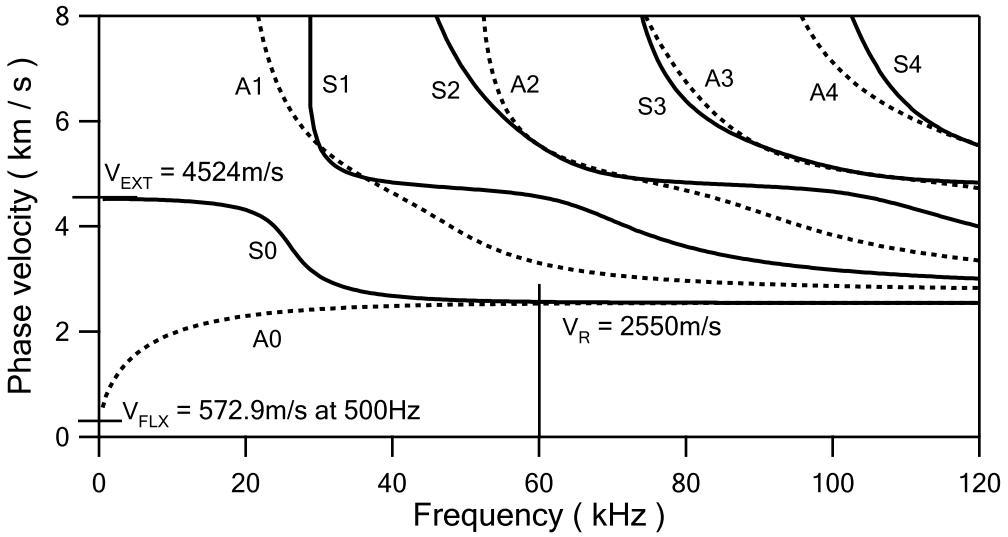

Figure 2.7: Dispersion curves for Lamb waves for a typical concrete plate with given parameters: half the thickness $h = 40mm$, P-wave velocity $V_P = 4800m/s$, and S-wave velocity $V_S = 2770m/s$

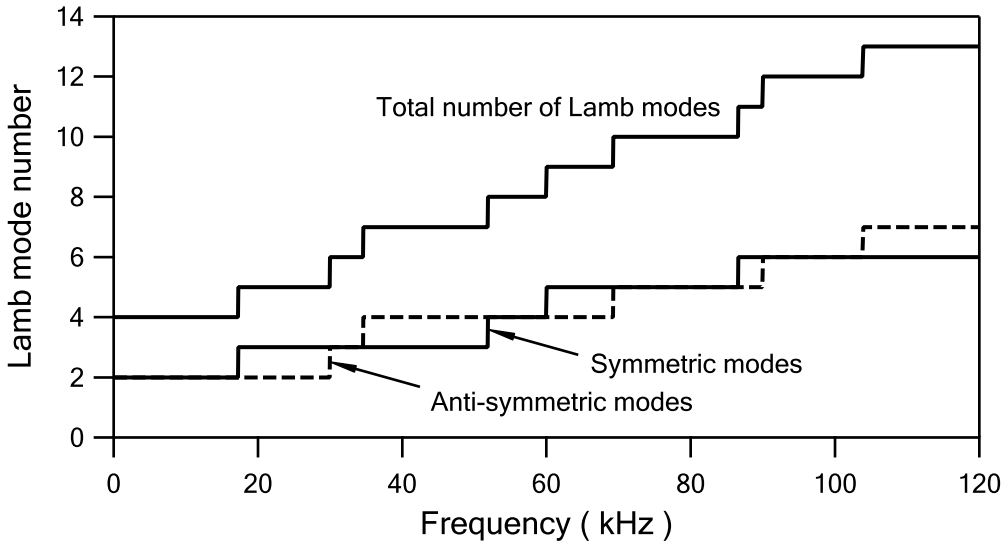

Figure 2.8: Numbers for symmetric Lamb modes, anti-symmetric Lamb modes and the total Lamb modes for the case given in Fig. 2.7.

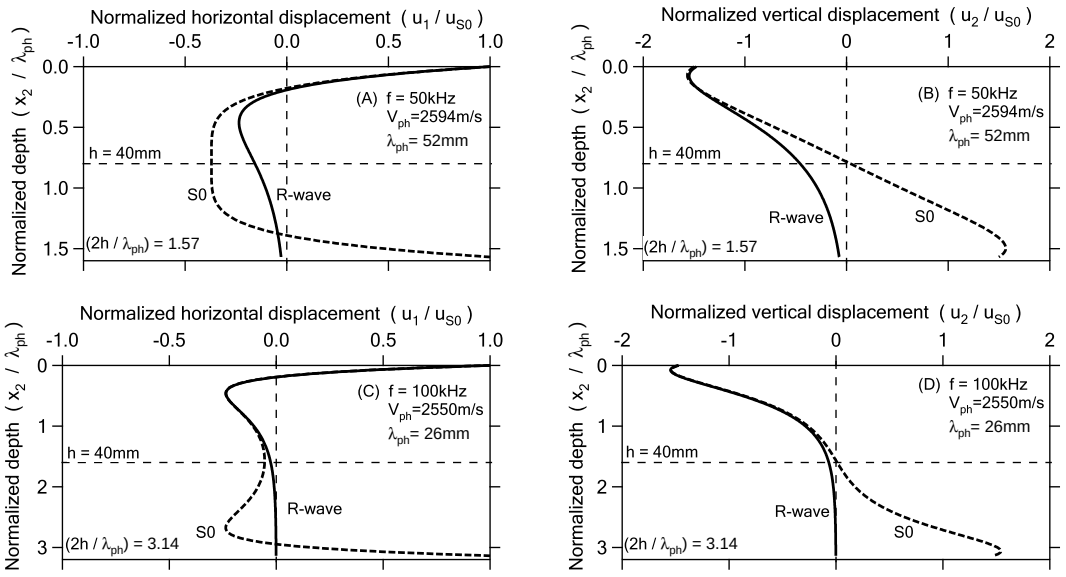

Figure 2.9: Comparison of the horizontal and vertical displacement amplitudes between the fundamental Lamb mode S0 and R-wave mode. The horizontal axis is normalized to the S0 horizontal displacement amplitude at surface (u_{S0}); while the vertical axis is normalized to the S0-wavelength (λ_{ph}).

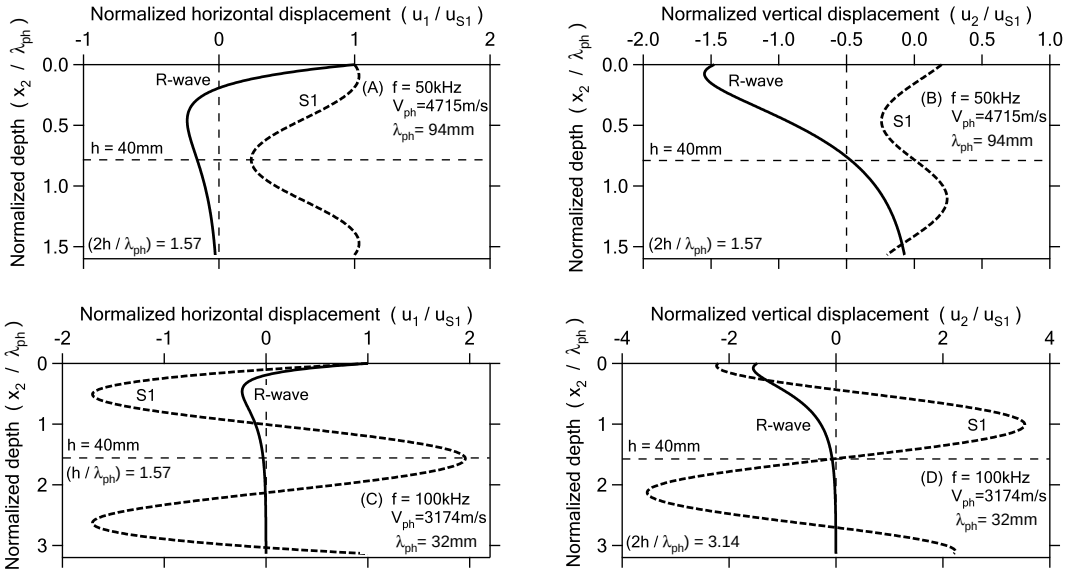

Figure 2.10: Comparison of the horizontal and vertical displacement amplitudes between the Lamb mode S1 and R-wave mode. The horizontal axis is normalized to the S1 horizontal displacement amplitude at surface (u_{S1}); while the vertical axis is normalized to the S1-wavelength (λ_{ph}).

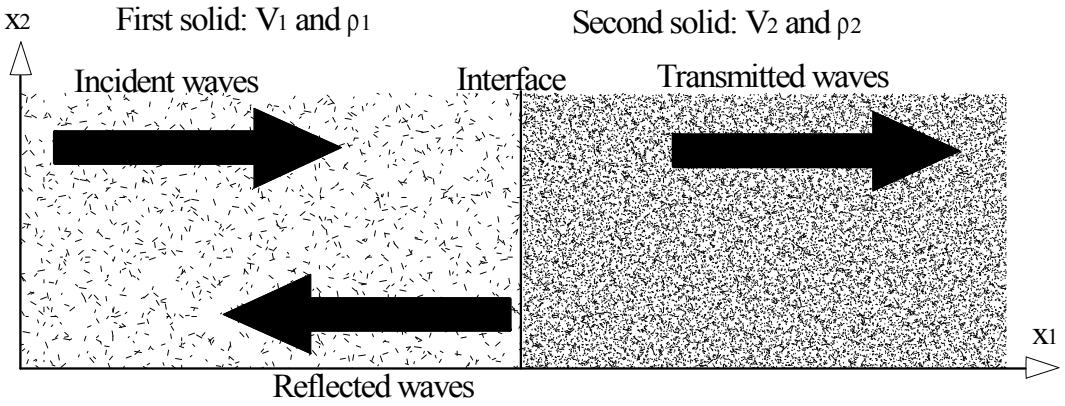

Figure 2.11: Wave transmission through and reflection from an interface between two different media.

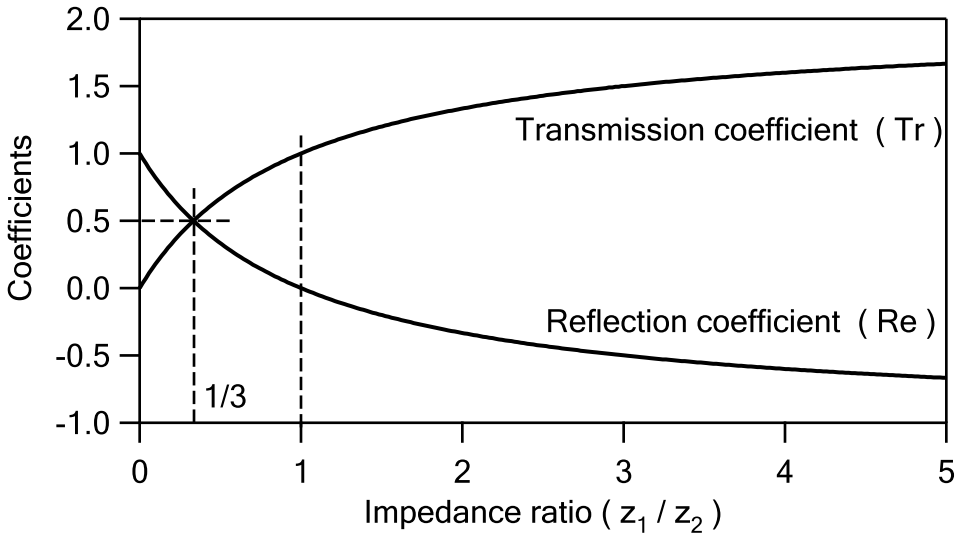

Figure 2.12: Wave transmission and reflection coefficients vs. acoustic impedance ratio for two different media.

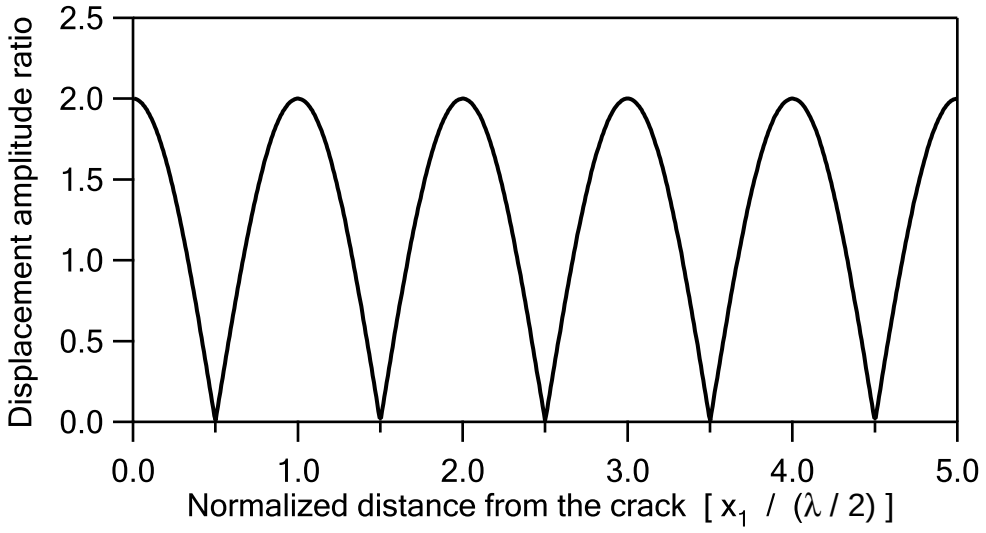

Figure 2.13: Ratio of superimposed waves to incident wave vs. normalized distance from a crack.

Chapter 3

Signal processing techniques

3.1 Introduction

The measured time signals can be analyzed with signal processing techniques to extract useful information for nondestructive tests. This chapter presents an introduction to Fourier transform that relates the time domain to the frequency domain, two-dimensional (2D) Fourier transform that relates the time-space domain to the frequency-wave number domain, the short-time Fourier transform that is also called windowed Fourier transform, and the wavelet transform that keeps both the time and frequency information. Finally, the spectral analysis of surface waves is discussed.

3.2 Fourier transform

3.2.1 1D Fourier transform

As a common technique in signal processing, the Fourier transform (FT) compares the time signals $g(t)$ with a set of complex exponentials $exp(-j\omega t)$ by doing a convolution. Then, the frequency spectrum $G(\omega)$ is obtained, which reflects the similarity between the time signal and each complex exponential, as well as the energy of a given complex exponential function in the original time signal. It is calculated in time:

$$G(\omega) = \int_{-\infty}^{\infty} g(t) \exp(-j\omega t) dt \tag{3.1}$$

where j is the imaginary unit; t is the time; ω is the angular frequency.

The inverse Fourier transform is calculated in frequency:

$$g(t) = \frac{1}{2\pi}\int_{-\infty}^{\infty} G(\omega)\exp(j\omega t)d\omega \tag{3.2}$$

If the time signal $g(t)$ is real, it holds: $G(\omega) = G^*(-\omega)$, and vice versa, where the star sign denotes the complex conjugate.

In practice, the time signal $g(t)$ is always collected and stored in a digital form; therefore, the Fourier transform and the inverse Fourier transform are implemented in a discrete form (*Santamarina* 1998):

$$G(n\Delta f) = \Delta t \sum_{i=0}^{N-1} g(i\Delta t)\exp(-j2\pi i\frac{n}{N}) \tag{3.3a}$$

$$g(n\Delta t) = \frac{1}{N\Delta t}\sum_{i=0}^{N-1} G(i\Delta f)\exp(j2\pi i\frac{n}{N}) \tag{3.3b}$$

where,

$$n = 0,\ 1,\ 2,\ \ldots N-1$$

and N is the total number of sampled points; Δt and Δf are the intervals in time and in frequency, respectively. Because they are reciprocally related as below, a trade-off should be considered to achieve a good resolution both in time and frequency for the Fourier transform.

$$\Delta t = \frac{1}{N\Delta f} \tag{3.4}$$

A Nyquist criterion is satisfied to avoid a phenomenon called "aliasing", so as to retain all frequency components of interests in the results of the Fourier transform. It requires the frequency of interests (f) be lower than the Nyquist frequency, which is equal to half the sampling frequency, $f_{nyqu} = f_{samp}/2$.

$$f < f_{nyqu} \tag{3.5}$$

The results in frequency from the discrete Fourier transform are composed of a series of complex numbers:

$$G(i\Delta f) = Re\left[G(i\Delta f)\right] + jIm\left[G(i\Delta f)\right] \tag{3.6}$$

where *Re* is the function to get the real component; while *Im* is the function to get the imaginary component.

For each complex number, the spectral amplitude *Am* and the phase angle *Ph* are given:

$$Am(i\Delta f) = \sqrt{Re^2\left[G(i\Delta f)\right] + Im^2\left[G(i\Delta f)\right]} \tag{3.7a}$$

$$Ph(i\Delta f) = \arctan\left[\frac{Im(i\Delta f)}{Re(i\Delta f)}\right] \tag{3.7b}$$

Furthermore, the spectral amplitude and phase angle define the i^{th} harmonic function:

$$g_i(t) = Am(i\Delta f)\cos[2\pi i\Delta f t + Ph(i\Delta f)] \tag{3.8}$$

The continuous time signal $g(t)$ can be approximately viewed as the superposition of a series of the harmonic functions:

$$g(t) \approx \sum_{i=0}^{N-1} g_i(t) = A_0 + \sum_{i=0}^{N-1} \{Am(i\Delta f)\cos\left[2\pi i\Delta f t + Ph(i\Delta f)\right]\} \tag{3.9}$$

where A_0 represents a DC component.

Each frequency component has the spectral energy, which is proportional to the square of the spectral amplitude. The cumulative spectral energy for all frequencies is calculated:

$$E_{total} = \int_{-\infty}^{\infty} |G(\omega)|^2 d\omega \tag{3.10}$$

The cumulative spectral energy can be calculated with an upper or lower bound for the integral:

$$E_{upper}(\omega) = \int_{-\infty}^{\omega} |G(\omega)|^2 d\omega \tag{3.11a}$$

$$E_{lower}(\omega) = \int_{\omega}^{\infty} |G(\omega)|^2 d\omega \tag{3.11b}$$

The time signal $g(t)$ is said to have a finite energy, if its cumulative spectral energy E_{total} (Eq. 3.10) is finite. Therefore, for signals having a finite energy, some localization parameters are defined (*Stark* 2005):

$$t_g = \frac{1}{E_{total}} \int_{-\infty}^{\infty} t|g(t)|^2 dt \tag{3.12a}$$

$$\Delta t_g = \sqrt{\frac{1}{E_{total}} \int_{-\infty}^{\infty} (t-t_g)^2 |g(t)|^2 dt} \tag{3.12b}$$

$$\omega_g = \frac{1}{2\pi E_{total}} \int_{-\infty}^{\infty} \omega |G(\omega)|^2 d\omega \tag{3.12c}$$

$$\Delta\omega_g = \sqrt{\frac{1}{E_{total}} \int_{-\infty}^{\infty} (\omega-\omega_g)^2 |G(\omega)|^2 d\omega} \tag{3.12d}$$

where t_g indicates where on the time axis $g(t)$ is located; Δt_g provides information about how $g(t)$ is localized around t_g; the same arguments apply to ω_g and $\Delta\omega_g$ in frequency.

Cross power spectrum is a representation in frequency of the cross correlation function between two time signals $g_1(t)$ and $g_2(t)$. If their frequency spectra are $G_1(\omega)$ and $G_2(\omega)$, respectively, the cross power spectrum is defined:

$$G_{12}(\omega) = G_1(\omega)\, G_2^*(\omega) \tag{3.13}$$

3.2.2 2D Fourier transform

The time signal $g(t,x)$ is a 2D function of the time and space; therefore, its 2D Fourier transformation $G(\omega,\kappa)$ changes the time information into the frequency domain, and the spatial information into the wave number domain as:

$$G(\omega,\kappa) = \int_{-\infty}^{\infty}\int_{-\infty}^{\infty} g(t,x)\exp[-j(\omega t - \kappa x)]dtdx \tag{3.14}$$

A discrete form of the 2D Fourier transform is given:

$$G(u\Delta\omega, v\Delta\kappa) = \sum_{n=0}^{N-1}\sum_{m=0}^{N-1} \{g(n\Delta t, m\Delta x)\exp[-j(u\Delta\omega\, n\Delta t - v\Delta\kappa\, m\Delta x)]\} \tag{3.15}$$

where Δt, Δx, Δf and $\Delta\kappa$ are the intervals in time, space, frequency and wave number, respectively; m, n, u and v are the counters.

The results from the 2D Fourier transform can be plotted in frequency-wave number domain, where incident, reflected and transmitted events in the wave propagation

are shown. A single event in time can be extracted by applying an inverse 2D Fourier transform on the filtered data. A typical 2D filter $W(\omega,\kappa)$ is given:

$$W(\omega,\kappa)=\begin{cases}0.5+0.5\cos\left(\frac{\omega-\omega^{<event>}(\kappa)}{BW}\right) & \text{if } \omega-\omega^{<event>}(\kappa)\leq\frac{BW}{2}\\ 0 & \text{if } \omega-\omega^{<event>}(\kappa)>\frac{BW}{2}\end{cases} \tag{3.16}$$

where a Hanning window is used; BW is the angular frequency bandwidth of the 2D filter; $\omega^{<event>}(\kappa)$ defines the relation of frequency and wave number for that single event; for example, $\omega^{<event>}(\kappa)$ is given from the dispersion curve for a single Lamb mode as shown in Fig. 2.7.

The time-space signal for the event is calculated:

$$g^{<event>}(t,x)=\int_{-\infty}^{\infty}\int_{-\infty}^{\infty}[G(\omega,\kappa)W(\omega,\kappa)]\exp[j(\omega t-\kappa x)]d\omega d\kappa \tag{3.17}$$

3.2.3 Short-time Fourier transform

Fourier transform has a serious drawback: in transforming to the frequency domain, time information is lost (no time information is contained in $G(\omega)$, Eq. 3.1) and determination of the arrival time of a particular event is impossible (*Ovanesova* 2004). To overcome this deficiency, the short-time Fourier transform is defined:

$$G(\omega,b)=\int_{-\infty}^{\infty}[g(t)w(t-b)]\exp(-j\omega t)dt \tag{3.18}$$

where b is the shift time used to localize the window function $w(t)$ at different locations in time axis.

The short-time Fourier transform is sometimes called windowed Fourier transform. The window function can be Hanning, Hamming, Kaiser, or Gaussian. A Gaussian windowed short-time Fourier transform is known as the Gabor transform.

In the short-time Fourier transform, the width of windowing is fixed for all of frequencies at different time locations; if very tiny signal details (high frequencies) are of interest in only a small neighborhood, eventually the signal part, which actually is not of interests, will be involved. Hence zooming into small details is not supported in the short-time Fourier transform.

A uncertainty condition is expressed below (*Qian* 2002), which states that no windowing function can be chosen, which is arbitrarily sharply concentrated both in time and frequency.

$$\Delta t_g \, \Delta \omega_g \geq \frac{1}{2} \tag{3.19}$$

where Δt_g and $\Delta \omega_g$ are given in Eq. 3.12b and 3.12d for the time signal $g(t)$.

The Gaussian function has a low bound of the above inequality, and is considered to be optimal window shape that has better resolution both in time and frequency.

3.3 Wavelet transform

3.3.1 Basic principles

Any function could be called a wavelet only if it has a finite cumulative spectral energy (Eq. 3.10); however it is usually a waveform of effectively limited duration. Like the short-time Fourier transform, the wavelet transform (WT) is a two-parameter transform. For time signals, the two domains of the wavelet transform are the shifted time and the frequency scale. As a main advantage of the wavelet transform, windowing with a variable size is used; therefore, wavelet analysis allows the use of long time duration where more precise low-frequency information is expected, and shorter regions where high-frequency information is expected.

Fourier transform consists of breaking up a signal into complex exponentials of various frequencies; while wavelet transform is the breaking up of a signal into shifted and scaled versions of the original wavelet. The wavelet transform of a time signal $g(t)$ is an example of a time-frequency scale decomposition by dilating and translating a chosen wavelet $\phi(t)$ as:

$$G^{<WT>}(a,b) = \frac{1}{\sqrt{a}} \int_{-\infty}^{\infty} g(t) \phi^* \left(\frac{t-b}{a} \right) dt \tag{3.20}$$

where a is the dilation parameter or frequency scale stretching or contracting the wavelet; b is the translation parameter localizing the wavelet in the time axis. The first fraction $(1/\sqrt{a})$ on the right is set for reasons of energy conservation, and the energy of the wavelets for all frequency scales is identical. The wavelet transform provides very natural way to view data deriving from a great number of natural phenomena, and also makes sense that local features can be described better with wavelets that have local extent.

An alternative equation for the wavelet transform that is calculated in frequency is given (*Qian* 2002):

$$G^{<WT>}(a,b) = \sqrt{a}\int_{-\infty}^{\infty} G(\omega)\Phi^{*}(a\omega)\exp(j\omega b)dt \tag{3.21}$$

where $G(\omega)$ and $\Phi(\omega)$ are the Fourier transforms for the time signals $g(t)$ and the wavelet $\phi(t)$, respectively. Therefore, the above equation can be viewed as a band-pass filter for the input signal $g(t)$, where $\Phi^{*}(a\omega)$ acts as the frequency response of the filter. The dilated wavelet function $\phi(t/a)$ corresponds to the frequency spectrum $\Phi(a\omega)$; therefore, contracting a wavelet in time is associated with stretching a wavelet in frequency, and vice versa.

The wavelet transform is continuous (CWT); however, a discrete form (DCWT) is given in time for the calculation in a computer:

$$G^{<WT>}(a,b) = \frac{1}{\sqrt{a}}\sum_{n=0}^{N-1}\left[G(n\Delta t)\phi\left(\frac{n\Delta t - b}{a}\right)\Delta t\right] \tag{3.22}$$

where N is the total number of sampled points. Note that the DCWT is fundamentally different from the discrete wavelet transform (DWT).

If the time signal $g(t)$ does not need to be recovered from the wavelet transform, the wavelet $\phi(t)$ could be any function. However, when a perfect reconstruction is needed, the selection of the wavelet is restricted. In general, the wavelet has to be such that (*Qian* 2002):

$$C_{\phi} = \int_{-\infty}^{\infty}\frac{|\Phi(\omega)|^{2}}{|\omega|}d\omega < \infty \tag{3.23}$$

The above equation is so-called the admissibility condition, and C_{ϕ} is the admission constant. It should hold, $\Phi(\omega = 0) = 0$, indicating that the DC component is null. Once the admissibility condition is satisfied, the time signal $g(t)$ is recovered by doing an inverse wavelet transform:

$$g(t) = \frac{1}{C_{\phi}}\int_{-\infty}^{\infty}\int_{-\infty}^{\infty}\frac{1}{a^{2}}G^{<WT>}(a,b)\Phi\left(\frac{t-b}{a}\right)da\,db \tag{3.24}$$

The dilation parameter (frequency scale) determines the frequency range of a wavelet, which is used in the wavelet transform to extract the information of a local feature within that range. However, the wavelet transform can be calculated in an extended form by giving a range for the dilation parameter in the integral, for example the dilation parameter

a varies from a_1 to a_2. The results becomes a function of the the shift time b:

$$G^{<EWT>}(b) = \int_{a_1}^{a_2} G^{<WT>}(a,b)da \tag{3.25}$$

3.3.2 Wavelet-based energy

The energy contribution of the time signal $g(t)$ contained at a specific frequency scale and a time location is given using the admission constant C_ϕ (Eq. 3.23):

$$E^{<WT>}(a,b) = \frac{1}{C_\phi}\left|G^{<WT>}(a,b)\right|^2 \tag{3.26}$$

A plot of $E^{<WT>}(a,b)$ is known as Scalogram; it can be integrated across the parameters a and b to recover the total cumulative energy:

$$E_{total}^{<WT>} = \frac{1}{C_\phi}\int_{-\infty}^{\infty}\int_{0}^{\infty}\left|G^{<WT>}(a,b)\right|^2 dadb \tag{3.27}$$

3.3.3 Morlet wavelet

The Morlet function is a well-known wavelet for its good resolution both in time and frequency domain according to the uncertainty principle (Eq. 3.19). This function is used for the source modeling of an ultrasonic piezoelectric transmitter. Therefore, it is chosen as a wavelet for the wavelet transform for this study. The Morlet function is given by a harmonic complex function in time modulated by a Gaussian function (*Lardies* 2007):

$$\phi(t) = \exp(j\omega_0 t)\,\exp\left(-\frac{t^2}{\tau^2}\right) \tag{3.28}$$

where f_0 is the central frequency of the Morlet function, $\omega_0 = 2\pi f_0$; τ is the modulation parameter that determines the frequency bandwidth.

The spectral amplitude of the above Morlet function is given in frequency:

$$|\Phi(\omega)| = \sqrt{\pi}\tau\exp\left[-\frac{\tau^2}{4}(\omega-\omega_0)^2\right] \tag{3.29}$$

The frequency bandwidth (BW) of the Morlet function is measured in frequency between two half-power points at which the spectral amplitudes reduce to 70.7% of the maximum spectral amplitude:

$$BW = \frac{\sqrt{\ln(4)}}{\pi\tau} \tag{3.30}$$

If they are given: $f_0 = 50kHz$, $\tau = 1.12 \times 10^{-5}$, and thus the frequency bandwidth is calculated: $BW = 33.46kHz$. Fig. 3.1 shows the Morlet function in time and frequency. In the wavelet transform using the Morlet function (Eq. 3.21), $|\Phi(a\omega)|$ reaches the maximum at $f_0 = 50kHz$ for given $a = 1$; therefore, the information of a local feature whose frequency components is centered at frequency $50kHz$ is mostly extracted from the time signals $g(t)$.

3.3.4 Wavelet transform for a SDOF system

For a viscously damped single degree freedom of system (SDOF), a free time response $g(t)$ is expressed:

$$g(t) = A\exp(-D\omega_n t)\cos(\omega_d t + \theta) \tag{3.31}$$

where A is the residue amplitude; θ is the initial phase; ω_n is the un-damped natural frequency; while ω_d is the damped natural frequency; they are related by the viscous damping ratio D:

$$\omega_d = \omega_n\sqrt{1-D^2} \tag{3.32}$$

If the system is under-damped, that is in general $0 < D \ll 1$, and thus $\omega_n \approx \omega_d$. The time signal $g(t)$ (Eq. 3.31) is asymptotic when $D > 0$, meaning $g(t)$ tends to be zero as time goes infinity. The wavelet transform for this case is given (*Lardies* 2007):

$$G^{<WT>}(a,b) = \frac{\sqrt{a}}{2}A\exp(-D\omega_n b)|\Phi(a\omega_d)|\exp[j(\omega_d b + \theta)] \tag{3.33}$$

The phase of the above wavelet transform is given:

$$Ph[G^{<WT>}(a,b)] = \omega_d b + \theta \tag{3.34}$$

The derivative of the above phase with respect to the shift time b gives in the damped frequency ω_d:

$$\frac{d}{db}Ph[G^{<WT>}(a,b)] = \omega_d \tag{3.35}$$

3.4 Spectral analysis of surface waves

The use of surface waves (Rayleigh waves) for shallow applications involves often the spectral analysis of surface waves (SASW) method (*Heisey* 1982; *Stokoe* 1983). In the SASW, two receivers are placed at two locations with a spacing Δx, and the phase difference $\Delta\theta$ is measured.

If a harmonic signal $g_1(t)$ of surface waves is received at the first location, and $g_2(t)$ is received at the second location after a time delay Δt; then:

$$g_1(t) = \cos(\omega t + \theta) \tag{3.36a}$$

$$g_2(t) = \cos[\omega(t + \Delta t) + \theta] \tag{3.36b}$$

The unwrapped phase difference $\Delta\theta$ between two locations is measured from the above equations as:

$$\Delta\theta = \omega\Delta t$$

Therefore, the phase velocity V_{ph} at frequency ω is related to the spacing Δx and the unwrapped phase difference $\Delta\theta$:

$$V_{ph}(\omega) = \frac{\Delta x}{\Delta t} = \omega\frac{\Delta x}{\Delta\theta} \tag{3.37}$$

In a conventional SASW test, only two receivers are used. Surface waves propagate at different velocities in different materials; therefore, surface waves become dispersive in a layered medium, and longer wavelength propagates at deeper material than shorter wavelength; long-wavelength velocities depend on the material properties in deeper range, while short-wavelength velocities depend only on the properties of the shallow materials. This is the main principle that allows a dispersion curve of surface wave velocity versus wavelength (or frequency) to be converted into a function of elastic modulus vs. depth. Once the SASW analysis is performed and a dispersion curve is obtained, forward or inversion modeling can be used to derive a profile of elastic modulus vs. depth for the layered medium.

Surface waves must propagate a minimum distance from the source before being fully formed (near-field effects). Conversely, low signal-to-noise ratios can be present at large distances from the source, relative to the wavelength (far-field effects). Surface

waves dominate surface response; however reflections and body waves affect the phase function significantly. To determine the range of wavelengths (λ) for which the phase is dominated by well-formed surface waves, different empirical relationships for given test geometries have been proposed. The most commonly employed is the Heisey criterion (*Heisey* 1982), where the spacing from the source to the first receiver is equal to the receiver spacing, Δx, and it is suggested:

$$\frac{\lambda}{3} \leq \Delta x \leq 2\lambda \tag{3.38}$$

The use of multi-channel analysis of surface waves (MASW) allows the relative comparison of the structural condition of different sections for a given structure. Better noise control, identification of higher modes, and faster data collection are among the advantages of MASW method with respect to the conventional SASW test. The location of the source and receivers has significant effect on the collected data (*Hiltunen* 1988). The spacing between the source and first receiver determines the largest developed wavelength in the measurements. On the other hand, the spacing between the receivers determines the smallest obtainable wavelength from the data. The source should produce enough energy in a wide frequency range.

The spectrum analysis of the data collected in MASW tests allows the evaluation of the phase angle of each frequency component as a function of distance. If the medium is horizontally uniform, the phase function will vary linearly with distance; if the medium is not uniform, the phase function will deviate from a linear trend. Therefore, variations in the phase function with distance can be used to identify areas where the phase velocity of the medium changes horizontally. The greater the number of receivers used in a test, the higher the resolution of the results, thereby improving the ability to detect changes in the horizontal properties of the medium.

3.5 Summary

The Fourier transform is commonly used for signal processing, which transforms time information into the frequency domain; however, time information is no longer kept in the Fourier transform results. The wavelet transform keeps both time and frequency information with a two-parameter transform, where windowing with a variable size is used; wavelet analysis allows the use of long time duration where more precise low-frequency information is expected, and shorter regions where high-frequency information is expected. The Morlet function is chosen as a wavelet for the wavelet transform in this

study, because it represents the source modeling of an ultrasonic piezoelectric transmitter. For a SDOF system, The derivative of the phase spectrum from the wavelet transform gives the damped frequency of the system.

The SASW method is used for the assessment of a layered medium. However, the use of MASW allows the relative comparison of the structural condition of differen sections for a given medium. Better noise control, identification of higher modes, and faster data collection are among the advantages of MASW method with respect to the conventional SASW test.

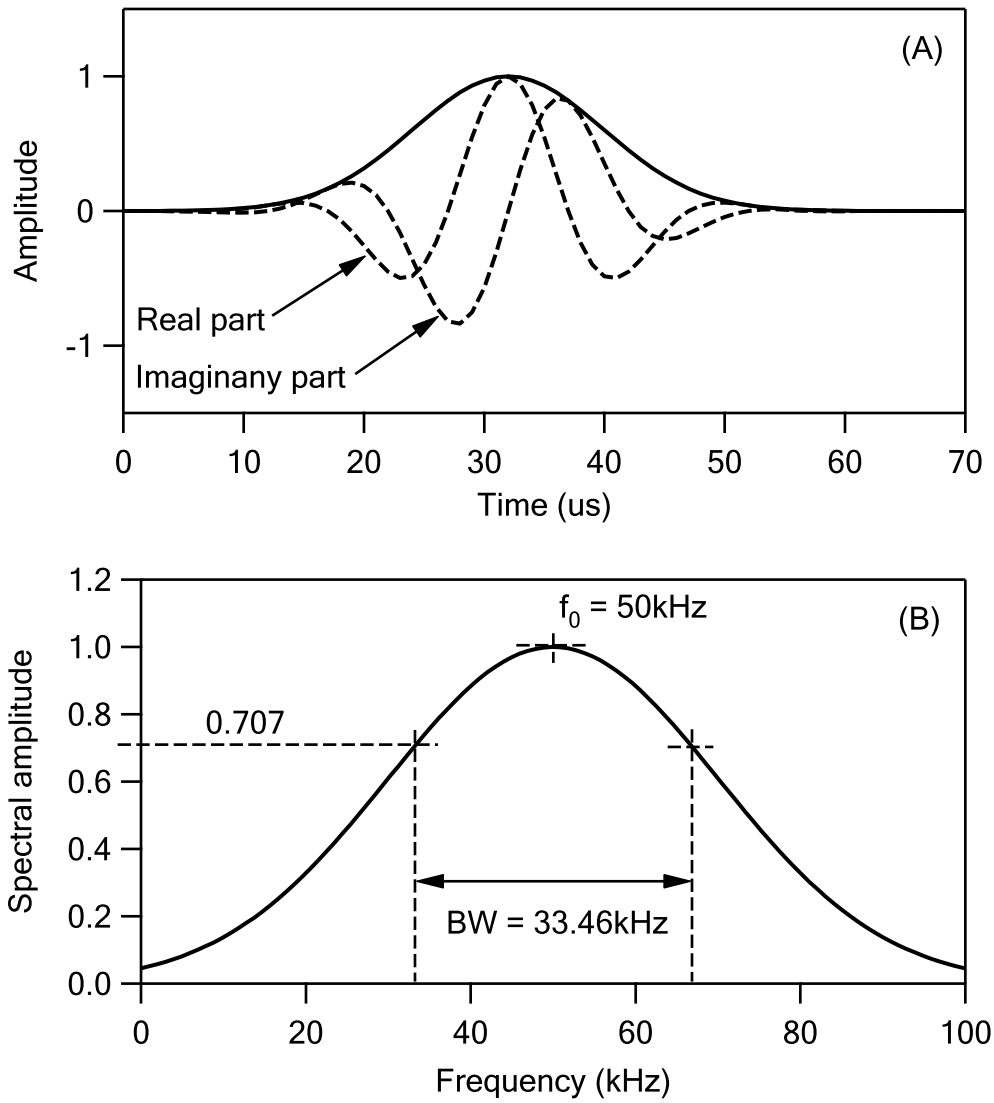

Figure 3.1: Morlet function: (A) in time; (B) in frequency. $f_0 = 50kHz$, $\tau = 1.12 \times 10^{-5}$, and $BW = 33.46kHz$.

Chapter 4

Literature review of previous studies

4.1 Introduction

This chapter reviews wave-propagation-based nondestructive testing techniques in the literature on the depth evaluation of surface-breaking cracks in concrete. Basically, two types of waves (P-waves and surface waves) are used; P-waves propagate spherically from a source at a highest velocity, and are usually received as the first arrival in the signal; while surface waves propagate cylindrically from a source and the wave propagation energy dominates the surface response. Previous studies for the depth evaluation of surface-breaking cracks in concrete have used P-waves; however, several recently published papers show better results using surface waves. The depth penetration of surface waves depends on their frequency; this important feature is useful for the crack depth evaluation. The Fourier transmission coefficient (FTC) is a promising technique, which is correlated to the crack depth.

4.2 P-wave method

A transient pulse is introduced into a medium by applying a mechanical impact or an ultrasonic emission on the surface. This pulse generates P-waves, S-waves and surface waves that propagate in a medium. P-waves have a spherical wave front that propagate at the highest wave velocity. If the presence of a surface-breaking crack completely intercepts the passage of wave propagation through the crack, the receiver that is located on the other side of the crack, would initially respond to the arrival of the diffracted P-waves, which result from the P-wave diffraction at the crack tip (Fig. 4.1).

In order to use the travel time or the initial amplitude of diffracted P-waves to evaluate the crack depth, the following conditions must be considered to have clear diffracted P-waves in the received signals:

- Along the wave path of P-wave propagation, the material is homogenous and flawless, and the P-wave velocity is relatively constant.
- The surface-breaking crack provides high contrast of the acoustic impedances at a solid-air interface to intercept the passage of direct wave propagation. *Sansalone* (1998) performed experimental measurements in concrete, where a surface-breaking crack is filled with air, water or grout; the results from an air-filled crack are identical to those from a water-filled crack. However, the diffracted P-waves are not readily identified for a partially grouted crack; *Song* (2003) indicated that methods using diffracted P-waves are not effective if the crack is tightly closed. For these cases, the interface at a crack does not provide enough contrast of the acoustic impedances, and some of P-wave energy propagate through the crack.
- The crack tip is well-defined (*Song* 2003), meaning that an intense discontinuity at the crack tip causes strong P-wave diffractions.

4.2.1 Time-of-flight technique

This is a widely reported method that has showed success in determining the depth of simulated surface-breaking cracks in concrete (*Sansalone* 1998). This method relies on the arrival time of P-waves that propagate from the source, and the crack tip to the receiver (Fig. 4.1). A mechanical impact is usually used as a source; it generates P-waves propagating spherically outward from the source, and the P-waves turn to be diffracted at the crack tip, where a new wave source is formed. The P-wave diffraction is picked up by the receiver that is placed on the other side of the crack. The arrival time t_r of P-waves is measured from the received time signal, and is used to calculate the crack depth d with known P-wave velocity V_P:

$$d = \sqrt{\left[\frac{(V_P t_r)^2 + S_1^2 - S_2^2}{2V_P t_r}\right]^2 - S_1^2} \tag{4.1}$$

where S_1 and S_2 are the spacings between the source and the crack, and between the crack and the receiver (Fig. 4.1), respectively.

If an equal spacing to the crack is used in the tests, $S_1 = S_2 = S$, the above equation reduces to the following:

$$d = \sqrt{\left(\frac{V_P t_r}{2}\right)^2 - S^2} \tag{4.2}$$

This technique shows a straightforward principle and simplicity. However, the intensity of P-wave diffraction depends on a clear tip of the crack. Generally, because of low energy of P-wave diffraction, the first P-wave arrival in the received signal is always difficult to be selected, especially in the presence of the background noises that may result from the measurement system, or in the case of long wave propagation path. *Hevin* (1998) numerically simulated the wave trains propagating through a surface-breaking crack, and different wave trains are shown; it states that in the case of experimental signals, measuring the time arrival of diffracted waves would be difficult due to low energy.

4.2.2 CECS 21:90 standard

Similar to the above time-of-flight technique, the Chinese national standard CECS 21:90, written in 1990 uses a group of transducers to evaluate the depth of surface-breaking cracks in concrete. A mechanical impactor produces stress waves propagating into a medium in all directions; while an ultrasonic piezoelectric transmitter used as a source for this standard produces an ultrasonic pulse in a focused direction (ACI Committee228 1998) and carries high frequency contents. The high frequencies give better resolution in time to calculate the crack depth.

The two groups of measurements are conducted, each with a series of transmitter-to-receiver spacings (S_1, S_2 ... S_n). First, a flawless area on the medium surface adjacent to the crack location is chosen for the first group of measurements (Fig. 4.2). Then, the measurement is repeated for the depth evaluation of a surface-breaking crack, where the transmitter and receiver are placed on the opposite sides of the crack and spaced equally to the crack.

The P-wave arrival times are measured from the two groups for different spacings (S_1, S_2 ... S_n); the arrival times are denoted as (t_1, t_2 ... t_n) for the first group of measurements at a homogenous and flawless area, and as (t'_1, t'_2 ... t'_n) for the second group of measurement with a crack.

Based on the first group of measurements, (S_1, S_2 ... S_n) and (t_1, t_2 ... t_n), the curve of spacing vs. time is plotted, and a linear curve fitting is made to calculate the P-wave velocity V_P:

$$S(t) = V_P t + C \tag{4.3}$$

where V_P represents the slope of the fitted line in Fig 4.3; C is the intercept at the vertical axis representing different spacings; the time delay that results from the measurement system is calculated as $t_{zero} = C/V_P$.

Based on the two groups of measurements, the crack depth for each transmitter-receiver spacing is calculated:

$$d_i = \frac{S_i}{2}\sqrt{\left(\frac{t_i' - t_{zero}}{t_i - t_{zero}}\right)^2 - 1} \tag{4.4}$$

where i is the counter that varies from 0 to n.

A concrete plate with dimensions: $1200 \times 300 \times 300mm$, was fabricated in NanJing Academy of Sciences for Water and Environmental Conservation in 1997, China. The concrete plate was bent to fracture and a $186mm$-deep crack is seen at one end of the plate. The measurements are performed by following the CECS 21:90 standard, and the results are given in Table 4.1. The average value of the calculated crack depths is $199mm$, and an acceptable error 6.9% is occurred relative to the manually measured depth ($186mm$).

4.2.3 Migration method

Liu (1996) adopted the method from reflection seismology. By using both the time and amplitude information of the first P-wave arrival to construct an image for the tip of a surface-breaking crack, the crack depth and the dip angle of the crack can be determined. The arrival time t_r is measured from the first P-wave arrival in the measured time signal, and used to calculate the distance of propagating P-waves, $S = V_P\, t_r$, where the P-wave velocity is assumed to be known. Suppose a surface-breaking crack is present in a half-space (Fig. 4.4), thus in a medium, any point connecting the source and receiver is a possible diffraction point, only if the distance of P-wave propagation through the source-that point-receiver path is equal to S. As a results, all of these possible points form an ellipse with the locations of source and receiver as its foci. When the source-receiver spacing is changed, different ellipses are obtained. However, those ellipses are intersected at the crack tip. Once the crack tip is located, a line connecting the crack tip and the surface point of the crack is drawn, and thus the crack depth and the dip angle of a surface-breaking crack can be determined.

In the measured signal, the time trace is represented as a function of amplitude vs. time; the amplitude can be converted into a gray-scale value and the time is used to locate

the pixel in a half-space. Therefore, the gray-scale image can be constructed by giving gray-scale value to each pixel in a medium. The procedure is described:

1. Divide a half-space into $N_1 \times N_2$ pixels in a 2D plane. For each pixel with a coordinate at (x_1, x_2), the distances to the source and receiver are denoted as S and R (Fig. 4.4), respectively, and the time for P-waves to propagate from the source to a pixel and then the receiver is denoted as t_r; it is given to each pixel in a medium:

$$t_r = \frac{S+R}{V_P} \tag{4.5}$$

2. The source and receiver are placed at different locations on the surface for a total number n of tests. For the i^{th} test, the amplitude at the time t_r for a pixel is given as $g_i(t_r)$, the final amplitude A_r for each pixel is obtained by summing up all amplitudes $g_i(t_r)$:

$$A_r = \frac{1}{n}\sum_{i=1}^{n} g_i(t_r) \tag{4.6}$$

3. The final amplitude A_r for each pixel is converted into grey-scale G_r with an appropriate upper bound U:

$$G_r = \begin{cases} -1 & \text{if } A_r \leq -U \\ \frac{A_r}{U} & \text{if } -U < A_r < U \\ 1 & \text{if } A_r \geq U \end{cases} \tag{4.7}$$

The modulated amplitude G_r is given to each pixel for the construction of a migration image. Obviously, a small value of the upper bound may give a clear elliptic trajectory; but if too small, a possibility of receiving the noise prior to the first arrival of the P-waves may happen. It has been found that the best is to have this upper bound slightly smaller than the first arrival amplitude of P-waves. Fig. 4.5 shows an example for this method (*Lin* 1996), where a 100*mm* surface-breaking vertical crack is shown.

4.3 Impact echo method

Impact echo method was developed in the mid 1980s and it has been used successfully for measuring the thickness of plate-like concrete structures (*Lin* 1996). In this method,

a mechanical impactor is applied on the surface of a plate-like medium, and the generated P-waves propagate into a medium spherically outward from the impact point. The P-waves are reflected when they encounter an internal defect or the external boundary. The wave reflections go back to the surface and are reflected again. The P-wave reflections between the surface and an internal defect or external boundary are recorded by a receiver that is placed on the surface, and the reflection frequency can be determined in the frequency domain through the Fourier transform. If P-wave velocity V_P is known, the depth d from the surface to an internal defect or the external boundary can be calculated:

$$d = \frac{V_P}{2f} \tag{4.8}$$

where f is the frequency of P-wave reflections.

The wave reflections occur at an interface between two different media. However, Eq. 4.8 is valid only at an interface where the tested medium is stiffer than another medium, for example, a crack gives an solid-air interface.

Lin (1996) found that when the impact point and receiver are located on both sides of a surface-breaking crack, the spectral amplitudes from the measured signal produce two peaks in the frequency domain, which correspond to the P-wave reflections between the top surface and the crack tip, and between the top and bottom surfaces in a medium. Although some results from this method have demonstrated a possibility for measuring the depth of a surface-breaking crack, questions arise in whether a multiple reflection event is able to produce significant wave energy so that the amplitude can be shown in the frequency domain.

4.4 Frequency analysis method

When a vertical force is applied on the surface of a plate-like medium, the different vibrational modes are generated, each mode with its distinct natural frequency. However, these natural frequencies are altered in the presence of a defect. Therefore, the natural frequency analysis can be used to predict the depth of a surface-breaking crack. A theoretical relationship (*Toutanji* 2003) is used to find an equation of moment for transversal waves propagating through a circular plate-like medium:

$$\rho \frac{\partial^2 u_2}{t^2} + \frac{E\,h^2}{12(1-\upsilon^2)} \nabla^2 u_2 = 0 \tag{4.9}$$

where u_2 is the vertical displacement of a point in the medium; ρ is the mass density; E is the Young's modulus; υ is the Poisson's ratio; h is the plate thickness; ∇^2 is the Laplacian operator.

The above equation is solved using the relationship between the Bessel function and the boundary conditions of a medium. The natural frequencies are given:

$$f_i = \pi \left(\frac{i}{12}\right)^2 \frac{h}{R^2} \sqrt{\frac{E}{\rho(1-\upsilon^2)}} \tag{4.10}$$

where f_i is the natural frequency for the i^{th} mode; R is the radius of the circular plate-like medium.

The above equation shows a relationship between the natural frequencies and other parameters. These parameters such as E and ρ are changed in the presence of defects; thus the natural frequency of a vibrational mode could be an indication for a defect.

4.5 Surface wave method

4.5.1 Numerical studies

Previous studies have used P-waves for the depth evaluation of surface-breaking cracks in concrete, where the first P-wave arrival time or initial amplitude is measured. However, surface waves exhibit unique properties suitable for the characterization of near surface defects (*Rix* 1990; *Kalinski* 1994), because: (a) surface waves dominate the surface response; a point load applied to the surface of a homogeneous half-space generates Rayleigh waves (R-waves), which contain 67% of the wave propagation energy; and (b) the depth penetration of Rayleigh waves depends on their frequency.

Previous studies provide several hypotheses on the diffraction patterns of surface waves for surface cracks. To summarize, the surface cracks can be viewed as reflector, low pass filter and delay gates (*Hevin* 1998); these three units produce reflected waves, low frequency transmitted waves and the delayed transmitted waves, accordingly. *Hevin* (1998) adapted a numerical model from earth physics to better understand the influence of the crack geometry on surface wave propagation. This model is based on the representation theorem and an indirect boundary element method (IBEM), and the three dimensional (3D) response for a 2D structure is calculated. In an elastic medium, the surface can be discretized into N segments of length ΔS; thus the displacement field in elastic domain is expressed in the following discrete form:

$$u_i(p_1) = u_i^0(p_1) + \sum_{n=1}^{N} \left[\varphi_j(p_2) g_{i,j}(p_1, p_2)\right] \tag{4.11a}$$

$$g_{i,j}(p_1, p_2) = \int_{p_2-\Delta S/2}^{p_2+\Delta S/2} G_{i,j}(p_1, p_2) dS_2 \tag{4.11b}$$

where $u_i(p_1)$ is the i^{th} component of displacement at the point p_1; $u_i^0(p_1)$ is defined as the free field of displacement in direction i at the point p_1 when surface waves propagate without the irregularity; $\varphi_j(p_2)$ is the force density in direction j at the point p_2; $G_{i,j}(p_1, p_2)$ is the Green function, for example, the displacement in direction i at the point p_1 due to a point force in direction j applied at the point p_2.

The resultant motion is the superposition of the free field and the diffracted wave field. The above equation can be solved by using some numerical simulation methods. The results for an incident wave propagating perpendicular to a surface-breaking crack with depths $5cm$, $10cm$ and $15cm$ are shown in Fig. 4.6. Three Rayleigh wave trains: the incident waves (marked as "a"), the reflected waves (marked as "c"), and the direct transmitted waves (marked as "b") have large energy. As the crack depth increases, the direct transmitted Rayleigh wave energy is reduced; while the reflected Rayleigh wave energy is increased.

4.5.2 Cut-off frequency and wavelength

The depth penetration of Rayleigh waves depends on their frequency or wavelength. In the presence of a surface-breaking crack, low frequency components propagate at a deep depth, and they are mostly transmitted; while high frequency components propagate at a shallow depth, and they are mostly reflected. Therefore, a surface-breaking crack plays a role as a low-pass filter, and a ratio of the spectral amplitudes between the transmitted and incident Rayleigh waves decreases with frequency. However, a cut-off frequency related to the crack depth is found in the following equation (*Hevin* 1998):

$$f_{cut} = \frac{V_R}{3d} \tag{4.12}$$

where the cut-off frequency f_{cut} is related to the crack depth d for Rayleigh waves propagating at a velocity of V_R. For frequencies higher than f_{cut}, Rayleigh waves are mostly reflected from the crack; while for frequencies lower than f_{cut}, Rayleigh waves propagate through the crack.

Accordingly, the crack depth d is equal to one third of the cut-off wavelength, $\lambda_{cut} = V_R/f_{cut}$:

$$d = \frac{\lambda_{cut}}{3} \tag{4.13}$$

Havin (1998) validated Eq. 4.12 in Fig. 4.7, which is from the measurements of synthetic seismograms and calculates the means of 50 curves using different couples of receivers with same distances from one to another. The ratio of the spectral amplitudes between the transmitted and incident Rayleigh waves (U_t/U_i) decreases with frequency, and the cut-off frequency is measured at a frequency value $9kHz$ in the plot. For given $V_R = 2318m/s$ and $d = 9cm$, Eq. 4.12 gives a close theoretical value $f_{cut} = 8.6kHz$.

4.5.3 Fourier transmission coefficient

Using a ratio of the spectral amplitudes between the transmitted and incident Rayleigh waves, the depth of a surface-breaking crack is measured in laboratory in so-called Fourier transmission coefficient (FTC) by *Popovics* (2000) and *Song* (2003). As shown in Fig. 4.8, two accelerometers are used as receivers, and a solenoid-driven impactor is used as a source. The source is first applied at point A; the generated waves propagate through points B and C, and the time signals are picked up by receivers and denoted as $g_{AB}(t)$ and $g_{AC}(t)$, where the first subscript represents the source location and the second subscript represents the receiver location.

If a medium is assumed globally isotropic and homogeneous, the corresponding frequency spectra $G_{AB}(\omega)$ and $G_{AC}(\omega)$ are expressed in frequency:

$$G_{AB}(\omega) = S_A(\omega)\, M_{AB}(\omega)\, C_B(\omega)\, R_B(\omega) \tag{4.14a}$$

$$G_{AC}(\omega) = S_A(\omega)\, M_{AC}(\omega)\, C_C(\omega)\, R_C(\omega) \tag{4.14b}$$

where S terms represent the source transfer functions at a point determined by the subscript; M terms represent the medium transfer functions for a range between two subscripts; C terms represent the coupling transfer functions; R terms represent the receiver transfer functions.

The S and C terms involve unknown conditions; while R terms are nonlinear for the amplitude responses of an accelerometer at high frequencies. As a result, the variations caused by S, C and R terms mask the desired M terms, which include the medium information. Therefore, a self calibrating technique (*Achenbach* 1992) is used to eliminate

the variations, which is accomplished by applying the source at point D. Similarly, the time signals $g_{DC}(t)$ and $g_{DB}(t)$ are obtained from a complementary measurement, and the corresponding frequency spectra $G_{DC}(\omega)$ and $G_{DB}(\omega)$ are expressed in frequency:

$$G_{DC}(\omega) = S_D(\omega)\, M_{DC}(\omega)\, C_C(\omega)\, R_C(\omega) \tag{4.15a}$$

$$G_{DB}(\omega) = S_D(\omega)\, M_{DB}(\omega)\, C_B(\omega)\, R_B(\omega) \tag{4.15b}$$

The wave transmission of surface waves through a surface-breaking crack is measured by the Fourier transmission coefficient (FTC), defined as:

$$FTC(\omega) = \sqrt{\frac{G_{AC}(\omega)\, G_{DB}(\omega)}{G_{AB}(\omega)\, G_{DC}(\omega)}} \tag{4.16}$$

The S, C and R terms are eliminated in the above calculation, because:

$$FTC(\omega) = \sqrt{\frac{M_{AC}(\omega)\, M_{DB}(\omega)}{M_{AB}(\omega)\, M_{DC}(\omega)}} \tag{4.17}$$

Therefore, the coupled receivers at points B and C have negligible effects on the FTC that is calculated from the passing surface waves, and the coupling of the receivers remains unchanged during testing. The nonlinear behaviors of the intrinsic transfer functions for an impact source and accelerometers as receivers can be also neglected.

The FTC is a function of frequency, and it can be considered as a ratio of the spectral amplitude at the far receiver to that at the near receiver. Therefore, a FTC value of 1 indicates total wave energy transmission through a surface-breaking crack from points B to C; whereas a FTC value of 0 indicates complete wave energy loss. However, in the case of a point source of stress waves, the FTC value should be less than 1, even for an uncracked, perfectly transmitting medium, since a considerable wave energy loss results from geometric spreading of a wave front.

Popovics and *Song* (2000 and 2003) measured in laboratory the relationship between the FTC and the normalized depth of a surface-breaking crack that is artificially induced on a concrete plate. The results are shown in Fig. 4.9. The FTC shows a sensitive range for the crack depth (d) normalized to the wavelength (λ) from $d/\lambda = 0$ to $1/3$. The FTC decreases significantly for this range, and a gradual decrease is shown for $d/\lambda = 1/3$ to 1.5; then FTC approaches a constant value for $d/\lambda > 1.5$. Importantly, no significant difference exists for the FTC results between a crack and a notch.

4.6 Summary of different methods

The methods discussed above are summarized in Table 4.2. Fourier transmission coefficient (FTC) shows potential because it uses surface waves. However, some problems exist:

- A mechanical impactor generates different frequency components that can not be controlled well, because they depend on some unknown factors such as contact duration of time or contact condition between an impactor and the tested medium. High frequency components are required for the depth evaluation of a small surface-breaking crack, but they are difficult to generate with a mechanical impactor. *Popovics* (1995) performed a series of impact tests and found the highest frequency that could be excited with an impact source is below $50kHz$.

- Rayleigh waves exist in a half-space; while for the case of a plate, the different Lamb modes are generated, and Lamb waves propagate at different velocities, a phenomenon called dispersion. The frequency components of the propagating Lamb waves vary with distance. Therefore, different frequency components are measured at points B and C (Fig. 4.8) because they are spaced unequally from the source. Lamb modes are not considered in the FTC method.

- The FTC method requires the Fourier transform of surface waves. However, it is impossible to identify the arrival of surface wave in frequency domain, because Fourier transform loses the time information; therefore a time windowing is required for the extraction of the arrival of surface wave in time domain; as a result, subjective variation occurs. Wavelet transform keeps both the time and frequency information, and the information of surface waves can be given in the results of the wavelet transform.

In this research, the FTC method is modified and improved by using an equal spacing configuration and by using the wavelet transform to calculate a new coefficient called wavelet transmission coefficient (WTC).

Table 4.1: Experimental results using CECS 21:90 standard

Items	Spacing between the transmitter and receiver (*mm*)							
	150	200	250	300	350	400	450	500
Arrival time (μs) at a flawless area	54.9	67.8	79.2	91.5	103.0	115.8	127.8	139.9
Arrival time (μs) with a crack	98.0	120.6	126.0	131.0	144.4	154.6	160.9	171.0
Calculated crack depth (*mm*)	168	204	203	194	210	211	202	203

Table 4.2: Depth evaluation of surface-breaking cracks in concrete

METHOD	SUMMARY	ADVANTAGES	LIMITATIONS
Diffracted P-waves	The time (amplitude) of the first arrival of the diffracted P-waves is used to calculate the crack depth.	Straightforward principle and simple calculation.	Identification of the first arrival of the diffracted P-waves is difficult.
Impact Echo	The reflections of P-waves between the tip of a crack and the surface of a medium is analyzed in frequency domain; the results show the presence of of a crack.	The frequency from the reflections of P-waves is used to calculate the crack depth.	The reflections of P-waves must be dominant in frequency response to produce an significant peak amplitude.
Frequency Analysis	If a dynamic force acts on a structure, different vibrational modes are excited. Their modal natural frequencies are related to the crack depth.	A general relation exists: the natural frequency is reduced with increasing the crack depth, and vice versa.	A relationship between the natural frequency and the crack depth has not been quantitatively determined. The crack depth is only relatively estimated.
Fourier Transmission Coefficient (FTC)	The FTC is sensitive to the crack depth (d) normalized to the wavelength (λ) in a range of $d/\lambda = 0$ to $1/3$.	Surface response is dominated by the surface waves; and the penetration depth depends on the frequency or wavelength.	Variations from the identification of surface wave arrival are subjective, because of a time window. Different Lamb modes affect the FTC calculation.

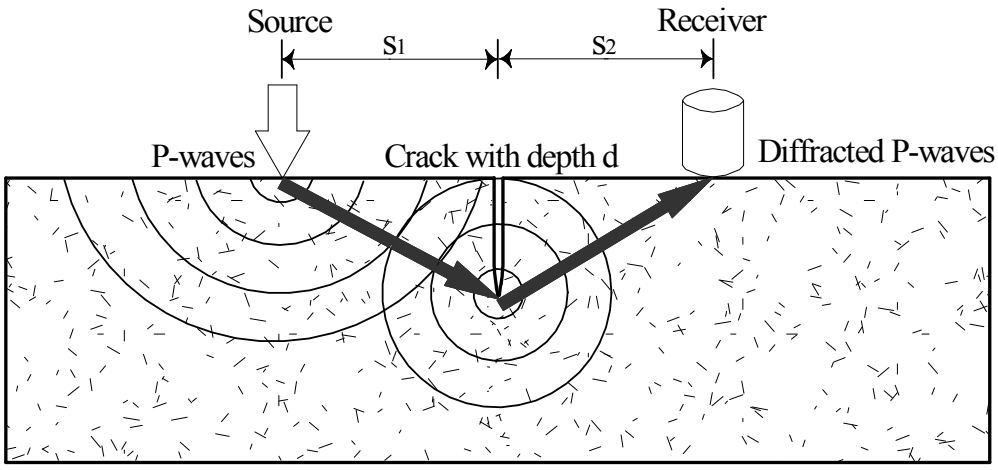

Figure 4.1: P-wave diffraction at the tip of a surface-breaking crack.

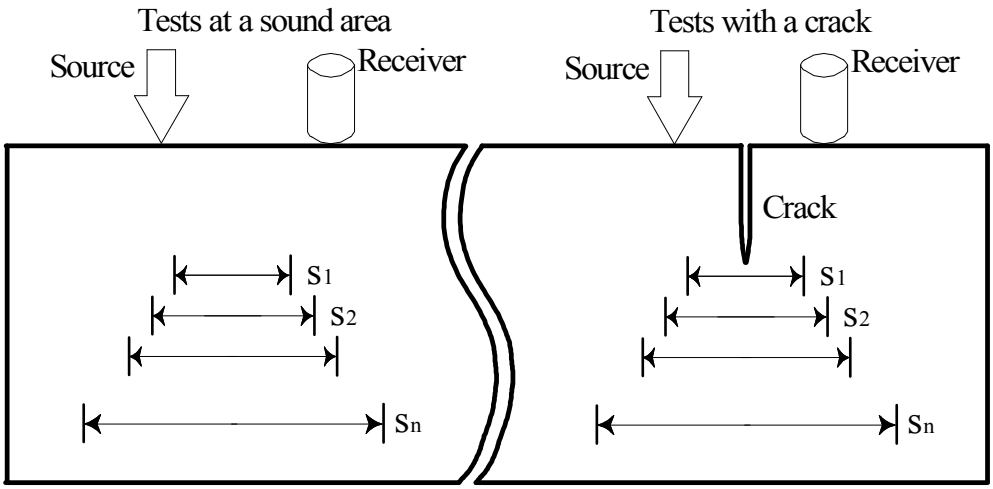

Figure 4.2: Measurements of P-waves for the depth evaluation of a surface-breaking crack using the CECS 21:90 standard.

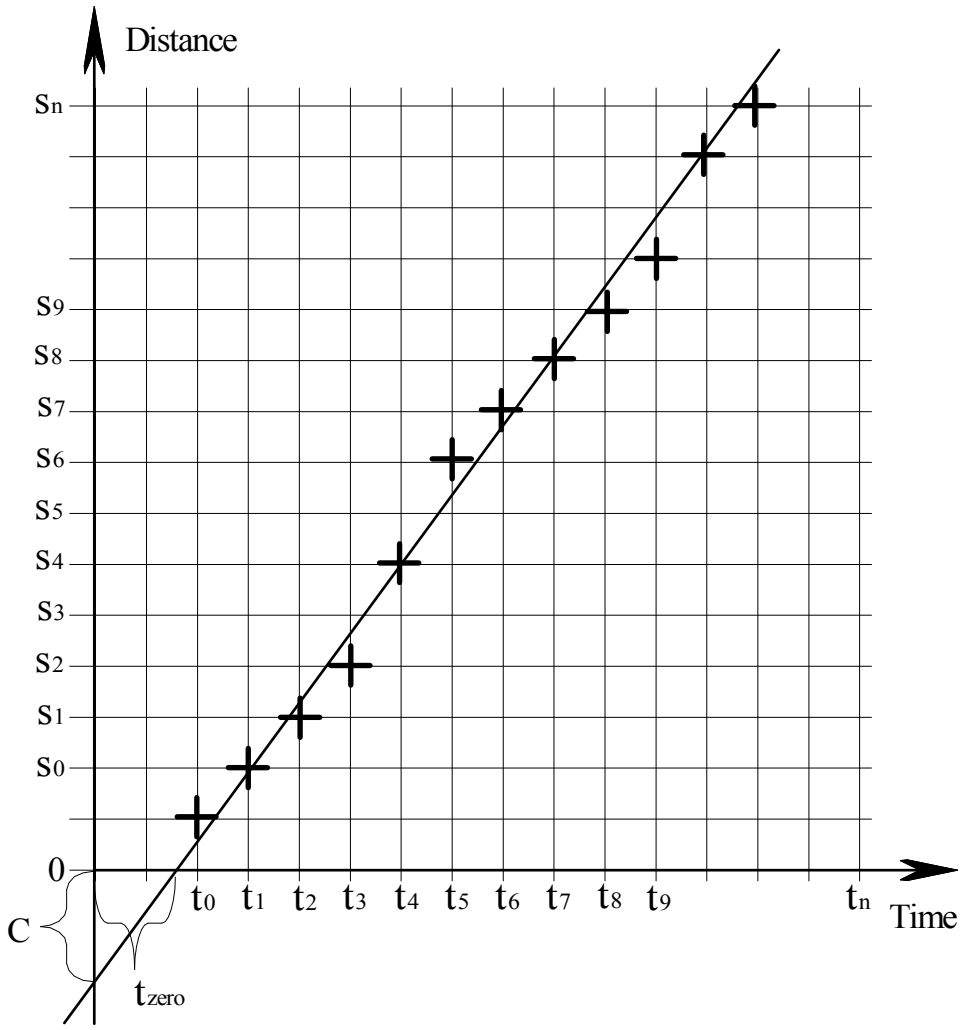

Figure 4.3: Measurements of the P-wave velocity and time delay from the plot of distance vs. time.

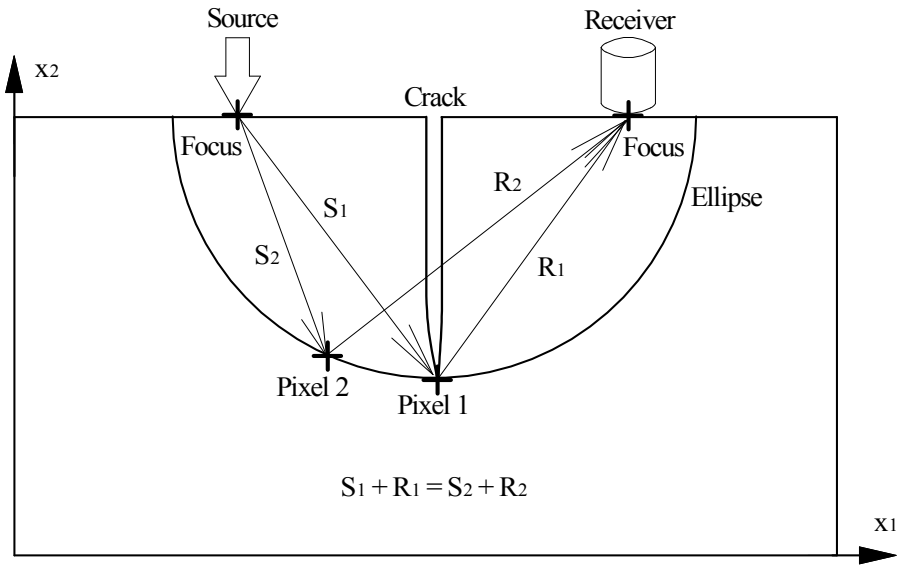

Figure 4.4: Measurements of the P-waves using the migration method for the depth evaluation of a surface-breaking crack.

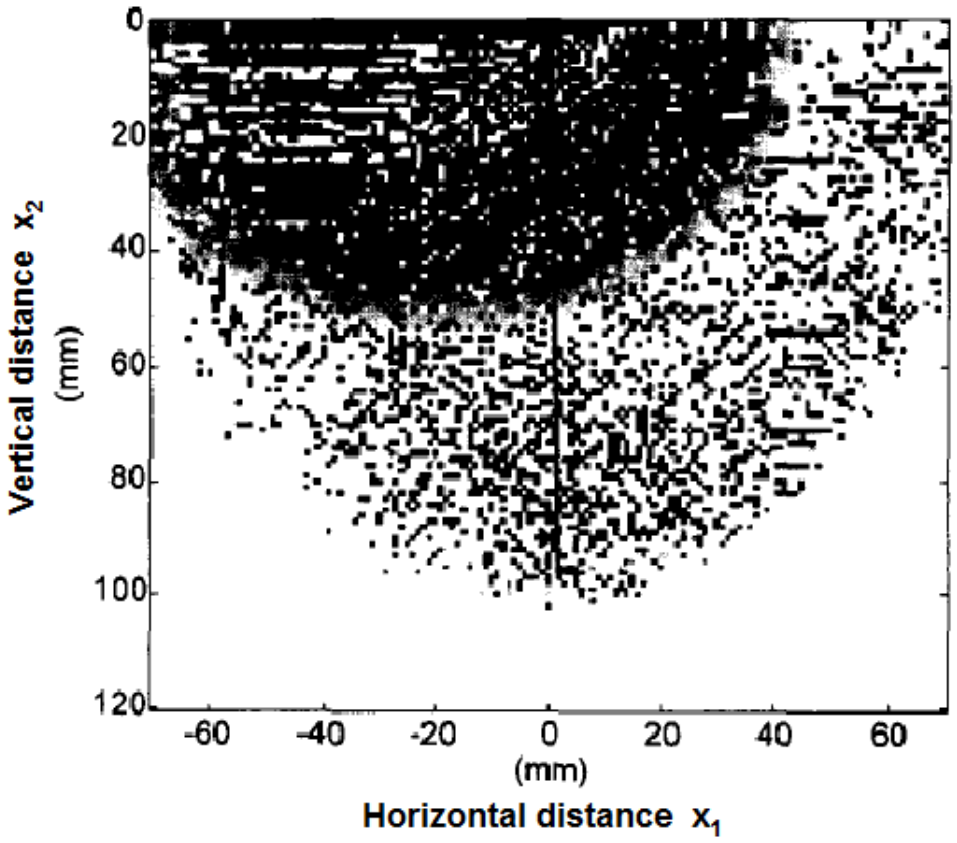

Figure 4.5: Migration image of a 100*mm* surface-breaking crack for a medium (*Liu* 1996).

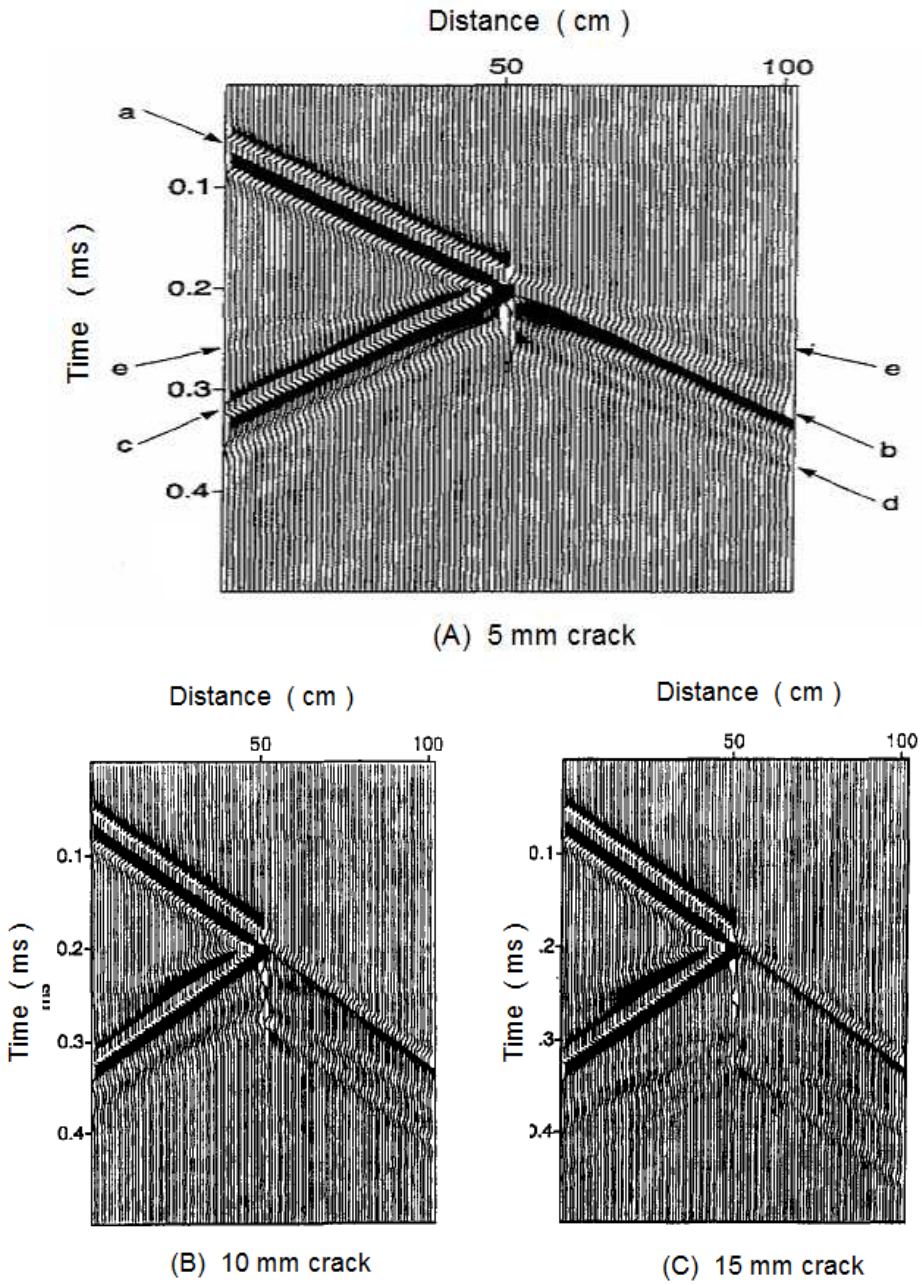

Figure 4.6: Rayleigh wave propagation through a surface-breaking crack with depths 5*cm*, 10*cm*, and 15*cm* (*Hevin* 1998). In the plot for a 5*mm* crack, the letter ”a” denotes the incident Rayleigh waves, the ”b” the direct transmitted Rayleigh waves, the ”c” the reflected Rayleigh waves, the ”d” the delayed transmitted Rayleigh waves, and the ”e” the body waves from the conversion mode of Rayleigh waves.

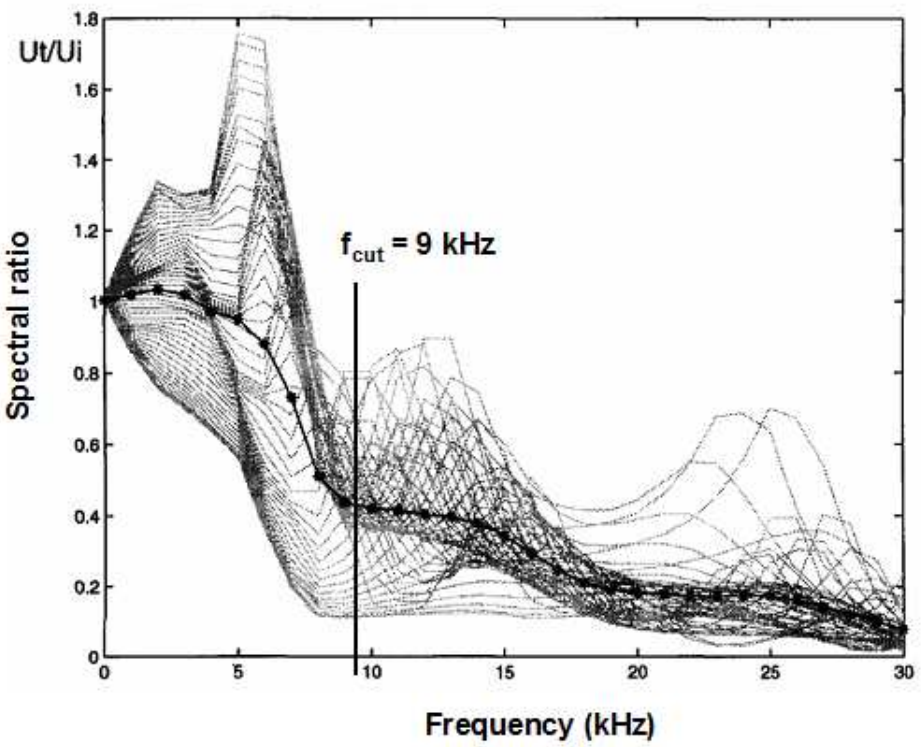

Figure 4.7: Ratio of the spectral amplitudes between the transmitted and incident Rayleigh waves for given Rayleigh wave velocity $V_R = 2318m/s$ and crack depth $d = 9cm$ (*Hevin* 1998).

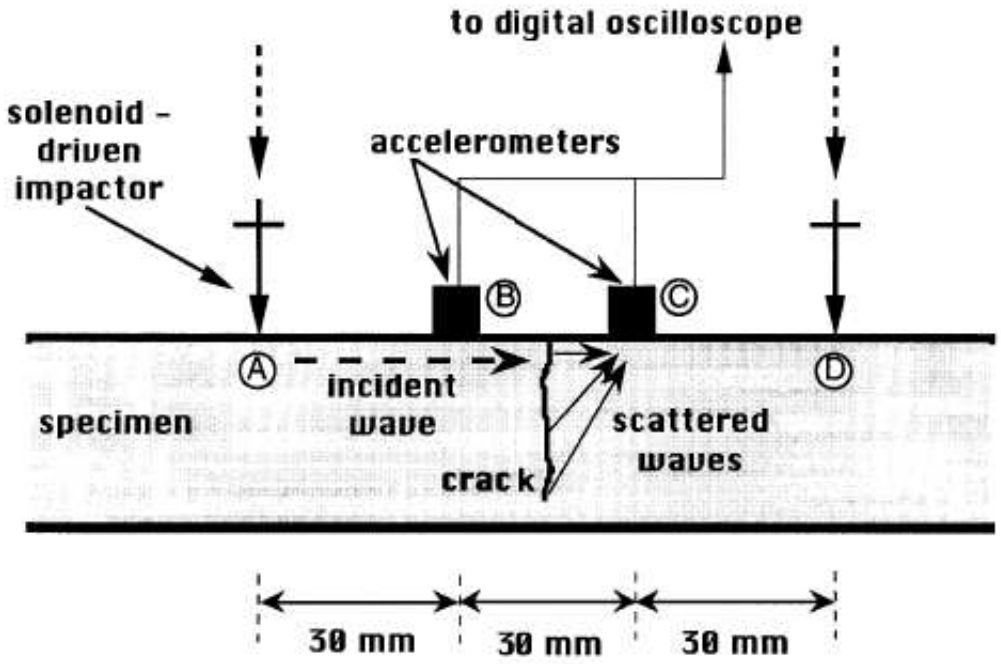

Figure 4.8: Experimental setup for the Fourier transmission coefficient (FTC) method (*Popovics* 2000).

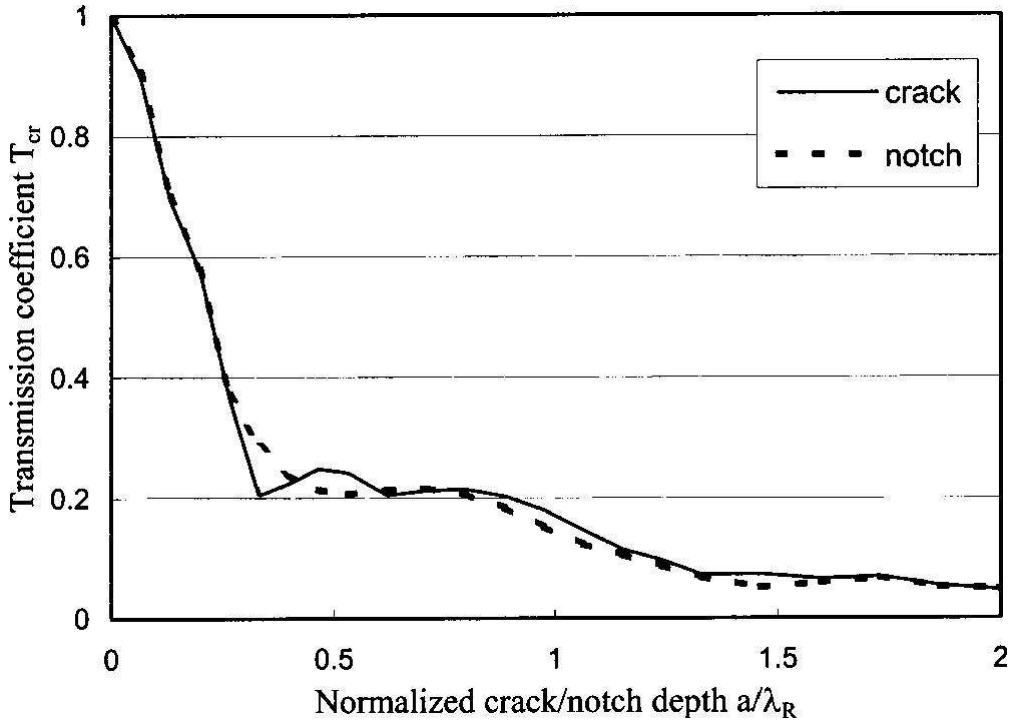

Figure 4.9: Fourier transmission coefficient (FTC) vs. normalized depth (*Song* 2003).

Chapter 5

Characteristics of surface wave propagation

5.1 Introduction

Nondestructive techniques based on surface waves are useful for the characterization of near-surface defects. Therefore, studies of characteristics for surface wave propagation are important. Some new findings for this research are presented in this chapter.

An ultrasonic piezoelectric transmitter as a source shows advantages over a traditional mechanical impactor, because the output force of the transmitter is modeled with a Morlet function. The penetration depth of surface waves depends on their frequency or wavelength. The Rayleigh wave energy concentrates in a depth of one third of the wavelength; while the penetration depth of Lamb waves depends on the mode shape. For Lamb wave propagation in a plate, a theoretical transfer function is derived and is used to study the Lamb mode dispersion and higher Lamb mode participation; the theoretical results show the frequency components of propagating Lamb waves vary with distance. A new methodology for the measurement of material damping ratio is proposed, where the tested medium is assumed to be represented by a viscously-damped single degree freedom of system (SDOF). The wave propagation of an ultrasonic pulse in the medium attenuates because of material damping. With the wavelet transform, the amplitude attenuation and phase variation with distance from surface responses are used to calculate the material damping ratio.

5.2 Source study for wave generation

In wave-propagation-based nondestructive testing, the type of sources employed to generate the stress wave is essential (*Popovics* 1995). Sources that have been reported for the application include mechanical impactor, piezoelectric transmitter, high-energy ultrasonic tone burst system, laser device, ultrasonic lithotripter, and so on. Usually, four factors are taken into account when choosing sources for the application: frequency range, penetrating strength (depth), repeatability and simplicity:

- A successful nondestructive testing method depends on the frequency range that is generated by a source. For example, in the measurement of cross-sectional vibration modes for a concrete beam, an expected vibration mode could not be excited due to an absence of certain frequencies in the generated pulse. For the depth evaluation of a small surface-breaking crack in a concrete plate, high frequency components are required.
- It is expected that sources can provide significant wave energy for waves to propagate in a desired distance, and to penetrate to a desired depth; therefore, the information from the inspected area in a medium can be given.
- An error may occur in the results from repeatable tests, and it can be measured by a consistency function. The reliable results require a high consistence, and so is a high-repeatable source.
- Consideration for the similarity of test setup is necessary in many in-situ situations, where reduced access is permitted, and long working time is not allowed.

5.2.1 Mechanical impactors

When the following conditions are satisfied for a spherical mechanical impactor (*Zukas* 1982):

- The spherical impactor and the target medium are linear elastic.
- Impact duration of time is long compared to stress-wave transit time in the spherical impactor.
- The impact is normal to the surface of the target medium.

The pressure distribution function $q(x_1,x_2,t)$ is given:

$$q(x_1,x_2,t) = q_0(t)\left(1-\frac{x_1^2}{R^2}-\frac{x_2^2}{R^2}\right)^{\frac{1}{2}} \tag{5.1}$$

where the coordinates x_1 and x_2 define a 2D plane on the surface of a medium; t represents the time; the contact area is given by a sunken circle with a radius denoted by the parameter R; the maximum pressure $q_0(t)$ occurs at the circle center, which is located at $x_1 = x_2 = 0$; while at the circle boundary, the pressure is equal to zero:

$$q(x_1,x_2,t) = 0 \quad if\ \tfrac{x_1^2}{R^2}+\tfrac{x_2^2}{R^2} = 1 \tag{5.2}$$

If the spherical impactor is small enough compared to the medium, the following terms are defined:

$$\begin{aligned}
k_1 &= \frac{1-\upsilon_1^2}{\pi E_1} \\
k_2 &= \frac{1-\upsilon_2^2}{\pi E_2} \\
V_1 &= \sqrt{2h_1 g} \\
M_1 &= \frac{1}{m_1} \\
\frac{1}{C_R} &= \frac{1}{R_{1m}}+\frac{1}{R_{1M}} \\
\alpha_1 &= \left(\frac{5V_1^2}{4M_1 n}\right)^{\frac{3}{5}} \\
n &= \frac{16}{3\pi(k_1+k_2)}\sqrt{\frac{C_R}{s^3}}
\end{aligned}$$

where E_1 and υ_1, E_2 and υ_2 are the Young's modulus and the Poisson's ratios for the spherical impactor and the medium, respectively; V_1 is the velocity of the impactor at the contact instant of time; h_1 is the drop height of the impactor; g denotes the gravity acceleration; m_1 is the mass of the spherical impactor; R_{1m} and R_{1M} are the principal radii of curvature for the spherical impactor at the contact point; s is the parameter that is a function of R_{1m} and R_{1M}.

Zukas (1982) gives the following equation to calculate the maximum pressure $q_0(t)$:

$$q_0(t) = \frac{3ns}{8\pi C_R mr}\sqrt{\alpha_1 \sin\left(\frac{\pi t V_1}{2.94\alpha_1}\right)} \tag{5.3}$$

Similar to the parameter s, m and r can be expressed as a function of R_{1m} and R_{1M}. *Zukas* (1982) suggested that $r = 1$, $s = 2$ and $m = 1$ when $R_{1m} = R_{1M}$. Therefore, the function of force vs. time is obtained by integrating $q(x_1, x_2, t)$ over the spherical contact area:

$$f(t) = \frac{4C_R\alpha_1}{s}\sin\left(\frac{\pi t V_1}{2.94\alpha_1}\right) \tag{5.4}$$

The total contact duration of time t_d for the spherical impactor and medium is calculated:

$$t_d = 2.94\left(\frac{5}{4nM\sqrt{V_1}}\right)^{\frac{2}{5}} \tag{5.5}$$

Hunter (1957) conducted experiments that show a half-sine-shaped function is a good approximation for the theoretical force-time response. *Sansalone* (1987) adopted the half-sine-shaped function to simulate the wave generation by a steel ball impactor using a numerical finite model for plates. *Zerwer* (1999) calculated that the total contact duration of time is $53\mu s$ for a $4.76mm$-diameter steel ball dropped to the Plexiglas surface from a $50.8mm$ height, and gave the curve of force vs. time in Fig. 5.1A, where an approximate half-sine-shaped function is shown. *Carino* (1986) addressed that in a stress pulse, the highest frequency component with significant amplitude has a frequency value that is approximately equal to the inverse of the contact duration of time; thus with the $53\mu s$ contact duration of time, a steel ball impactor generates significant energy for frequencies below $19kHz$ (Fig. 5.1B).

Although the frequency components in the generated pulse by an impact source can be controlled by varying the size and the drop height (*Popovics* 1995), in reality the control of the frequency components is limited because of the inelastic and inhomogeneous properties of concrete and the complex surface conditions at a micro scale level. *Popovics* (1995) performed a series of impact tests on a Plexiglas plate using different sizes of the steel balls dropped at a constant height of $150mm$, and concluded that the larger the diameter, the lower the upper cut-off frequency; however, most wave energy concentrates below frequency $50kHz$, even when a small diameter ball ($3.9mm$) is used. Additionally, the repeatability of impact tests is low. An ultrasonic piezoelectric transmitter shows advantages over a mechanical impactor, as they are compared in Table 5.1.

5.2.2 Ultrasonic piezoelectric transmitters

The structure of an ultrasonic piezoelectric transmitter is shown in Fig. 5.2. It consists mainly of three layers: backing plate, active element and matching layer. The active element is usually made of piezoelectric crystal, the matching layer is a wear plate or epoxy bonding for protection, and the backing plate is used to absorb the reflected wave energy. An ultrasonic piezoelectric transmitter usually relies on the piezoelectric crystal which has ability to convert electrical energy into acoustic energy (*Brown* 2000). Conversely, the piezoelectric crystal in a piezoelectric receiver plays a reverse role where acoustic energy is converted back into electrical energy. By selecting an active element that is $1/2$ wavelength thick and a matching layer that is $1/4$ wavelength thick, waves generated by the active element are in phase with the wave reverberating in the matching layer (*Panametrics-NDT* 2006). Therefore, the signal amplitudes are additive and greater amplitudes of wave enter the test medium. The complete transfer function of an ultrasonic piezoelectric transmitter is complicated, because modeling the electric and acoustic fields of the transmitter requires considerable information about piezoelectric and acoustic properties of the transmitter; therefore, a simplified form of the transmitter is used for the numerical study in this research.

An electric pulser employed in measurement systems, can produce an electric spike to electrically drive an ultrasonic piezoelectric transmitter. The pulser is composed of the electric circuits, and the output electric spike is expressed (*Brown* 2000):

$$V_k(t) = \begin{cases} 0 & \text{if } t \leq 0 \\ -V_\infty[1-\exp(-a_1 t)] & \text{if } 0 < t \leq t_0 \\ -V_0 \exp[-a_2(t-t_0)] & \text{if } t > t_0 \end{cases} \tag{5.6}$$

where,

$$V_\infty = \frac{V_0}{1-\exp(-a_1 t_0)}$$

The negative spike reaches its maximum amplitude (V_0) at the time t_0; a_1 and a_2 are the decreasing and the increasing rates of the output electric spike. The frequency spectrum of the output electric spike is given:

$$FT_k(\omega) = \frac{V_\infty\{1-\exp[-(a_1-j\omega)t_0]\}}{a_1-j\omega} + \frac{V_\infty[1-\exp(j\omega t_0)]}{j\omega} - \frac{V_0\exp(j\omega t_0)}{a_2-j\omega} \tag{5.7}$$

When $V_0 = 200volts$, $t_0 = 0.01\mu s$, $a_1 = 0.2$, and $a_2 = 50$, Fig. 5.3 shows an example

of an output electric spike in time and frequency. The spike is shaped like a Dirac-Delta function and the wave energy is distributed in a broad frequency bandwidth.

An ultrasonic piezoelectric transmitter can be viewed as a two-port system in Fig. 5.4 (*Deng* 2002): an electric port with the voltage V and current I flowing into, an acoustic port where the force F and velocity V_P are coming out. The two ports have transfer matrixes (**TRe**) and (**TRa**), respectively. By modeling the electric field and the acoustic field in the piezoelectric transmitter as a 1D field, an explicit expression known as Sittig model for the transfer matrix component is given, which only describes a plane P-wave ultrasonic piezoelectric transmitter.

$$\begin{bmatrix} V \\ I \end{bmatrix} = [\mathbf{TRe}]\,[\mathbf{TRa}] \begin{bmatrix} F \\ V_P \end{bmatrix} \tag{5.8}$$

where $det\{[\mathbf{TRe}][\mathbf{TRa}]\} = 1$,

$$[\mathbf{TRe}] = \begin{bmatrix} \frac{1}{h_{33}C_0} & \frac{h_{33}}{j\omega} \\ -j\omega C_0 & 0 \end{bmatrix}$$

$$[\mathbf{TRa}] = \frac{1}{Z_b - jZ_a\tan(\frac{\kappa d}{2})} \begin{bmatrix} Z_b + jZ_a\cot(\kappa d) & Z_a^2 + jZ_aZ_bcot(\kappa d) \\ 1 & Z_b - 2jZ_a\tan(\frac{\kappa d}{2}) \end{bmatrix}$$

and the parameters κ, d, h_{33} and C_0 represent the wave number, the thickness, the piezoelectric stiffness and the clamped capacitance of the piezoelectric crystal plate, respectively; Z_a is the acoustic impedance of the piezoelectric crystal plate; Z_b is the acoustic impedance of the backing plate.

Considerable details about the material properties of an ultrasonic piezoelectric transmitter are required for calculations of the transfer matrices. They are usually not given by manufacturers. Meanwhile, a satisfactory experimental method to determine the transfer matrices is not available (*Deng* 2002).

However, an approximation of the transfer function for an ultrasonic piezoelectric transmitter is given in a simplified form (*Fitting* 1981), which defines the relationship between the input voltage and the output force as:

$$H(\omega) = \frac{[1-\exp(-j\omega t_n)][1-R_B\exp(-j\omega t_n)]}{1-R_AR_B\exp(-j2\omega t_n)} \tag{5.9}$$

where t_n is the transit time of an ultrasonic pulse through the transmitter and it mostly depends on the active element; R_A and R_B are the reflection coefficients between the

active element and matching layer, and between the active element and backing plate, respectively.

According to the information provided by the manufacturer, Table 5.2 is created for the ultrasonic piezoelectric transmitter used in the experiments. The active element is 12.7*mm* thick and made of PZT-4 material with silver-coated top and bottom surfaces; the matching layer is made of stainless steel (grade 303S31) and the backing plate is made of Perspex material. Because the output electric spike from an electric pulser has an exponential decay, which is so fast that it can be approximately considered as a Dirac-Delta function. As a result, the excited force output from an ultrasonic piezoelectric transmitter depends directly on its transfer function. With the known parameters in Table 5.2, the transfer function of the transmitter is calculated in frequency, and then in time through an inverse Fourier transform. It is found in Fig. 5.5 to match well with a Morlet function (Eq. 3.28) for given $f_0 = 50kHz$ and $\tau = 1.12 \times 10^{-5}$ ($BW = 33.46kHz$). Therefore, this Morlet function is used for a modeling of the output force for the transmitter, and it is applied as a wave source in the numerical models.

5.2.3 Numerical sources

In addition to a Morlet source, sinusoidal tone burst source and Lamb source can be used in the numerical simulations.

A sinusoidal tone burst source $S_b(t)$ is given as a harmonic function multiplied by a Hanning window function $whn(t)$:

$$S_b(t) = \sin(2\pi f_0) whn(t) \tag{5.10}$$

where,

$$whn(t) = \begin{cases} 0.5 + 0.5\cos\left[\frac{2\pi f_0}{n}\left(t - \frac{n}{2f_0}\right)\right] & \text{if } t \leq \frac{n}{f_0} \\ 0 & \text{otherwise} \end{cases}$$

and f_0 is the frequency of a harmonic function; n is the number of the time cycles contained in sinusoidal tone burst source; the larger the number of time cycles, the narrower the frequency bandwidth is, and vice versa. Fig. 5.6 shows an example for given $f_0 = 50kHz$ and $n = 10$.

The Lamb's problem (*Lamb* 1904) is useful for the numerical calibration. For a half space, Rayleigh waves are generated with a Lamb source, which is defined:

$$Lm(t) = \frac{F_b\,\eta}{\pi(t^2+\eta^2)} \tag{5.11}$$

where F_b controls the force amplitude; η determines the width of the force pulse.

For the applied Lamb source, the theoretical solution $w(t,x)$ to the vertical displacements of Rayleigh waves at a horizontal distance x from the source, is given:

$$w(x,t) = \frac{A\,F_b}{4\pi G\eta^2 V_R}\sqrt{\frac{2\eta V_R}{x}}\cos\left(\frac{\pi}{4}-\frac{3}{2}z\right)cos^{\frac{3}{2}}(z) \tag{5.12}$$

where,

$$z = \arctan\left(\frac{V_R t - x}{V_R\,\eta}\right)$$

and A is a constant that depends on elastic properties of the medium; G is the shear modulus. Fig. 5.7 shows an example for given $\eta = 1.78\times10^{-6}$, where the wave energy is shown in a broad frequency bandwidth.

5.2.4 Cumulative spectral energy for sources

A cumulative spectral energy of the sources is calculated to show the spectral energy concentration. Eq. 3.11A calculates the spectral energy accumulated to a frequency as an upper bound in the integral; while Eq. 3.11B calculates the spectral energy accumulated from a frequency as a lower bound in the integral.

The wave energy concentrations for four different sources are studied: (a) sinusoidal tone burst source ($f_0 = 50kHz$, $n = 10$), shown in Fig. 5.6; (b) Lamb source ($\eta = 1.78\times10^{-6}$, $Fb = 1$), shown in Fig. 5.7; (c) Morlet source ($f_0 = 50kHz$, $\tau = 1.12\times10^{-5}$, $BW = 33.46kHz$), shown in Fig. 5.5; and (d) Morlet source ($f_0 = 100kHz$, $\tau = 5.6\times10^{-6}$, $BW = 66.92kHz$).

Their cumulative spectral energy are calculated using Eq. 3.11, and shown in Fig. 5.8 to Fig. 5.11. A changing area in the vertical axis in the plots represents a frequency bandwidth where the wave energy are concentrated. The sinusoidal tone burst source shows a narrow frequency bandwidth for the wave energy concentration; while Lamb source provides wave energy in a broad frequency bandwidth. For Morlet sources, a wider frequency bandwidth for the wave energy concentration is given by a Morlet function that has a higher central frequency.

5.3 Penetration depth of surface wave energy

Surface waves propagate along the surface of a medium, and the wave energy concentrates in a subsurface depth that depends on the frequency or wavelength.

Rayleigh waves exist in a half-space, and the wave energy concentrates in a depth of one-third of the wavelength ($\lambda/3$) (*Hevin* 1998). The penetration depth of surface waves can be shown using a function of the cumulative spectral energy vs. normalized depth. For Lamb waves in a plate, different Lamb modes are generated; fundamental Lamb modes behave similar to Rayleigh waves for high frequencies, where the wavelength is small relatively to the thickness of a plate.

For the case given in given in Fig. 2.7, where $V_P = 4800m/s$, $V_S = 2770m/s$, $V_R = 2550m/s$, and the plate thickness $2h = 80mm$, the cumulative spectral energy E_{upper} (Eq. 3.11A) are calculated in Fig. 5.12 for Rayleigh wave mode, fundamental Lamb mode S0 and higher Lamb mode S1 at frequency $f = 50kHz$. Rayleigh wave mode reaches 90% of the highest wave energy at a normalized depth of $d/\lambda_R = 0.528$; while this value comes earlier for the fundamental Lamb mode S0, $d/\lambda_R = 0.429$, indicating the wave penetration of fundamental Lamb mode S0 is a little shallower than Rayleigh wave mode for this case. The wave penetration for higher Lamb modes show a complicated pattern, for example, the wave energy for higher Lamb mode S1 is shown to concentrate from $d/\lambda_R = 0.3$ to 0.7.

5.4 Transfer function for Lamb wave propagation

5.4.1 Theoretical derivation and analysis

This section presents a theoretical transfer function for Lamb wave propagation in a plate to study the effects of Lamb mode desertion and higher Lamb mode participation. The weighing factor 0.8 is assumed for the mode S0 contribution to represent a case where the mode S0 dominates in surface response; while for the case of higher Lamb mode participation in the wave propagation, the weighing factor 0.2 is assumed for 20% of total energy from the mode S1.

When a vertical force is applied on the surface of a plate, it generates different Lamb modes. Suppose $g_0(t)$ and $G_0(\omega)$ represent the time signal and the frequency spectrum for the surface response at the source location, respectively. When Lamb waves propagate in a plate, each frequency component generated at the source location is transformed

by the transfer functions of Lamb modes. In a linear system, modal superposition allows the time signal $g(t,x)$, measured on surface at a distance x from the source to be expressed in frequency domain as:

$$G(\omega,x) = \sum_i [w_i H_i(\omega,x) G_0(\omega)] \tag{5.13}$$

where i is an index representing different Lamb modes; w_i is the weighing factor of each i^{th} Lamb mode in the surface response; $H_i(\omega,x)$ is the transfer function for the single i^{th} Lamb mode.

Because of the complexity of Lamb mode participation, the weighing factors are difficult to evaluate. However, if material damping is negligible, the contribution of a single Lamb mode is given:

$$g(t,x) = g_0\left(t \pm \frac{x}{V_{ph}}\right) \tag{5.14}$$

where the sign $\pm$ represents the direction of wave propagation; V_{ph} is the phase velocity, which varies with frequency for Lamb modes as shown in Fig. 2.7.

In the frequency domain, the above equation is written as:

$$G(\omega,x) = G_0(\omega)\exp\left(\pm j\omega\frac{x}{V_{ph}}\right) = G_0(\omega)\exp(\pm j\kappa x) \tag{5.15}$$

Therefore, the transfer function for a single Lamb mode is given below; because the amplitude of the transfer function is equal to 1, the amplitudes for all frequencies and wave numbers are unchanged for the wave propagation of a single Lamb mode.

$$H(\omega,x) = \frac{G(\omega,x)}{G_0(\omega)} = exp(\pm j\kappa x) \tag{5.16}$$

where the wave number κ is a function of frequency (ω) and phase velocity (V_{ph}).

The time signals $g(t,x_1)$ and $g(t,x_2)$, measured at two distances x_1 and x_2 from the source can be calculated by applying the inverse Fourier transform of the corresponding frequency spectra given by Eq. 5.15. As an example, the surface response at the source location is given with a Morlet function $\phi(t)$ (Eq. 3.28), where $f_0 = 100kHz$ ($\tau = 5.6\times 10^{-6}$) or $50kHz$ ($\tau = 1.12\times 10^{-5}$), and the wave propagation of the Morlet function is shown in Fig. 5.13.

The transfer function $H(\omega,x)$ (Eq. 5.16), where the wave number κ is obtained from the dispersion curve for the modes S0 or/and S1 (Fig. 2.7), is used to calculate the time

responses at two distances (x_1 and x_2). For the mode S0 at $f_0 = 100kHz$ ($\lambda = 0.0255m$), it gives $x_1 = 0.077m$ and $x_2 = 0.153m$; while for the mode S0 at $f_0 = 50kHz$ ($\lambda = 0.051m$), it gives $x_1 = 0.156m$ and $x_2 = 0.311m$; therefore, it holds: $(x_2 - x_1)/\lambda = 3$.

Figs. 5.13A and B show the wave propagation of the mode S0 ($f_0 = 100kHz$ or $50kHz$). The $100kHz$ Morlet function propagates as the mode S0 without dispersion; whereas, because of a frequency bandwidth for the Morlet function centered at $50kHz$, some frequency components exist in a slightly-non-flat region of the mode S0 in the dispersion curve, indicating a slight dispersion, which causes the original shape of the Morlet pulse [$\phi(t)$] to be slightly distorted in time with distance.

The spectral amplitudes of the time responses in Figs. 5.13A and B are the same, and they are given in Fig. 5.13D. It indicates the frequency components of the propagating Lamb waves are not affected when only a single Lamb mode is present, and the transmission coefficient $G(\omega, x_2)/G(\omega, x_1)$ is constant and equal to 1.

In the example showing higher Lamb mode participation when $f_0 = 50kHz$, the transfer function is calculated as $0.8\,H_{S0}(\omega, x) + 0.2\,H_{S1}(\omega, x)$ for Fig. 5.13C, and the corresponding spectral amplitude and the transmission coefficient are shown in Figs. 5.13E and F, respectively. All frequency components are practically affected in this case, and the transmission coefficient is no longer constant with frequency for different distances.

By using the unwrapped phase difference between the two frequency spectra [$G_0(\omega)$ and $G(\omega, x)$], which are calculated from the time signals at the source location ($x = 0$) and at a distance x from the source ($x = x_1$ or x_2), the phase velocity $V_{ph}(\omega, x)$ of the propagating Lamb waves can be calculated with Eq. 3.37. In the presence of a single Lamb mode, the calculated dispersion curve (phase velocity vs. frequency) matches the theoretical dispersion curve (Fig. 2.7) well. For case given in Fig. 5.13C, where higher Lamb mode participates and the fundamental Lamb mode S0 has a 80% distribution, the unwrapped phases are calculated in Fig. 5.14A, and the calculated phase velocities are compared with the theoretical results for the mode S0 in Fig. 5.14B, where discrepancy is found only in low frequencies.

5.4.2 Non-equal spacing effect analysis

A single frequency component generated at source location propagates along the surface, and the surface response in a distance x from the source is modulated by a modulation function $m(t, x)$ as:

$$g(t, x) = m(t, x)\cos(\omega t + \theta) \tag{5.17}$$

The amplitude of a single frequency component varies with distance as it propagates. If the time signal $g(t,x)$ is asymptotic, the amplitude from the wavelet transform using a Morlet wavelet (Eq. 3.28) is given (*Lardies* 2007):

$$|G^{<WT>}(a,b,x)| = \frac{1}{2}\sqrt{\pi a}\,\tau\, m(b,x)\,\exp\left[-\frac{\tau^2}{4}(a\omega-\omega_0)^2\right] \tag{5.18}$$

If the parameter a is selected to equal ω_0/ω, the amplitude of the wavelet transform is proportional to the modulation function $m(b,x)$. Therefore, using a Morlet function centered in a frequency, $\omega_0 = 2\ pif_0$ as a wavelet, the amplitude from the wavelet transform can be measured to indicate the amplitude variation of the frequency components with distance as waves propagate along the surface.

For the case given in Fig. 5.13A, where the mode S0 is present and the central frequency of the Morlet function ($f_0 = 100kHz$) is at a non-dispersive range of frequency, the maximum amplitudes of the wavelet transform are practically the same at two distances (x_1 , x_2), $WT_{max} = 1.0$.

However, Fig. 5.15 shows the amplitude from the Morlet wavelet transform that is calculated for cases given in Figs. 5.13B and C. For a $50kHz$ Morlet function propagating in the presence of the single mode S0, because of a dispersion, the maximum amplitudes are slightly reduced in Fig. 5.15A with distances at x_1: $WT_{max} = 0.973$, and at x_2: $WT_{max} = 0.922$.

For case given in Fig. 5.13C, where both the Lamb mode dispersion ($f_0 = 50kHz$) and higher Lamb mode participation, $H(\omega,x) = 0.8\,H_{S0}(\omega,x) + 0.2\,H_{S1}(\omega,x)$, are present, the maximum amplitudes of the Morlet wavelet transform are largely reduced in Fig. 5.15B, and they are $WT_{max} = 0.743$ at x_1, and $WT_{max} = 0.753$ at x_2.

In contrast with the Lamb waves, Rayleigh waves propagate at a constant velocity V_R along the surface of a half-space as a non-dispersive mode. In this case, $g(t,x)$ is obtained by simply shifting $g_0(t)$ in the time axis (Eq. 5.14),and the frequency components of the propagating Rayleigh waves are the same for different distances. While, Lamb waves propagate at different velocities in a plate as multiple Lamb modes; as results, the frequency components of the propagating Lamb waves vary with distance. Fig. 5.16 shows in a contour plot the spectral amplitudes at different distances (0 to $200mm$) for the wave propagation of a Morlet function, $g_0(t) = \phi(t)$, $f_0 = 50kHz$, and $\tau = 1.12^{-5}$ (Eq. 3.28).

For Fig. 5.16A, the Morlet function propagate as Rayleigh waves at a velocity $V_R = 2550m/s$; while for Fig. 5.16B, it propagates as Lamb waves in the presence of the modes S0 and S1 from case in Fig. 5.13C, where $H(\omega,x) = 0.8\,H_{S0}(\omega,x) + 0.2\,H_{S1}(\omega,x)$.

Accordingly, the Morlet wavelet transforms are applied with Eq. 3.20. Fig. 5.17A shows the amplitudes at different distances from the wavelet transforms for a Morlet function ($f_0 = 50kHz,\ \tau = 1.12 \times 10^{-5}$) propagating as Rayleigh waves; the contour line shows a slope that gives Rayleigh wave velocity ($V_R = 2550m/s$), and the amplitudes are constant with distance as Rayleigh waves propagate. While, Fig. 5.17B shows the amplitudes at different distances for a Morlet function ($f_0 = 50kHz,\ \tau = 1.12 \times 10^{-5}$) propagating as Lamb waves in the presence of the modes S0 and S1, $H(\omega,x) = 0.8\,H_{S0}(\omega,x) + 0.2\,H_{S1}(\omega,x)$; in this case, the contour line shows a slope that gives a value close to the Rayleigh wave velocity, and the amplitudes vary with distance as Lamb waves propagate.

In the above studies, the frequency components of propagating waves are analyzed with the Fourier transform and the Morlet wavelet transform for different distances. The theoretical results show that the frequency components are constant with distance as Rayleigh waves propagate as a non-dispersive mode; while for the Lamb waves in a plate, because of the Lamb mode dispersion and higher Lamb mode participation, the frequency components of the propagating Lamb waves vary with distance. Therefore, this variation affects the FTC measurement in a plate, where the non-equal spacing configuration is used.

5.5 Measurement of material damping ratio

5.5.1 Introduction

Material damping is important for the dynamic analysis of material specimens and structures. In geomaterials, the wave propagation depends strongly on the physical state and saturation conditions, for example, the wave attenuation caused by material damping in dry, saturated or frozen rocks, or cemented soil varies much more than the wave velocities for these conditions. However, the experimental measurement of material damping ratio is more difficult than the measurement of wave velocity (*Toksoz* 1979). The dynamic response of structures is predominantly controlled by damping (*Liu* 1995); therefore, monitoring variation of damping is useful for the assessment of structural health or deterioration. Moreover, the presence of a defect in a medium generates a reduction in stiffness and an increase in damping; thus damping measurements can be used to detect or locate defects, for example crack initiation and propagation in a structural element can be monitored by measuring changes in wave attenuation in a given frequency range.

Resonant column and cyclic triaxial loading are two common laboratory methods to

measure the dynamic properties of material specimens such as soil (*Khan* 2006). The samples are taken in-situ from a medium that is being inspected; as a result, the disturbances are introduced to the medium; meanwhile, the samples tested in laboratory may not keep the original conditions as in the medium. The determination of the dynamic properties for a civil structure usually requires full experimental model measurements; the structure is excited with a known pattern of forces and the corresponding responses are measured at various locations on the structure, and then the damping is evaluated with a modal analysis technique (*Zhong* 2008). Considerable efforts are required for the implementation of this method.

Nondestructive testing techniques based on wave propagation shows advantages, because they are non-invasive, efficient and cost effective, where material damping is measured at a low-strain level ($< 10^{-5}$). Surface waves are useful, because they dominate in the surface response, and the penetration depth depends on their frequency or wavelength. The existing methods using surface waves such as spectral ratio (*Wang* 2006), use the Fourier transform to measure material damping ratio; however, a time window is required for the spectral ratio method to extract the arrival of surface wave, and subjective variations occurs; in addition, the spectral ratio is a function of frequency, and using linear curve fitting,a slope of the spectral ratio in frequency domain needs to be determined; however, the fitted slope varies for different frequency ranges, and the selection of a reliable frequency range is difficult.

Based on surface wave propagation, a new methodology is proposed to measure material damping ratio in a medium. The medium is assumed to be represented by a single-degree-freedom system (SDOF), and a theoretical equation for the calculation of material damping ratio using the wavelet transform is derived, which uses the maximum amplitude and phase information of the propagating surface waves; neither a time window nor a reliable frequency range are required.

In the numerical simulations, Rayleigh damping ratio as a function of frequency is given to the numerical models. The material damping ratio is calculated from the numerical results using the wavelet transform, and it gives a global value that represents an average effect for a frequency bandwidth determined by source. In the experimental tests, an ultrasonic piezoelectric transmitter as a source is used on the surface of a sand box, and the output force of the source is modeled with a Morlet function. The wave propagation of the generated ultrasonic pulse is measured on surface, and is analyzed with the wavelet transform. Both the numerical and experimental results show potential for practical applications.

5.5.2 Geometric attenuation and material damping

Wave propagation attenuates with distance because of geometric attenuation, which results from the increasing surface area of propagating wave front, and material damping, which gives energy dissipation due to internal particle friction of the material. Therefore, a spectral ratio is calculated with two distances x_1 and x_2 from the source, and it is related to the geometric attenuation and material damping (*Zerwer* 2002):

$$\frac{|G(\omega,x_1)|}{|G(\omega,x_2)|} = \left(\frac{x_1}{x_2}\right)^{\beta} \exp\left[\alpha_x(x_1 - x_2)\right] \tag{5.19}$$

where ω is the angular frequency; $|G(\omega,x)|$ is the spectral amplitude at a distance x from the source; β is a constant describing the geometric attenuation, which is determined by a type of the propagating wave fronts: $\beta = -0.5$ for surface waves (cylindrical wave fronts); $\beta = -1$ for body waves (spherical wave fronts) propagating inside the medium, and $\beta = -2$ for body waves propagating along the medium surface; α_x is the spatial coefficient of wave attenuation caused by material damping.

From Eq. 5.19, it is given:

$$\alpha_x = \frac{1}{x_2 - x_1}\left\{\ln\left[\frac{|G(\omega,x_2)|}{|G(\omega,x_1)|}\right] - \beta \ln\left(\frac{x_2}{x_1}\right)\right\} \tag{5.20}$$

The spatial attenuation coefficient α_x is related to the material damping ratio D (*Zerwer* 2002):

$$D = V\,\frac{\alpha_x}{\omega} \tag{5.21}$$

where V is the wave velocity. Using the spectral amplitudes from the Fourier transform, the spatial attenuation coefficient is calculated in Eq. 5.20, where the geometric attenuation is eliminated. Then, material damping ratio calculated with Eq. 5.21 gives a function of frequency.

5.5.3 Rayleigh damping ratio

The wave motion for a structural system is governed by:

$$[\mathbf{M}]\{\ddot{u}\} + [\mathbf{C}]\{\dot{u}\} + [\mathbf{K}]\{u\} = \{f\} \tag{5.22}$$

where $\{\ddot{u}\}$, $\{\dot{u}\}$ and $\{u\}$ are the acceleration, velocity and displacement vectors, respectively; $[\mathbf{M}]$, $[\mathbf{C}]$ and $[\mathbf{K}]$ are the mass, damping and stiffness matrices, respectively; $\{f\}$ is the force vector applied to the system.

For a small level of damping, a reasonable approximation for damping matrix in Eq. 5.22 is a common Rayleigh damping, by which the existence of a real mode can decouple the system's equation of wave motion (*Caughey* 1960, *Bathe* 1976). The Rayleigh damping matrix is given:

$$[\mathbf{C}] = [\mathbf{M}] \sum_{i=0}^{n-1} \left[\eta_i \left([\mathbf{M}]^{-1} [\mathbf{K}] \right)^i \right] \tag{5.23}$$

The simplest case of Rayleigh damping matrix consists of only two proportional terms when $n = 2$ (this may not accommodate for microstructure):

$$[\mathbf{C}] = \eta_0 [\mathbf{M}] + \eta_1 [\mathbf{K}] \tag{5.24}$$

where η_0 and η_1 are the mass and stiffness damping constants, respectively.

Many numerical finite element or finite difference codes adopt this two-parameter model to simulate damping for dynamic analysis. The Rayleigh damping ratio ξ is given as a function of frequency (*Itasca* 2000):

$$\xi = \frac{\eta_0}{2\omega} + \frac{\eta_1 \omega}{2} \tag{5.25}$$

The mass damping ratio (the first term on the right in Eq. 5.25) decreases with frequency; while the stiffness damping ratio (the second term on the right in Eq. 5.25) increases with frequency; they intersect at frequency ω_{min}, $\omega_{min} = 2\pi f_{min}$, where the Rayleigh damping ratio is the minimum (ξ_{min}) for different frequencies. Therefore, the mass damping influence more the low frequencies; while the stiffness damping has more of an influence at the high frequencies.

These two parameters ξ_{min} and f_{min} are used in the numerical models to define a relationship of Rayleigh damping ratio vs. frequency, and they are related to the mass and stiffness damping constants in Eq. 5.26. For given $\xi_{min} = 0.01$ and $f_{min} = 50kHz$, Fig. 5.18 shows an example of Rayleigh damping ratio, mass damping ratio and stiffness damping ratio for different frequencies.

$$\xi_{min} = \sqrt{\eta_0 \eta_1} \tag{5.26a}$$

$$\omega_{min} = \sqrt{\frac{\eta_0}{\eta_1}} \tag{5.26b}$$

5.5.4 Material damping ratio from wavelet transform

The wavelet transform of a time signal $g(t)$ is a time-scale decomposition by dilating and translating a chosen wavelet, as defined in Eq. 3.20. In Fig. 5.19, an ultrasonic piezoelectric transmitter is used on the surface of a medium, and generates surface wave propagation along the surface. If the medium represents a SDOF system, the surface responses at different distances from the source can be analyzed with the wavelet transform.

From Eq. 3.31, a free vibration response $g(t,x)$ for a viscously-damped SDOF system at a distance x from the source is given:

$$g(t,x) = A\exp[-\alpha_t \omega_n(x)(t-t_x)]\exp(-\alpha_x x)\cos[\omega_d(x)t + \theta(x)] \tag{5.27}$$

where A is a constant; t_x is the arrival time at a distance x; $\omega_n(x)$ and $\omega_d(x)$ are the natural and damped frequencies for a distance x, respectively, $\omega_n(x) \approx \omega_d(x)$ for a small damping; $\theta(x)$ is the initial phase. α_t and α_x are the attenuation coefficients in time and in space, respectively.

The output force of an ultrasonic piezoelectric transmitter is modeled with a Morlet function $\phi(t)$ (Eq. 3.28), which is applied at $x = 0$; therefore, the signal $g(t,x)$ is correlated with the Morlet function and this correlation varies with distance as waves propagate. Because $g(t,x)$ is asymptotic, from Eq. 3.33, its wavelet transform using a Morlet function $\phi(t)$ as a wavelet can be expressed by means of asymptotic techniques:

$$\begin{aligned} G^{<WT>}(a,b,x) = {} & \frac{A}{2}\sqrt{a}\exp[-\alpha_t \omega_n(x)(b-t_x)]\exp(-\alpha_x x)\ |\Phi[a\omega_d(x)]| \\ & \exp\{j[\omega_d(x)b + \theta(x)]\} \end{aligned} \tag{5.28}$$

where $\Phi(\omega)$ is the frequency spectrum for the Morlet function $\phi(t)$. The phase spectrum from the above equation is given:

$$\Theta(a,b,x) = \omega_d(x)b + \theta(x) \tag{5.29}$$

The amplitude of the wavelet transform is attenuated in time and space because of the two attenuation coefficients α_t and α_x; however, for given $a = 1$, it is the maximum at $b = t_x$ for a fixed distance x from the source. Therefore, for given $a = 1$ and $b = t_x$, the maximum amplitude $Y(x)$ from the wavelet transform $[G^{<WT>}(a,b,x)]$ at different distances is:

$$Y(x) = \frac{A}{2} \exp(-\alpha_x x) \; |\Phi[\omega_d(x)]| \tag{5.30}$$

From Eq. 5.29, the damped frequency $\omega_d(x)$ is obtained by taking a derivative of the phase spectrum of the wavelet transform with respect to the shift time b:

$$\frac{\partial}{\partial b}[\Theta(a,b,x)] = \omega_d(x) \tag{5.31}$$

The maximum amplitudes $Y(x_1)$ and $Y(x_2)$ can be measured at two distances; therefore, the attenuation coefficient α_x is solved from Eq. 5.30:

$$\alpha_x = -\frac{1}{x_2 - x_1} \left[\ln\left(\frac{Y(x_2)}{|\Phi[\omega_d(x_2)]|} \right) - \ln\left(\frac{Y(x_1)}{|\Phi[\omega_d(x_1)]|} \right) \right] \tag{5.32}$$

When $(x_2 - x_1)$ tends to be 0, the above equation becomes a derivative, and it is written:

$$\alpha_x = -\frac{d}{dx} \ln\left(\frac{Y(x)}{|\Phi[\omega_d(x)]|} \right) \tag{5.33}$$

Eq. 5.21 is rewritten in Eq. 5.34, which calculates the material damping ratio as a function of distance; with the wavelet transform, $\alpha_x(x)$ is obtained from a derivative using the maximum amplitude information (Eq. 5.33), and $\omega_d(x)$ is obtained from the derivative using the phase spectrum (Eq. 5.31).

$$D(x) = V \, \frac{\alpha_x(x)}{\omega_d(x)} \tag{5.34}$$

5.5.5 Summary

An ultrasonic piezoelectric transmitter as a source shows advantages over a traditional mechanical impactor, because it generates high frequencies, which is suitable for the depth evaluation of a shallow crack, and the source modeling can be represented with a Morlet function for the numerical simulations. Rayleigh waves have a useful property

for the evaluation of crack depth; their penetration depth concentrates at a depth of one third of the wavelength. Lamb waves are more complex, because different Lamb modes exist in a plate. However, the penetration depth of the fundamental Lamb mode energy depends on the mode shape, and it is similar to the Rayleigh wave mode when the wavelength is small compared to the plate thickness. A theoretical transfer function is derived and is used to study the Lamb mode dispersion and the participation of higher Lamb mode. The theoretical results show that the frequency components of Lamb waves vary with distance.

A new equation for the evaluation of material damping ratio using the wavelet transform is derived. The surface responses for the medium are modeled using single degree freedom of systems (SDOF). In the new equation, the attenuation coefficient is obtained from the variation of the maximum amplitudes of the wavelet transform, and the damped frequency is obtained from the derivative of the phase spectra. The maximum amplitude and phase information are calculated from the wavelet transform of the surface responses at different distances from the source. The calculated material damping represents an average damping for the frequency bandwidth determined by the source.

Table 5.1: Comparison of an ultrasonic piezoelectric transmitter and a mechanical impactor

Source	Applications	Characteristics
Ultrasonic piezoelectric transmitter	Ultrasonic pulse velocity, ultrasonic hole-logging.	Better wave orientation, concentrated energy, well-controlled high frequency range, great repeatability.
Mechanical impactor	Seismic, *SASW*, Impact-Echo.	Strong penetrability, broad frequency range, good simplicity.

Table 5.2: Characteristics of the ultrasonic piezoelectric transmitter used.

Active Element		Acoustic Properties
Thickness:	$h_0 = \lambda_0/2 = 12.7cm$	Typical impedance for steel *: $Z_1 = 45 \times 10^6 kg/m^2 s$
Wavelength:	$\lambda_0 = 2h_0 = 25.4cm$	Typical impedance for PST-4 *: $Z_2 = 39 \times 10^6 kg/m^2 s$
Resonance:	$f_0 = 50kHz$	Typical impedance for Perspex *: $Z_3 = 3.22 \times 10^6 kg/m^2 s$
P-wave velocity:	$V_P = \lambda_0 f_0 = 1270m/s$	Reflection coefficient: $R_A = (Z_1 - Z_2)/(Z_1 + Z_2) = 0.071$
Transit time:	$t_n = h_0/V_P = 10\mu s$	Reflection coefficient: $R_B = (Z_2 - Z_3)/(Z_2 + Z_3) = 0.847$

**Panametrics-NDT* 2006; *Park* and *Shrout* 1996.

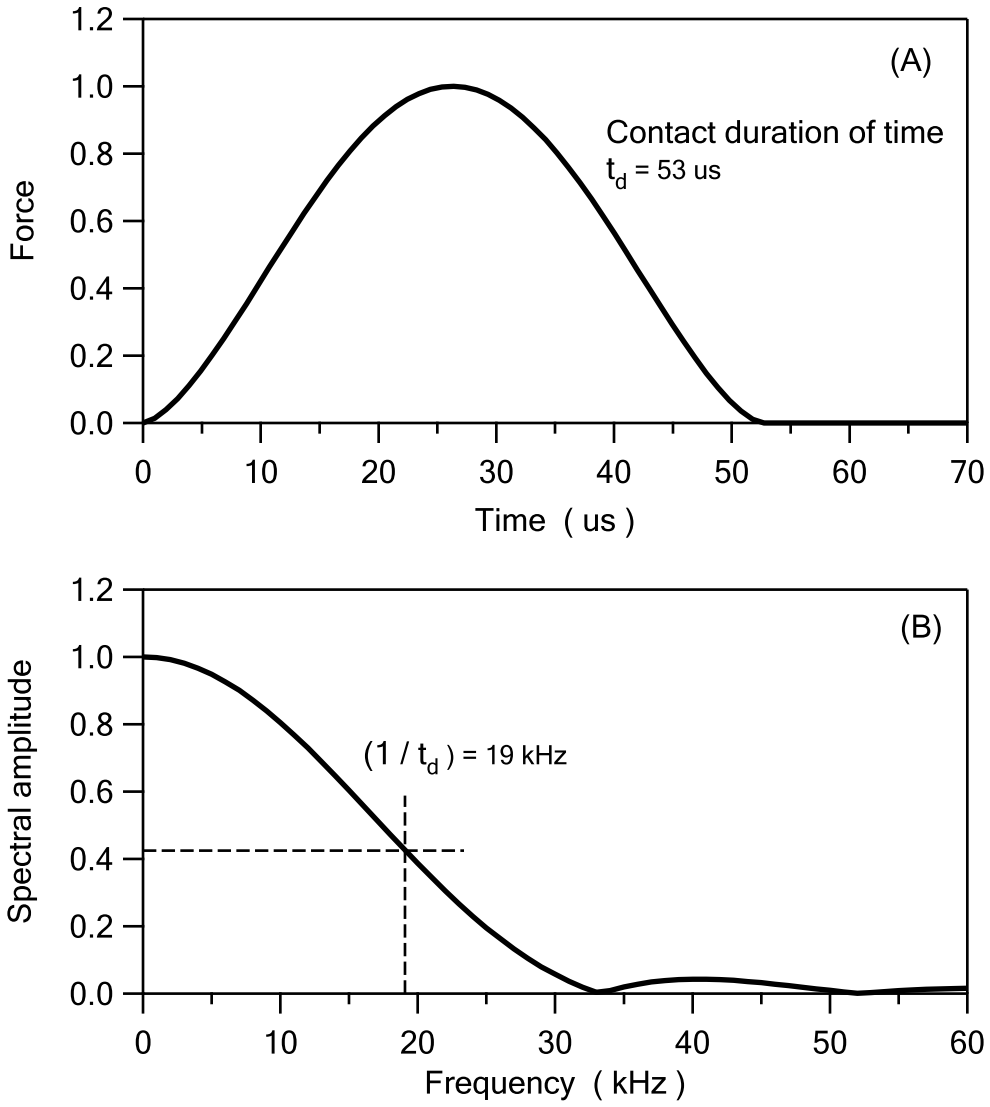

Figure 5.1: A 4.76*mm* diameter steel ball as an impact source dropped to the Plexiglas surface from a 50.8*mm* height. (A) force vs. time; (B) spectral amplitude vs. frequency.

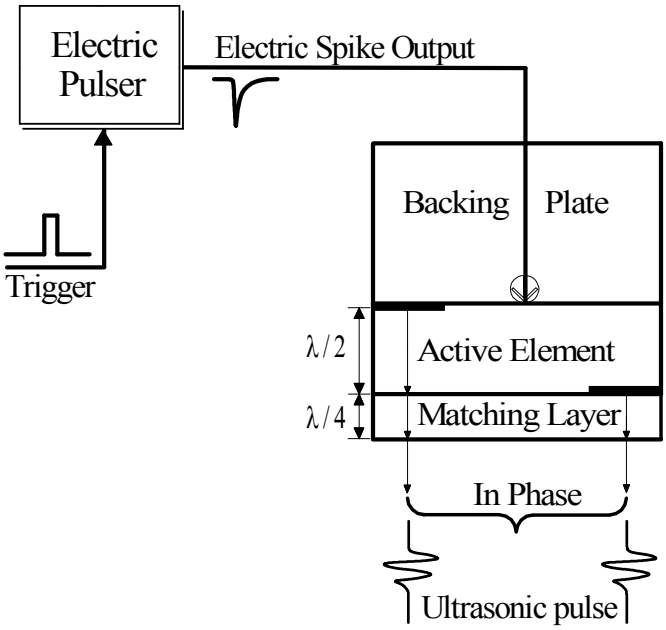

Figure 5.2: Structure of an ultrasonic piezoelectric transmitter.

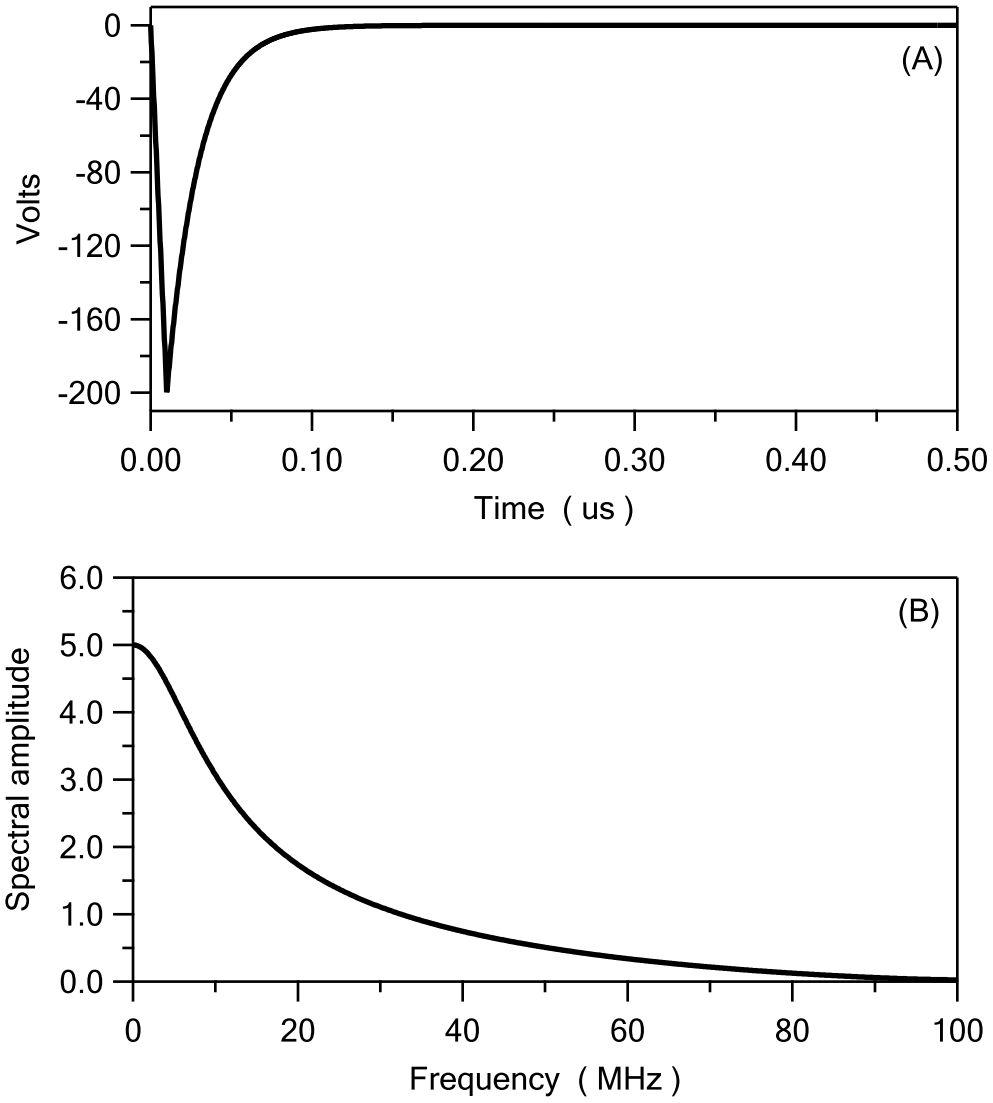

Figure 5.3: Output electric spike of a pulser. (A) in time; (B) in frequency.

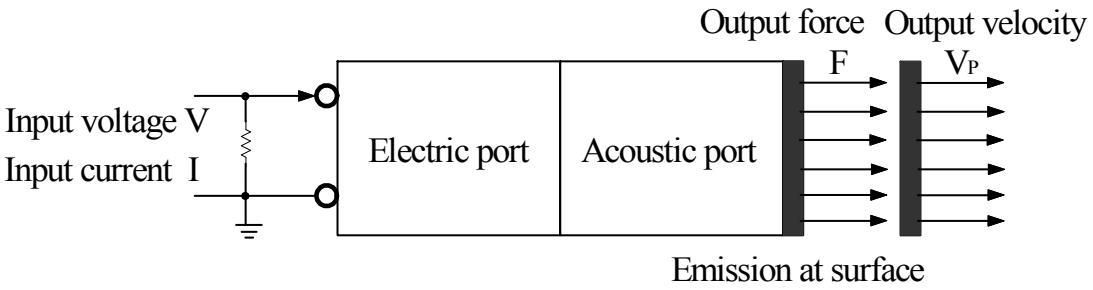

Figure 5.4: Electric and acoustic ports for an ultrasonic piezoelectric transmitter.

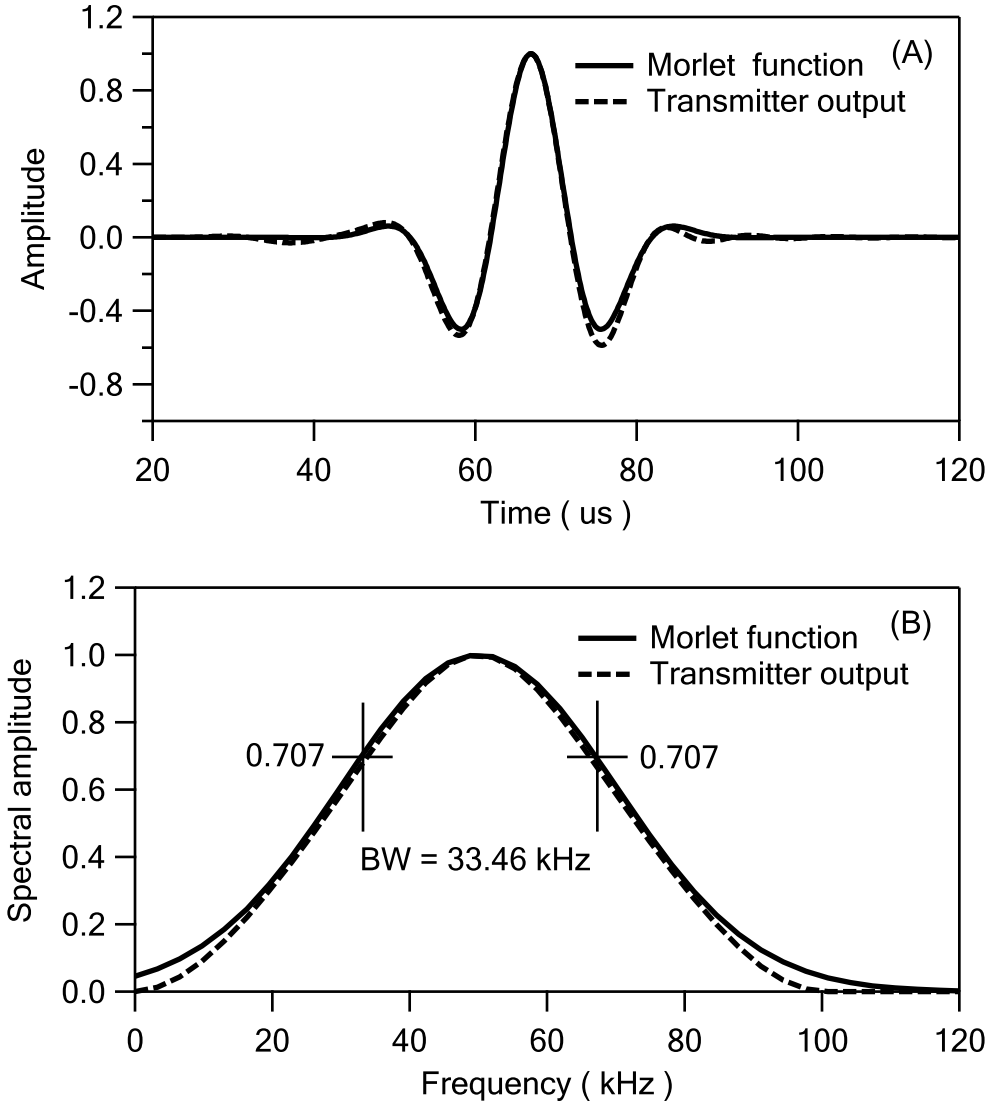

Figure 5.5: Comparison of the transfer function of an ultrasonic piezoelectric transmitter with the real part of a Morlet function for given $f_0 = 50kHz$ and $\tau = 1.12 \times 10^{-5}$ ($BW = 33.46kHz$). (A) in time; (B) in frequency.

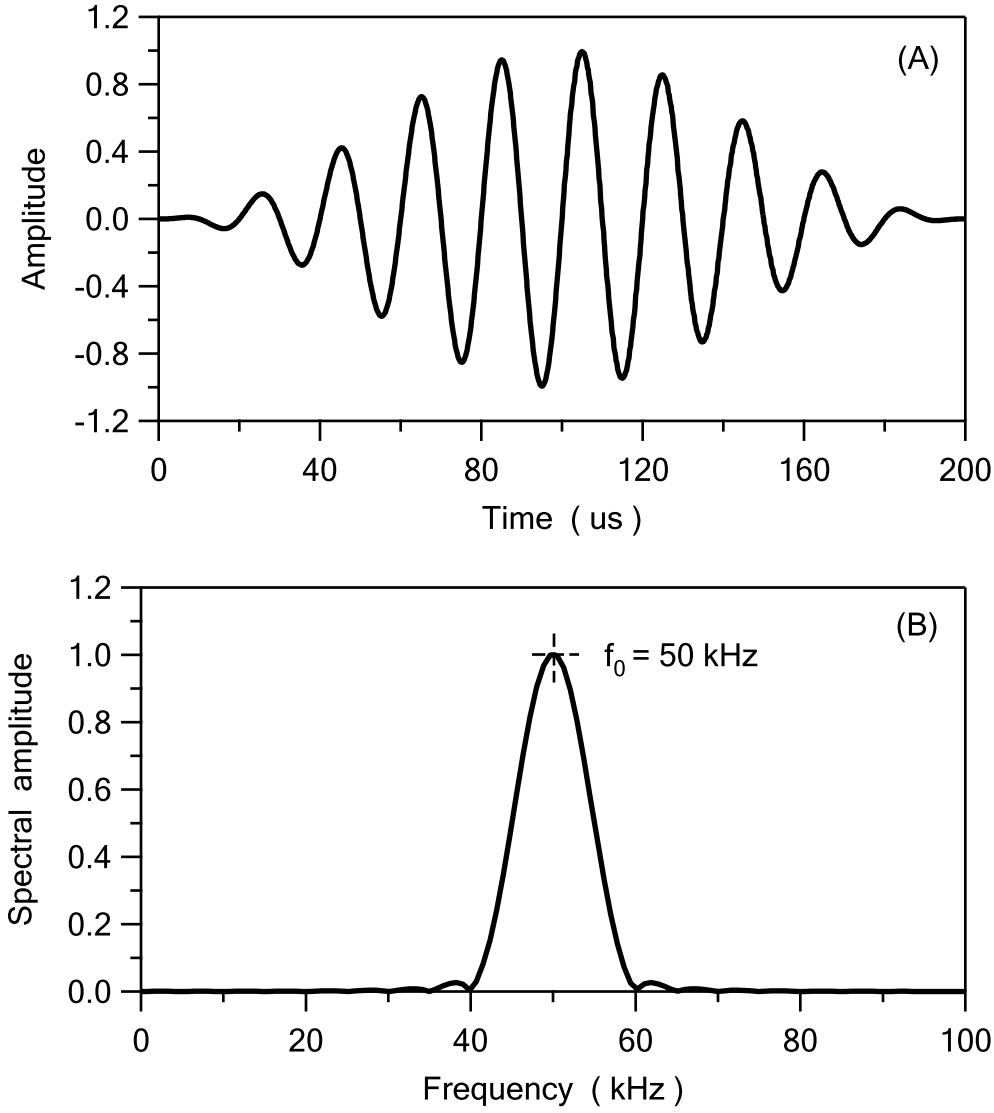

Figure 5.6: Numerical sinusoidal tone burst source ($f_0 = 50kHz$, $n = 10$). (A) in time; (B) in frequency.

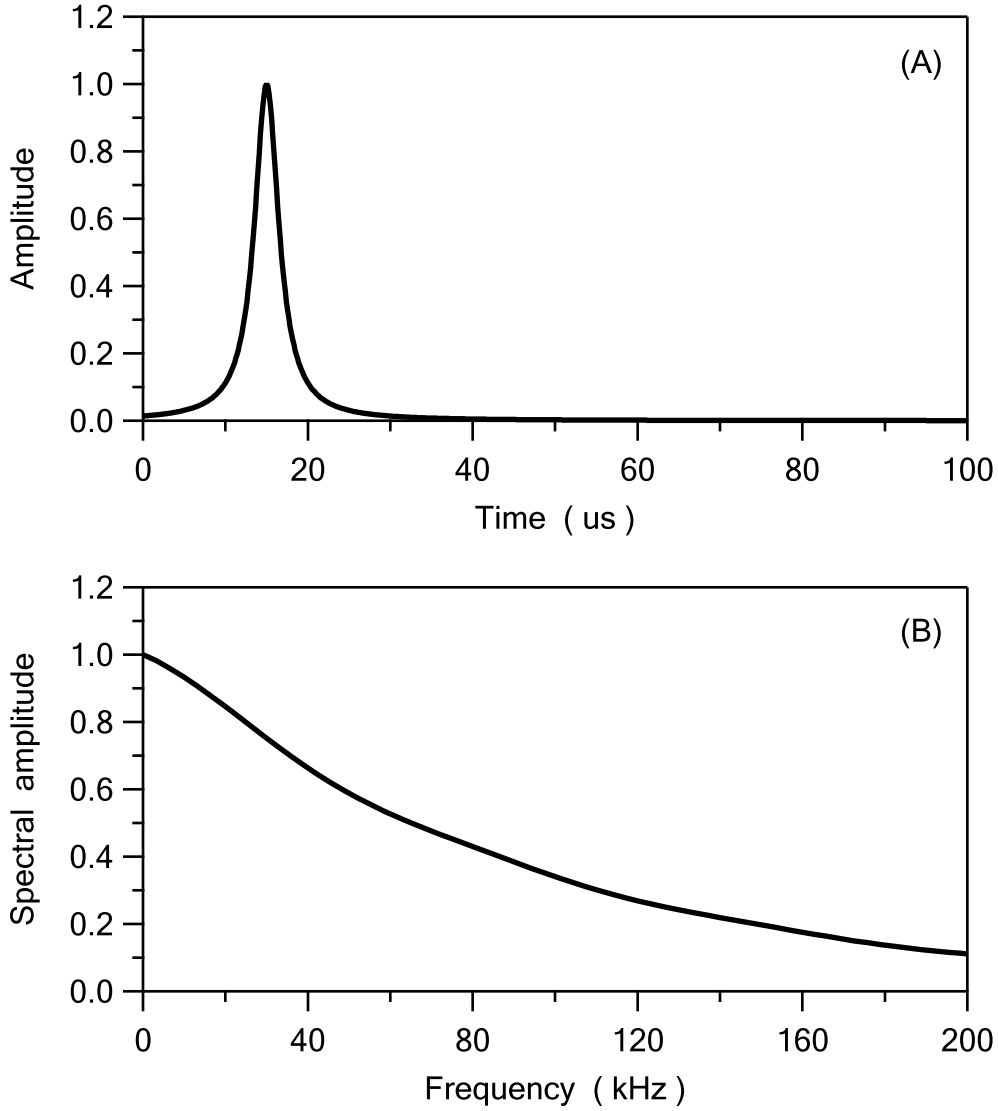

Figure 5.7: Numerical Lamb source ($\eta = 1.78 \times 10^{-6}$). (A) in time; (B) in frequency.

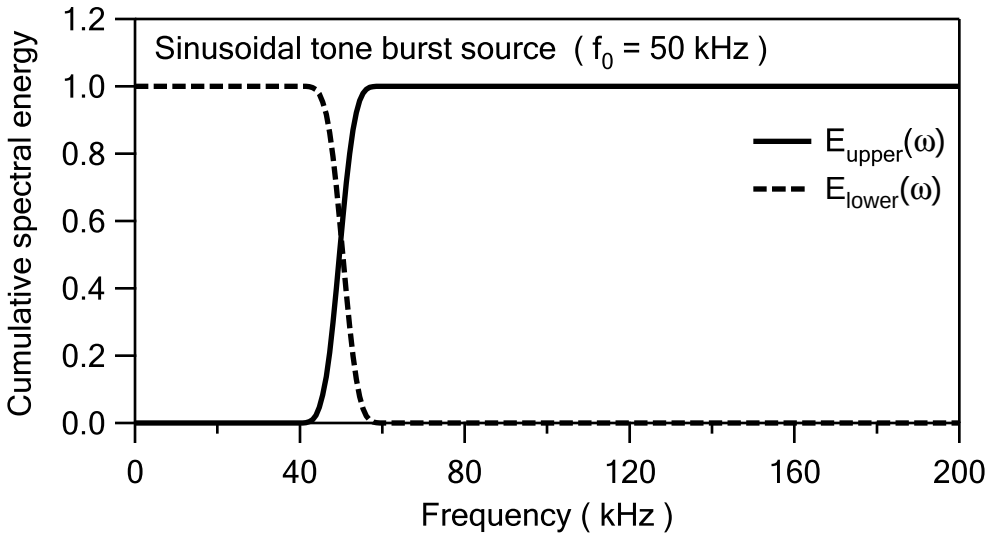

Figure 5.8: Cumulative spectral energy for sinusoidal tone burst source ($f_0 = 50kHz$, $n = 10$).

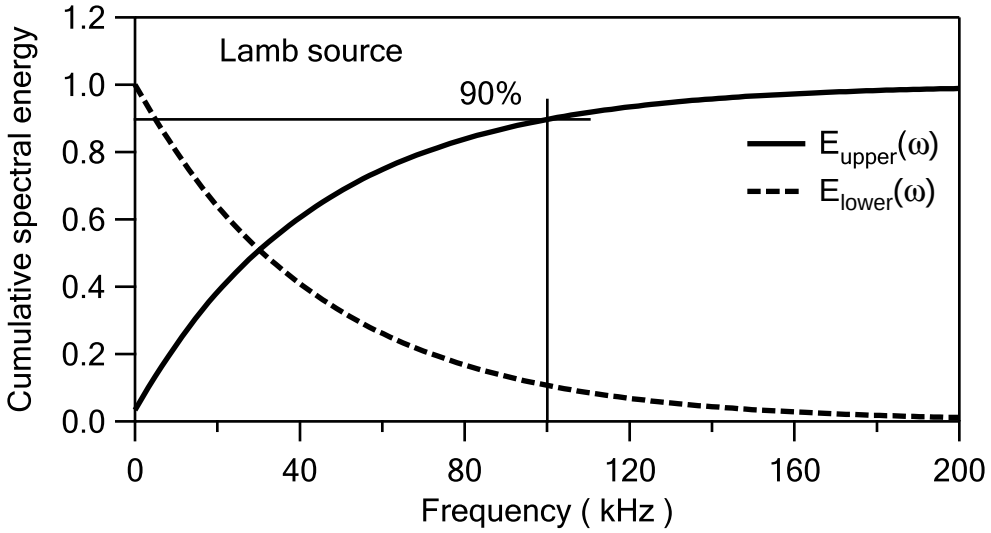

Figure 5.9: Cumulative spectral energy for Lamb source ($\eta = 1.78 \times 10^{-6}$).

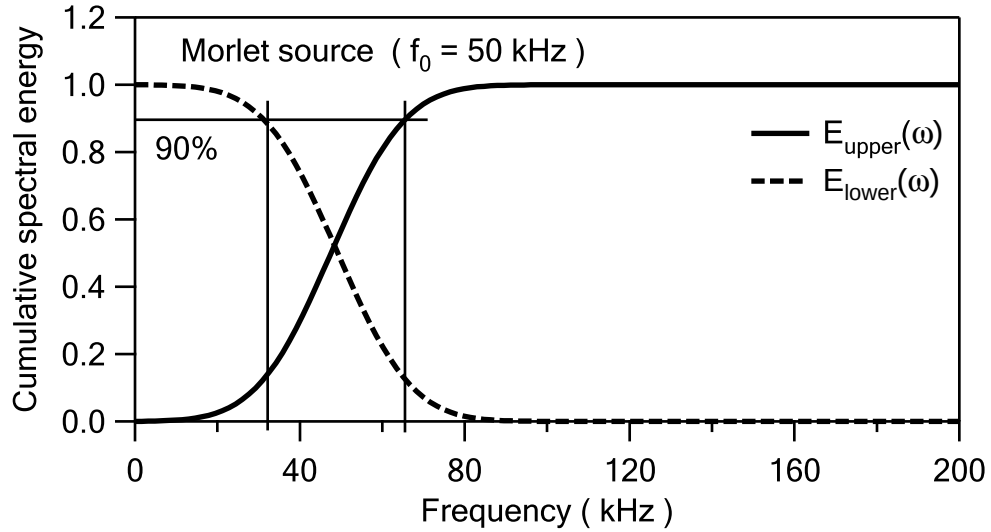

Figure 5.10: Cumulative spectral energy for Morlet source ($f_0 = 50kHz$, $\tau = 1.12 \times 10^{-5}$, $BW = 33.46kHz$).

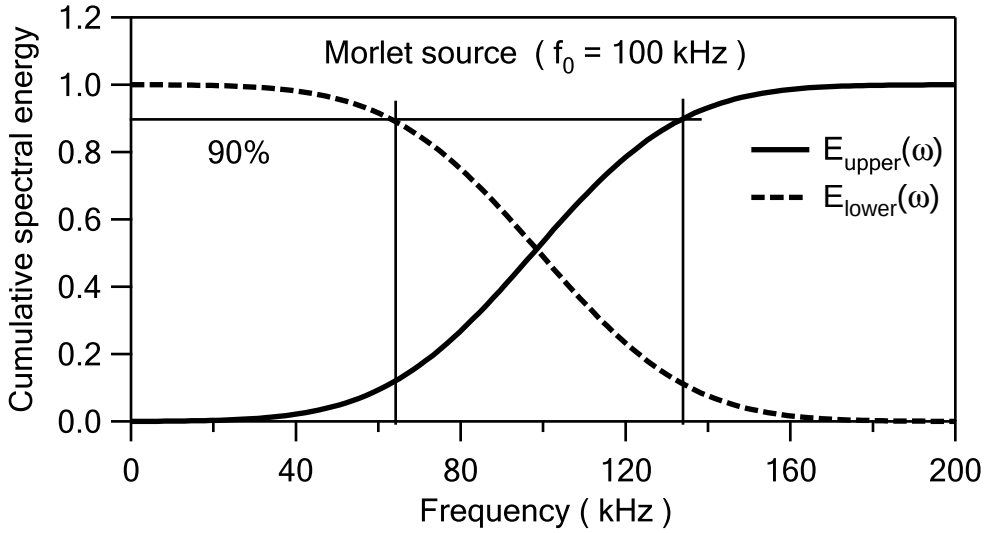

Figure 5.11: Cumulative spectral energy for Morlet source ($f_0 = 100kHz$, $\tau = 5.6 \times 10^{-6}$, $BW = 66.92kHz$).

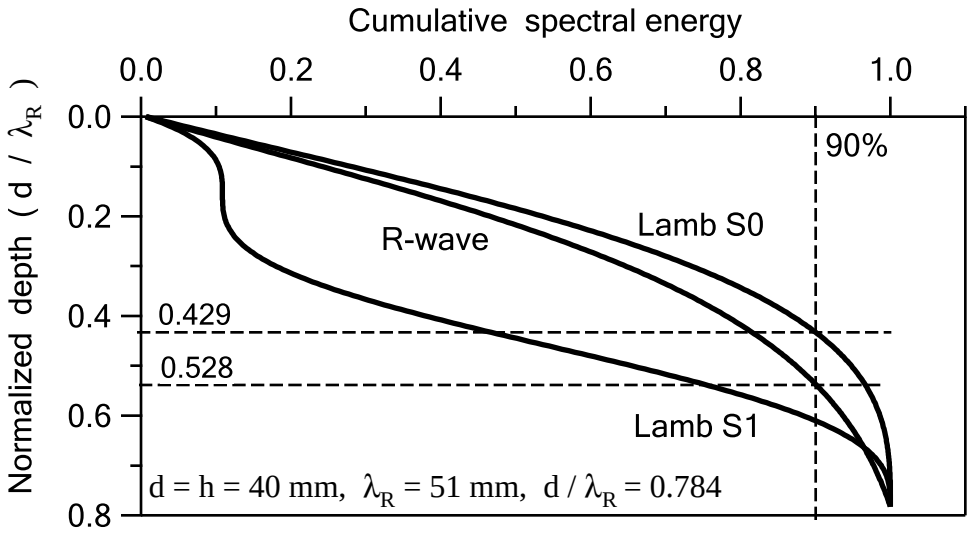

Figure 5.12: Cumulative spectral energy for Rayleigh wave mode, fundamental Lamb mode S0and higher Lamb mode S1. λ_R represents the wavelength of Rayleigh wave mode at $f = 50kHz$, where $V_P = 4800m/s$, $V_S = 2770m/s$, and $V_R = 2550m/s$.

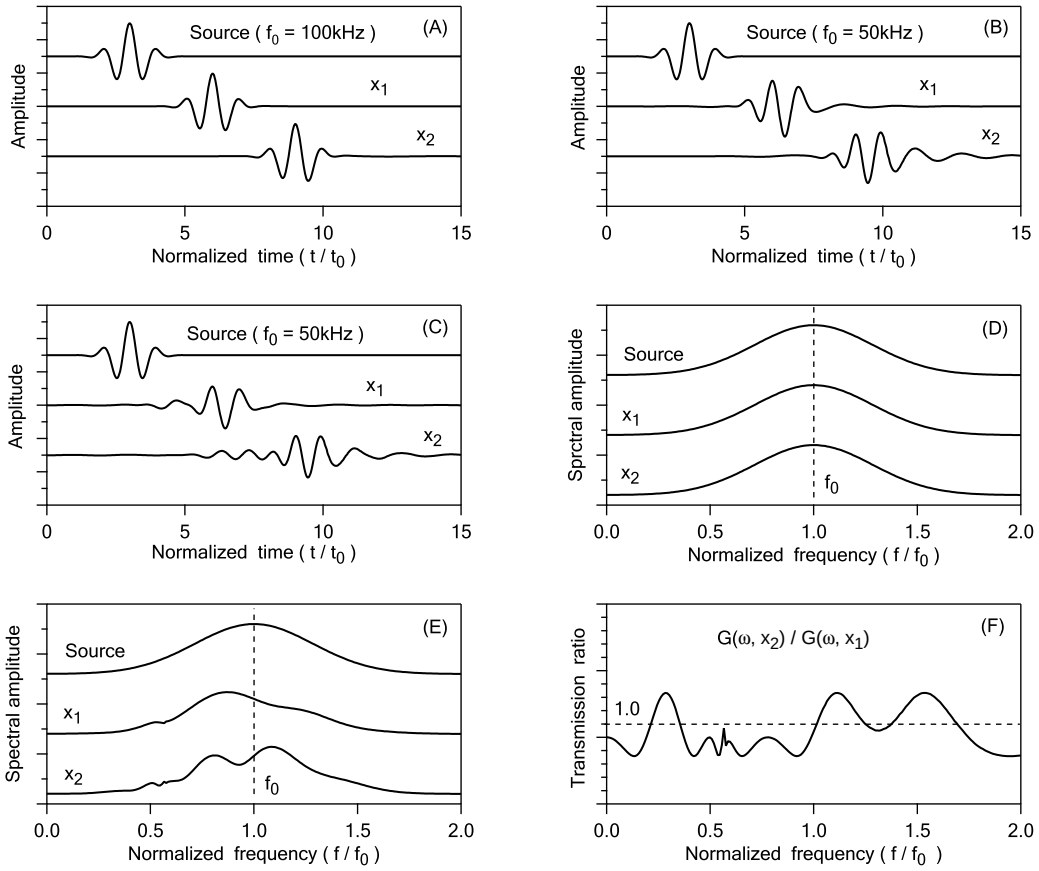

Figure 5.13: Propagation of a Morlet pulse as a (A) Lamb mode S0, $f_0 = 100kHz$; (B) Lamb mode S0, $f_0 = 50kHz$; (C) combination of Lamb modes S0 and S1, $H(\omega,x) = 0.8\,H_{S0}(\omega,x) + 0.2\,H_{S1}(\omega,x)$, $f_0 = 50kHz$. (D) spectral amplitudes of time signals for Figs. 5.13A and B; (E) spectral amplitudes of time signals for Fig. 5.13C; (F) transmission ratio for Fig. 5.13C. The time and frequency axes are normalized, $t_0 = 1/f_0$ and $(x_2 - x_1)/\lambda = 3$.

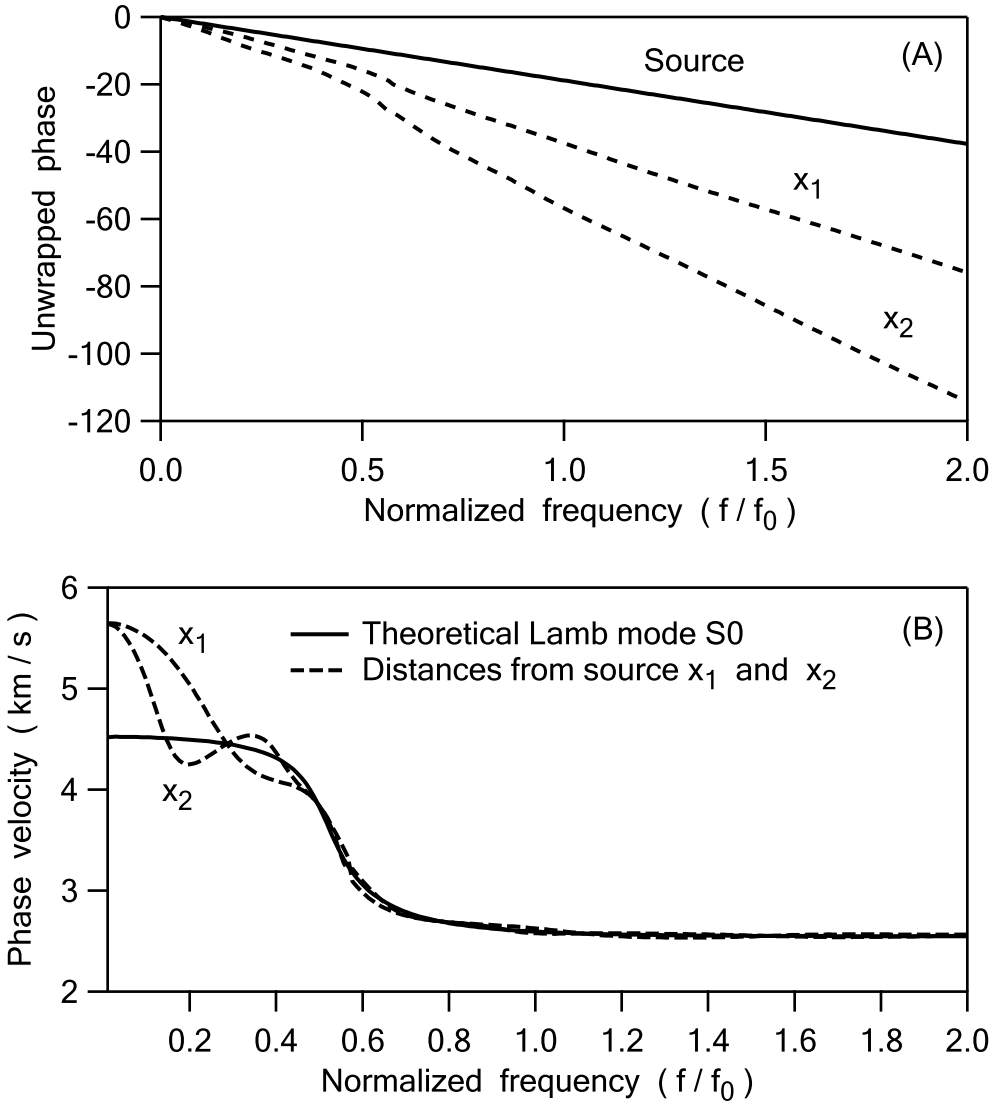

Figure 5.14: Phase velocity using unwrapped phase for case in Fig. 5.13C. (A) unwrapped phases calculated from the frequency spectra $G_0(\omega)$, $G(\omega,x_1)$ and $G(\omega,x_2)$; (B) phase velocities calculated from the unwrapped phases, and compared with the theoretical results for Lamb mode S0.

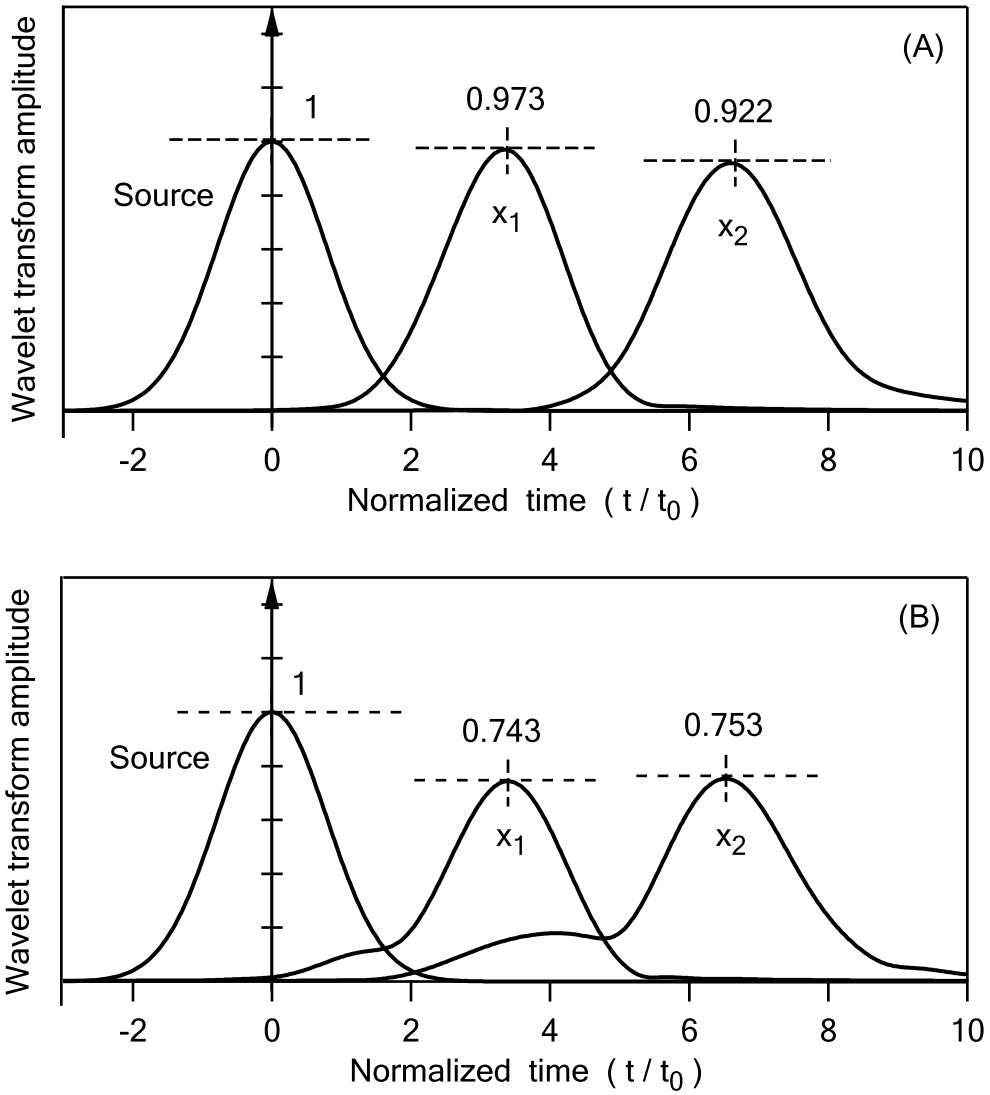

Figure 5.15: Amplitude from the wavelet transform for cases in (A) Fig. 5.13B; and (B) Fig. 5.13C. $f_0 = 50kHz$ for both cases, and $t_0 = 1/f_0$.

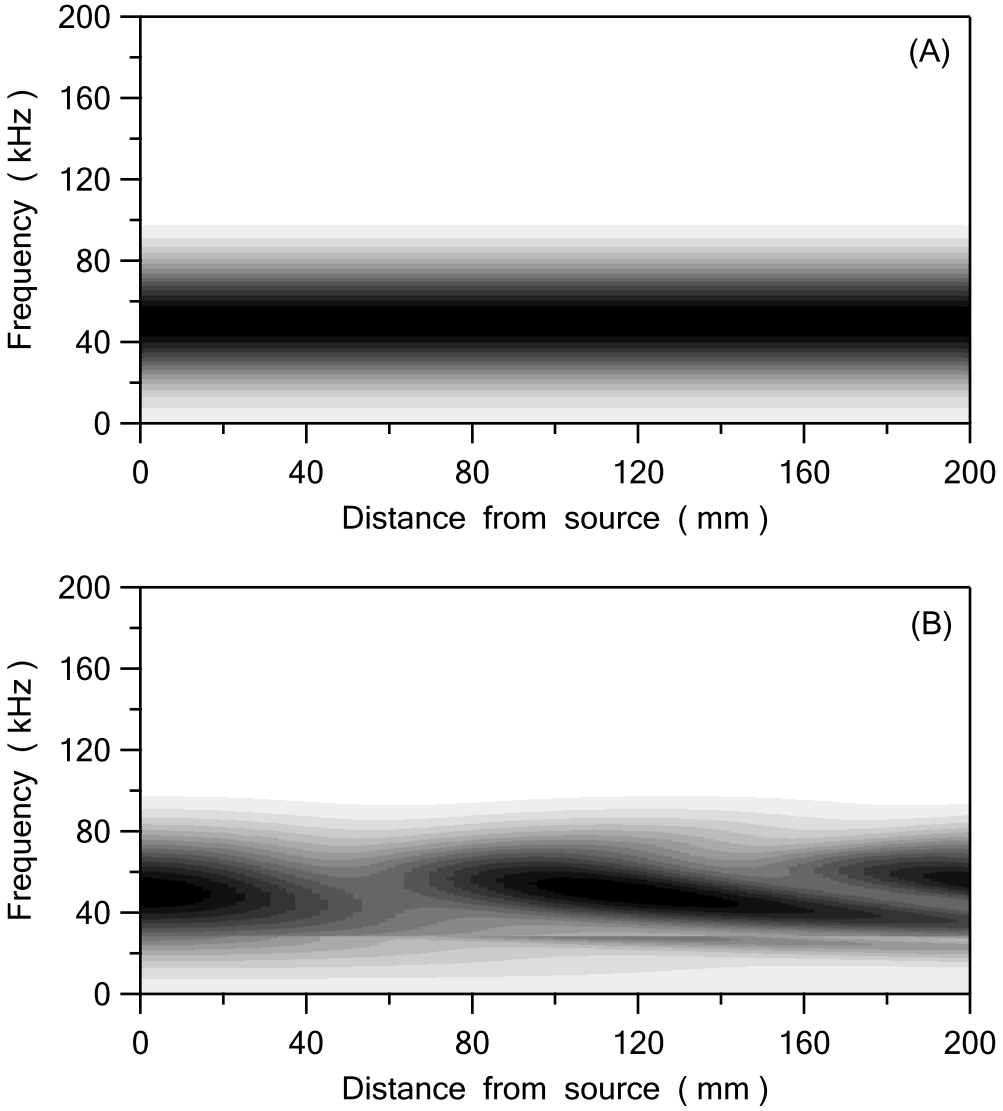

Figure 5.16: Spectral amplitudes at different distances (0 to 200mm) for the wave propagation of a Morlet function ($f_0 = 50kHz$ and $\tau = 1.12 \times 10^{-5}$) as: (A) Rayleigh waves in a half-space; (B) Lamb waves in a plate.

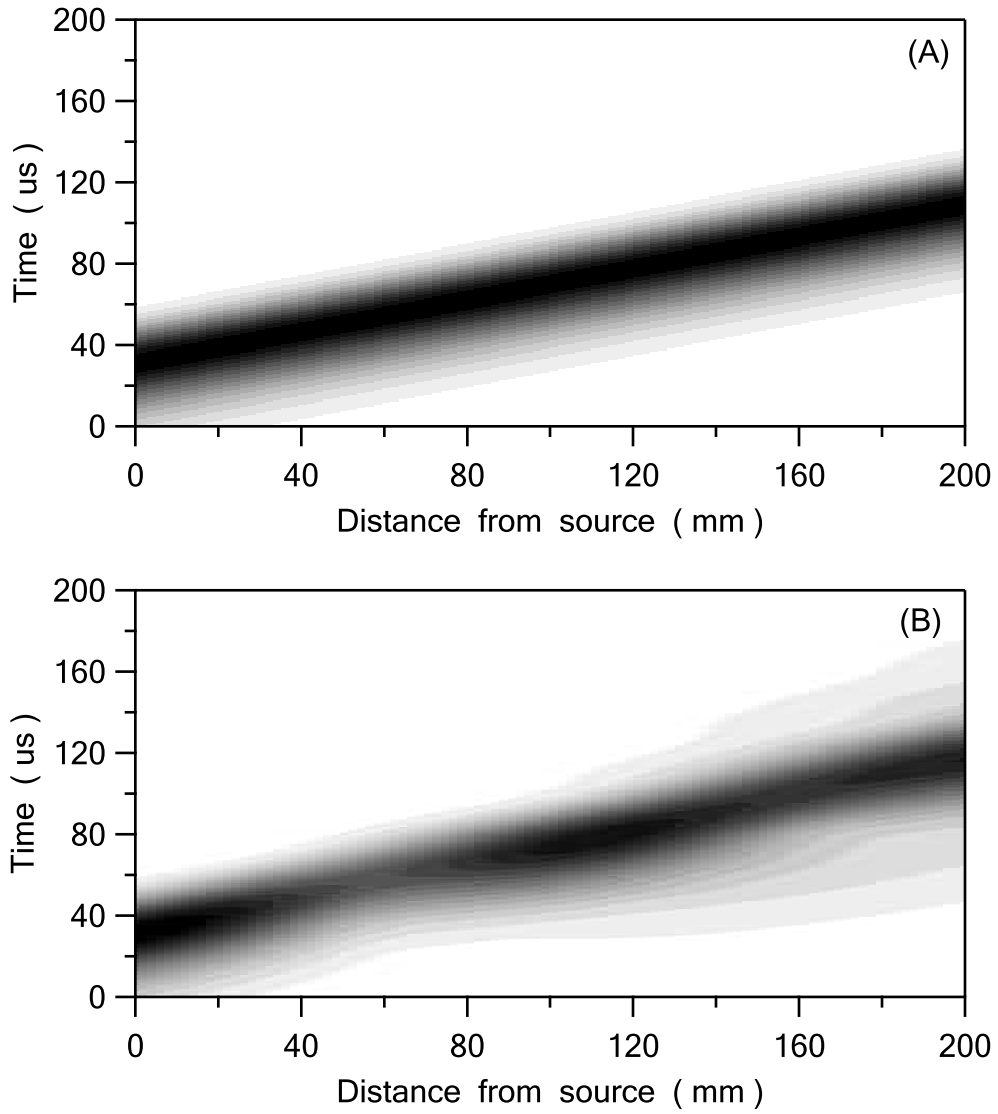

Figure 5.17: Amplitudes of the Morlet wavelet transforms at different distances (0 to 200*mm*) for the wave propagation of a Morlet function ($f_0 = 50kHz$, $\tau = 1.12 \times 10^{-5}$) as: (A) Rayleigh waves in a half-space; (B) Lamb waves in a plate.

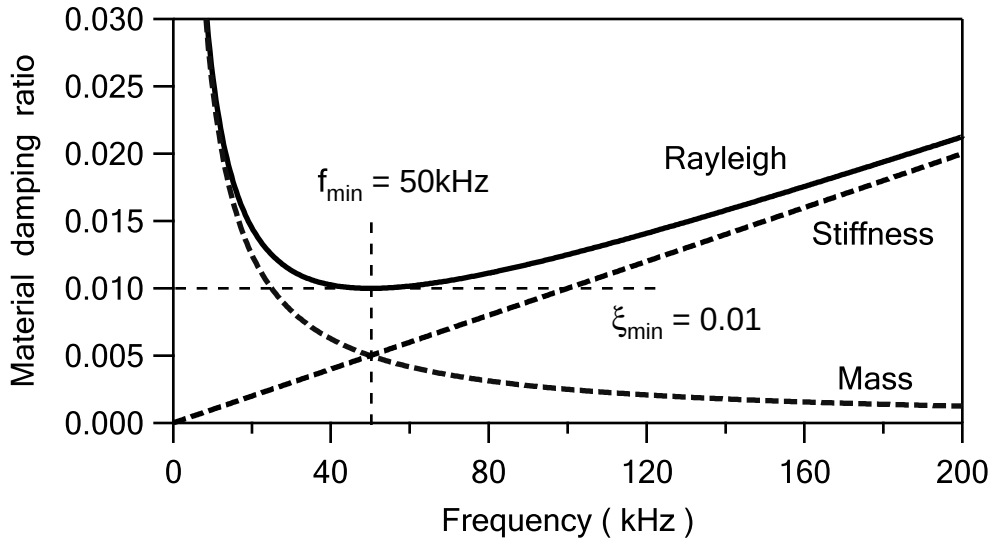

Figure 5.18: Rayleigh damping ratio, mass damping ratio and stiffness damping ratio vs. frequency for given $\xi_{min} = 0.01$ and $f_{min} = 50kHz$.

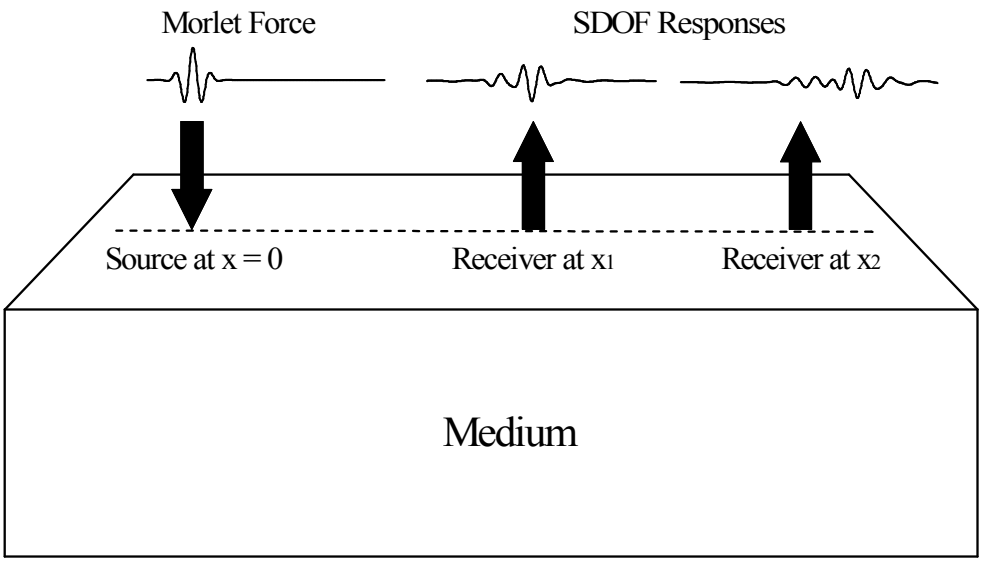

Figure 5.19: Surface wave propagation of an ultrasonic pulse along the surface of a medium, where the surface response is modeled as a SODF system.

Chapter 6

Experimental methodology and setups

6.1 Introduction

Different methods for the depth evaluation of surface-breaking cracks in concrete are summarized in **Chapter 4.6**; thereinto, the Fourier transmission coefficient (FTC) is promising. In this research, the wavelet transmission coefficient (WTC) is proposed to overcome the problems that exist in the FTC method by performing the following works:

- An ultrasonic piezoelectric transmitter is used as a source. It can provide wave concentration, high repeatability, and high frequency components that are suitable for the depth evaluation of small surface-breaking cracks. Moreover, the output force of the transmitter can be modeled with a Morlet function.
- The equal spacing configuration is used for the WTC measurements. The frequency components of the propagating Lamb waves vary with distance; in addition, wave attenuation caused by geometric attenuation and material damping are different for two receiver locations if they are unequally spaced from the source. By placing two receivers equally spaced from the source, the variation of the frequency components at two receivers is attributed only to the presence of a surface-breaking crack, and the variation increases with the crack depth.
- An ultrasonic pulse generated by an ultrasonic piezoelectric transmitter carries wave energy in a frequency bandwidth. The wave propagation along the surface is analyzed with the wavelet transform, and the results integrate the effects of a surface-breaking crack over the frequency bandwidth and give as output a global coefficient that is related to the depth of a surface-breaking crack. The coefficient is

calculated from the results of the wavelet transform that corresponds to the arrival time of an ultrasonic pulse.

Experimental tests for the depth evaluation of a surface-breaking crack are performed. In laboratory, two types of concrete plates are used as specimens, one with plain concrete, and another with reinforced concrete. In-situ tests are performed using concrete pipe specimens. First, different crack depths are found at a concrete pipe specimen, and they are tested using the WTC method. Then, D-loading is applied to a concrete pipe specimen to initiate crack, and as a D-loading increases, the crack depth is tested using the WTC method.

For the measurement of material damping ratio, the amplitude and phase information from the wavelet transform of surface waves are used. The experimental tests are performed on a sand box and a concrete plate specimen, respectively. A typical value of material damping ratio for uncracked and low-stress concrete, is in a range from 0.007 to 0.010 (*Cremer* 1988). In the sand box, the top layer is filled with cemented sand. Using resonant column (*Khan* 2006), the material damping ratio and Poisson's ratio for this cemented sand were measured as 0.4% and 2%, respectively. Different cement contents affect the damping ratio and Poisson's ratio of cemented sands; however, this effect is not studied in this research.

6.2 Depth evaluation of a surface-breaking crack

6.2.1 Laboratory setup

For the depth evaluation of surface-breaking cracks in concrete, a picture for the experimental setup is shown in Fig. 6.1. The concrete plate specimens with dimensions: $1200 \times 800 \times 80mm$ are used to measure the variation of the wavelet transmission coefficient (WTC) with the depth of a notch. Previous experimental works (*Popovics* 2000) show that no significant difference exists for the depth evaluation in concrete between a crack and a notch using the FTC method; the same is expected to hold for the WTC method. Therefore, a notch is cut at the center of the specimens to simulate a surface-breaking crack with depths of $5mm$, $10mm$, $15mm$, $20mm$, and $30mm$, respectively.

The two types of concrete plate specimens were cast for laboratory tests (Fig. 6.2). One type is not reinforced (plain concrete), and another is reinforced with rebars, which are welded with a mesh size of $100 \times 100mm$ and flatly laid at a depth of $40mm$ in the specimens before casting. The concrete properties are measured as reference values,

used for the numerical simulations, but not to predict the real values of the concrete properties; therefore, a total of the three specimens are used. The mechanical properties of the concrete are measured from one cylindrical specimen: density $\rho = 2340 kg/m^3$ and compressional strength $\acute{f_c} = 35 MPa$. The compressional strength and the density are evaluated as the average of three specimens. Based on the ultrasonic pulse velocity (UPV) method, the P-wave velocity is measured as $V_P = 4800 m/s$, using one specimen.

6.2.2 Instrumentation

A miniature accelerometer (PCB353B65, frequency range for a flat amplitude response: $1 Hz$ to $25 kHz$ at $\pm 3 dB$, resonant frequency: $52 kHz$, sensitivity: $102.9 mV/g$) is used as a receiver, and a commercial glue is used as a coupling. The accelerometer is powered with an external power supply (PCB483A), its response is filtered with a $200 kHz$ low-pass filter (KROHN-HITE 3384) to avoid aliasing, and recorded with a 16-channel data acquisition system (WaveBook/516E, 16 bits resolution, $1 MHz$ sampling rate). Two Pundit ultrasonic transmitters with a resonant frequency $50 kHz$ are used as excitation sources. The excitation frequency is selected to coincide with the resonant frequency to obtain a high signal-noise ratio (SNR). The effect of ringing of the transducers is reduced in the calculations of the wavelet transform, where the final results are dominated by the first arrivals. Nonlinear effects in the amplitude response of the receiver are reduced in the calculation of the WTC because of a ratio.

6.2.3 Wavelet transmission coefficient

As shown in Fig. 6.2, an equal spacing configuration is used for the proposed wavelet transmission coefficient (WTC) method, where two ultrasonic piezoelectric transmitters are fixed at points A and D, and an accelerometer is placed at point B or C. The four vertices A-B-C-D define a square, and an ultrasonic pulse from the source location propagates the same distance to the receiver locations. Similar to the FTC method, in these tests, the effects from coupling (bond fixity) and nonlinear transfer function of transducers are eliminated or reduced by using the self calibrating technique (Achenbach 1992).

In the tests, the accelerometer is first placed at point B, and the time signals $g_{AB}(t)$ and $g_{DB}(t)$, where the first subscript represents the source location and the second subscript represents the receiver location, are obtained by exciting the transmitters at points A and D, respectively. Similar to the FTC method, to eliminate the effects from the nonlinear behavior of the transducer's transfer functions and variations of the couplings,

a self-calibrating technique is performed by a complementary test (*Achenbach* 1992); therefore, the accelerometer is moved to point C, and the time signals $g_{AC}(t)$ and $g_{DC}(t)$ are measured. Because of a high repeatability for the ultrasonic piezoelectric transmitter, $g_{AB}(t)$ and $g_{AC}(t)$ are assumed to be measured simultaneously with the same source applied, and the same is assumed for $g_{DB}(t)$ and $g_{DC}(t)$.

The Fourier transmission coefficient (FTC) is given as a ratio of the spectral amplitudes; similarly, the wavelet transmission coefficient (WTC) is defined as a ratio of the maximum amplitudes from the extended wavelet transform (Eq. 3.25):

$$WTC(b=t_r) = \sqrt{\frac{\left|G_{AC}^{<EWT>}(b)\right| \left|G_{DC}^{<EWT>}(b)\right|}{\left|G_{AB}^{<EWT>}(b)\right| \left|G_{DB}^{<EWT>}(b)\right|}} \tag{6.1}$$

where t_r corresponds the arrival time of an ultrasonic pulse at receivers.

In the above equation, the numerators $\left[G_{AC}^{<EWT>}(b)\right]$ and $\left[G_{DC}^{<EWT>}(b)\right]$ represent the wavelet transform results from the wave paths where a surface-breaking crack is present; while the denominators $\left[G_{AB}^{<EWT>}(b)\right]$ and $\left[G_{DB}^{<EWT>}(b)\right]$ represent the wavelet transform results from the wave paths without a crack. Therefore, the calculation for a ratio of the wavelet transform amplitudes gives a variation, which increases with the crack depth, and vice versa.

The extended wavelet transform is calculated using Eq. 3.25, where a Morlet function ($f_0 = 50kHz$, $\tau = 1.12 \times 10^{-5}$, $BW = 33.46kHz$) is used as a wavelet. The frequency range is selected as $f_2 = 40kHz$ to $f_1 = 80kHz$, which corresponds to a range of the dilation parameter a (frequency scale) as a variable in the integral: $a_1 = f_0/f_1 = 0.625$, and $a_2 = f_0/f_2 = 1.25$. The amplitude of the extended wavelet transform varies with shift time b; however, it usually reaches the maximum at $b = t_r$.

6.2.4 In-situ tests

The wall of concrete pipes can be represented with a plate in the laboratory tests, because the transducer's spacing ($30mm$) is small relative to the diameter of the pipes. To test a real crack in concrete pipes, the in-situ experimental tests were performed twice at the Hanson Pipe and Precast Inc., Cambridge, Ontario, Canada, in June 2008. The tested concrete pipe specimens (Fig. 6.3) are $2.44m$ long, and the diameter and the wall thickness are $1.35m$ and $0.16m$, respectively.

For the first test, two cracks were found on the interior wall surface of a concrete pipe specimen; one is shallow, and another is deep. The cracks were distributed from the

one end of the specimen to a location close to the middle of the length. From the one end of the specimen (Fig. 6.4), the two crack depths were estimated as 50*mm* and 150*mm* deep, respectively. Normally, when a crack is initiated in concrete by a load, it develops to a depth that is not very shallow. For this reason, a crack with a shallower depth than 50*mm* is difficult to find at the site.

The test position is located at a distance of 60*mm* from the one end of the specimen, and an experimental setup for transducers is shown in (Fig. 6.5). The WTC measurements follow the same procedures as done for the laboratory tests. Four time signals are measured for each crack depth, and the 30*mm* equal spacing configuration is used.

For the second test, a newly-cast concrete pipe specimen was taken for a D-loading tests (Fig. 6.6). According to the D-loading chart from the Canadian standard CSA A257.2 M-9, the maximum load of 392.4*kN* was applied to the tested concrete pipe specimen, and the width of a crack was measured with a gauge. The standard requires the crack width be smaller than 0.3*mm*; otherwise, the concrete pipe specimen is considered not acceptable.

At a location of the interior wall surface of the concrete pipe specimen, the WTC are measured at different D-loading stages. The first measurement is performed on a flawless of the interior wall surface before the D-loading starts. Then, the load increases until a crack is observed on the interior wall surface, when the load is 242.4*kN* at the second stage. The measurement for the third stage is performed at the same location when the load increases to 290.8*kN*. At the fourth stage, the load reaches the maximum, which is 392.9*kN*. Finally, the load is released at the fifth stage, and the measurement is performed to check a recovery of the crack depth. In Fig. 6.7, a technician tried to locate a possible crack and measure its width.

6.3 Measurement of material damping ratio

6.3.1 Laboratory setup

The experimental program for the measurement of material damping ratio is performed in laboratory using a sand box and a concrete plate as specimens. The sand box has two layers (Fig. 6.8); the top layer is filled with cemented sand and is 300*mm* deep; the bottom layer is filled with dry sand and is 450*mm* deep; the horizontal dimensions are $1060 \times 870mm$; an underground void in the sand box has a size of $15 \times 10cm$, and is located in a center position that is 8*cm* below the surface. This cemented sand is used for the measurement of material damping ratio (void ratio of the sand material = 0.62, and

void ratio of the cemented sand = 0.50). The concrete plate (Fig. 6.9) is the same one used for the depth evaluation of a surface-breaking crack, which does not have rebars and notch.

On the surface of the sand box specimen, The source location is 350*mm* and 300*mm* spaced from the left and front boundaries, respectively; the first receiver location is selected at 220*mm* from the source. Then, the receiver is moved to the right with a spacing of 20*mm* for total 12 measurements. For the concrete plate specimen, the source is located at the center on the plate surface; the receiver locations are 30*mm*, 60*mm*, 90*mm*, and 120*mm* for total 4 measurements. For both specimens, the receivers are aligned with the source.

6.3.2 Instrumentation

Similar to the depth evaluation of a surface-breaking crack, an ultrasonic piezoelectric transmitter (Pundit, resonant frequency: $50kHz$) is used as a source and fixed at the surface location; a miniature accelerometer (PCB353B65, frequency range for a flat amplitude response: $1Hz$ to $25kHz$ at $3dB$, resonant frequency: $52.0kHz$, sensitivity: $102.9mV/g$) is used as a receiver to record the surface responses at different receiver locations. The receiver is placed at different locations for each measurement. Because of a high repeatability, an ultrasonic piezoelectric transmitter is assumed to generate the same ultrasonic pulse for each measurement; therefore, the signals for different receiver locations can be assumed to be measured simultaneously.

6.3.3 Typical values of material damping ratio

For cemented sand, 0.4% is a reference value of material damping ratio for this laboratory test, which is measured using resonant column (*Khan* 2006).

For concrete, material damping ratio is related to the intrinsic stress condition and the extent of cracking. Different values of material damping ratio for concrete are given in Table 6.1. The tested specimen is uncracked, and low-stress concrete; therefore, a measured value for material damping ratio from 0.007 to 0.010 is acceptable.

6.4 Summary

Two new methodologies are proposed for the depth evaluation of a surface-breaking crack and the measurement of material damping ratio, respectively. Based on the wavelet transforms of four measured time signals, the wavelet transmission coefficient is defined, which is related to the crack depth. The laboratory and in-situ experimental setups are described. The material damping ratio is measured in the laboratory; the tested materials are cemented sand and concrete; typical material damping ratios for these materials are presented.

Table 6.1: Material damping ratio for concrete (Cremer 1988)

Concrete	Material damping ratio
Reinforced concrete	
Small Stress Intensity (uncracked)	0.007 to 0.010
Medium Stress Intensity (fully cracked)	0.010 to 0.040
High Stress Intensity (fully cracked but no yielding of reinforcement)	0.005 to 0.008
Prestressed Concrete (uncracked)	0.04 to 0.07
Partially Prestressed Concrete (slightly cracked)	0.008 to 0.0124

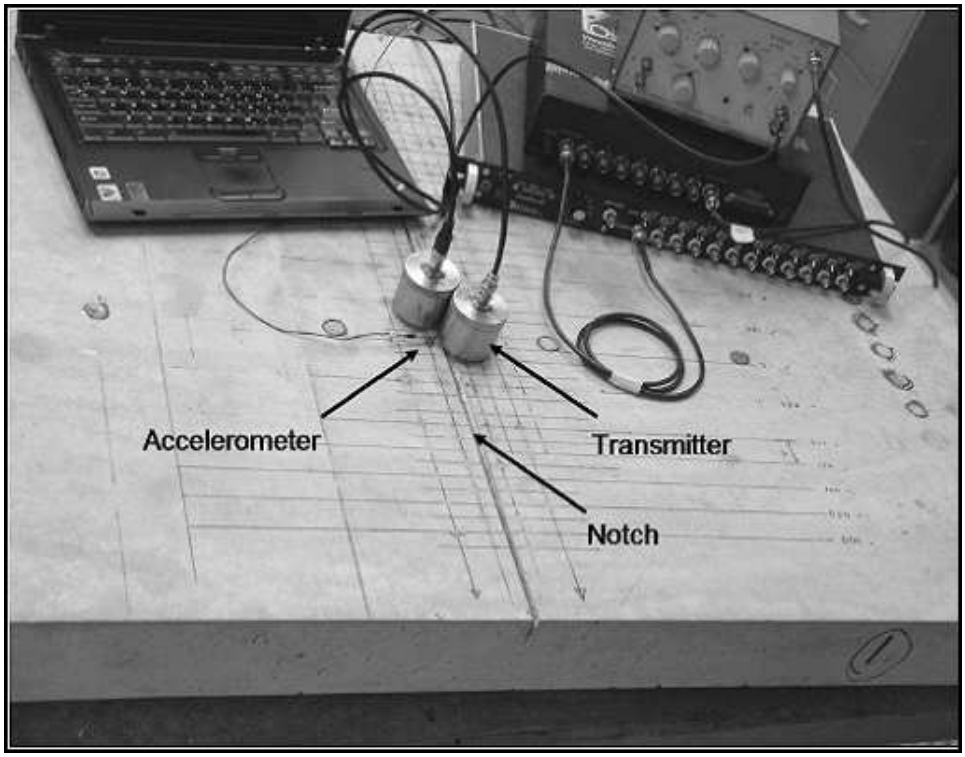

Figure 6.1: Depth evaluation of a notch in laboratory.

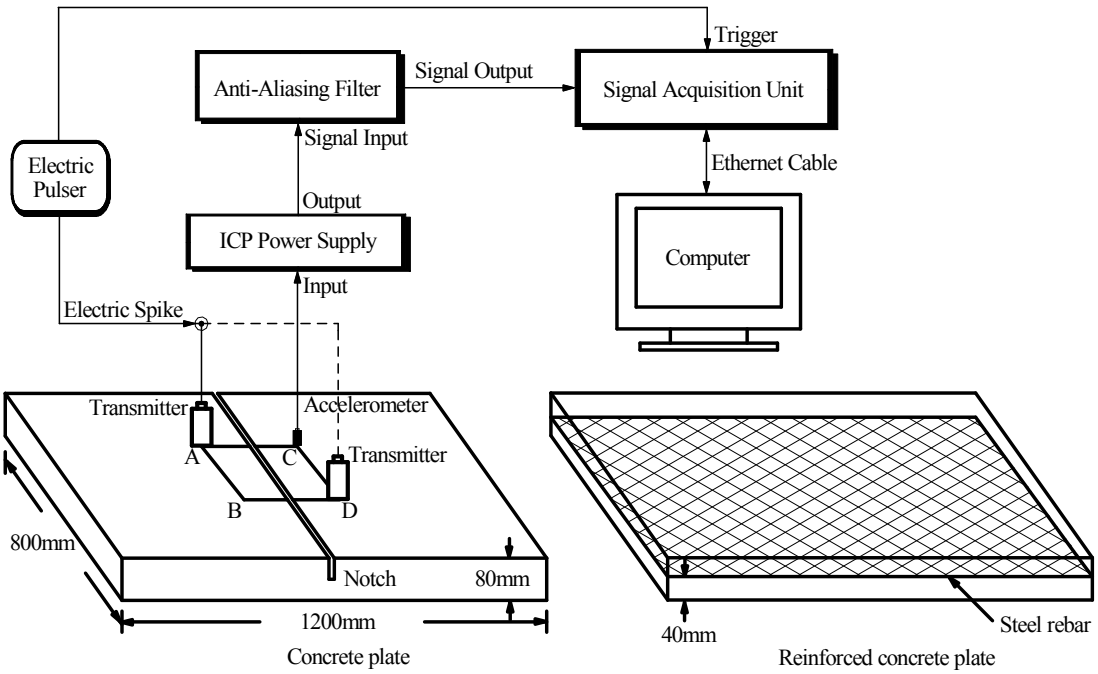

Figure 6.2: Laboratory WTC measurement for the depth evaluation of a surface-breaking crack.

Figure 6.3: Concrete pipe specimen in-situ.

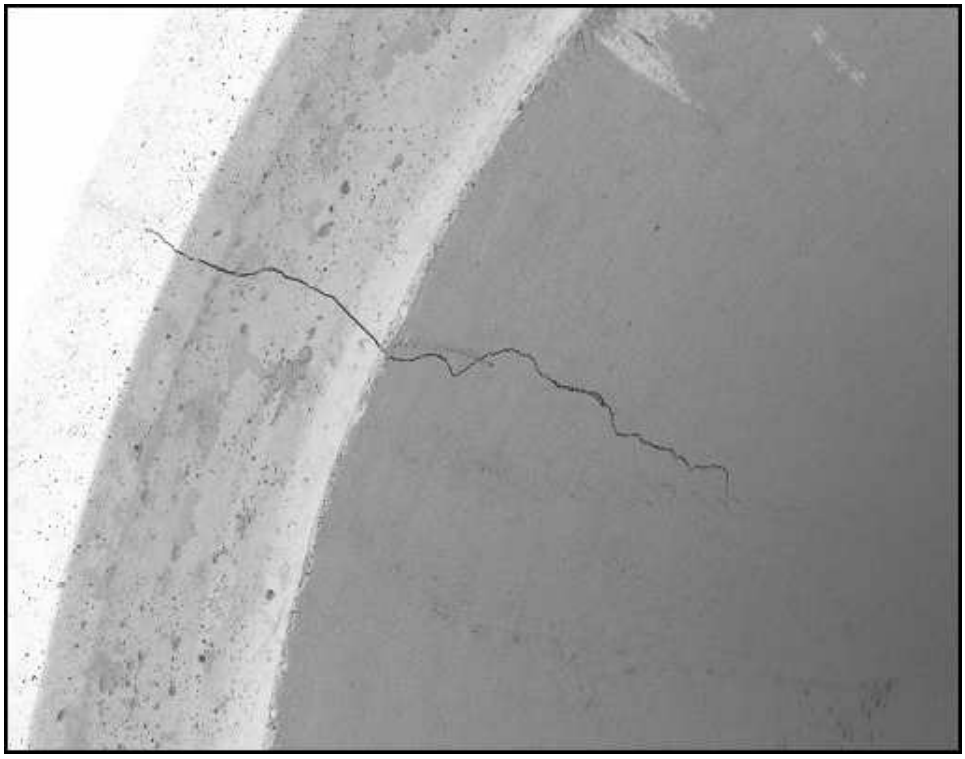

Figure 6.4: Crack depth estimation from the one end of a concrete pipe specimen.

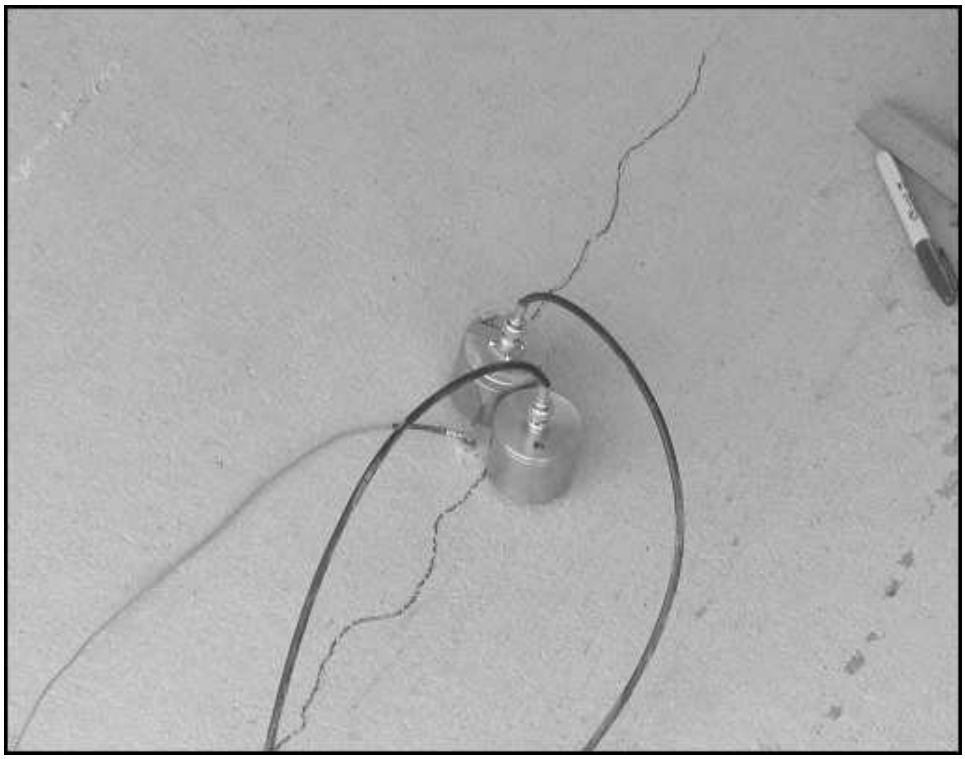

Figure 6.5: In-situ setup for transducers.

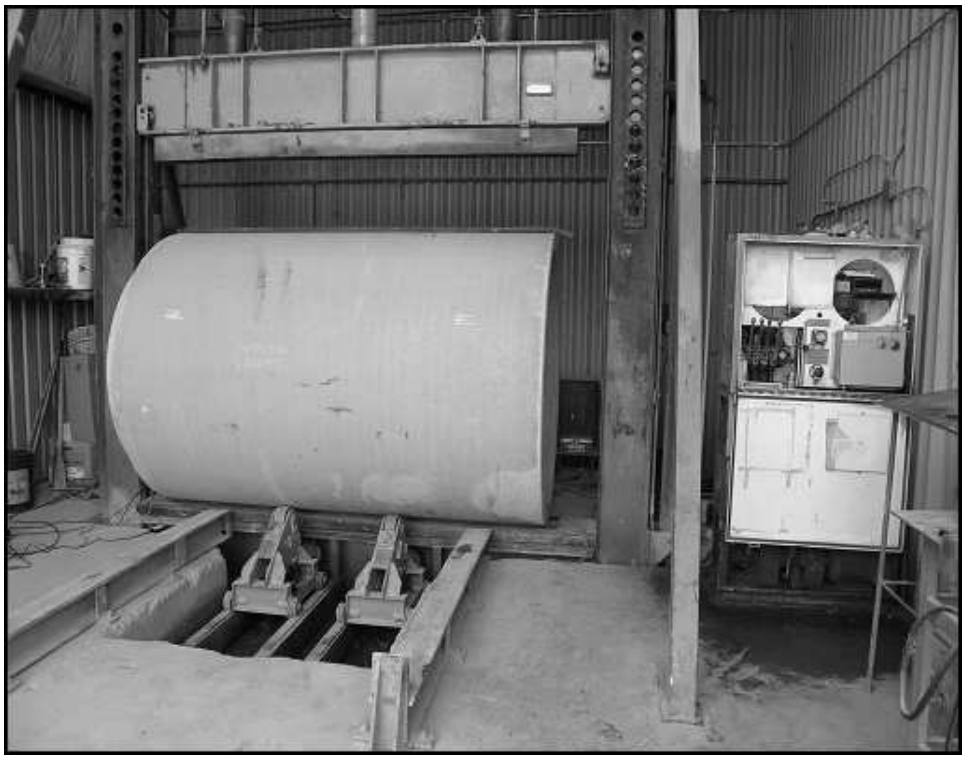

Figure 6.6: D-loading tests.

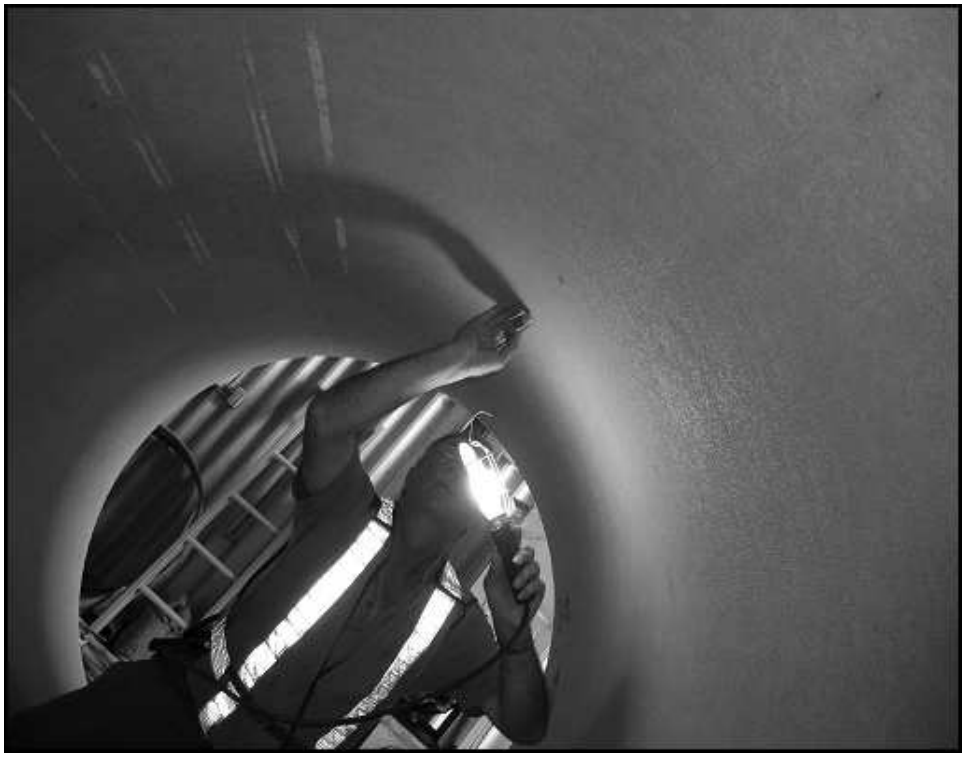

Figure 6.7: Locating a possible crack.

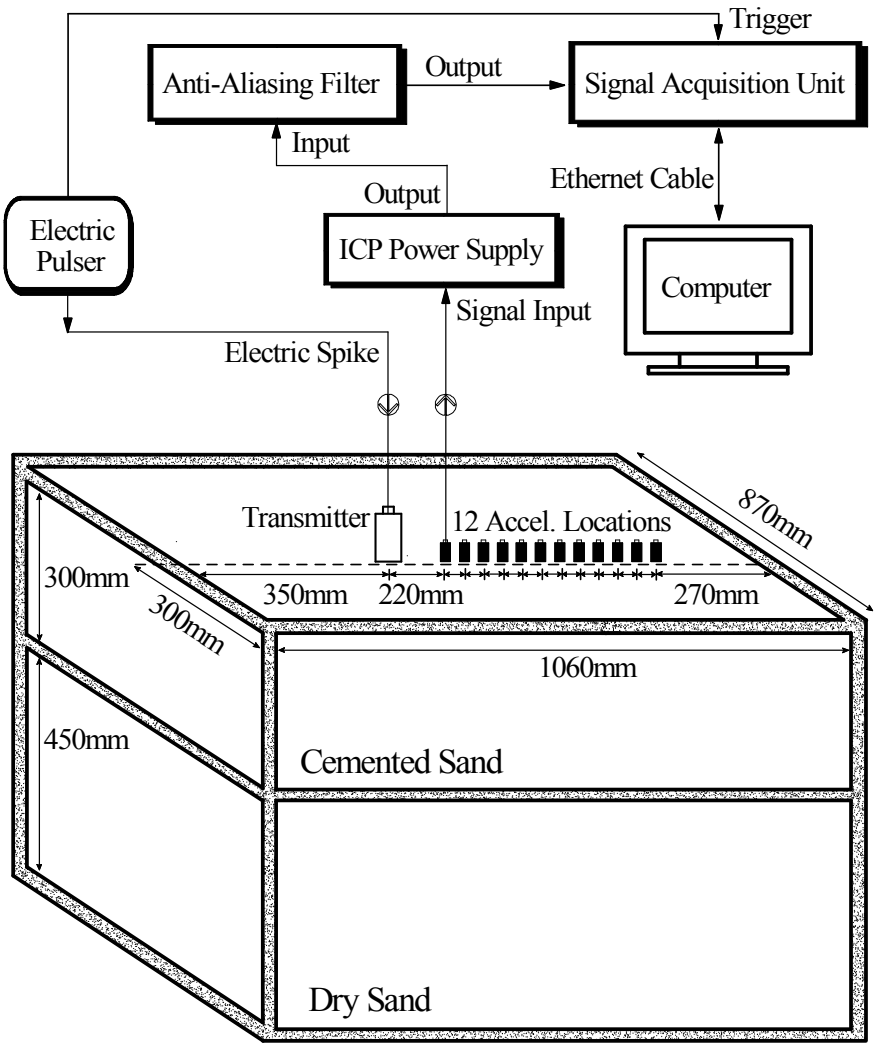

Figure 6.8: Laboratory measurement of material damping ratio on a sand box.

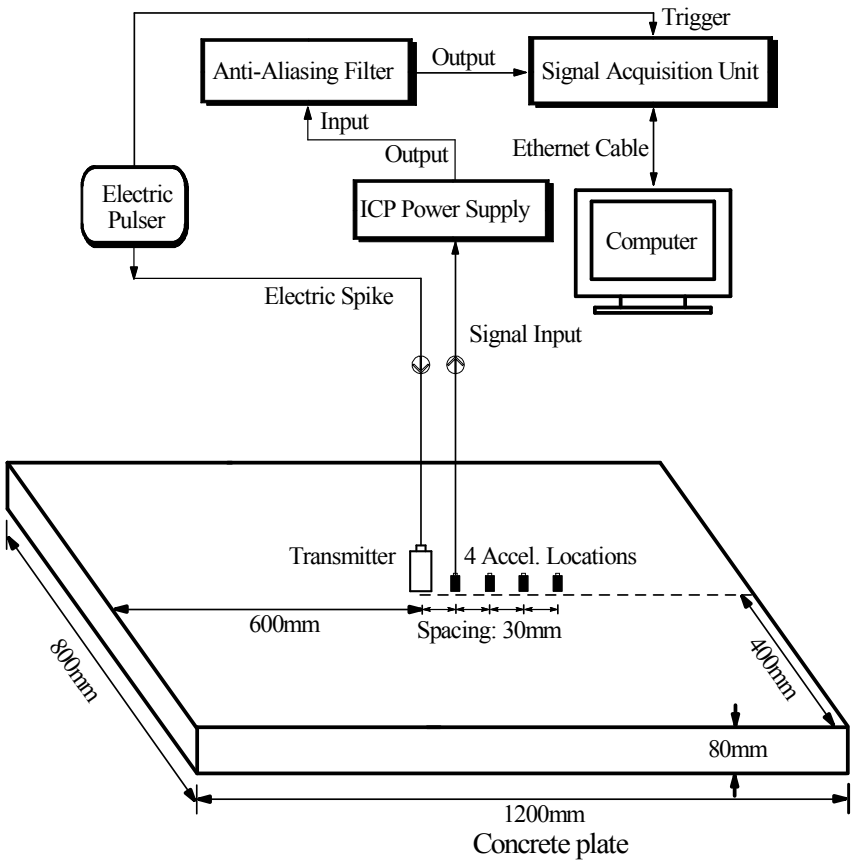

Figure 6.9: Laboratory measurement of material damping ratio on a concrete plate.

Chapter 7

Numerical finite difference modeling

7.1 Introduction

The finite difference method (FDM) is commonly used for the solution of sets of differential equations under given initial conditions. In this method, every derivative in the governing equations is replaced directly by an algebraic expression in terms of the field variables at discrete points in space and time; these variables are not defined within the elements; whereas in the finite element method (FEM), specific functions (shape functions) are required to describe the field variables within the elements, the formulation involves the adjustment of these functions to minimize the error terms. Both the FDM and FEM yield a set of algebraic equations to solve. In specific cases, the resulting equations are identical although they are derived in different ways. Therefore, it is pointless to argue about the relative merits of two methods (*Itasca* 2000). However, compared to the FEM, the FDM is less accurate because it combines the values of mass and damping at nodes.

Usually the FDM uses an explicit method, where the equations always operate on known values that are assumed to be constant for the duration of the calculations in the one time increment. This assumption may seem unreasonable, because a stress change in one element will influence other field variables, as well as neighbors; however, the time increment is small enough so that information can not physically pass from one element to another, and the neighboring elements can not really affect with each other for that duration of calculation; therefore, a large number of time increments must be taken and a large computational effort is required. In an implicit method that is usually used in the FEM, every element communicates with every other element during one time increment through global matrices, and several cycles of iteration may be necessary

before compatibility and equilibrium are reached.

The explicit-solution procedure requires the known values for calculation at each time increment; therefore, it is not unconditionally stable, unless the calculation speed to obtain the known values keeps ahead of the physical wave speed, so-called numerical stability condition, which should be satisfied in the numerical simulations.

This chapter introduces some basic principles about the FDM. A commercial software package, FLAC ^{TM} (fast Lagrangian analysis of continua) is used for the numerical simulations for this research. The numerical models using FLAC ^{TM} are constructed for different studies, and the numerical results can be used only if the numerical models are appropriately calibrated.

7.2 Difference forms of field equations

In the FDM, the medium is discretized into the numerical spatial grids; the displacement field is then specified by a discrete set of nodal points represented by the indices m, n, and p in a three-dimensional (3D) dimension. Therefore, the displacement function is represented by:

$$u_{m,n,p} = u(m\Delta x_1,\ n\Delta x_2,\ p\Delta x_3)$$

where Δx_1, Δx_2, and Δx_3 indicate the spatial increments in x_1, x_2, and x_3 directions.

For time-varying 3D problems, it is modified:

$$u_{m,n,p,q} = u(m\Delta x_1,\ n\Delta x_2,\ p\Delta x_3,\ q\Delta t)$$

where Δt is the time increment.

In the FDM, the derivatives in the equations of wave motion and constitutive law are replaced with the difference forms, and the explicit algebraic equations are formed. They can be solved in a finite difference program and the solutions for the field variables (displacement, velocity and acceleration) at grid nodes are obtained.

The typical difference forms for the first and the second derivatives are derived using Tailor expansions (*Lick* 1989):

$$\left(\frac{\partial u_i}{\partial x_i}\right)^{<n>} \approx \frac{u_i^{<n+1>} - u_i^{<n-1>}}{2\,\Delta x_i} \tag{7.1a}$$

$$\left(\frac{\partial^2 u_i}{\partial x_i^2}\right)^{<n>} \approx \frac{u_i^{<n+1>} - 2u_i^{<n>} + u_i^{<n-1>}}{\Delta x_i^2} \tag{7.1b}$$

where u_i represents the displacement in x_i direction (i = 1, 2 or 3); the superscript n represents the grid node number.

Eq. 7.1 is refereed to as centered scheme, because it is symmetric to a center point at n. With a simple change, the derivatives can be applied with respect to another variable, for example the time t.

For simplicity, a one-dimensional (1D) elastic bar is taken as an example to describe the basic principles of the FDM. The general equation of wave motion based on Eq. 2.3 is:

$$\rho \frac{\partial^2 u_1}{\partial t^2} = \frac{\partial \sigma_{11}}{\partial x_1} \tag{7.2}$$

where ρ is the mass density.

A constitutive law or a generalized Hooke's law based on Eq. 2.4 becomes for this case:

$$\sigma_{11} = E \frac{\partial u_1}{\partial x_1} \tag{7.3}$$

where E is the Young's modulus.

By using velocity v_1 in x_1 direction, the difference form of Eq. 7.2 is given at grid node n:

$$\rho \frac{v_1^{<n>}(t+\Delta t) - v_1^{<n>}(t-\Delta t)}{2\,\Delta t} = \frac{\sigma_{11}^{<n+1>}(t) - \sigma_{11}^{<n-1>}(t)}{2\Delta x_1} \tag{7.4}$$

Rearranging the above equation results in:

$$v_1^{<n>}(t+\Delta t) = v_1^{<n>}(t-\Delta t) + 2\Delta t \, \frac{\sigma_{11}^{<n+1>}(t) - \sigma_{11}^{<n-1>}(t)}{2\rho \Delta x_1} \tag{7.5}$$

Integrating the both sides of the above equation gives the displacements as:

$$u_1^{<n>}(t+\Delta t) = u_1^{<n>}(t-\Delta t) + 2\Delta t \, v_1^{<n>}(t) \tag{7.6}$$

The difference form of Eq. 7.3 is given at grid node n:

$$\sigma_{11}^{<n>}(t) = E\,\frac{u_1^{<n+1>(t)} - u_1^{<n-1>}(t)}{2\Delta t} \tag{7.7}$$

Eqs. 7.5, 7.6 and 7.7 are used for the calculation of velocities or displacements at the grid nodes in the FDM for a 1D elastic bar. It is an explicit method, because the quantities on the right for all difference equations are known. However, Eq. 7.7 must be evaluated at first for all grid nodes before moving to Eqs. 7.5 and 7.6.

7.3 Boundary conditions and initial values

The boundary conditions are for some field variables to satisfy along a boundary curve or boundary plane, where an abrupt change in rigidity happens; the initial values are a known distribution of some field variables throughout the medium at some particular instant of time.

The continuity condition of stress and displacement should be satisfied in a physical boundary, for example:

$$u(x_1^-, x_2^-, x_3^-, t) = u(x_1^+, x_2^+, x_3^+, t) \tag{7.8a}$$
$$\sigma(x_1^-, x_2^-, x_3^-, t) = \sigma(x_1^+, x_2^+, x_3^+, t) \tag{7.8b}$$

where u is the displacement; σ is the stress; the coordinates x_1^-, x_2^-, and x_3^- indicate a position in the boundary on one side; while x_1^+, x_2^+, x_3^+ indicate the same position, but on another side.

An infinite medium can not be numerically simulated directly due to the limitation of finite storage and speed for a computer; therefore, the waves reflected from the boundary of a finite medium reach the recording locations and produce contamination. A simple way to be free of this contamination is to put the boundary as far as it is feasible, or have a length of recording time short enough; thus, the reflected waves do not appear within that length of time at the recording points.

Lysmer and *Kuhlemeyer* (1969) describe a general method in which an infinite system can be simulated by a finite system using an artificial viscous boundary condition, or a so-called energy absorbing boundary. When waves propagate from interior region to exterior region, this condition can be considered as a situation with infinitesimal dashpots

supporting normal and tangential to the boundary in order to absorb the energy. However, the effectiveness of this absorption is related the angle of incident waves, a nearly perfect absorption occurs when the incident angle is larger than 30°.

7.4 Numerical stability, convergence and consistence

Numerical stability, convergence and consistence are the most basic properties for a numerical algorithm. The numerical stability is related to the accuracy of the numerical algorithm. Usually, an numerical algorithm for solving numerical differential equations is stable only if the solutions at a fixed time remains bounded as the step size goes to zero. An algorithm is said to be consistent if the truncation error vanishes as the grid spacing Δx_1, Δx_2, Δx_3, and time increment Δt tend to zero. The convergence means that the solution to the difference equations approaches the solution to the differential equations in the limit Δx_1, Δx_2, Δx_3, and Δt going to zero.

The Lax equivalence theorem (*Strikwerda* 1989) states that a numerical algorithm converges if it is consistent and stable. By inserting the solution to the differential equations into the corresponding deference equations, the the truncation error is measured in order to check the consistence of a numerical algorithm, and it is given in a mathematical form:

$$O(\Delta x_1^{\alpha}, \Delta x_2^{\alpha}, \Delta x_3^{\alpha}, \Delta t^{\alpha}) \Longrightarrow 0 \quad as \quad \Delta x_1, \Delta x_2, \Delta x_3, \Delta t \longrightarrow 0 \tag{7.9}$$

where α is the degree of accuracy of the numerical algorithm.

For simplicity, numerical stability is studied by considering a single degree of freedom system (SDOF) in Fig. 7.1. The equations of wave motion are expressed:

$$F(t) = -k\,u(t) \tag{7.10a}$$

$$v(t+\frac{\Delta t}{2}) = v(t-\frac{\Delta t}{2}) + \frac{F(t)}{m}\Delta t \tag{7.10b}$$

where u is the displacement; v is the velocity; m is the mass; k is the stiffness of a spring; F is the applied force; t is the time variable; Δt is the time increment.

Integrating the both sides of Eq. 7.10B and shifting time by $-\Delta t/2$ results in:

$$u(t) = u(t-\Delta t) + v(t-\frac{\Delta t}{2})\,\Delta t \tag{7.11}$$

Combining two time steps for Eqs. 7.10 and 7.11 results in:

$$u(t+\Delta t) + u(t)\left(\frac{k}{m}\Delta t^2 - 2\right) + u(t-\Delta t) = 0 \tag{7.12}$$

This above difference equation yields a stable, periodic solution if $\Delta t < \Delta t_{crit}$:

$$\Delta t_{crit} = 2\sqrt{\frac{m}{k}} = \frac{T}{\pi} \tag{7.13}$$

where T represents the eigen-period of time for a SDOF system. For a multi-degree of freedom system, the eigen-period of time is selected as the smallest one.

A 1D elastic bar can be discretized as a series of elements consisting masses and springs, shown in Fig. 7.2. The smallest eigen-period of time for the system can be determined by an inspection, since it corresponds to alternate masses moving in opposite directions, as shown in Fig. 7.3. In this case, each mass appears to be a SDOF system, connected to two half-springs in parallel as shown in Fig. 7.4; therefore, the effective stiffness is equal to $4k$. Because:

$$k = \frac{EA}{\Delta x} \tag{7.14a}$$
$$m = \rho A \Delta x \tag{7.14b}$$

where A is the cross area; E is the Young's modulus; Δx is the length of an element.

Substituting Eq. 7.14 into Eq. 7.13 results in:

$$\Delta t_{crit} = \Delta x\sqrt{\frac{\rho}{E}} = \frac{\Delta x}{V_P} \tag{7.15}$$

where V_P is the P-wave velocity, a fastest velocity at which information can propagate.

This leads to an important conclusion: if the stability is satisfied in Eq. 7.13, the time increment used in an explicit solution is sufficiently small so that information cannot propagate between elements in one time increment.

7.5 FLAC models and numerical calibrations

7.5.1 Introduction

FLAC ^{TM} (fast Lagrangian analysis of continua) is a 2D finite difference program for numerical simulations, where a set of recursive finite difference equations and boundary conditions are used with the explicit Lagrangian calculation scheme and the mixed-discretization techniques (*Itasca* 2000). This program can implement the dynamic analysis by solving the full equations of wave motions, where the structure properties including the dimensions are predefined. Materials are represented by elements which form a grid. Each element can be given a separate material model, for example, isotropic elastic model or null model (10 built-in material models in total). Different material models can be incorporated into one structure, for example, by making some elements null, the effects of the presence of a surface-breaking crack in a homogeneous concrete can be simulated. For boundary conditions, velocity, displacement or stress can be specified at any boundary orientation.

The general computation sequence is shown in Fig. 7.5. The equation of wave motion is invoked first to derive new velocities and displacements from stresses and forces; then the strain rates are calculated from velocities; finally, the one cycle of calculation ends up with the new stresses or forces obtained from strain rates and all field variables at grids are updated from known values.

It is important to satisfy the numerical stability condition for a square element, which requires the time increment Δt be small enough. Therefore, each element appears to be physically isolated from its neighbors during one time cycle, so that the calculations speed of wave front is no later than the fastest wave velocity V_P (*Itasca* 2000):

$$\Delta t_{crit} = \frac{\Delta x}{\sqrt{2}\, V_P} \tag{7.16}$$

where Δt_{crit} is the critical time increment; Δx is the length of that square element; V_P is the P-wave velocity. Unlike a 1D elastic bar in Eq. 7.15, a 2D square element is considered in Eq. 7.16, and thus the term of square root of 2 results.

Numerical dispersion is caused by numerical discretization in space, causing different frequencies of waves to propagate at different velocities. Therefore, the critical size Δx_{crit} of a square element to avoid the numerical dispersion is suggested (*Virieux* 1986):

$$\Delta x_{crit} = \frac{\lambda_{min}}{10} \tag{7.17}$$

where $\lambda_{min} = V_P/f_{max}$; f_{max} is the maximum frequency of interests; thus λ_{min} gives the smallest wavelength.

7.5.2 Numerical models for different studies

The 2D numerical models are constructed in Fig. 7.6 using FLAC ^{TM} for different numerical studies of the wave propagation. The material properties are specified with three parameters: density $\rho = 2340kg/m3$, bulk modulus $K = 30GPa$ and shear modulus $G = 18GPa$, and other elastic parameters can be calculated in Table 7.1.

The numerical modeling configuration can be axisymmetric where the left boundary is fixed in the horizontal direction to represent an axis of symmetry, or plane-strain where the thickness of a plate is small in comparison with other dimensions. The boundary conditions can be quiet (an artificial viscous boundary condition) (Caughey 1960) to avoid wave reflections, or free to simulate a real boundary condition for plates. For different studies, the sources are placed at different surface locations $0mm$, $555mm$, and $585mm$ from the left boundary. Three types of sources are used in the numerical models:

- Lamb source with $\eta = 1.78 \times 10^{-6}$; it is shown in Fig. 5.7.
- Real part of a Morlet function with $f_0 = 50kHz$ and $\tau = 1.12 \times 10^{-5}$ ($BW = 33.46kHz$); it is shown in Fig. 5.5.
- Real part of a Morlet function with $f_0 = 100kHz$ and $\tau = 5.6 \times 10^{-6}$ ($BW = 66.92kHz$).

The plate thickness is given different values to study the thickness effects in the wave propagation; however, for the study of the depth evaluation of a surface-breaking crack, the plate thickness is $80mm$. The location for a surface-breaking crack is at $600mm$ from the left boundary of the numerical model; and the crack depth varies from 0 to $40mm$. Rayleigh damping is given to the numerical models through the minimum Rayleigh damping ratio ξ_{min} (Eq. 5.26), and the corresponding frequency f_{min}; for the Morlet sources, $f_{min} = f_0$, and for the Lamb source, $f_{min} = 50kHz$.

For the study of the depth evaluation of a surface-breaking crack, the plate in the numerical models has the same physical dimension as the experimental specimens ($1200 \times 80mm$). The numerical models are given a uniform grid size (4800×320); therefore, the numerical element size is equal to $\Delta x = 0.25mm$. According to Eq. 7.17, $\lambda_{min} = 2.5mm$, and thus for given P-wave velocity $V_P = 4804m/s$ (Table 7.1), the numerical dispersion can be avoided only if the highest frequency of interests f_{max}:

$$f_{max} = \frac{V_P}{\lambda_{min}} \leq 1.922MHz \tag{7.18}$$

In addition to the numerical element size, another important parameter is the numerical time increment, which is determined in consideration of the storage capacity and calculation speed for a computer. Importantly, the numerical stability (Eq. 7.16) is satisfied when the following equation holds for given $V_P = 4804m/s$ and $\Delta x = 0.25mm$:

$$\Delta t_{crit} \leq 36.22ns \tag{7.19}$$

Therefore, it is given in the numerical models: $\Delta t = 7.5ns$.

To prevent free-body motion, the left-bottom node in the numerical models is fixed in both horizontal and vertical directions; while the right-bottom node is fixed only in horizontal direction. The surface responses of displacement, velocity and acceleration are recorded with an array of 201 receivers that are placed on the surface of the numerical models, starting at $400mm$ from the left boundary with a receiver-spacing of $2mm$; therefore, the last receiver is at $800mm$ from the left boundary.

7.5.3 Numerical calibrations

Numerical models can be used to study the wave propagation problems only if they are appropriately calibrated. For this study, The Lamb's problem (Eqs. 5.11 and Eq. 5.12) is first used for the numerical calibration for a simulated half space, and then the numerical model for a plate is calibrated by using a nearly non-dispersive region of the dispersion curve for the fundamental Lamb mode S0.

Numerical calibration using Lamb's problem for a simulated half space

The settings in Table 7.2 are given for the numerical mode in Fig. 7.6:

- Numerical modeling configuration: axisymmetric
- Boundary conditions. Left: symmetric axis; right: quiet; bottom: quiet.
- Lamb source ($\eta = 1.78 \times 10^{-6}$) at surface, $x = 0mm$ from the left boundary.
- Plate thickness: $80mm$.
- No Rayleigh damping.

- No crack present.

Therefore, the numerical model simulates a half-space with the Lamb source applied at its center. The theoretical vertical displacements at distances 400mm, 500mm, 600mm, 700mm, and 800mm from the source are calculated, and compared with the numerical results in Fig. 7.7. The time signals arrive at different distances at a velocity that is close to the Rayleigh wave velocity, $V_R = 2550m/s$. The time signals agree, but with a slight variation. The corresponding spectral amplitudes agree well only for high frequencies. For low frequencies, variations appear in a frequency bandwidth, which gets wider as distance from the source increases. For example, at distance 400mm, the frequency components below 40kHz propagate not well; while at distance 800mm, the frequency components below 60kHz propagate not well.

The plate in the numerical model has a thickness of 80mm. Even though the bottom boundary of the numerical model is set to be quiet for a half-space simulation, the effectiveness for a quiet boundary depends on the angle of incident waves, and the quiet boundary at the bottom for this case does not work perfectly. As a result, the thickness effects of a plate still exist. Since low frequencies have large wavelengths, their wave propagation is mostly affected by the thickness effects of a plate. As shown in Fig. 7.7B, more low frequency components are affected as waves propagate with distance.

Surface waves attenuate with distance because of theoretical geometric attenuation (Eq. 5.19). In the numerical model, the maximum amplitudes at distances 400mm to 800mm from the source are measured in time and frequency, and they are calibrated with the theoretical results of geometric attenuation in Fig. 7.8. The numerical maximum amplitudes measured in time and frequency match perfectly, and both show the same trend as the theoretical prediction.

A 2D Fourier transform plot is useful for the evaluation of the numerical dispersion, which is caused by an inappropriate size for an square element in the numerical models. The numerical time signals at different distances from the surface responses are used to calculate the 2D Fourier transform (Eq. 3.14), and the plot is shown in Fig. 7.9, where a straight contour line is present in the frequency-wave number domain, indicating the nonexistence of the numerical dispersion; the line's slope determines the wave velocity that is close to the value of Rayleigh wave velocity ($V_R = 2550m/s$).

Numerical calibration using fundamental Lamb mode S0 for a plate

The study of the numerical calibration for wave propagation in a plate is important. The numerical model in Fig. 7.10 is used to simulate a plate with free boundary conditions; in

the numerical model, the right-top and right-bottom nodes are fixed to prevent free-body motion, and the gravity acceleration is set to be zero for this case. The settings for the numerical model are given:

- Numerical modeling configuration: plane-strain
- Boundary conditions: free for left, and right and bottom boundaries.
- Morlet sources with central frequency at $f_0 = 10kHz$, applied to all the nodes of the left boundary.
- Plate thickness: $80mm$.
- No Rayleigh damping.
- No crack present.

For the case of an $80mm$-thick plate, the dispersion curve is shown in Fig. 2.6, where higher Lamb modes are null at $10kHz$, and the fundamental Lamb mode S0 is nearly non-dispersive in a small frequency range. Therefore, two Morlet sources with central frequency at $f_0 = 10kHz$, but in different frequency bandwidths ($BW = 4.74kHz$, $1.79kHz$) are used as sources. They are shown in Fig. 7.11.

To generate a pure fundamental Lamb mode S0, Morlet sources are moved to the left boundary of the numerical model (Fig. 7.10). The real part of the Morlet functions is applied to each node (321 modes in total) with both the horizontal and vertical displacements given in Eq. 2.31, where a $\pi/2$ phase difference exists between the displacements in two directions. The displacements for the fundamental Lamb S0 are normalized to the amplitude for the horizontal displacement at surface (u_{10}), and it is shown in Fig. 7.12. The horizontal displacements are anti-symmetric, and the vertical displacements are symmetric with respect to the cross section of the plate at a depth of $40mm$.

The time signals received at distances $400mm$, $500mm$, $600mm$, $700mm$, and $800mm$ from the left boundary (Fig. 7.10) are shown in Fig. 7.13. They are compared with a theoretical non-dispersive mode propagating at a constant velocity $4487m/s$, which corresponds the phase velocity for the fundamental Lamb mode S0 at $10kHz$ (Fig. 2.6).

For the case of the Morlet source with the wide frequency bandwidth ($\tau = 7.9 \times 10^{-5}$, $BW = 4.74kHz$), the first cycle of the time signals match well in Fig. 7.13A, and they arrive at different distances with a velocity that is close to the theoretical value ($4487m/s$). However, variation occurs after the first cycle, because the wide frequency bandwidth

covers the dispersive region in the dispersion curve of the fundamental Lamb mode S0. While, for the case of the Morlet source with the narrow frequency bandwidth ($\tau = 2.1 \times 10^{-4}$, $BW = 1.79kHz$), variation is significantly reduced as shown in Fig. 7.13B.

7.6 Summary

The finite difference method (FDM) is commonly used for numerical simulations. Boundary conditions, numerical stability, convergence and consistence are important properties for a numerical model. Quiet boundary is a condition with infinitesimal dashpots supporting normal and tangential to the boundary in order to absorb the energy, which can be used for the simulation of a infinite medium. Numerical stability is studied by taking a single degree of freedom system (SDOF) as an example; if the numerical stability is satisfied, the time increment used in the numerical simulations should be sufficiently small so that information can not propagate between elements in one time increment.

The numerical model is constructed using a commercial software package FLAC ^{TM} (fast Lagrangian analysis of continua) for different studies. The element size is selected to avoid numerical dispersion (frequency components propagate at different velocities because of an inappropriate element size), and the time increment is selected to satisfy the numerical stability.

The numerical model is calibrated using three different procedures. First, the time histories and frequency spectra of the surface responses from the numerical model are compared with the theoretical solutions for the Lamb problem. Then, the 2D Fourier transform of the time histories is used to show that there is no numerical dispersion. Finally, the time histories generated by the propagation of the fundamental Lamb mode in a plate at low frequencies are compared with the theoretical solution. All the numerical results are in agreement with the theoretical analysis.

Table 7.1: Material properties for the numerical models

Given Parameters		Calculated Parameters	
Mass density:	$\rho = 2340 kg/m^3$	Possion's ratio:	$\upsilon = 0.25$
		Young's modulus:	$E = 45 MPa$
Bulk modulus:	$K = 30 GPa$	Constraint modulus:	$M = 54 GPa$
		P-wave velocity:	$V_P = 4804 m/s$
Shear modulus:	$G = 18 GPa$	S-wave velocity:	$V_S = 2774 m/s$
		R-wave velocity:	$V_R = 2550 m/s$

Table 7.2: Settings for the numerical models

ITEMS		SETTINGS
Numerical modeling configurations:		Axisymmetric and plane-strain
Boundary conditions	Left:	Symmetric axis, quiet, and free
	Right:	Quiet and free
	Bottom:	Quiet and free
Sources	Type:	Lamb and Morlet
	Location:	0*mm*, 555*mm*, and 585*mm*
Plate thicknesses		20*mm*, 40*mm*, 60*mm*, and 80*mm*
Minimum Rayleigh damping ratios		0, 0.008, 0.02, and 0.05
Different depths of a surface-breaking crack		0*mm* to 40*mm*

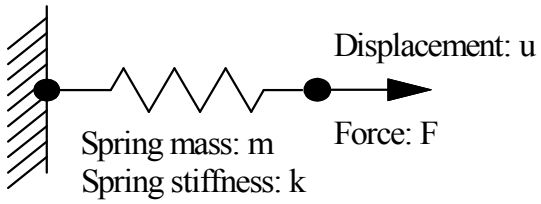

Figure 7.1: A single degree of freedom system.

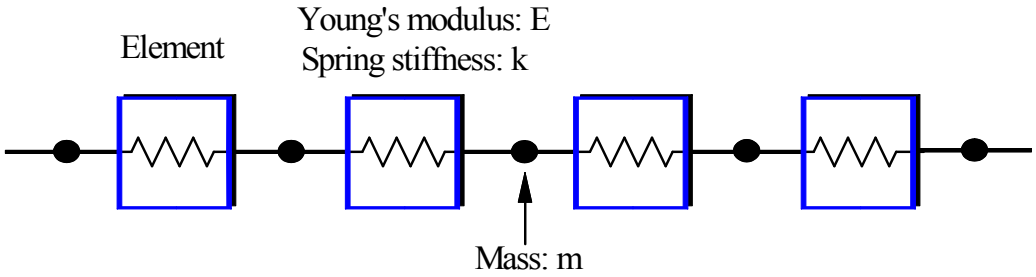

Figure 7.2: A series of discretized elements for an elastic bar.

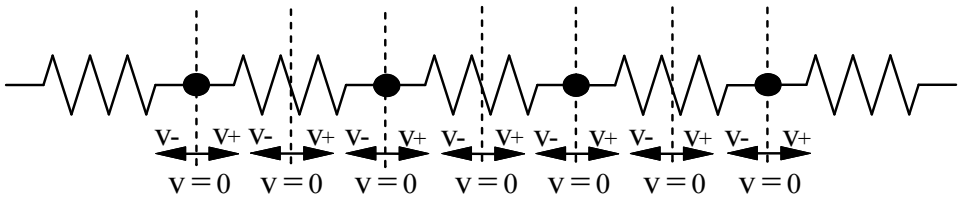

Figure 7.3: An inspection on alternate mass move.

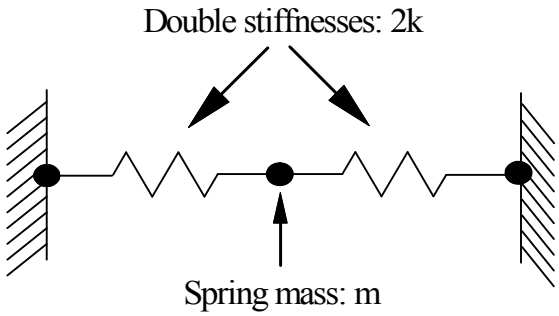

Figure 7.4: Two half-springs in parallel for each mass.

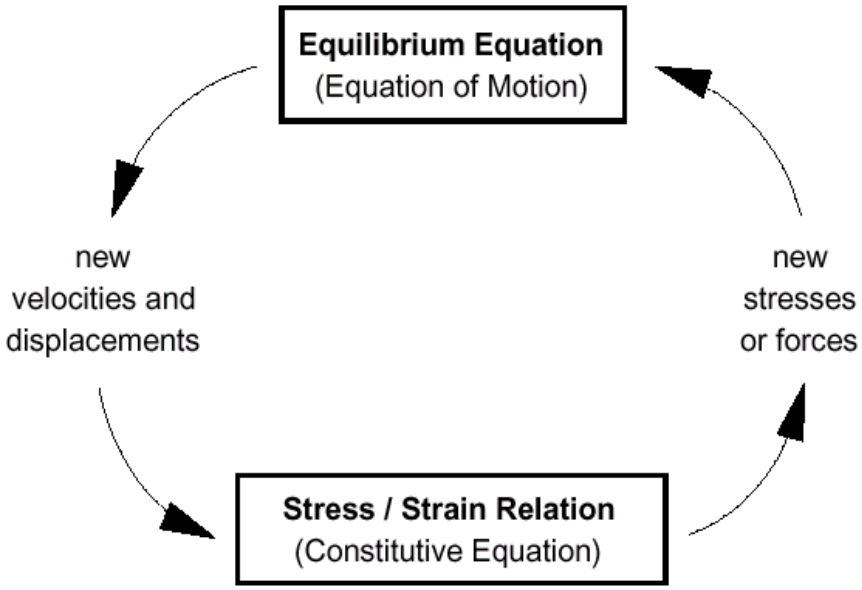

Figure 7.5: General computation sequence in FALC.

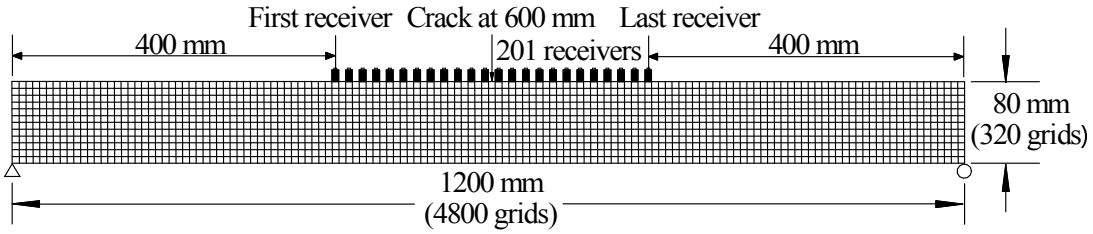

Figure 7.6: Numerical model for different studies.

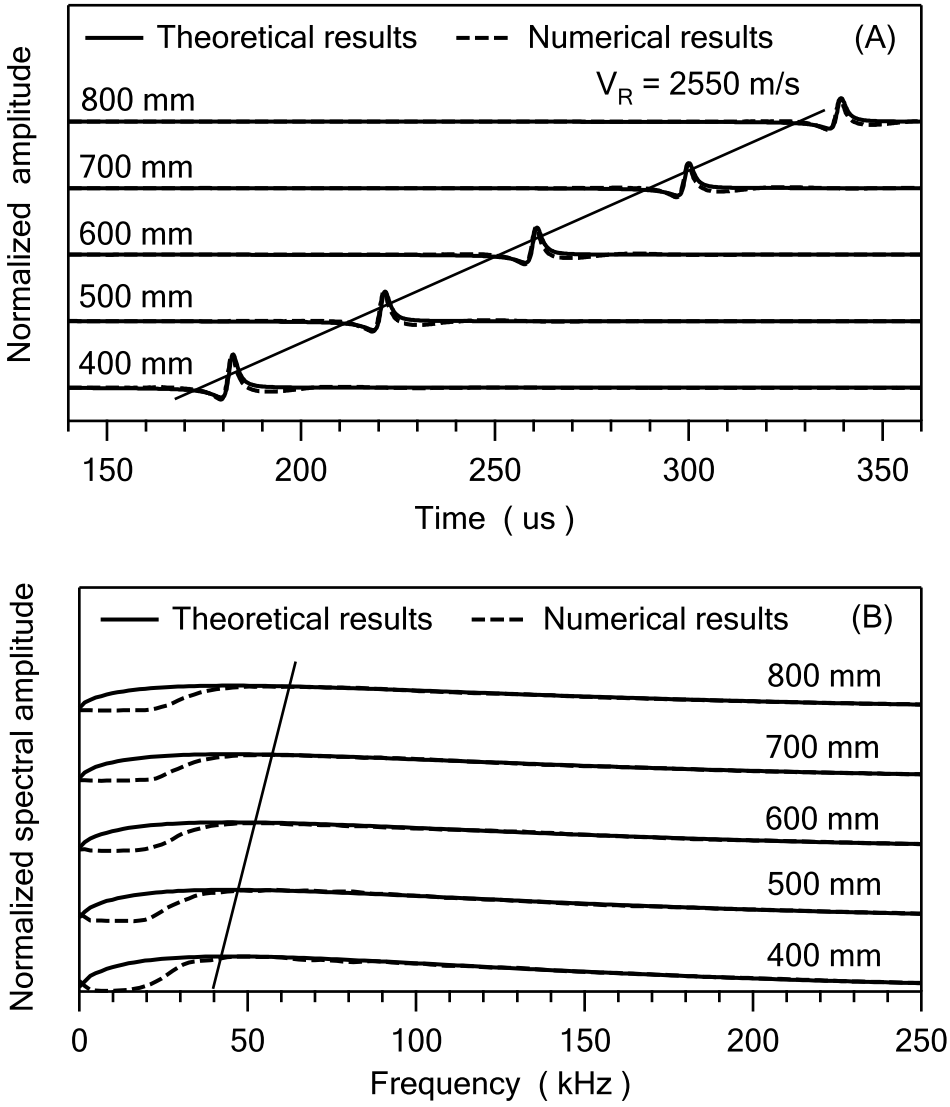

Figure 7.7: Numerical calibration. (A) time signals at different distances from the source; (B) spectral amplitudes at different distances from the source.

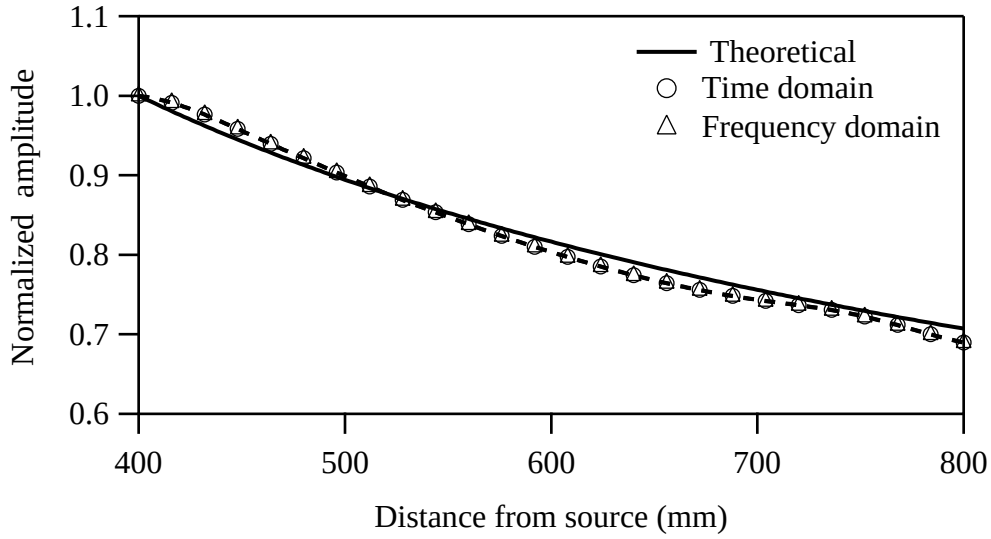

Figure 7.8: Numerical calibration of the geometric attenuation for surface wave propagation.

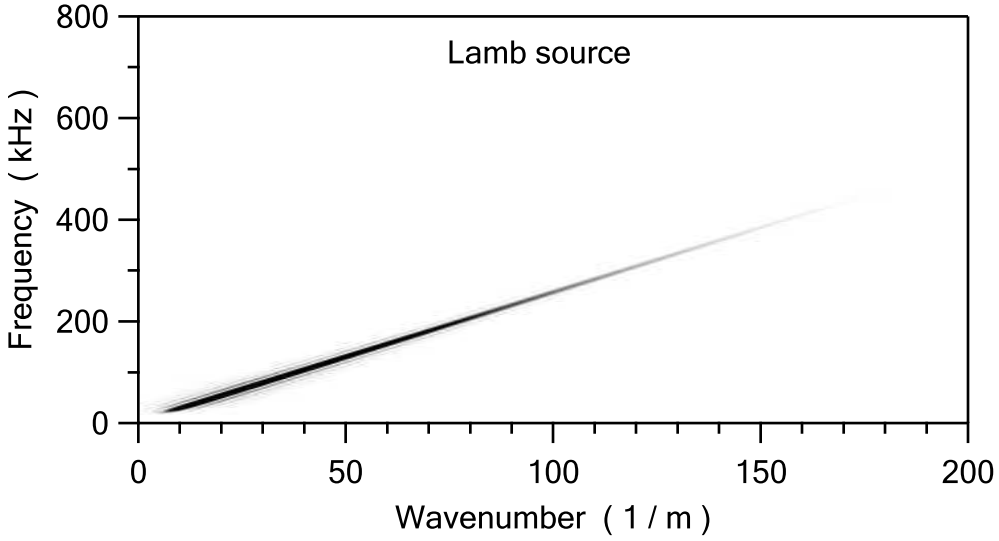

Figure 7.9: Numerical calibration with 2D Fourier transform.

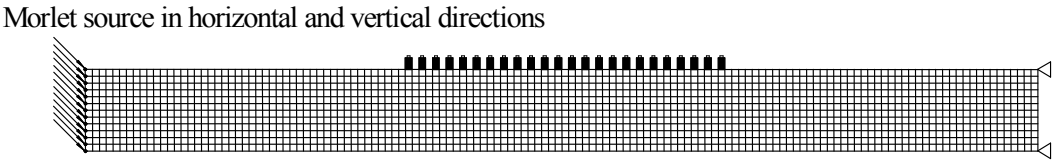

Figure 7.10: Numerical model for the calibration of a plate.

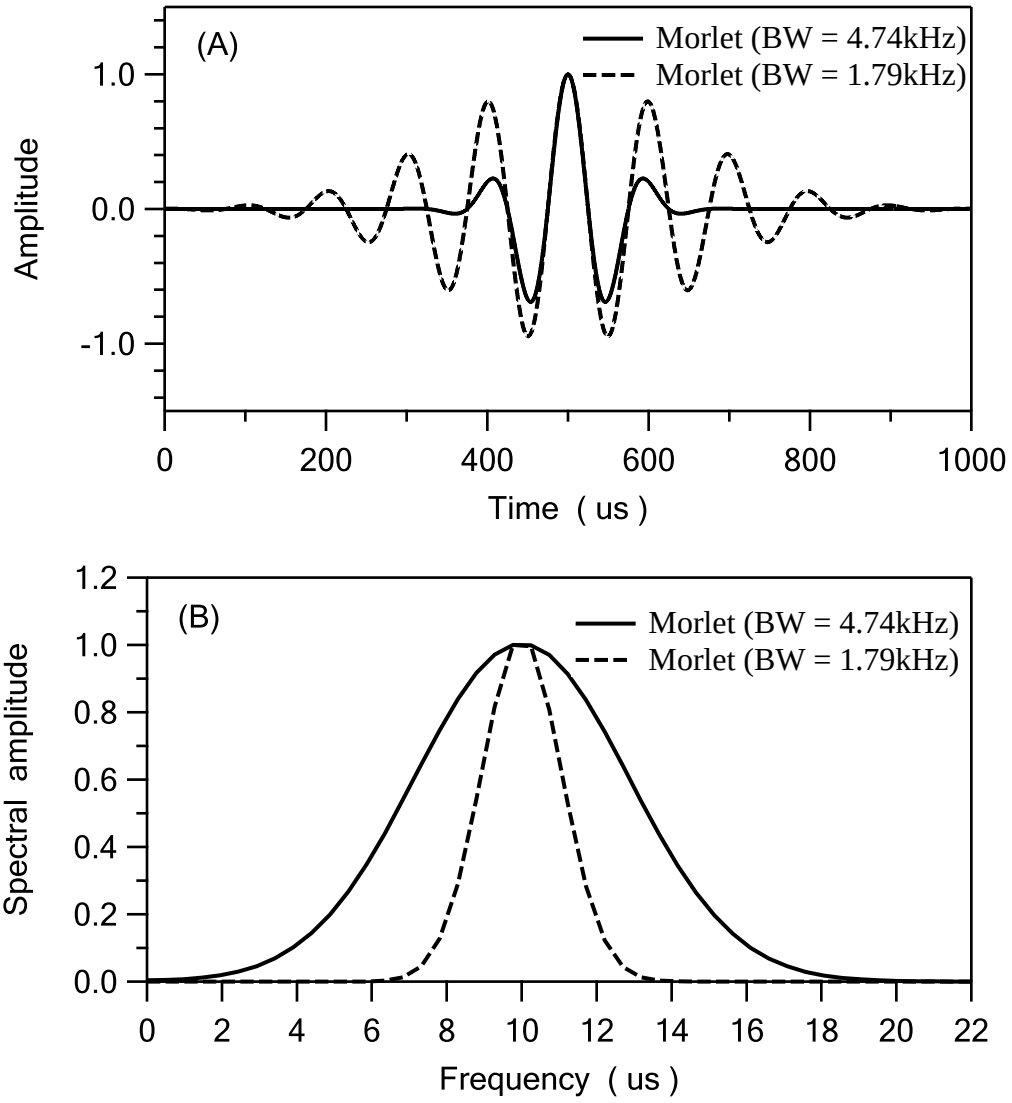

Figure 7.11: Morlet sources with $\tau = 7.9 \times 10^{-5}$ ($BW = 4.74kHz$) and $\tau = 2.1 \times 10^{-4}$ ($BW = 1.79kHz$) used for the numerical calibrations. (A) in time; (B) in frequency.

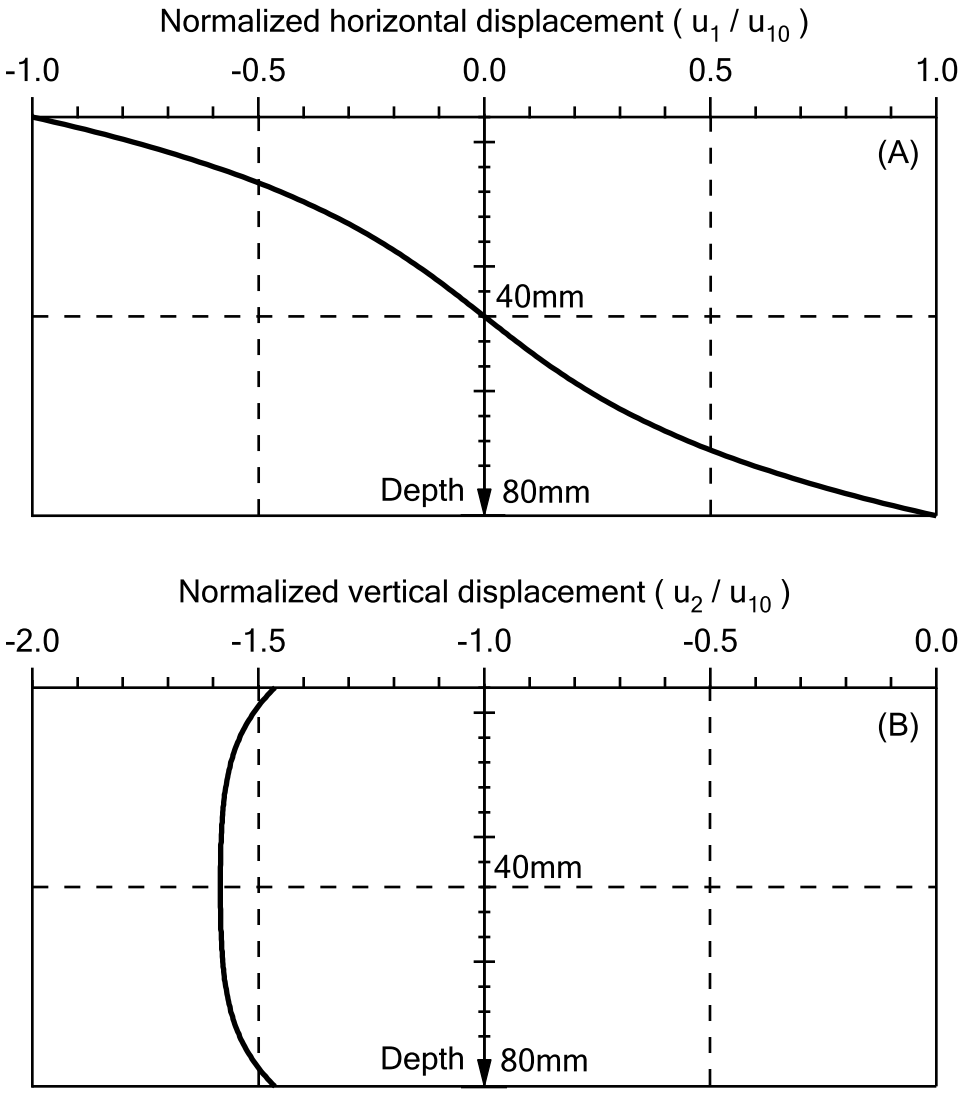

Figure 7.12: Displacements for the fundamental Lamb mode S0 at a frequency of $10kHz$. (A) normalized horizontal displacement vs. vertical depth; (B) normalized vertical displacement vs. vertical depth. u_{10} is the amplitude for the horizontal displacement at the surface.

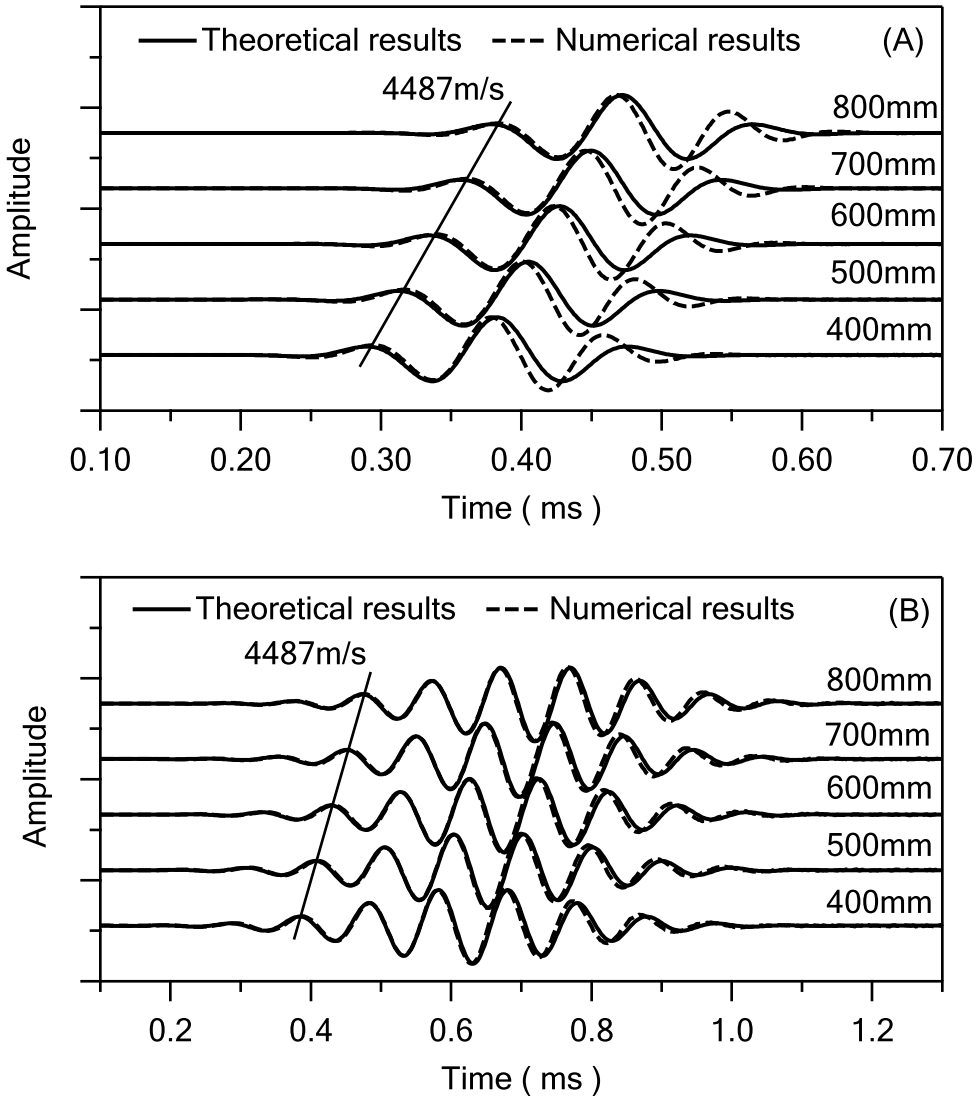

Figure 7.13: Numerical calibrations with the time signals from the numerical surface responses using the two Morlet sources with: (A) $f_0 = 10kHz$, $\tau = 7.9 \times 10^{-5}$, and $BW = 4.74kHz$; (B) $f_0 = 10kHz$, $\tau = 2.1 \times 10^{-4}$, and $BW = 1.79kHz$.

Chapter 8

Results and discussion

8.1 Depth evaluation of a surface-breaking crack

8.1.1 Introduction

This chapter presents the results of numerical analysis and experimental testing which were done using the methodologies described in **Chapter 5**, **Chapter 6**, and **Chapter 7**. The four numerical studies are conducted to simulate the wave propagation for different conditions; they are: (1) axisymmetric numerical modeling for a half-space, where Rayleigh wave propagation in a half space is studied; (2) plane-strain numerical modeling for an infinite plate, where the effect of wave reflections from a surface-breaking crack is studied; (3) plane-strain numerical modeling for a finite plate, where Lame wave propagation in a plate is studied; and (4) plane-strain numerical model of the experimental specimen is used to validate the experimental results. In the numerical models, the surface responses are recorded with an array of 201 receivers, which are placed on the surface at distances 400*mm* to 800*mm* from the left boundary; the vertical displacements of the surface responses are used for numerical analysis, and the wave propagation features are analyzed with the Fourier transform and wavelet transform.

Following the numerical studies, the experimental results are presented. For the depth evaluation of surface-breaking cracks in concrete, the experimental tests are performed on concrete plate specimens in laboratory and concrete pipe specimens in-situ. For the measurement of material damping ratio, the laboratory tests are performed on a sand box and a concrete plate to measure different values.

8.1.2 Numerical study I: axisymmetric numerical modeling for a half-space

The numerical simulations start with a simple case: Rayleigh wave propagation in a half space. Rayleigh waves as a non-dispersive mode propagate at a constant velocity; this wave feature can be shown in time domain and frequency domain. Using 2D Fourier transform, Rayleigh waves are present in wave number-frequency domain as a single mode. However, a half space does not exist in reality. Using axisymmetric numerical modeling, a half space is simulated with a plate, which has a finite thickness and an artificial quiet boundary at bottom. The quiet boundary does not work perfectly; therefore, the thickness effect of a plate is studied, where a ratio of wavelength vs. plate thickness is important, because the thickness effect decreases as this ratio decreases.

The numerical models for this study are configured:

- Axisymmetric numerical modeling configuration.
- Boundary conditions. Left, right, and bottom: quiet.
- Lamb ($\eta = 1.78 \times 10^{-6}$) and Morlets sources ($f_0 = 50kHz$, $100kHz$) at $x = 0mm$.
- Plate thickness: $20mm$, $40mm$, $60mm$, and $80mm$.
- No Rayleigh damping.
- No crack present.

The plate thickness is $80mm$, and a Morlet source ($f_0 = 50kHz$ or $BW = 33.46kHz$) is applied at the surface center ($x = 0mm$) in an axisymmetric numerical model. The surface responses at distances $400mm$ to $800mm$ are used. Fig. 8.1 shows in a 2D contour plot the time signals and spectral amplitudes. Rayleigh waves propagate without dispersion as shown in Fig. 8.1A, and the wave velocity is given by the slope of the contour line, which is equal to the theoretical value, $V_R = 2550m/s$. In the 2D plot of the spectral amplitudes (Fig. 8.1B), the spectral energy concentrates in a frequency bandwidth with center frequency slightly higher than $f_0 = 50kHz$, and frequency components are constant for all distances.

The time signals given in Fig. 8.1A are analyzed using the wavelet transform (Eq. 3.20), and the amplitude results for different times and distances ($400mm$ to $800mm$) are shown in a 2D contour plot in Fig. 8.2. The straight contour line in the plot indicates that Rayleigh waves are non-dispersive and propagate at a constant velocity, $V_R = 2550m/s$.

In a half space, Rayleigh waves dominate in the surface responses. Through the 2D Fourier transform, different modes can be shown in wave number-frequency domain. Therefore, for the time signals given in Fig. 8.1A, Fig. 8.3 shows the 2D Fourier transform plots, where only Rayleigh waves are present because of their dominant energy. In Fig. 8.3A, a Morlet source with $f_0 = 50kHz$ and $BW = 33.46kHz$ is used, and a narrow frequency bandwidth in shown in the plot; while in Fig. 8.3B, a Morlet source with $f_0 = 100kHz$ and $BW = 66.92kHz$ is used, the plot shows a wide frequency bandwidth. The straight contour lines in the two plots indicate that Rayleigh waves are non-dispersive and the Rayleigh wave velocity is determined by the slope of the contour lines ($V_R = 2550m/s$).

Using axisymmetric numerical modeling, a half space is simulated with a plate which has a finite thickness; however, the thickness effect of a plate exists because of the use of a quit boundary at bottom. For the study of this effect, a Lamb source ($\eta = 1.78 \times 10^{-6}$) is used, because it provides wave energy in a wide frequency bandwidth (Figs. 5.9). For different plate thicknesses $20mm$, $40mm$, $60mm$, and $80mm$, the surface responses at distance $400mm$ from the source are used. Fig. 8.4 shows the time signals and the corresponding spectral amplitudes, where the amplitudes are normalized to the maximum amplitude from the case of the $80mm$ thickness. The variation of the time signals between the theoretical Lamb solution (Eq. 5.12) and the numerical results increases as the plate thickness decreases. In the spectral amplitude plot, the variations occur in a low frequency range, and this frequency range becomes wider as the plate thickness decreases.

For different thicknesses of a plate, the numerical spectral amplitudes are normalized to the theoretical spectral amplitudes (Lamb solution) for each frequency. The results as a spectral ratio are shown in Fig. 8.5. If the theoretical and numerical results are considered to agree well at a value of spectral ratio higher than 0.9, the corresponding low-bound frequencies are: $39kHz$ for the thickness $80mm$, $54.1kHz$ for the thickness $60mm$, $86kHz$ for the thickness $40mm$, and $200kHz$ for the thickness $20mm$. Accordingly, the wavelengths are calculated with given Rayleigh wave velocity ($V_R = 2550m/s$). The calculated wavelengths are normalized to the corresponding plate thicknesses, and the results are shown in Fig. 8.6. For the normalized wavelengths below the curve shown in the plot, their frequency components have more than 90% agreement with the theoretical Lamb solution; the value of the normalized wavelength increases with the plate thickness.

Fig. 8.7 gives a RMS error of the spectral amplitudes between the theoretical Lamb solution (Eq. 5.12) and the numerical results from different thicknesses of a plate. Low frequencies are shown to be mostly affected because of the plate thickness effect, and the variation becomes bigger as the plate thickness decreases.

The correlation between two frequency spectra can be calculated using the cross power spectrum (Eq. 3.13). Therefore, Fig. 8.8 shows the cross power spectra between the theoretical Lamb solution (Eq. 5.12) and the numerical results from the two plate thicknesses (80mm and 40mm). Because of the thickness effect of a plate, the frequency components that are not correlated are in a low frequency range, and more frequency components join this frequency range when the plate thickness reduces from 80mm to 40mm.

Surface waves propagating in the axisymmetric numerical models present geometric attenuation (Eq. 5.19). In Fig. 8.9, the maximum amplitudes from the wavelet transform at different distances are compared with the theoretical attenuation for the three sources, which are Lamb source ($\eta = 1.78 \times 10^{-6}$) and Morlet sources ($f_0 = 50kHz$, $100kHz$). The geometric attenuation is predicted well with the numerical results. However, the differences of the numerical results among the three sources result from the thickness effects of a plate. A Lamb source generates more low frequency components which attenuate faster; in contrast, a Morlet source with central frequency at $f_0 = 100kHz$ matches better with the theoretical results because of less low frequency components generated.

8.1.3 Numerical study II: plane-strain numerical modeling for an infinite plate

Rayleigh wave reflections in the presence of a surface-breaking crack are studied in this section. A surface-breaking crack plays a role as a low-pass filter that allows low frequency components to transmit, and as a reflector where high frequency components are reflected. In the non-equal spacing configuration used for the measurement of the FTC, a source is aligned with receivers; therefore, a wave propagates on surface at a normal incidence through a surface-breaking crack, it is reflected and transmitted. For locations before a crack, the incident and reflected waves are superimposed, and the effect from the wave reflections depends on a distance from the crack.

The numerical models for this study are configured:

- Plane-strain numerical modeling configuration.
- Boundary conditions. Left, right, and bottom: quiet.
- Lamb ($\eta = 1.78 \times 10^{-6}$) source at $x = 200mm$.
- Plate thickness: 80mm.

- No Rayleigh damping.
- Different depths of a surface-breaking crack.

The Rayleigh waves are generated by a Lamb source ($\eta = 1.78 \times 10^{-6}$) in the numerical models, and the surface responses at distances $400mm$ to $800mm$ are used. The spectral amplitudes in the presence of a $10mm$ surface-breaking crack are normalized to the spectral amplitudes in the absence of a crack for each distance. The results as a spectral ratio are shown in a 2D contour plot in Fig. 8.10.

The Rayleigh waves concentrate in a depth of one third of the wavelength; therefore, $f_{cut} = 85kHz$ for a $10mm$ surface-breaking crack (Eq. 4.12). In the contour plot, the transmitted waves are shown lower than frequency f_{cut}, and higher than $35kHz$ because of the thickness effect of a plate. In seismic reflections, appearance of a quadratic curve indicates the wave reflections from an underground object. Similarly, the spectral ratios for locations before a crack show a quadratic ripple, which is caused by the wave reflections.

Rayleigh waves in a frequency range of $85kHz$ to $500kHz$ are mostly reflected from a $10mm$ surface-breaking crack, and the wave reflections affect the locations before a crack. Therefore, for each frequency in this frequency range and each location before a crack, the spectral ratios of spectral amplitudes between the two cases, one with the presence of a $10mm$ surface-breaking crack, and another with no crack, are plotted in dots in Fig. 8.11. In this plot, the horizontal axis representing a distance from the crack is normalized to the wavelength, and the vertical axis represents a spectral ratio. An amplification or constructive interference takes place at distances multiple of half the wavelength ($\lambda/2$); whereas, de-amplification or destructive interference takes place at distances multiple of half the wavelength plus one quarter of a wavelength ($\lambda/2 + \lambda/4$).

For the simulation of the Rayleigh wave propagation in the non-equal spacing configuration, which is used for the measurement of the FTC, and in the equal spacing configuration, which is used for the measurement of the WTC, two surface locations "A" and "B" in the numerical models are selected. Location "A" is before a crack and location "B" is after a crack; they are equally spaced from a crack, and the spacing between "A" and "B" are $30mm$ and $60mm$, respectively. For the non-equal spacing configuration, the spectral ratio is calculated as the spectral amplitude at location "B" divided by the spectral amplitude at location "A"; while, for the equal spacing configuration in a 2D numerical model, the spectral ratio is calculated as the spectral amplitudes at location "B" in the presence of a crack, divided by the spectral amplitude at "B" but in the absence of a crack.

For the case of a $10mm$ surface-breaking crack, Fig. 8.12 shows the spectral ratio from the simulations of the two configurations, where the horizontal axis represents the crack depth normalized to the wavelength, and the vertical axis represents the spectral ratio. A frequency range of $39kHz$ to $500kHz$ is used to avoid the thickness effect of a plate. Fluctuations of the spectral ratios occur for the non-equal spacing configuration, which show the effects of the wave reflections. Higher amplitudes of fluctuations are present for the $30mm$ spacing because of shorter distance from a crack. More fluctuation events are present for the $60mm$ spacing, because longer spacing allows more wave reflections to be received at location "A". The spectral ratio for the equal spacing configuration is sensitive to the crack depth in the normalized range $d/\lambda = 0.1$ to 0.3.

8.1.4 Numerical study III: plane-strain numerical modeling for a finite plate

For the case of a finite plate, Lamb waves propagate; therefore, an understanding to Lamb wave propagation is important for the depth evaluation of a surface-breaking crack. Different Lamb modes can be generated in a plate, and they are analyzed with the Fourier transform and wavelet transform to show the Lamb mode dispersion and multiple Lamb mode participation. In the presence of a surface-breaking crack, the transmitted and reflected Lamb modes are shown in different halve using 2D Fourier transform; fundamental Lamb mode is useful for the depth evaluation of a surface-breaking crack in a plate, because it dominates both the transmitted and reflected waves.

The numerical models for this study are configured:

- Plane-strain numerical modeling configuration.
- Boundary conditions. Left, right, and bottom: free.
- Morlet sources ($f_0 = 50kHz$, $100kHz$) at $x = 200mm$.
- Plate thickness: $80mm$.
- No Rayleigh damping.
- Different depths of a surface-breaking crack.

A Morlet source is applied at $200mm$ from the left boundary of the numerical model, and the surface responses at distances $400mm$ to $800mm$ are used. Fig. 8.13 shows in a 2D contour plot the time signals and spectral amplitudes. Lamb waves propagate with

dispersion, and multiple Lamb modes exist. As a results, the dispersion is shown in the time signals (Fig. 8.13A), and the frequency components of the propagating Lamb waves vary with distances (Fig. 8.13B); however, the spectral energy concentrates in a frequency bandwidth with center frequency slightly higher than $f_0 = 50kHz$.

The wavelet transforms (Eq. 3.20) are applied to the time signals given in Fig. 8.13A, and the amplitude results are given in Fig. 8.14, where the dispersion of Lamb wave propagation is shown.

With a Morlet source ($f_0 = 50kHz$, $BW = 33.46kHz$), different Lamb modes are generated as shown in a 2D Fourier transform plot in Fig. 8.15A, where a crack is absent. To identify the maximum wave energy, for a given frequency, the maximum amplitude for different wave numbers can be found at a wave number; thus, a series of frequencies and wave numbers define a Lamb mode. The Lamb mode that has the maximum amplitudes in the frequency and wave number domain dominates the surface responses, and it is compared with the theoretical fundamental Lamb mode S0 in Fig. 8.15B; an agreement is shown for frequencies higher than $25kHz$. In Fig. 8.15A, the contour line for the fundamental Lamb mode S0 is slightly inclined at low frequencies showing dispersion, and higher Lamb modes appear above fundamental Lamb mode S0.

Fig. 8.16 is given in the presences of a $20mm$ surface-breaking crack, where a Morlet source ($f_0 = 50kHz$, $BW = 33.46kHz$) is used. The incident or transmitted Lamb modes are shown in the first half, where the wave numbers are positive; while the reflected Lamb modes are shown in the second half, where wave numbers are negative. Similar to Fig. 8.15B, for different frequencies and wave numbers, the maximum amplitude in the second half of Fig. 8.16A is compared with the theoretical fundamental Lamb mode S0 in Fig. 8.16B, and the dominant reflected wave energy is identified from the fundamental Lamb mode S0 for frequencies higher than $40kHz$. Therefore, a vertical force as a Morlet function with $f_0 = 50kHz$ generates most wave energy from the fundamental Lamb mode S0, and the reflected wave energy from a crack is also dominated by the fundamental Lamb mode S0.

When a Morlet source with $f_0 = 100kHz$ and $BW = 66.92kHz$ is used, Fig. 8.17A shows in a 2D Fourier transform plot different Lamb modes in the absence of a crack. Similarly, the fundamental Lamb mode S0 is identified in Fig. 8.17B. Because a Morlet source ($f_0 = 100kHz$ and $BW = 66.92kHz$) generates higher frequency components in a wide frequency bandwidth, the contour line of fundamental Lamb mode S0 in Fig. 8.17A is longer, and is straight showing a non-dispersive behavior. Fig. 8.18 shows the 2D Fourier transform results in the presence of a $10mm$ surface-breaking crack, where a Morlet source with $f_0 = 100kHz$ and $BW = 66.92kHz$ is used. The dominant reflected

wave energy is identified from the fundamental Lamb mode S0 in Fig. 8.18B.

The incident, transmitted, and reflected wave energy of the fundamental Lamb mode S0 can be extracted in wave number and frequency domain using a 2D filter (Eq. 3.16). The frequency bandwidth BW of the filter is equal to the frequency bandwidth of the Morlet sources. The extracted Lamb mode from the first half of the 2D Fourier transform plot is transformed into the time and spatial domain by an inverse 2D Fourier transform; then the obtained time signals for receiver locations before a crack correspond to the incident Lamb mode; while the time signals after a crack correspond to the transmitted Lamb mode. The reflected Lamb mode is extracted from the second half in the 2D Fourier transform plot, and the time signals that are obtained using an inverse 2D Fourier transform correspond to the receiver locations before a crack.

The wavelet transforms (Eq. 3.20) are applied to the time signals from different extracted Lamb modes. With a Morlet source ($f_0 = 100kHz$, $BW = 66.92kHz$) and the presence of a $10mm$ surface-breaking crack, Fig. 8.19A shows the amplitudes from the wavelet transform at different distances for the incident and transmitted fundamental Lamb mode S0. Fig8.19B shows the corresponding maximum amplitudes at different distances, where the incident Lamb mode is shown before the crack location ($600mm$) and the transmitted Lamb mode after the crack location. The side edges become dull because of the digitized effects from the Fourier transform. The WT transmission ratio can be calculated between the two maximum amplitudes at $700mm$ and $500mm$, which is equal to $(4.34/21.55) = 0.2$ for this case. Whereas, based on the extraction of the reflected Lamb mode, the WT reflection ratio can be calculated as the maximum amplitudes at $500mm$ for different crack depths, and then normalized to the maximum value.

Fig. 8.20 shows the variation of the WT transmission and reflection ratios for different crack depths. Because the wave energy concentrates in a depth of one third of the wavelength ($\lambda/3$), the maximum depth of a crack that can be evaluated with Morlet sources at $f_0 = 50kHz$ and $100kHz$, are $17mm$, and $8.5mm$, respectively. They are in agreement with the numerical results of the WT transmission ratio. However, the WT reflection ratio is less sensitive to the crack depth; it is likely because of the complex wave pattern developed in front of a crack.

8.1.5 Numerical study IV: plane-strain numerical model of the experimental specimen

The WTC is measured in the laboratory tests on concrete plate specimens. To validate the experimental results, the numerical simulations using the plane-strain numerical models

of the experimental specimen are conducted.

The numerical models for this validation are configured:

- Plane-strain numerical modeling configuration.
- Boundary conditions. Left, right, and bottom: free.
- Morlet source ($f_0 = 50kHz$) at $x = 585mm$.
- Plate thickness: $80mm$.
- Rayleigh damping ratio: $\xi_{min} = 0.001$ at frequency $f_{min} = 50kHz$.
- Different depths of a surface-breaking crack.

A Morlet source with $f_0 = 50kHz$ and $BW = 33.46kHz$ is used to simulate the output force for an ultrasonic piezoelectric transmitter. In the numerical model, the source is applied at distance $585mm$ from the left boundary, and the location for a crack is at $600mm$. The surface response at $615mm$ is used to validate the experimental results; thus, the source-receiver spacing is $30mm$, which is the same as in the experimental tests.

In the experimental tests, the WTC is measured using the experimental setup in Fig. 6.2, where a 3D condition is shown. In this equal spacing configuration, the wave propagation from points "A" to "B" and points "D" to "C" come without a crack; while the wave propagation from points "A" to "C" and points "D" to "B" come with a crack. Both cases are simulated with the two 2D numerical models, where a crack is absent or present, accordingly. The complementary test for a self-calibrating technique is no longer needed in the numerical simulations.

Without a crack, Fig. 8.21 shows the time signals and corresponding spectral amplitudes in a 2D contour plot, where the amplitudes in time are normalized to the maximum value for each location. In the time-distance plot, the wave propagation starts at the source location ($585mm$), and a slight dispersion is observed. In the spectral amplitude plot, variations are shown with distances.

In the presence of a $20mm$ surface-breaking crack, the time signals and corresponding spectral amplitudes in a 2D contour plot are shown in Fig. 8.22, where the amplitudes in time are normalized to the maximum value for each location. In Fig. 8.22A, a slight time delay is observed at the crack location when wave propagates through the crack, indicating that a crack plays a role not only as a high frequency reflector and a low frequency pass filter, but also as a time delay gate. The both transmitted and reflected

waves are present in the time-distance plot. In the spectral amplitude plot (frequency-distance), the variations are shown with distance, and low frequency components are transmitted; however, at locations after 700*mm*, high frequency components are shown, it is likely to be caused by the wave reflections.

The 2D Fourier transforms are applied to the time signals given in Fig. 8.21 and Fig. 8.22, respectively, and the results are shown in Fig. 8.23. In the absence of a crack (Fig. 8.23A), the waves propagate as the fundamental Lamb mode in the two directions, because the source is at 585*mm*; however, in the presence of a 20*mm* surface-breaking crack (Fig. 8.23B), the reflected fundamental Lamb mode is shown at high frequencies, and the transmitted fundamental Lamb mode is shown at low frequencies.

The wavelet transforms (Eq. 3.20) are applied to the time signals from the two cases of no crack and a 20*mm* surface-breaking crack, which are given in Figs. 8.21 and 8.22, respectively. The amplitude results from the wavelet transform are shown in Fig. 8.24. In the presence of a 20*mm* surface-breaking crack, the transmitted and reflected waves for the fundamental Lamb mode are shown in Fig. 8.24B.

The surface responses at distance 615*mm* are shown in time and frequency in Fig. 8.25. For the time signals, the maximum amplitude is attenuated because of the presence of a 20*mm* surface-breaking crack, and the wave shape is changed for the first 1.5 time cycles. In frequency, the spectral amplitudes are reduced for most frequencies. However, the spectral amplitude reduction is not constant for all frequencies; it indicates a difficulty for the depth evaluation of a surface-breaking crack using Fourier transform.

Using the extended wavelet transform in Eq. 6.1, where $a_1 = 0.625$ and $a_2 = 1.25$, the maximum amplitudes at different distances are shown in Fig. 8.26; a relatively constant reduction is shown for locations after a crack, indicating the presence of a 20*mm* surface-breaking crack. The reduction at distance 615*mm* is measured with a numerical WT ratio between the two maximum amplitudes, which is equal to $0.178/0.341 = 0.523$ for the case of a 20*mm* surface-breaking crack. For different depths of a surface-breaking crack, the numerical WT ratios are given in Table 8.1.

8.1.6 Laboratory tests on concrete plates

With Fig. 6.2, the laboratory tests are conducted on the two types of concrete plate specimens, one with plain concrete, and another with reinforced concrete. A notch is cut on the concrete plate specimens with different depths to simulate a surface-breaking crack. Based on four measured time signals $g_{AB}(t)$, $g_{AC}(t)$, $g_{DC}(t)$, and $g_{DB}(t)$, the experimental WTC is calculated using Eq. 6.1 for different depths of a notch.

As an example to show typical experimental results, Fig. 8.27 shows the time signals and corresponding spectral amplitudes for the case of the reinforced concrete plate specimen with a 15*mm* notch. For this case, the extended wavelet transforms (Eq. 3.25) are applied to the four measured time signals. The amplitude results are shown as a function of shift time in Fig. 8.28. The maximum amplitudes occur at a signal arrival, and they are used to calculate the experimental WTC, which is equal to 0.539 for a 15*mm* notch. The experimental WTC results from the laboratory tests are given in Table 8.2 for both the plain and reinforced concrete plate specimens.

In Fig. 8.29, the experimental WTC results are compared with the numerical WT ratios from Table 8.1. Both the experimental and numerical results show a similar trend. However, the equal spacing configuration in Fig. 6.2 shows a 3D condition; while the numerical simulation is conducted in a 2D numerical model. Therefore, differences may exist. For example, the wave propagation from points "A" to "B" or points "D" to "C" in Fig. 6.2 is affected by the wave reflections from the side boundary of a crack (notch), but it is not the case in the numerical simulations. For the crack depths deeper than 15*mm*, experimental WTC results give a lower value than numerical results, and the variation becomes bigger for a crack depth of 30*mm*.

8.1.7 In-situ tests on concrete pipes

In-situ tests were performed twice at the Hanson Pipe and Precast Inc., Cambridge, Ontario, Canada, in June 2008. Effects of a curved surface on wave propagation are not studied here, because the transducer's spacing is small relative to the diameter of the pipes.

For the first test, two cracks are found on a concrete pipe specimen, and their depths are estimated as 50*mm* and 150*mm*, respectively. For the shallow crack, the four measured time signals and the corresponding amplitudes from the extended wavelet transform are shown in Figs. 8.30 and 8.31, respectively. While, for the deep crack, they are shown in Figs. 8.32 and 8.33, respectively. The experimental WTC are calculated using Eq. 6.1, which is 0.25 for the shallow depth, and 0.041 for the deep depth. A significant reduction for the WTC occurs for this shallow crack, and the further reduction indicates the presence of a deep crack.

For the second test, the experimental WTC is measured at different loading stages. The first measurement is performed on a flawless area of the interior wall surface of a concrete pipe specimen before the load starts. Then, the load increases until a crack is observed on the interior wall surface, when the load is 242.4*kN* at the second stage. The

measurement for the third stage is performed at the same location when the load increases to 290.8kN. At the fourth stage, the load reaches the maximum, which is 392.9kN. Finally, the load is released at the fifth stage, and the measurement is performed to check a recovery of the crack depth.

For the second stage to the fifth stage, the time signals and corresponding amplitudes from the extended wavelet transform are shown in Figs. 8.34 to 8.41. The experimental WTC are given in Table 8.5, and plotted in Fig. 8.42. In reality, a crack is initiated normally with a deep depth; therefore, from the first stage to the second stages, the experimental WTC is significantly reduced indicating the presence of a deep crack. From the second to the third stages, the crack depth still increases. However, at the fourth stage, where the load reaches the maximum (392.4kN), the experimental WTC does not change much. At the last stage, the experimental WTC goes higher a little, indicating the crack recovery is limited after the D-loading is released.

8.2 Measurement of material damping ratio

8.2.1 Introduction

The numerical models shown in Fig. 7.6 are well-calibrated; therefore, they are used for the numerical study of the measurement of material damping ratio. By applying three numerical sources and giving four values to the minimum Rayleigh damping ratio, the twelve numerical models are constructed in Table 8.3.

The numerical models for the damping study are configured:

- Axisymmetric numerical modeling configuration.
- Boundary conditions. Left, right, and bottom: quiet.
- Three numerical sources: Lamb source ($\eta = 1.78 \times 10^{-6}$) and Morlet sources ($f_0 = 50kHz$, $100kHz$) at $x = 0mm$.
- Plate thickness: $80mm$.
- Four values of the minimum Rayleigh damping ratio: $\xi_{min} = 0$, 0.008, 0.02, and 0.05.
- No crack present.

The numerical data are analyzed with the Fourier transform, which gives the material damping ratio as a function of frequency, and the wavelet transform, which gives a global value of the material damping ratio, which represents an average damping effect for a frequency bandwidth determined by source.

Following the numerical results, the experimental results are presented, which are from the laboratory tests on a sand box and a concrete plate specimen.

8.2.2 Material damping ratio from Fourier transform vs. frequency

The surface responses at two distances $400mm$ and $800mm$ from the source are used to calculate the material damping ratio using Eq. 5.21, and the damping result is a function of frequency. In Fig. 8.43, the numerical results are validated with theoretical Rayleigh damping ratio ξ (Eq. 5.25). For three numerical sources, the numerical and theoretical results agree in a wide frequency bandwidth for low values of ξ_{min}. At low frequencies, the numerical results show a high value; it is likely due to the thickness effect of a plate.

8.2.3 Maximum amplitude from the wavelet transform vs. normalized distance

The surface responses from the 201 receivers incorporate the effects from both the material damping and the geometric attenuation. The maximum amplitudes at different distances from the wavelet transform (Eq. 3.20) are shown in a logarithmic scale in Fig. 8.44, where the horizontal axis is the distance normalized to the wavelength. The logarithms of the maximum amplitudes decrease almost linearly with distance. Lamb source and Morlet source with central frequency at $50kHz$ generate low frequency components; in contrast, Morlet source with central frequency at $100kHz$ generates high frequency components. Therefore, high frequency components attenuate faster than low high frequency components as shown in Fig. 8.44.

8.2.4 Normalized damped frequency from the wavelet transform vs. normalized distance

Using the surface responses at distances $400mm$ to $800mm$, the damped frequencies for a SDOF system are calculated by taking a derivative of the phase from the wavelet transform (Eq. 3.20). Fig. 8.45 shows the variation of normalized damped frequency vs. normalized distance for three numerical sources. For a small value of ξ_{min}, the damped frequency is slightly higher than the central frequency f_0; while for a large value, the damped frequency is lower.

8.2.5 Material damping ratio from the wavelet transform vs. normalized distance

Eq. 5.34 calculates the material damping ratio using the amplitude and phase information from the wavelet transform; the damping results are shown in Fig. 8.46. Unlike the material damping ratio that is calculated from the Fourier transform (Eq. 5.21), the result from the wavelet transform gives a global value that represents an average effect of the material damping for a frequency bandwidth, which is determined by the source.

As shown in Fig. 8.43, the Rayleigh damping ratio gives a high value at low frequencies, for example in a range when $(f/f_0) < 0.5$. In Fig. 8.46, Lamb source and Morlet source with central frequency at $50kHz$ provide the frequency components at a low frequency range, and thus the material damping ratios are higher than the minimum Rayleigh damping ratio ξ_{min}; whereas, Morlet source with central frequency at $100kHz$

provides high frequency components, and thus the material damping ratios show a close value to the minimum Rayleigh damping ratio ξ_{min}.

In Table 8.4, the mean values for the material damping ratios at different distances, and a difference relative to the minimum Rayleigh damping ratio ξ_{min} are calculated for a comparison. Similarly, for the reason that the Rayleigh damping ratio gives a high value for low frequencies, Lamb source produces the highest error, the Morlet source with central frequency at $50kHz$ is the next, and the Morlet source with central frequency at $100kHz$ gives the closest results to ξ_{min}.

8.2.6 Laboratory tests on a sand box

Using the experimental setup in Fig. 6.8, Laboratory tests are conducted for different source-reviver spacings ($220mm$ to $400mm$). For the measurement of material damping ratio, geometric attenuation needs to be eliminated from the time signals. As an example, Fig. 8.47 shows at the first receiver location ($220mm$ from the source) the time signal, spectral amplitude and wavelet transform results. The first P-wave arrival (marked as "P1") and the first surface wave arrival (marked as "P2") are identified in the time signal, and they produce the two peaks ("P1" and "P2") for the amplitude of the wavelet transform. The damped frequency (ω_d) is calculated as a derivative of the phase from the wavelet transform, which is a function of shift time; $\omega_d = 35.56kHz$ at the first surface wave arrival. The maximum amplitude and damped frequency corresponding to the first surface wave arrival are used to calculate the material damping ratio.

The arrival times for the first P-wave and the first surface wave at different receiver locations are shown in Fig. 8.48. By doing a linear curve fitting, the P-wave and surface wave velocities are obtained: $V_P = 2186m/s$ and $V_R = 1208m/s$. With these two values, Poisson's ratio is calculated as 0.21, which is close to a typical value 0.20 for cemented sand, which is measured using resonant column (*Khan* 2006).

For the numerical simulations, a $50kHz$ Morlet function is used as a wave source , and a ratio of the wavelength to the plate thickness is equal to $\lambda/h = 0.64$. While, for the wave propagation in the sand box with given Rayleigh wave velocity, $V_R = 1208m/s$, and frequency, $f = 50kHz$, the wavelength is calculated as $\lambda = V_R/f = 24mm$. Therefore, a ratio of the wavelength to the top layer thickness ($h = 300mm$) is given, $\lambda/h = 0.08$. Because of a relatively small wavelength for the wave propagation in the sand box, Rayleigh waves are mostly generated, which are suitable for the measurement of material damping ratio.

From the wavelet transform, the maximum amplitudes of the first surface wave arrival

("P2" in Fig. 8.47) at different receiver locations are shown in a logarithmic scale in Fig. 8.49, where variation appears; it is likely due to the effects of the wave reflections from the boundaries or the underground void. Therefore, a linear curve fitting is used to reduce this variation, and the spatial attenuation coefficient is obtained as a slope of the fitted line, $\alpha_x = 0.725$.

The damped frequencies at different receiver locations are shown in Fig. 8.50, and they are lower than $50kHz$. In Fig. 8.51, The material damping ratio is calculated from the wavelet transform using Eq. 5.34, where the spatial attenuation coefficient is given as a constant number, $\alpha_x = 0.725$, the damped frequency ω_d is given from Fig. 8.50, and the velocity is equal to $V_R = 1208m/s$. A mean value for material damping ratios at different receiver locations is calculated as $\xi = 0.384\%$, which is close to a value measured from resonant column (*Khan* 2006), $\xi = 0.4\%$.

8.2.7 Laboratory tests on a concrete plate

Using the experimental setup in Fig. 6.9, laboratory tests are conducted for different source-receiver spacings, which $30mm$, $60mm$, $90mm$, and $120mm$, respectively. For the measurement of material damping ratio, geometric attenuation needs to be eliminated from the time signals.

The time signals and spectral amplitudes are shown in Fig. 8.52. Amplitude vs. shift time from the wavelet transform (Eq. 3.20) is shown in Fig. 8.53A, where the maximum amplitude occur at different arrival times: $t_1 = 104\mu s$ for receiver location at $30mm$, $t_2 = 120\mu s$ for receiver location at $60mm$, $t_3 = 135\mu s$ for receiver location at $90mm$, and $t_4 = 152\mu s$ for receiver location at $120mm$. The damped frequency is calculated with a derivative of the phase from the wavelet transform in Fig. 8.53B, which varies with the shift time; however, the damped frequencies corresponding to the arrival times (t_1, t_2, t_3, and t_4) are selected for the calculation of the material damping ratios at different receiver locations. The experimental results of material damping ratio using the wavelet transform are shown for different receiver locations in Fig. 8.54. A mean value of material damping ratio for different receiver locations is equal to 0.01, which is in a range of the material damping ration for an uncracked and low stress concrete given in Table 6.1.

Table 8.1: Numerical WT ratio from the extended wavelet transform vs. crack depth

Crack depth (mm)	Numerical WT ratio
0	1
5	0.833
10	0.69
15	0.615
20	0.523
25	0.46
30	0.348
35	0.246
40	0.201

Table 8.2: Experimental WTC vs. notch depth for the plain and reinforced concrete plate specimens

Notch depth (mm)	Experimental WTC	
	(plain concrete)	(reinforced concrete)
0	0.982	1.003
5	0.874	0.904
10	0.682	0.732
15	0.557	0.539
20	0.467	0.469
25	N / A	0.413
30	0.227	0.274

Table 8.3: Numerical models for the damping measurements

Model No.	Source	Rayleigh damping	
		ξ_{min}	f_{min}
M1	Lamb source ($\eta = 1.58 \times 10^{-6}$)	0	50kHz
M2		0.008	
M3		0.02	
M4		0.05	
M5	Morlet source ($f_0 = 50kHz$, $BW = 33.46kHz$)	0	50kHz
M6		0.008	
M7		0.02	
M8		0.05	
M9	Morlet source ($f_0 = 100kHz$, $BW = 66.92kHz$)	0	100kHz
M10		0.008	
M11		0.02	
M12		0.05	

Table 8.4: Mean values and a difference for material damping ratios

Source	Minimum Rayleigh damping ratio (ξ_{min})	Mean value	% Difference
Lamb source ($\eta = 1.58 \times 10^{-6}$)	0.008	0.01	25%
	0.02	0.023	15%
	0.05	0.056	12%
Morlet source ($f_0 = 50kHz$)	0.008	0.0096	20%
	0.02	0.022	10%
	0.05	0.054	8%
Morlet source ($f_0 = 100kHz$)	0.008	0.008	0%
	0.02	0.02	0%
	0.05	0.051	2%

Table 8.5: Experimental WTC vs. D-loading for different stages

Stage No.	1	2	3	4	5
D - load (kN)	0	242.4	290.8	392.9	0
Experimental WTC	0.975	0.219	0.141	0.135	0.15

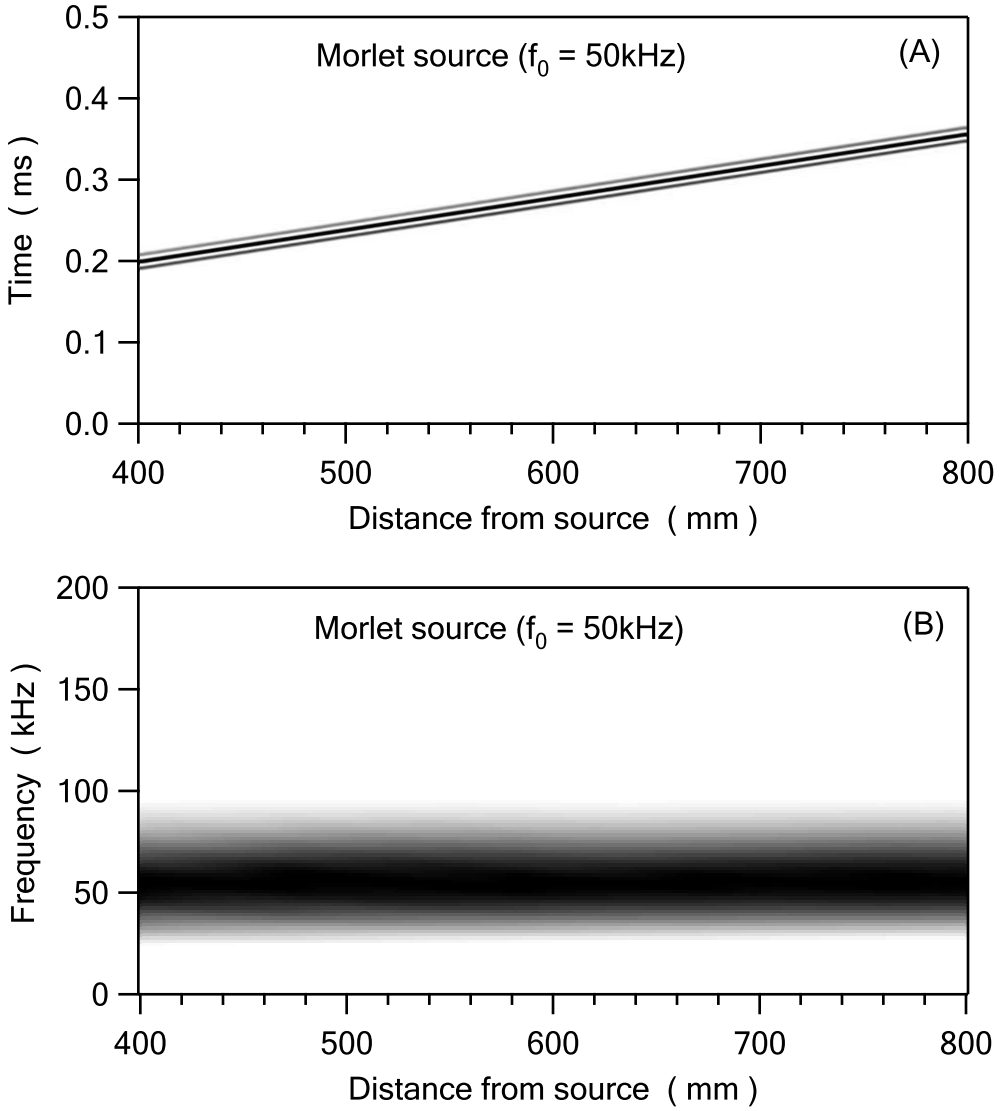

Figure 8.1: Numerical Rayleigh wave propagation in a simulated half-space with a Morlet source ($f_0 = 50kHz$, $BW = 33.46kHz$). (A) in time and distance; (B) in frequency and distance.

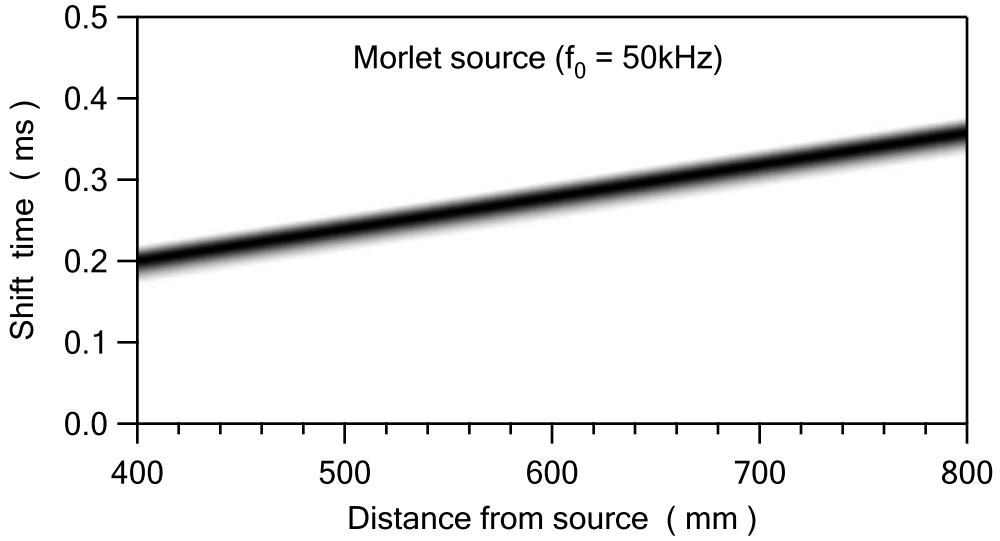

Figure 8.2: Amplitudes of the wavelet transform in time and distance domain for numerical Rayleigh wave propagation in a simulated half-space. A Morlet source is used ($f_0 = 50kHz$, $BW = 33.46kHz$).

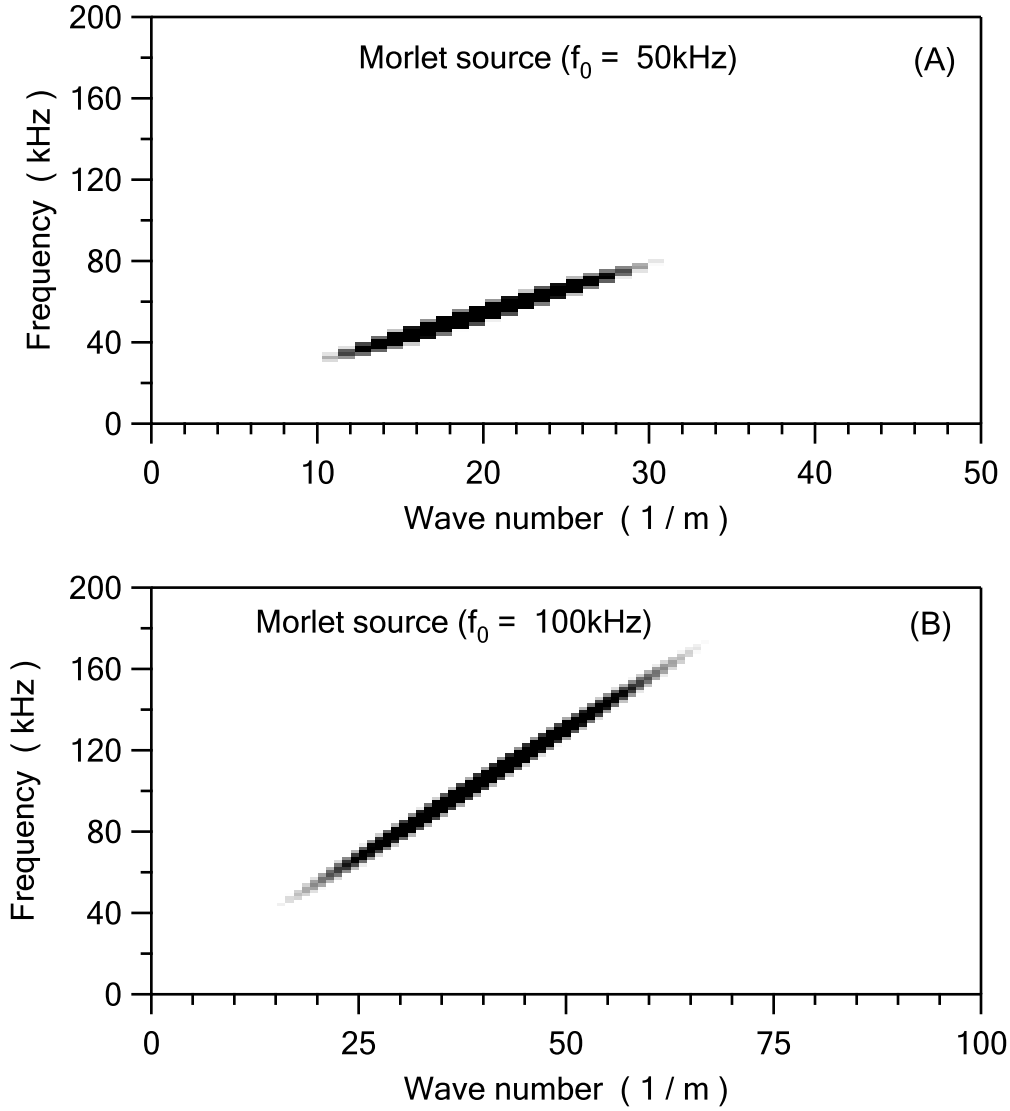

Figure 8.3: 2D Fourier transform for the numerical Rayleigh wave propagation in a half-space with: (A) a Morlet source ($f_0 = 50kHz$, $BW = 33.46kHz$); (B) a Morlet source ($f_0 = 100kHz$, $BW = 66.92kHz$).

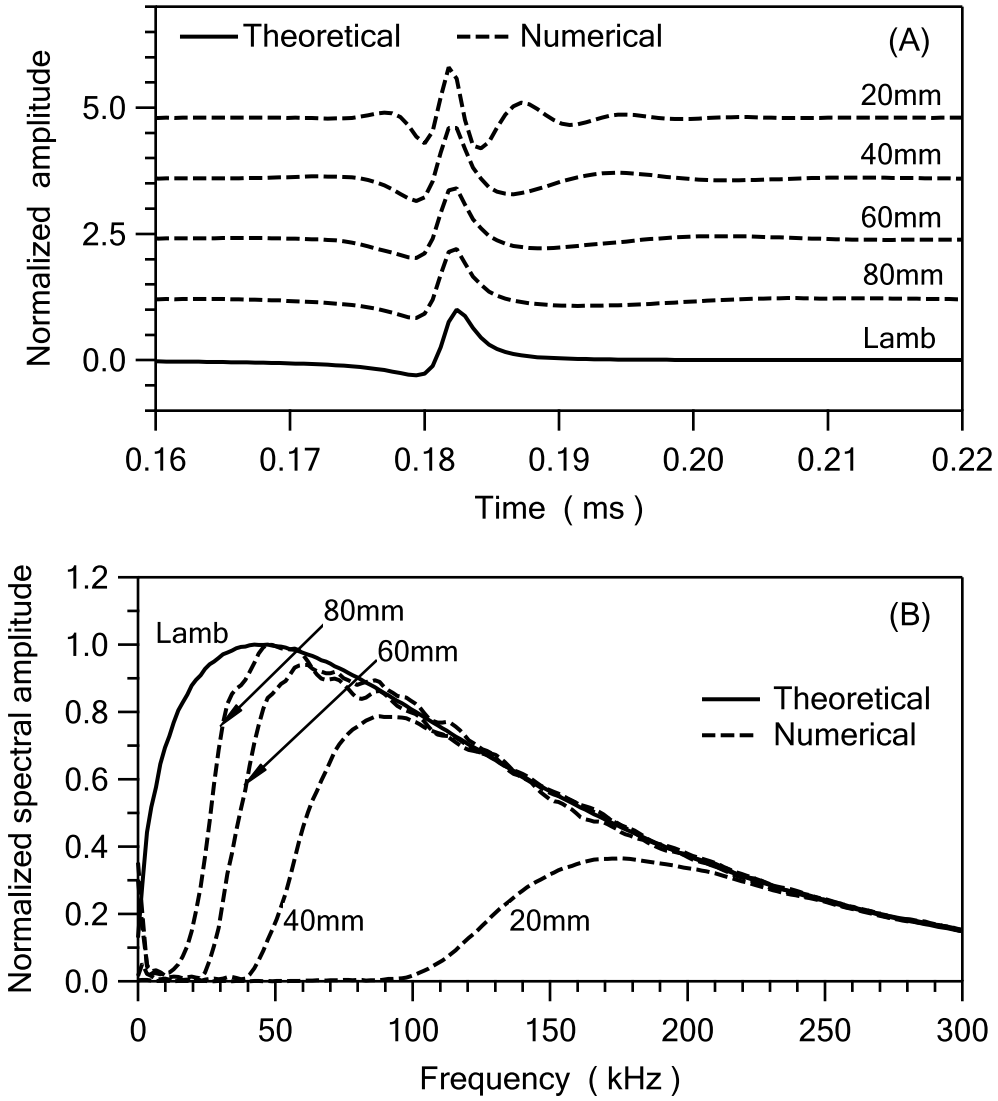

Figure 8.4: Comparison of the theoretical Lamb solution with the numerical results (at distance 400*mm* from the source). (A) time signals; (B) spectral amplitudes. The plate thicknesses are 20*mm*, 40*mm*, 60*mm*, and 80*mm*, respectively.

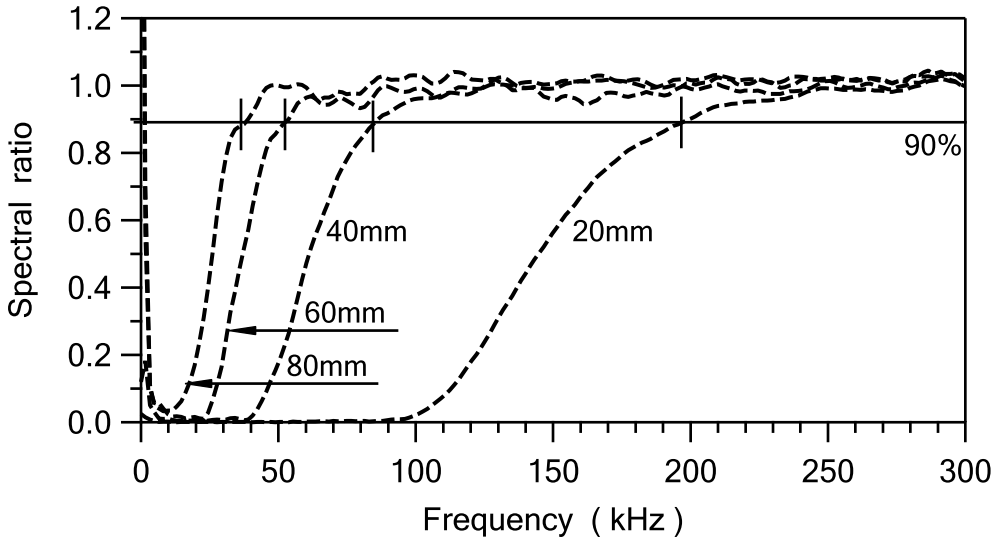

Figure 8.5: Spectral ratio between the numerical results (at distance 400*mm* from the source) and the theoretical Lamb solution. The plate thicknesses are 20*mm*, 40*mm*, 60*mm*, and 80*mm*, respectively.

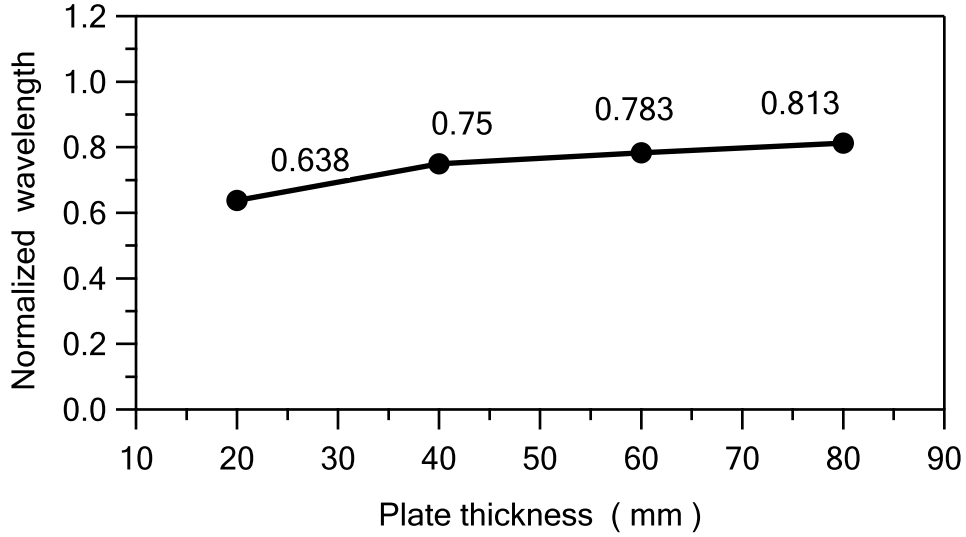

Figure 8.6: Normalized wavelength for different plate thicknesses, calculated from the low-bound frequencies (Fig. 8.5).

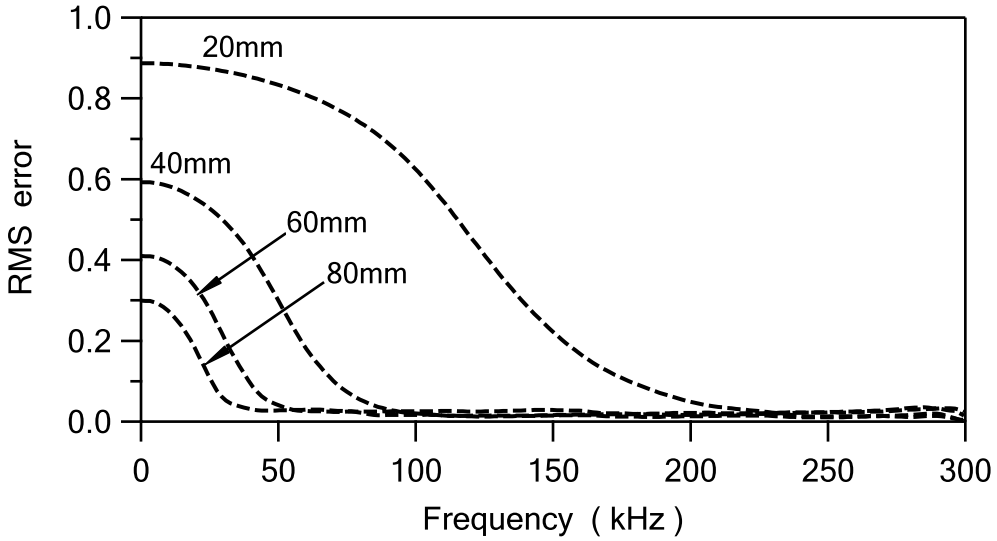

Figure 8.7: RMS error of the numerical spectral amplitudes relative to the theoretical Lamb solution (at distance 400*mm* from the source). The plate thicknesses are 20*mm*, 40*mm*, 60*mm*, and 80*mm*, respectively.

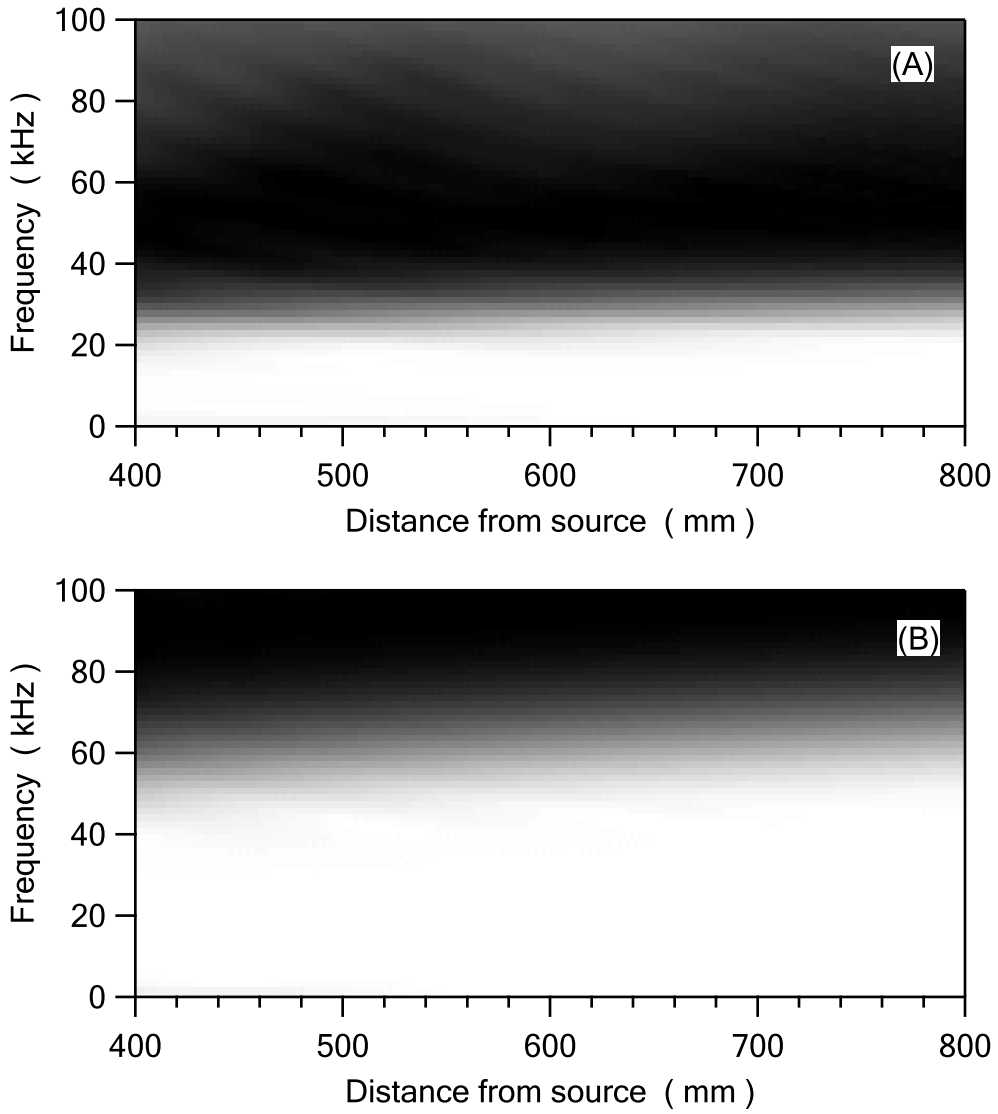

Figure 8.8: Numerical cross power spectra at different distances. (A) between the theoretical Lamb solution and the numerical result (the plate thickness 80*mm*); (B) between the theoretical Lamb solution and the numerical result (the plate thickness 40*mm*).

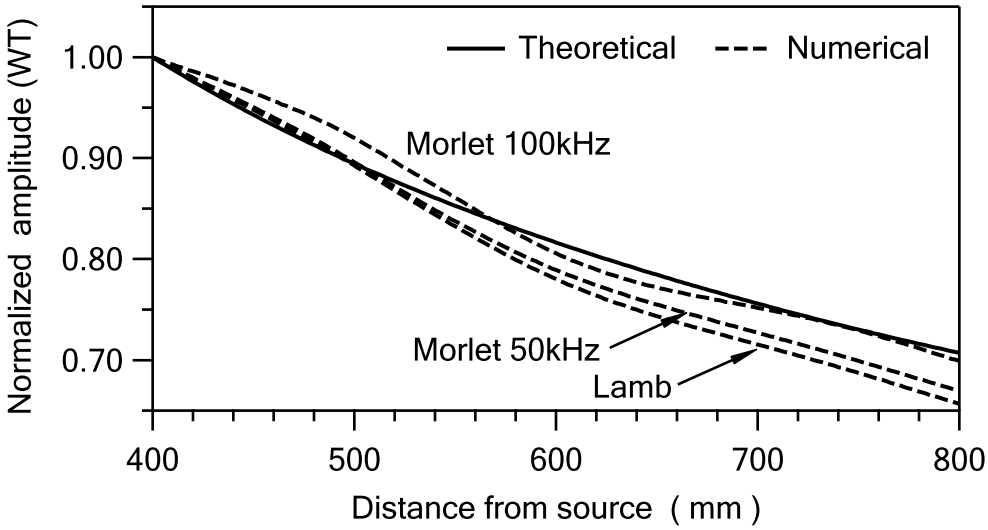

Figure 8.9: Numerical geometric attenuation predicted with the maximum amplitudes from the wavelet transform at different distances. Three sources are used: Lamb source ($\eta = 1.78 \times 10^{-6}$) and Morlet sources ($f_0 = 50kHz$, $100kHz$).

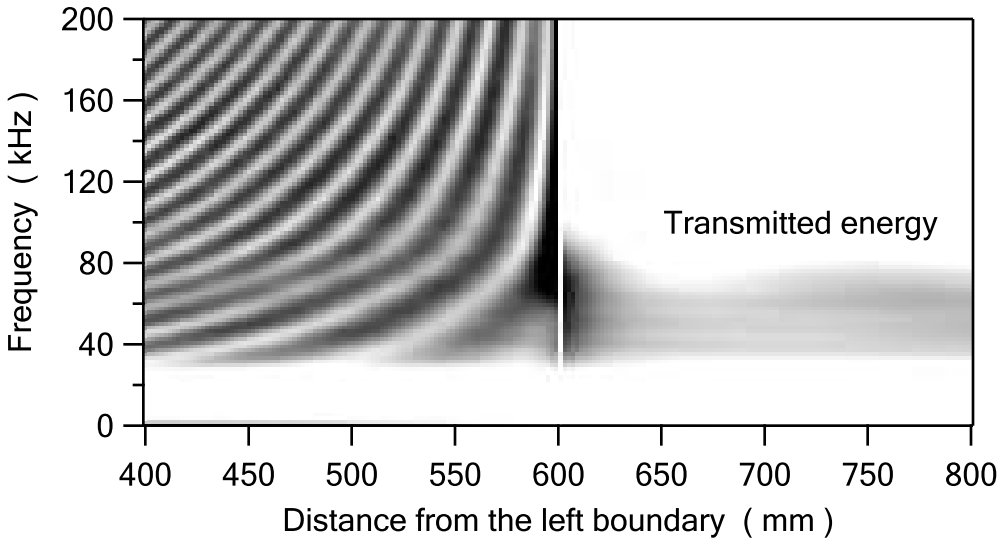

Figure 8.10: Numerical 2D plot of the spectral ratios at different distances. A Lamb source is use ($\eta = 1.78 \times 10^{-6}$)d.

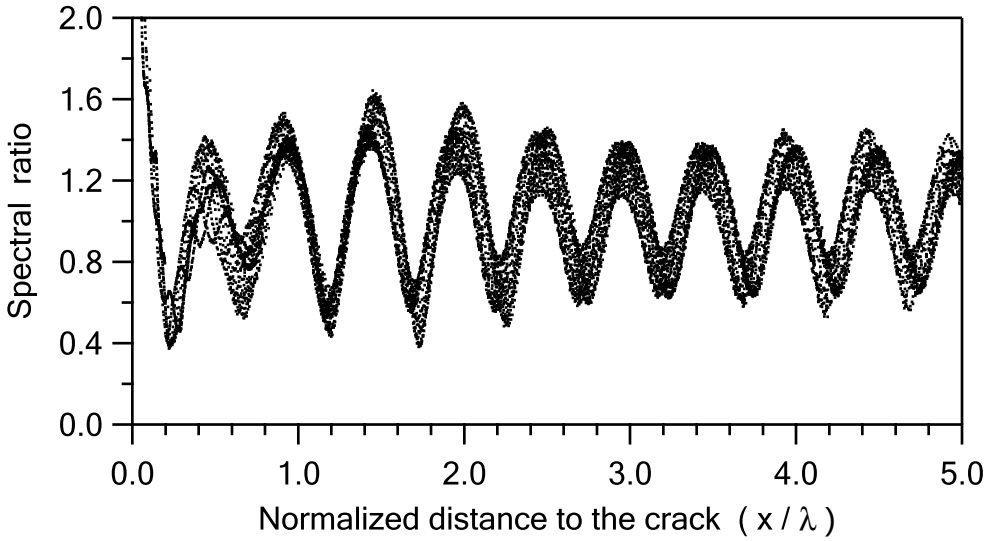

Figure 8.11: Numerical spectral ratio vs. normalized distance from the crack. A Lamb source is used ($\eta = 1.78 \times 10^{-6}$).

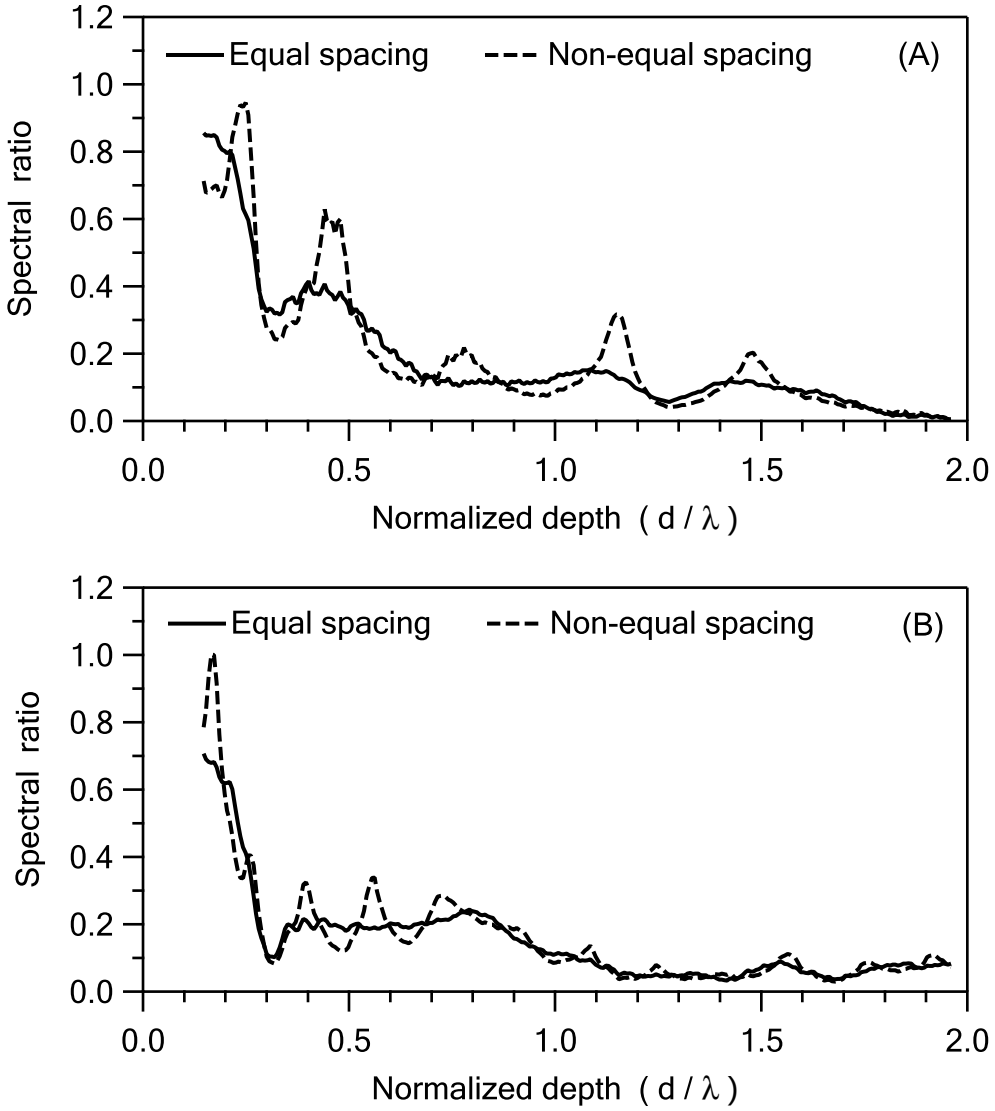

Figure 8.12: Numerical spectral ratio vs. normalized distance from the crack. A Lamb source is used ($\eta = 1.78 \times 10^{-6}$).

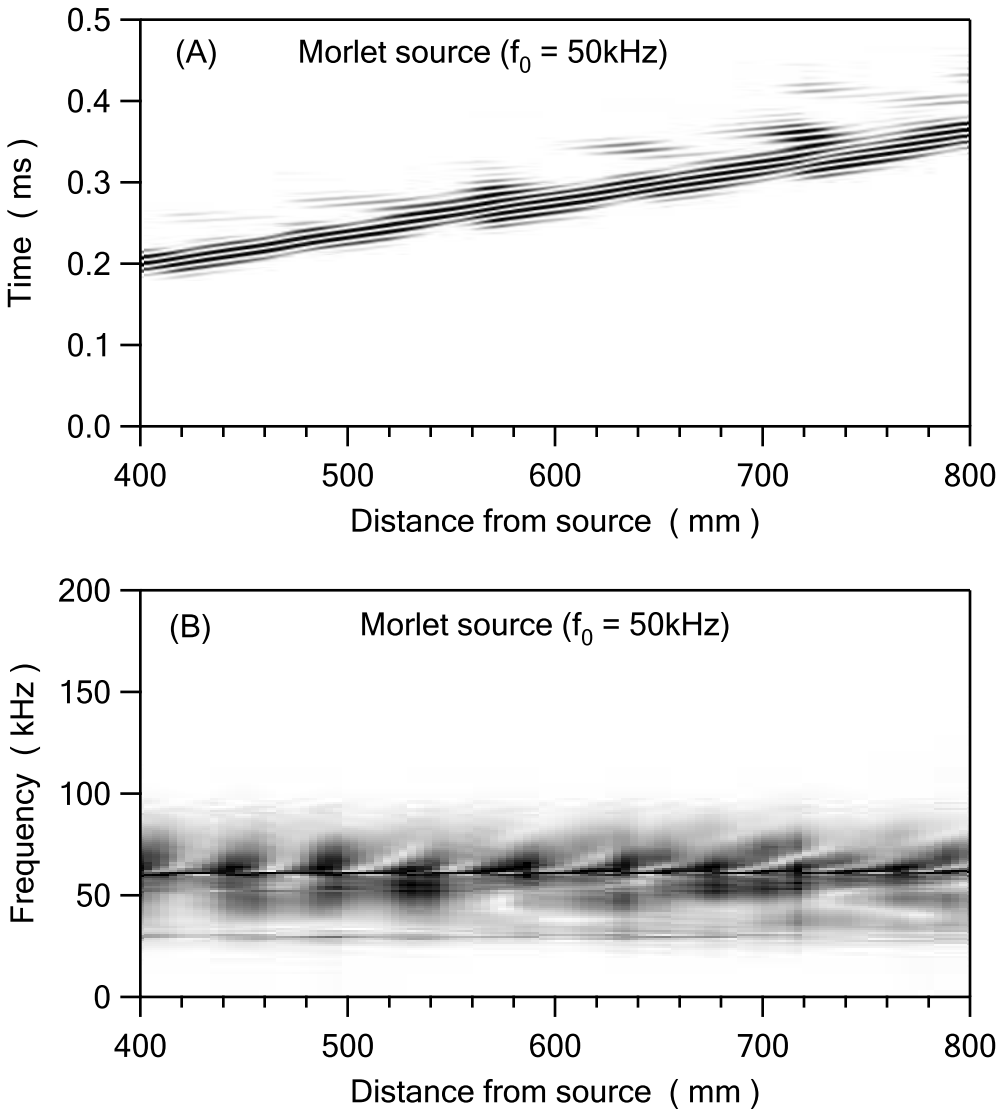

Figure 8.13: Numerical Lamb wave propagation in an 80*mm* plate. (A) in time and distance; (B) in frequency and distance. A Morlet source is used ($f_0 = 50kHz$, $BW = 33.46kHz$).

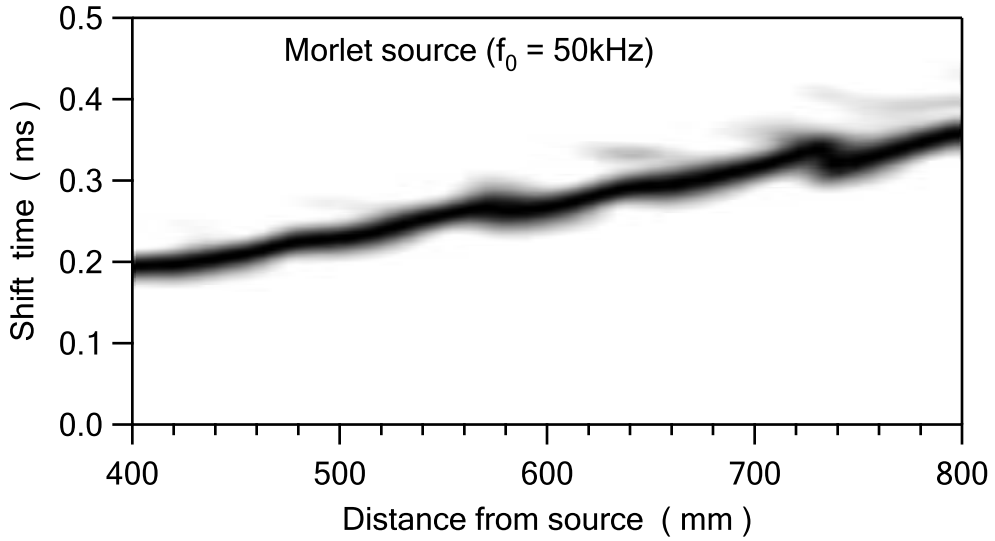

Figure 8.14: Amplitudes of the wavelet transform for numerical Lamb wave propagation in an 80mm plate. A Morlet source is used ($f_0 = 50kHz$, $BW = 33.46kHz$).

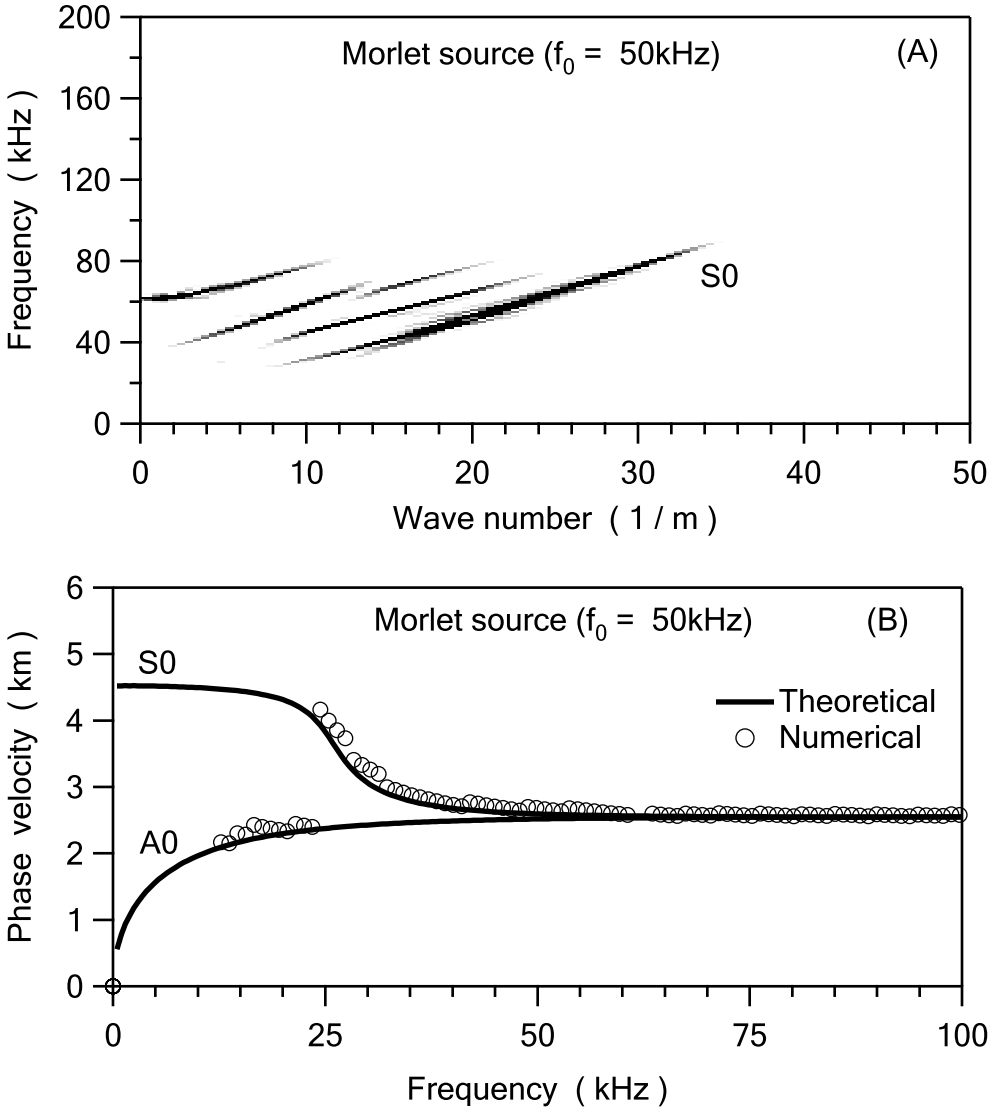

Figure 8.15: Numerical Lamb wave propagation in an 80*mm* plate without a crack. (A) 2D Fourier transform; (B) fundamental Lamb mode S0 compared with the theoretical results. A Morlet source is used ($f_0 = 50kHz$, $BW = 33.46kHz$).

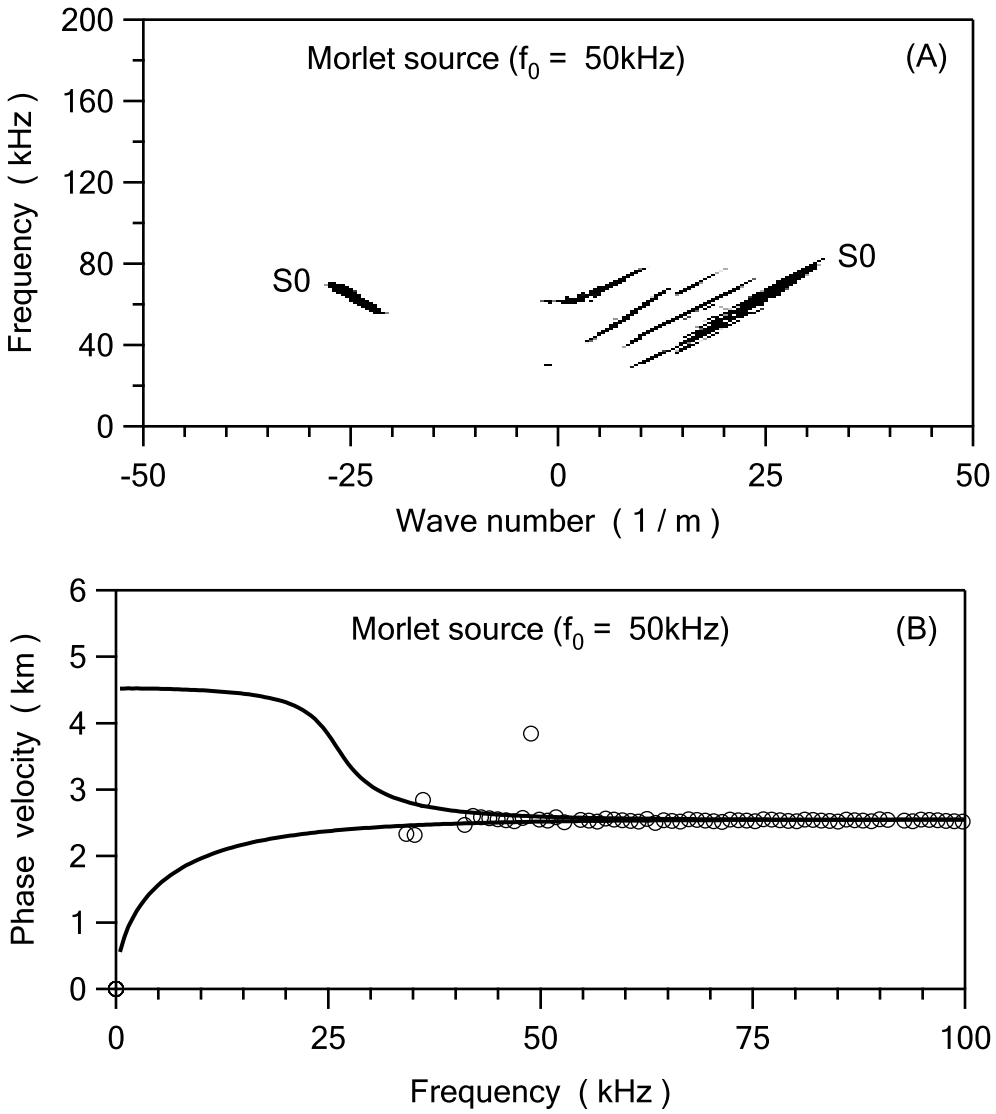

Figure 8.16: Numerical Lamb wave propagation in an 80mm plate with a 20mm crack. (A) 2D Fourier transform; (B) reflected fundamental Lamb mode S0 compared with the theoretical results. A Morlet source is used ($f_0 = 50kHz$, $BW = 33.46kHz$).

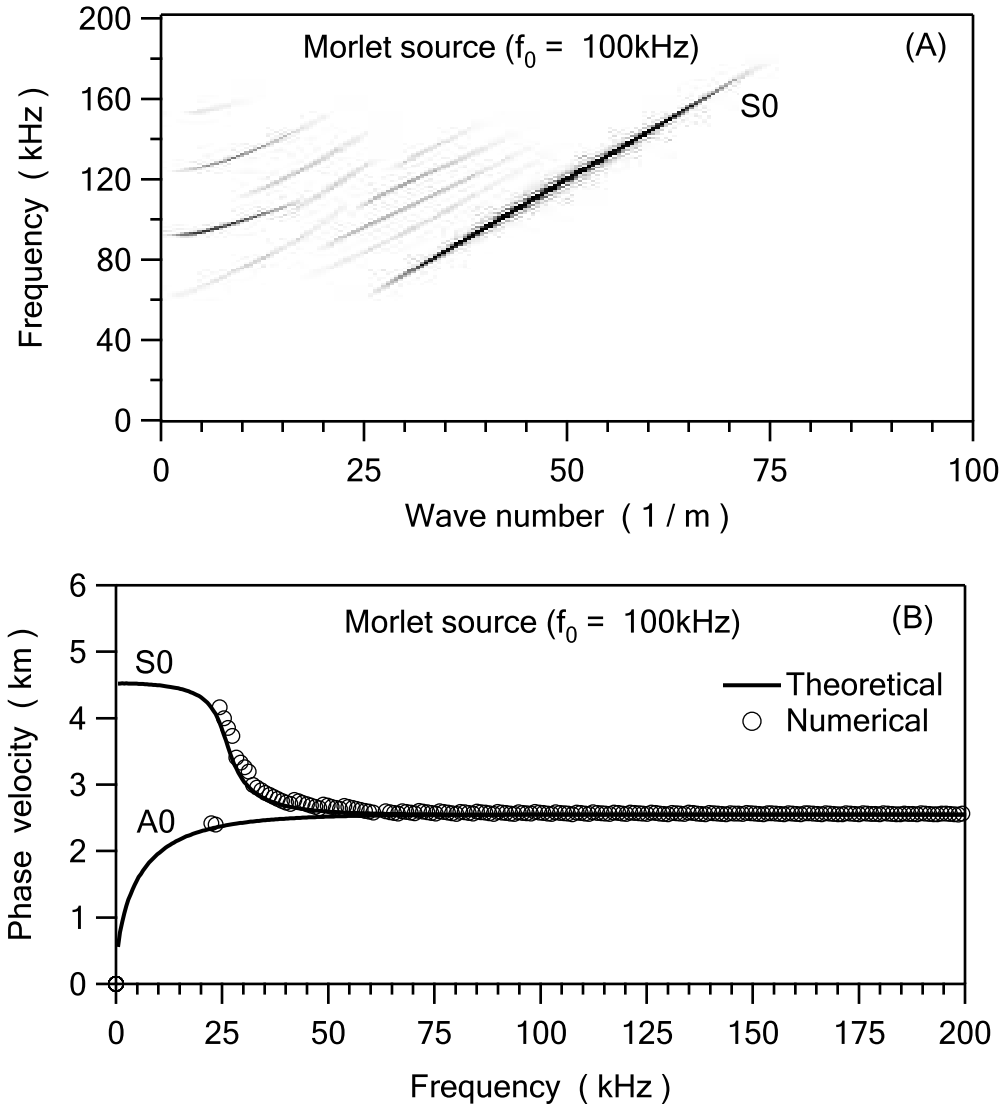

Figure 8.17: Numerical Lamb wave propagation in an 80*mm* plate without a crack. (A) 2D Fourier transform; (B) fundamental Lamb mode S0 compared with the theoretical results. A Morlet source is used ($f_0 = 100kHz$, $BW = 66.92kHz$).

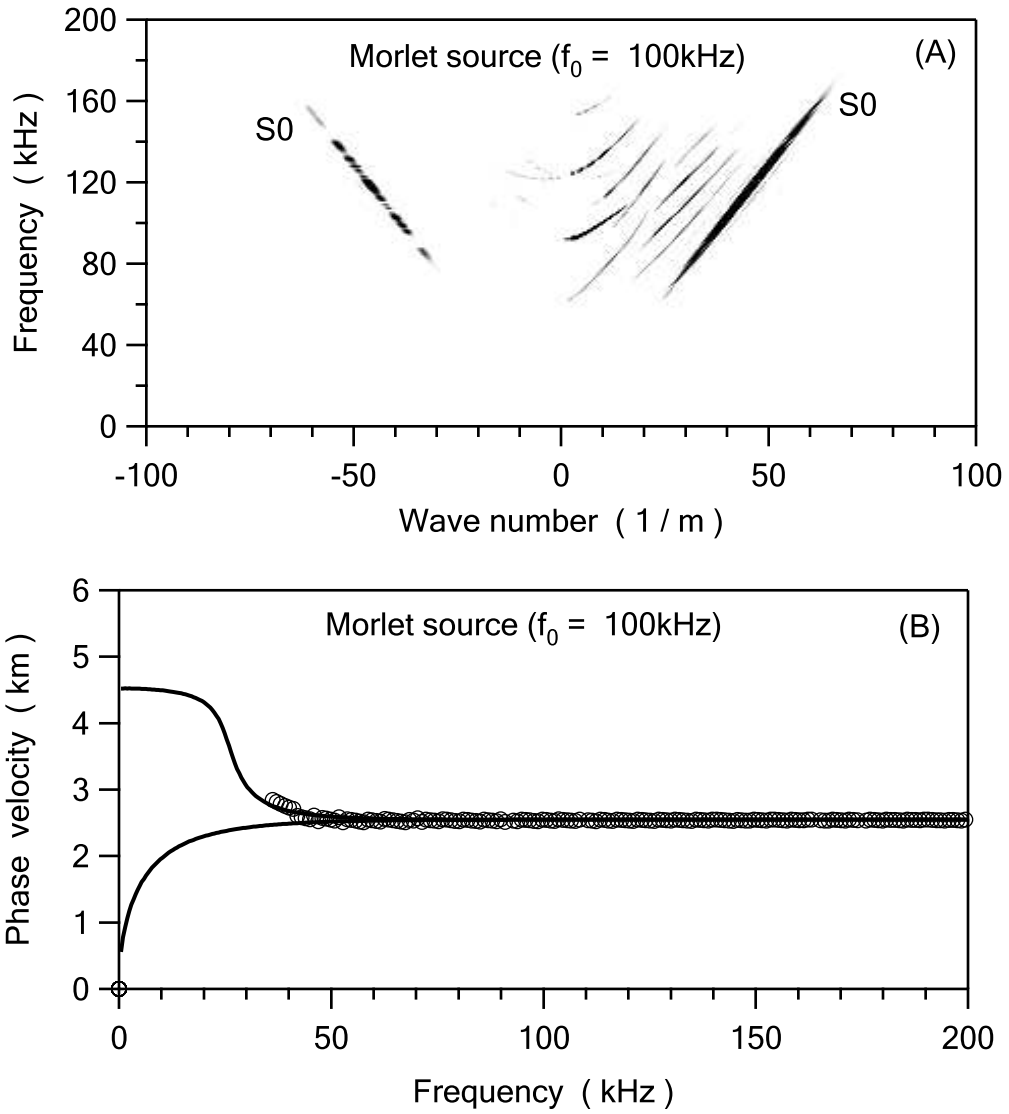

Figure 8.18: Numerical Lamb wave propagation in an 80*mm* plate with a 10*mm* crack. (A) 2D Fourier transform; (B) reflected fundamental Lamb mode S0 compared with the theoretical results. A Morlet source is used ($f_0 = 100kHz$, $BW = 66.92kHz$).

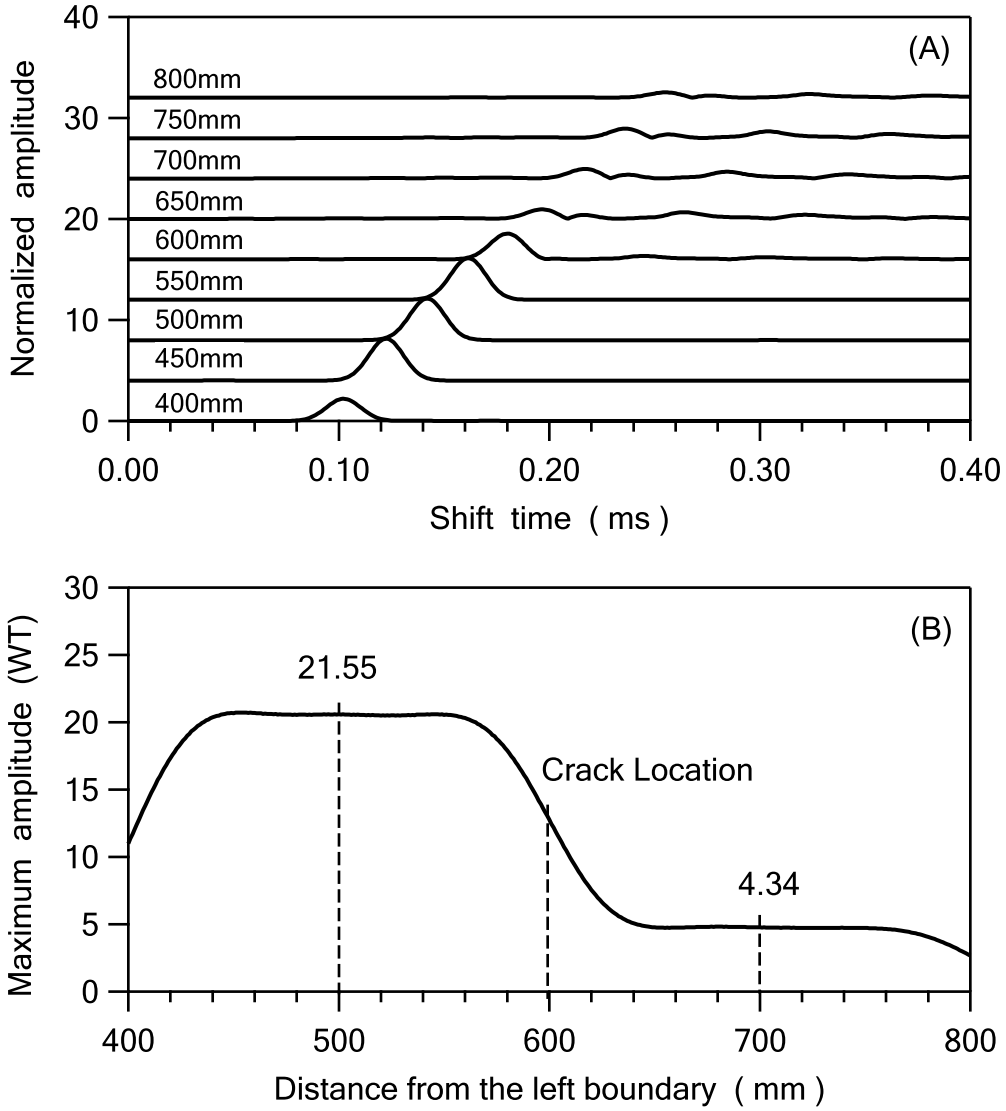

Figure 8.19: Numerical results from the wavelet transform with the extraction of the incident and transmitted fundamental Lamb mode S0 in the presence of a 10*mm* crack. (A) amplitude vs. shift time for different distances ; (B) maximum amplitudes at different distances. A Morlet source is used ($f_0 = 100kHz$, $BW = 66.92kHz$).

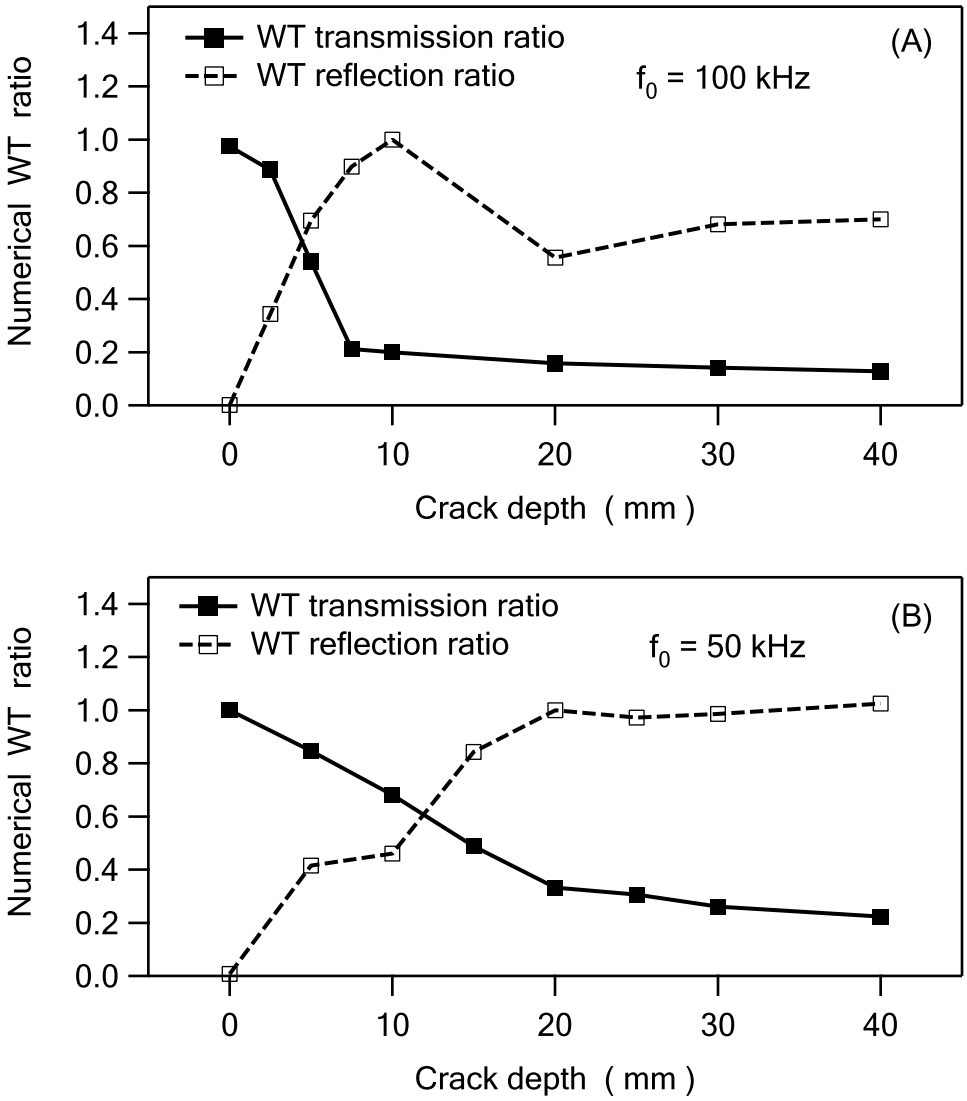

Figure 8.20: Numerical WT transmission and reflection ratio vs. crack depth for the extracted fundamental Lamb mode S0. (A) Morlet source ($f_0 = 100kHz$, $BW = 66.92kHz$); (B) Morlet source ($f_0 = 50kHz$, $BW = 33.46kHz$).

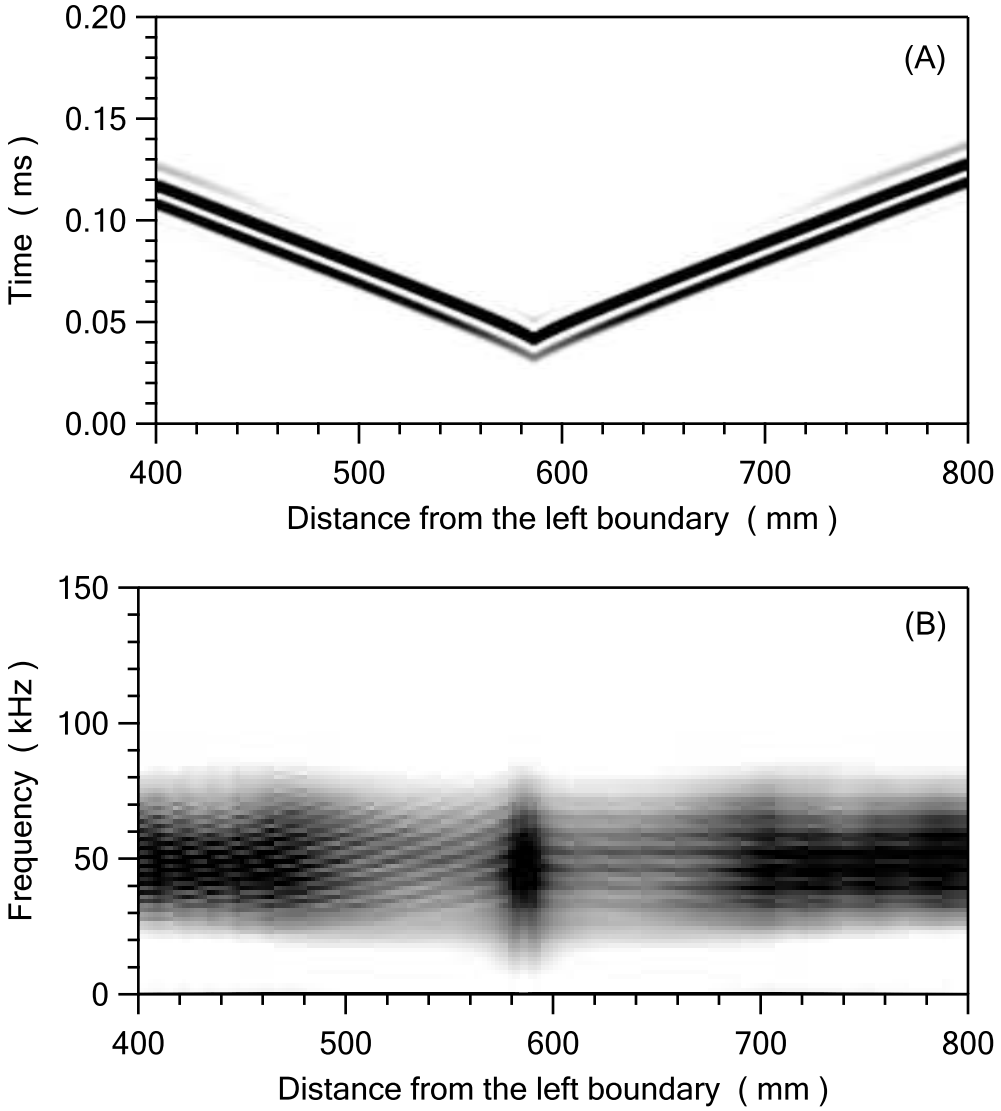

Figure 8.21: Numerical wave propagation with a Morlet source ($f_0 = 50kHz$, $BW = 33.46kHz$) applied at $585mm$ in the absence of a crack. (A) amplitude in time and distance; (B) spectral amplitude in frequency and distance.

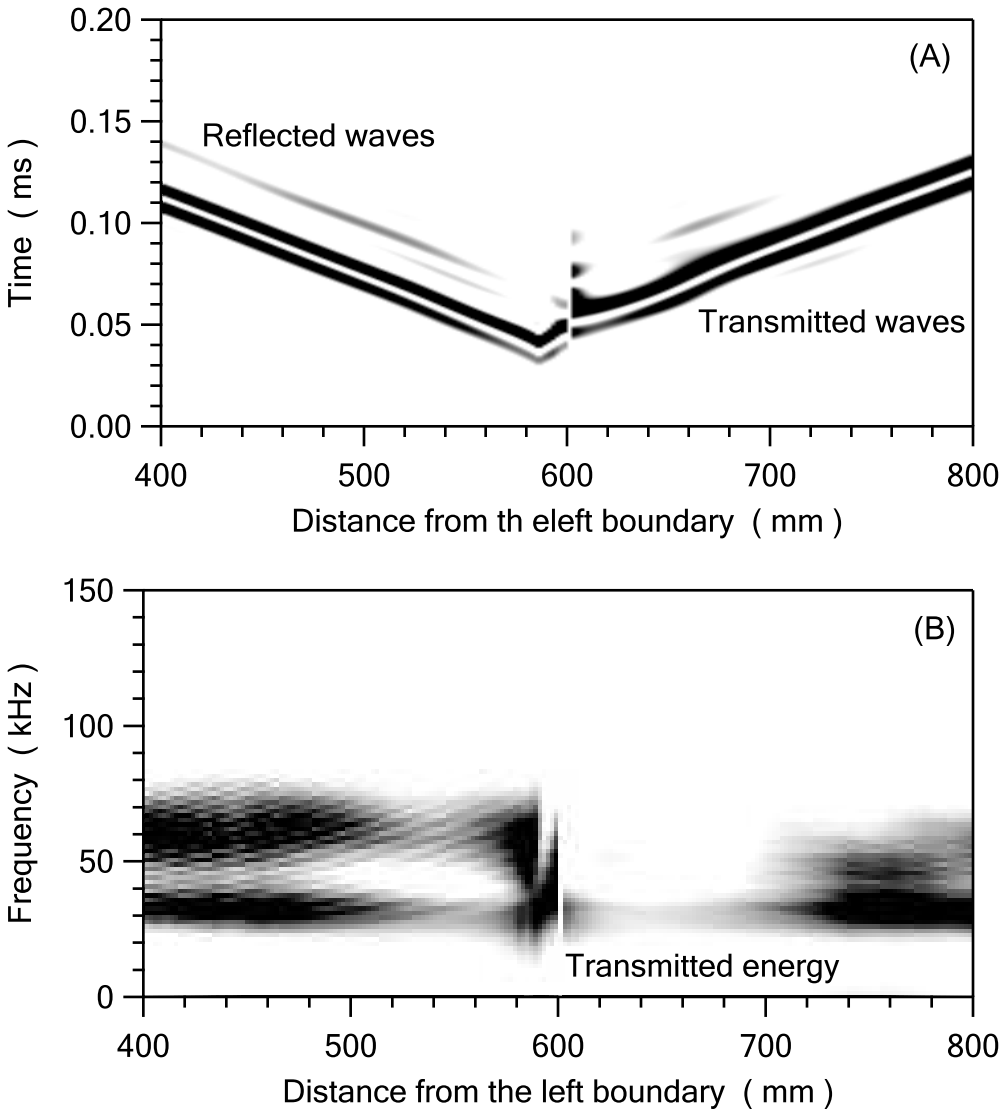

Figure 8.22: Numerical wave propagation with a Morlet source ($f_0 = 50kHz$, $BW = 33.46kHz$) applied at $585mm$ in the presence of a $20mm$ crack. (A) amplitude in time and distance; (B) spectral amplitude in frequency and distance.

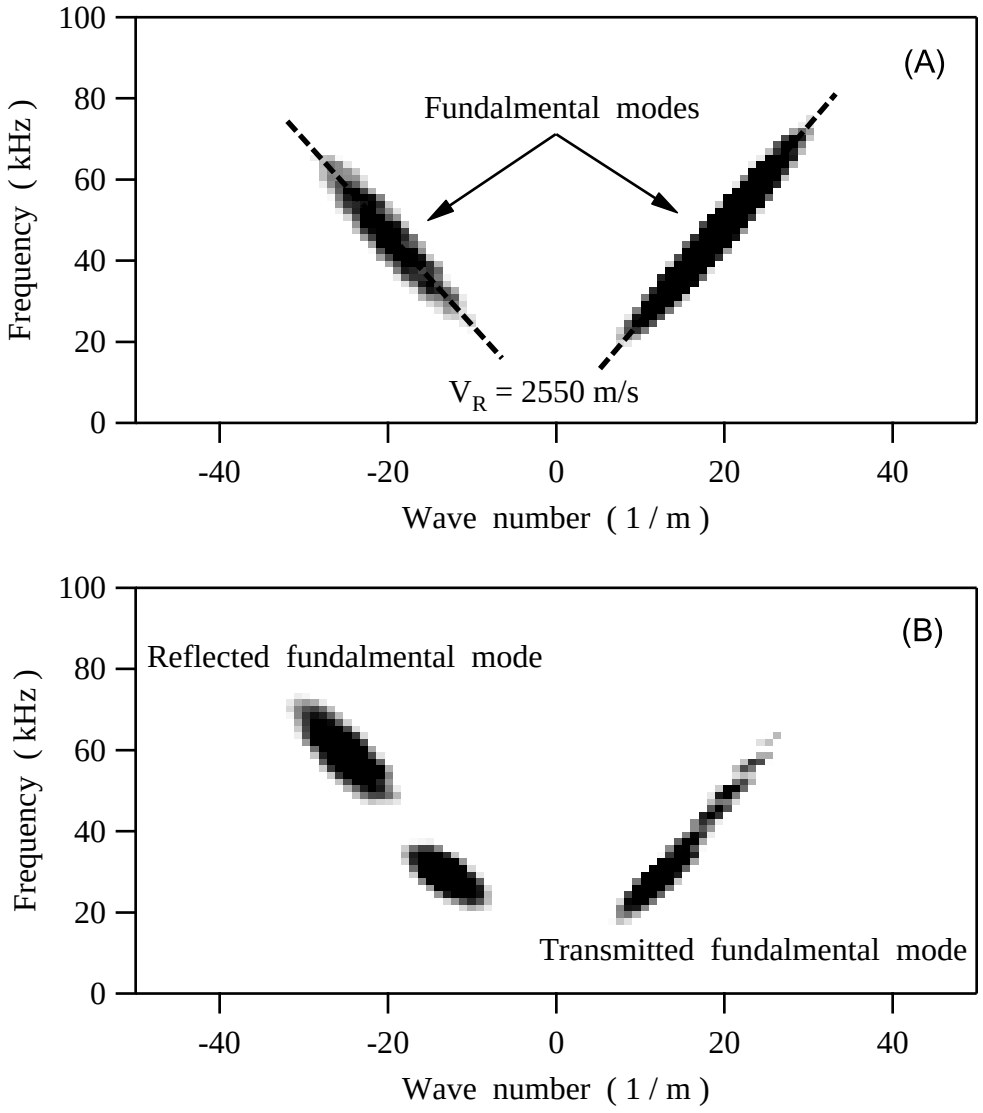

Figure 8.23: Numerical 2D Fourier transform with a Morlet source ($f_0 = 50kHz$, $BW = 33.46kHz$) applied at $585mm$. (A) no crack; (B) a 20mm crack.

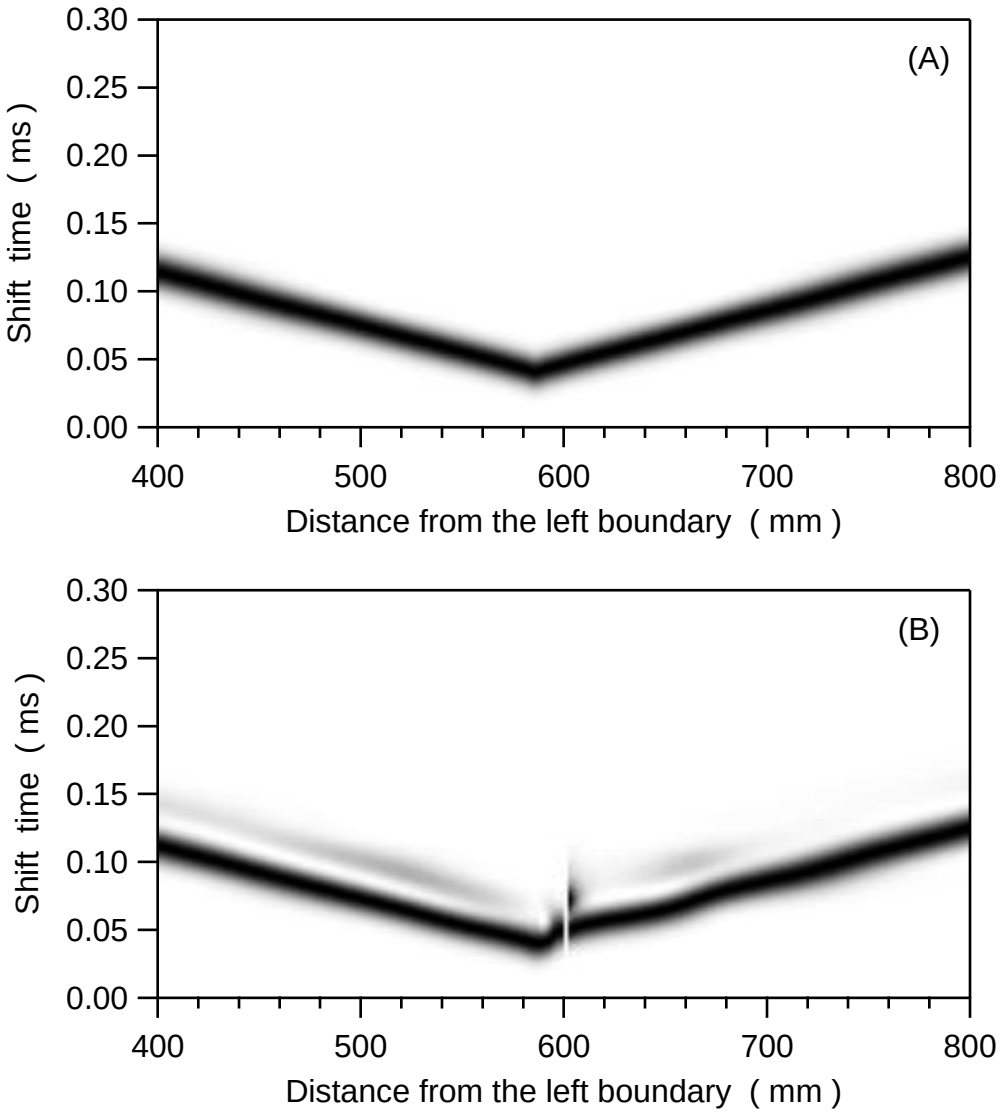

Figure 8.24: Numerical amplitudes from the wavelet transform with a Morlet source ($f_0 = 50kHz$, $BW = 33.46kHz$) applied at $585mm$. (A) no crack; (B) a $20mm$ crack.

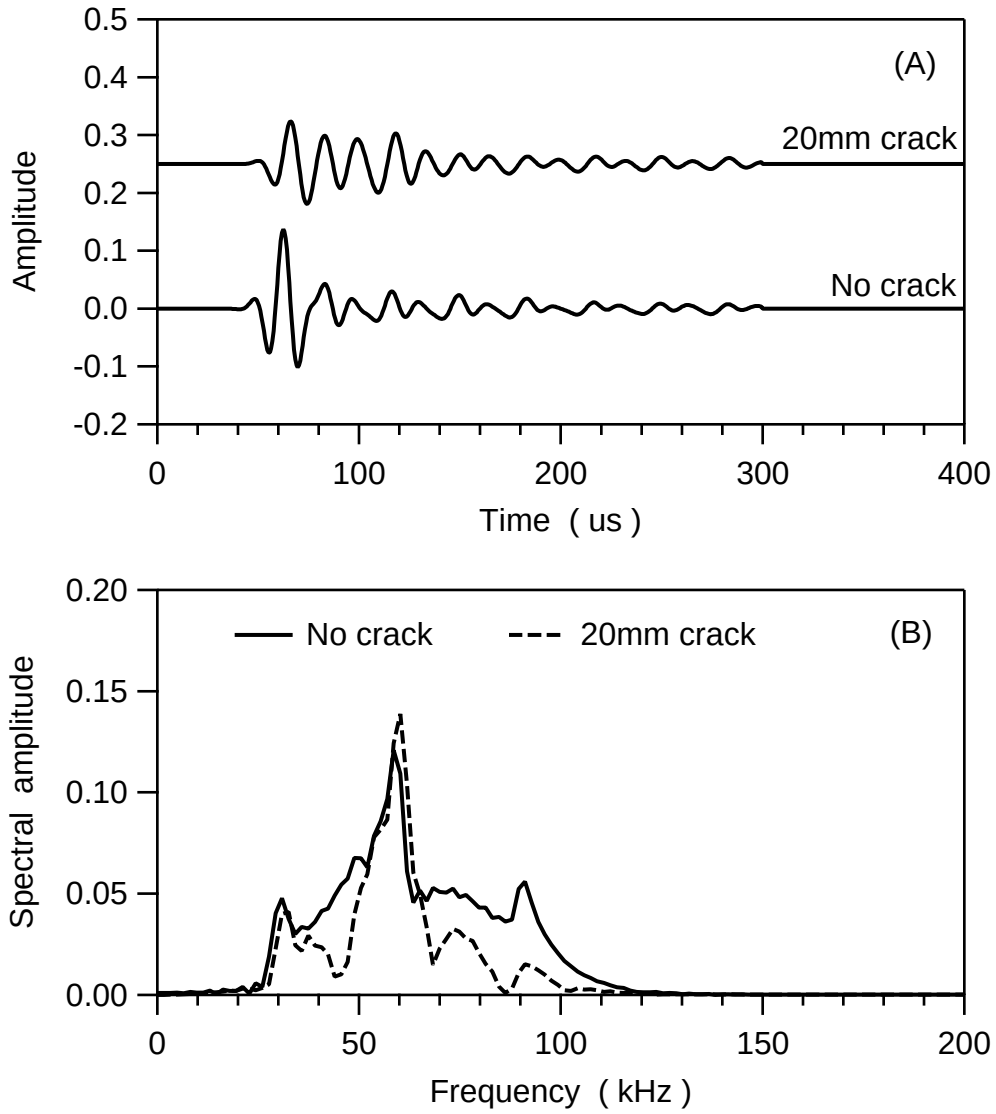

Figure 8.25: Numerical surface responses at 615mm with a Morlet source ($f_0 = 50kHz$, $BW = 33.46kHz$) applied at 585mm for cases of no crack and a 20mm crack. (A) in time; (B) in frequency.

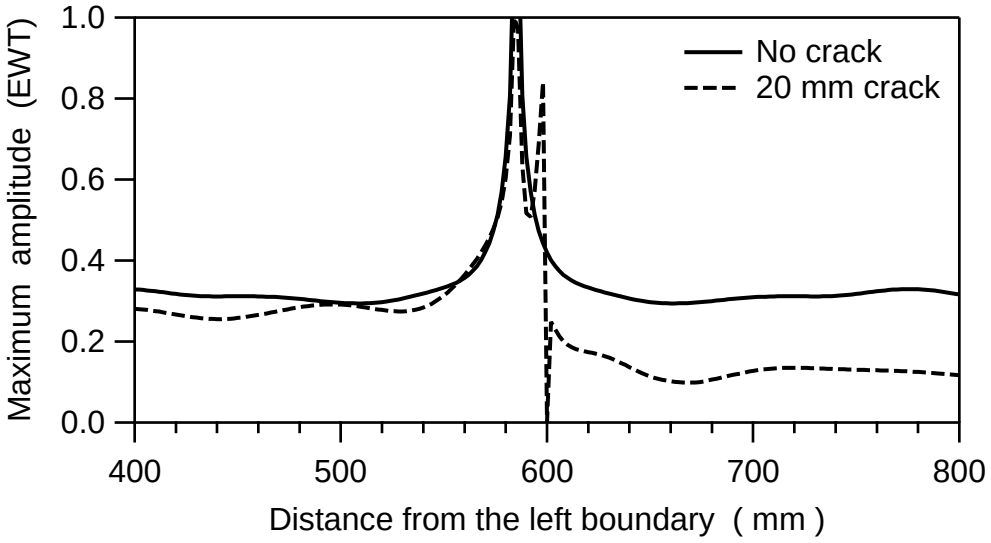

Figure 8.26: Numerical maximum amplitudes from the extended wavelet transforms at different distances. A Morlet source at $585mm$ is used ($f_0 = 50kHz$, $BW = 33.64kHz$).

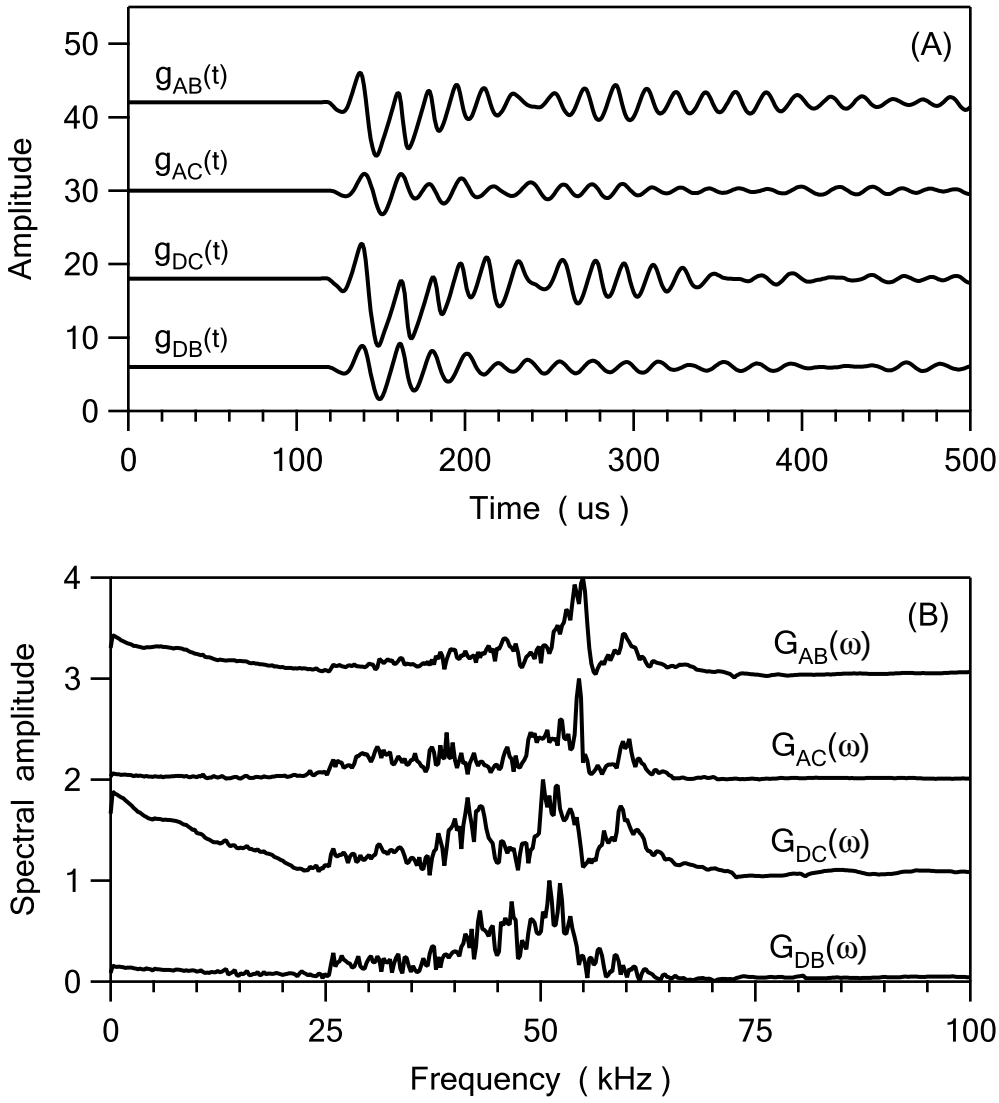

Figure 8.27: Laboratory results from the reinforced concrete plate with a 15*mm* notch. (A) in time; (B) in frequency.

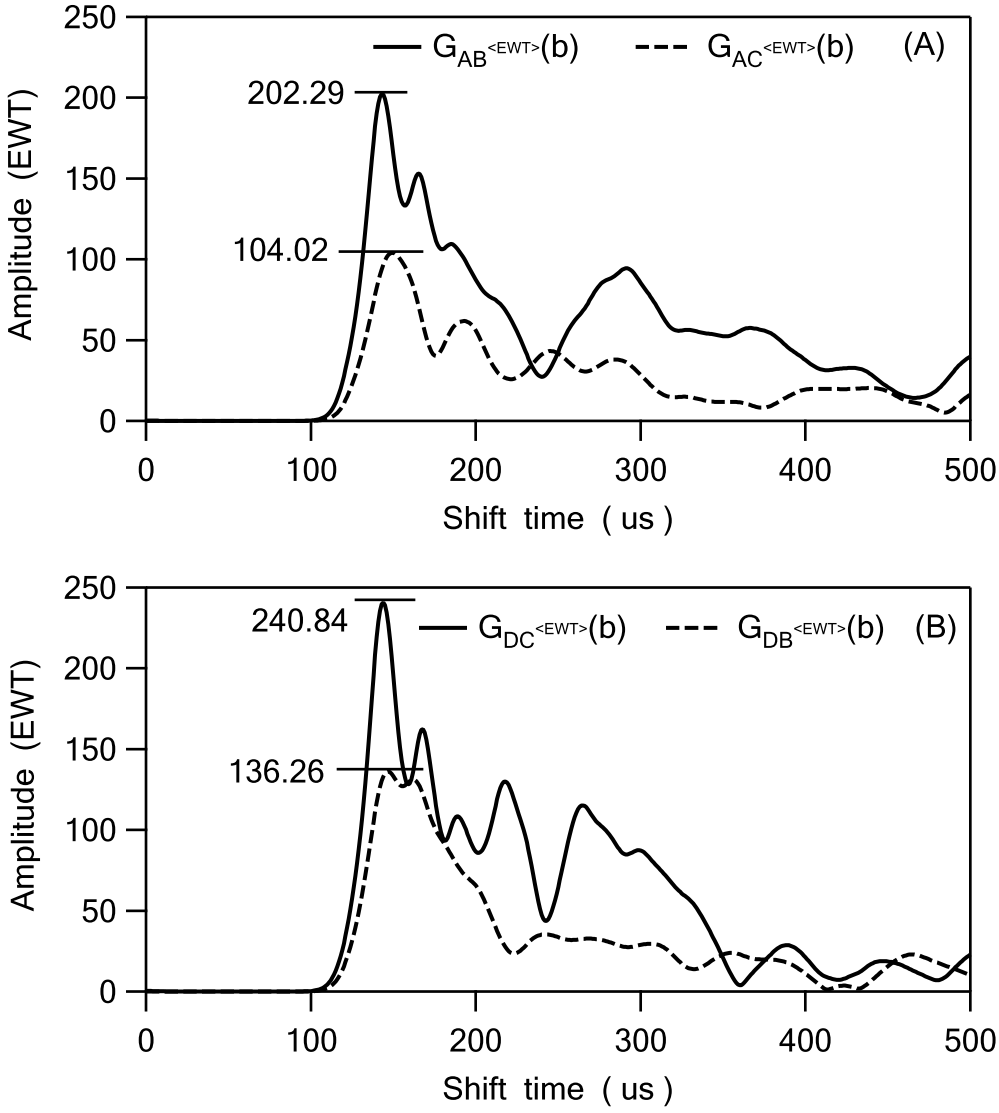

Figure 8.28: Amplitudes from the extended wavelet transform for the laboratory tests on the reinforced concrete plate with a 15*mm* notch.

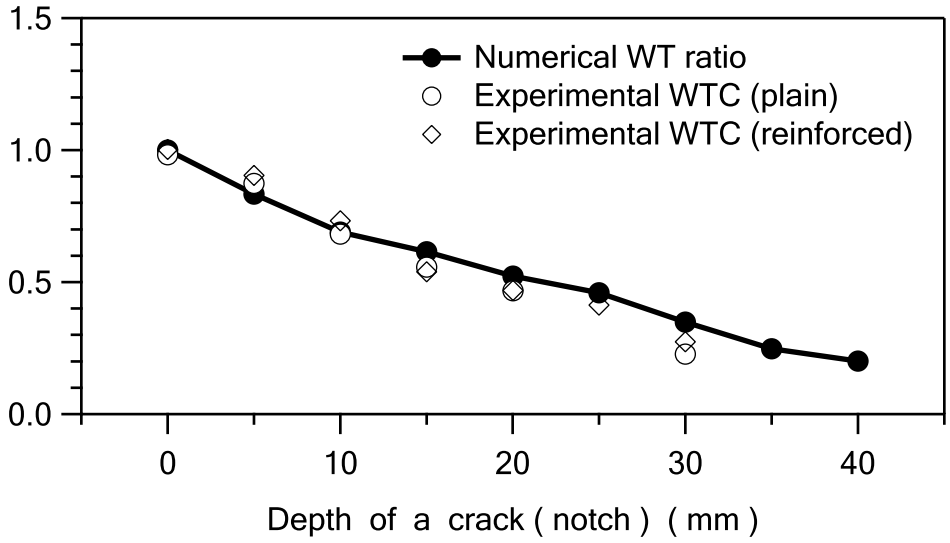

Figure 8.29: Experimental WTC and numerical WT ratio for different crack depths.

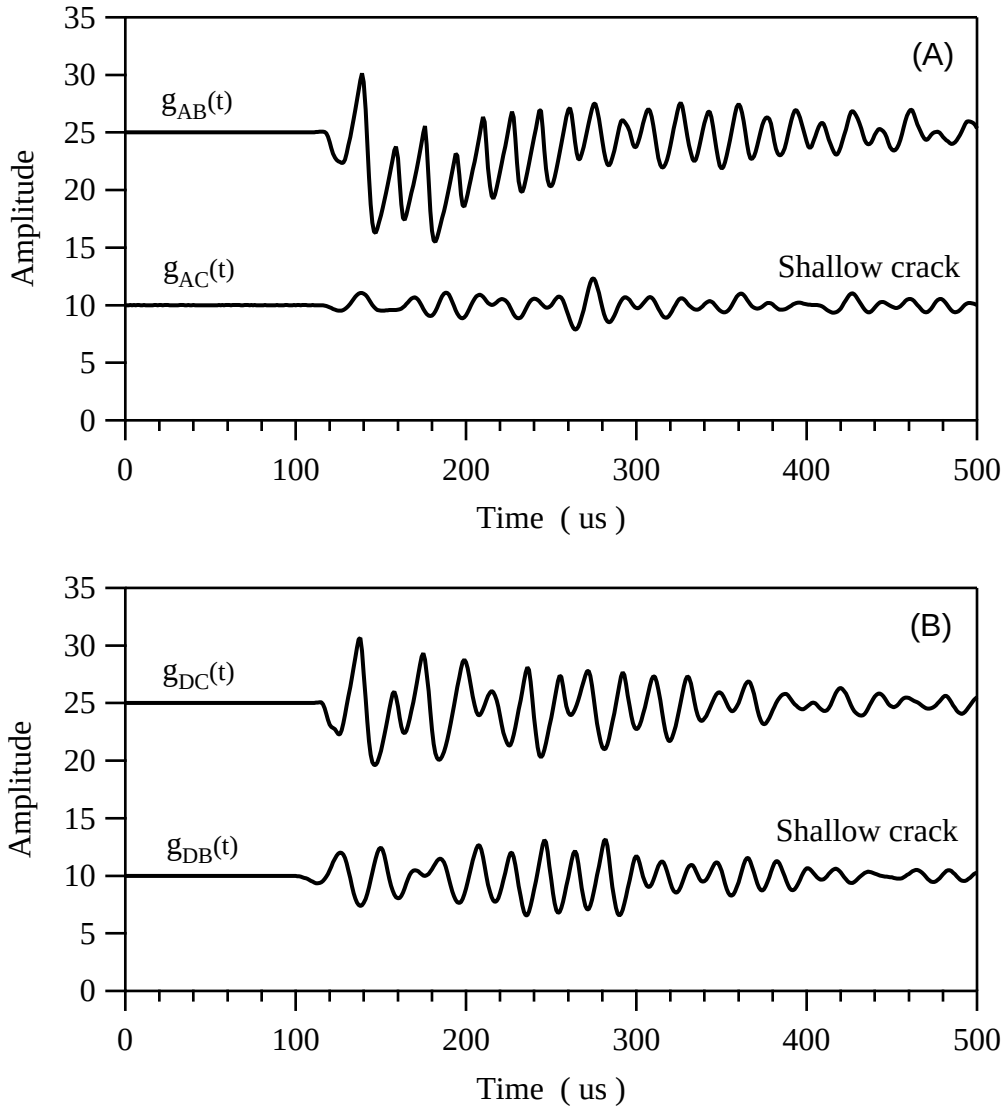

Figure 8.30: Time signals measured in-situ for the shallow crack.

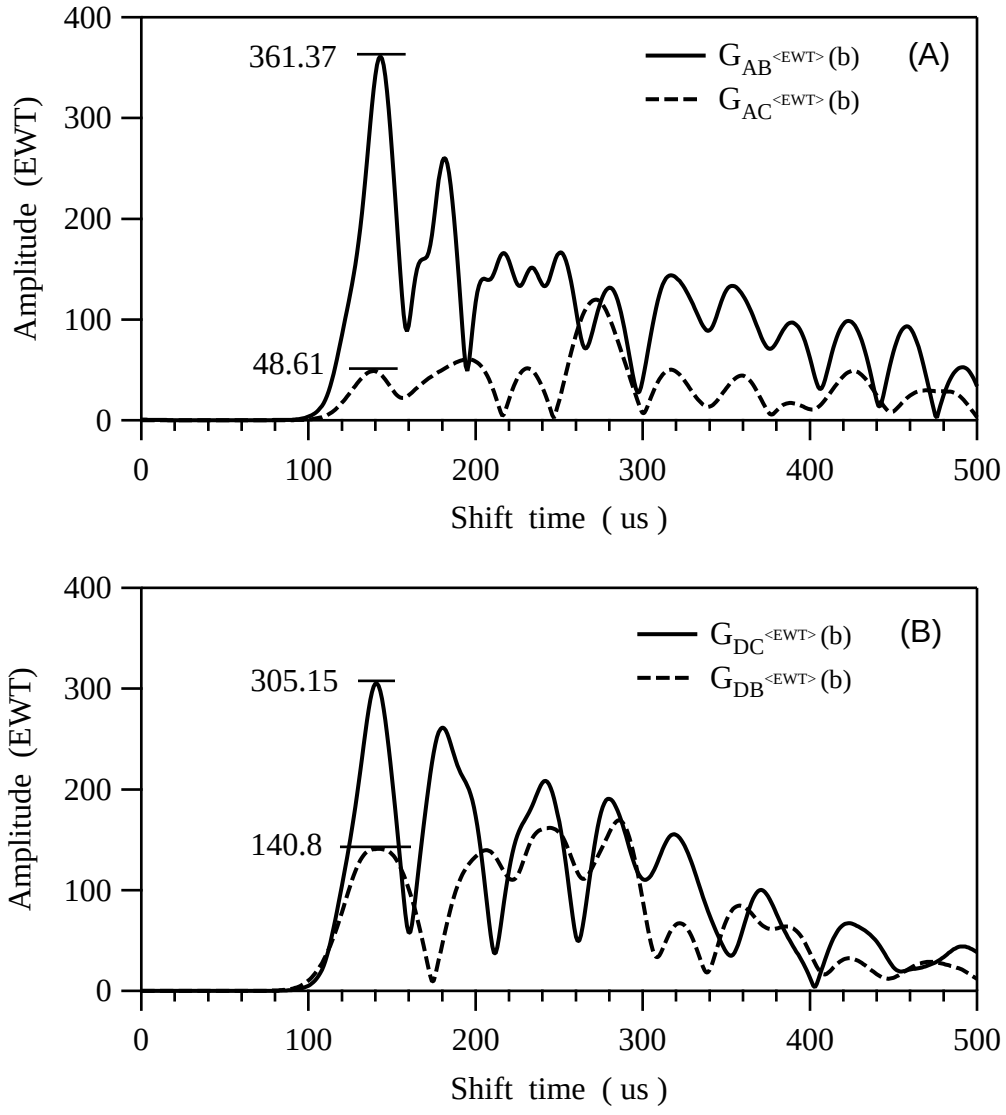

Figure 8.31: Amplitudes from the extended wavelet transforms for the shallow crack in-situ. Calculated WTC = 0.25.

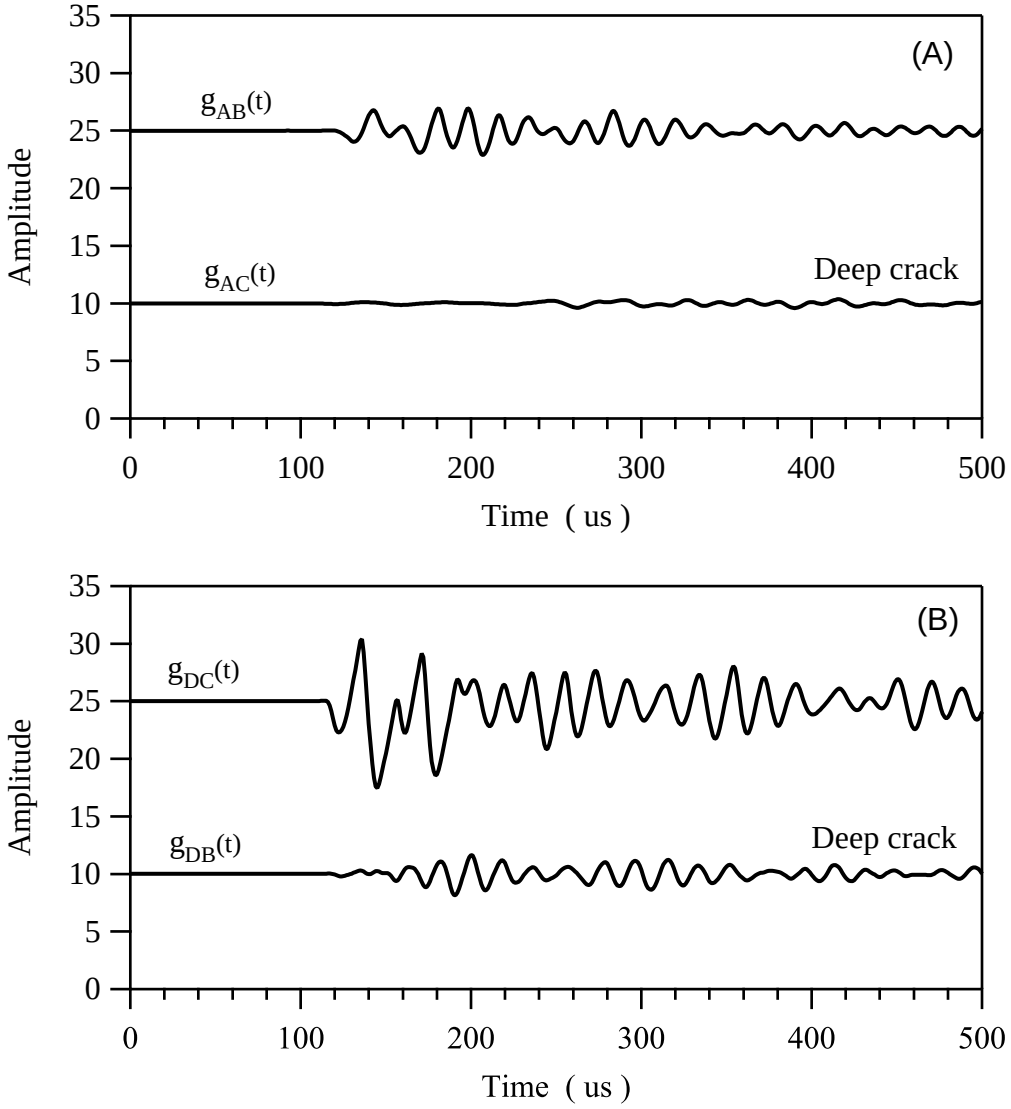

Figure 8.32: Time signals measured in-situ for the deep crack.

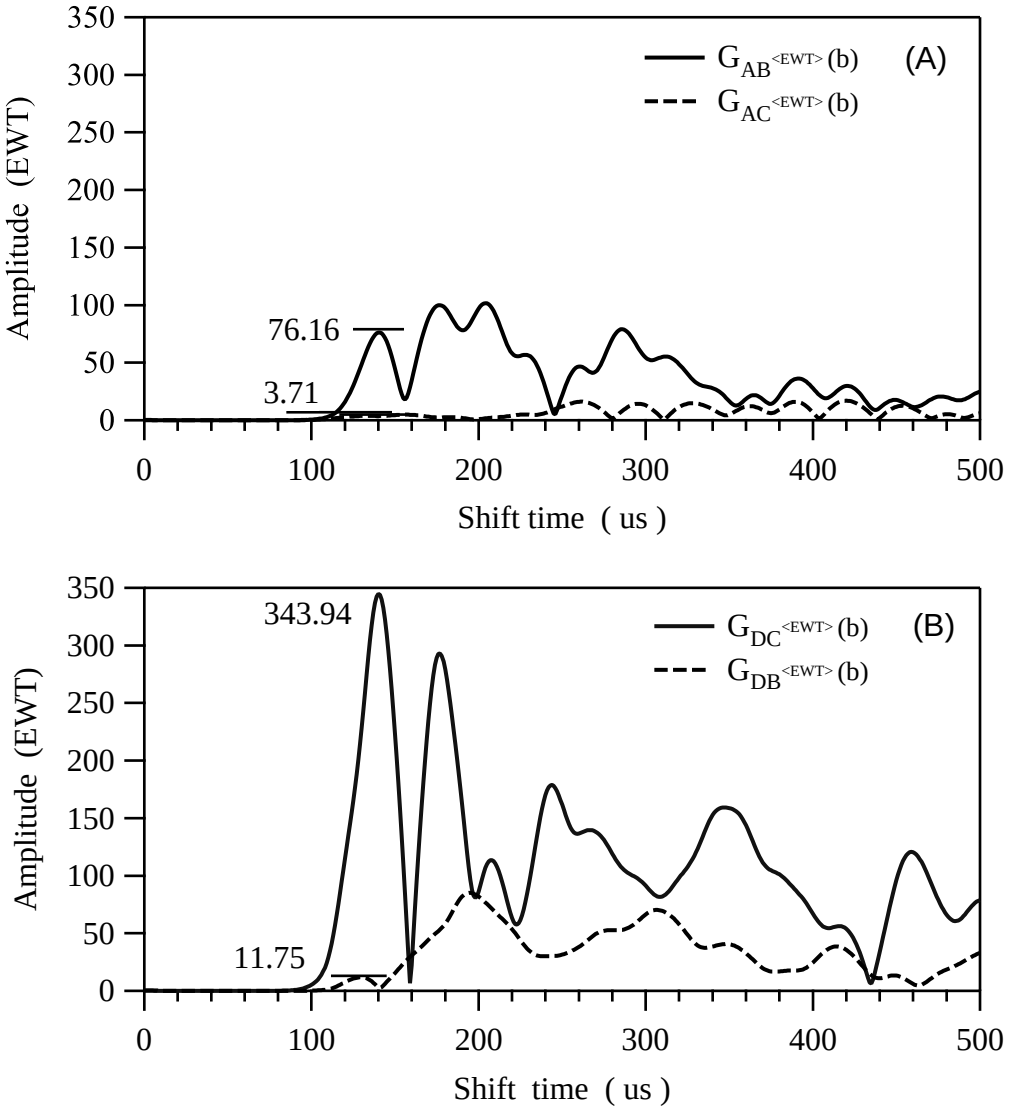

Figure 8.33: Amplitudes from the extended wavelet transforms for the deep crack in-situ. Calculated WTC = 0.041.

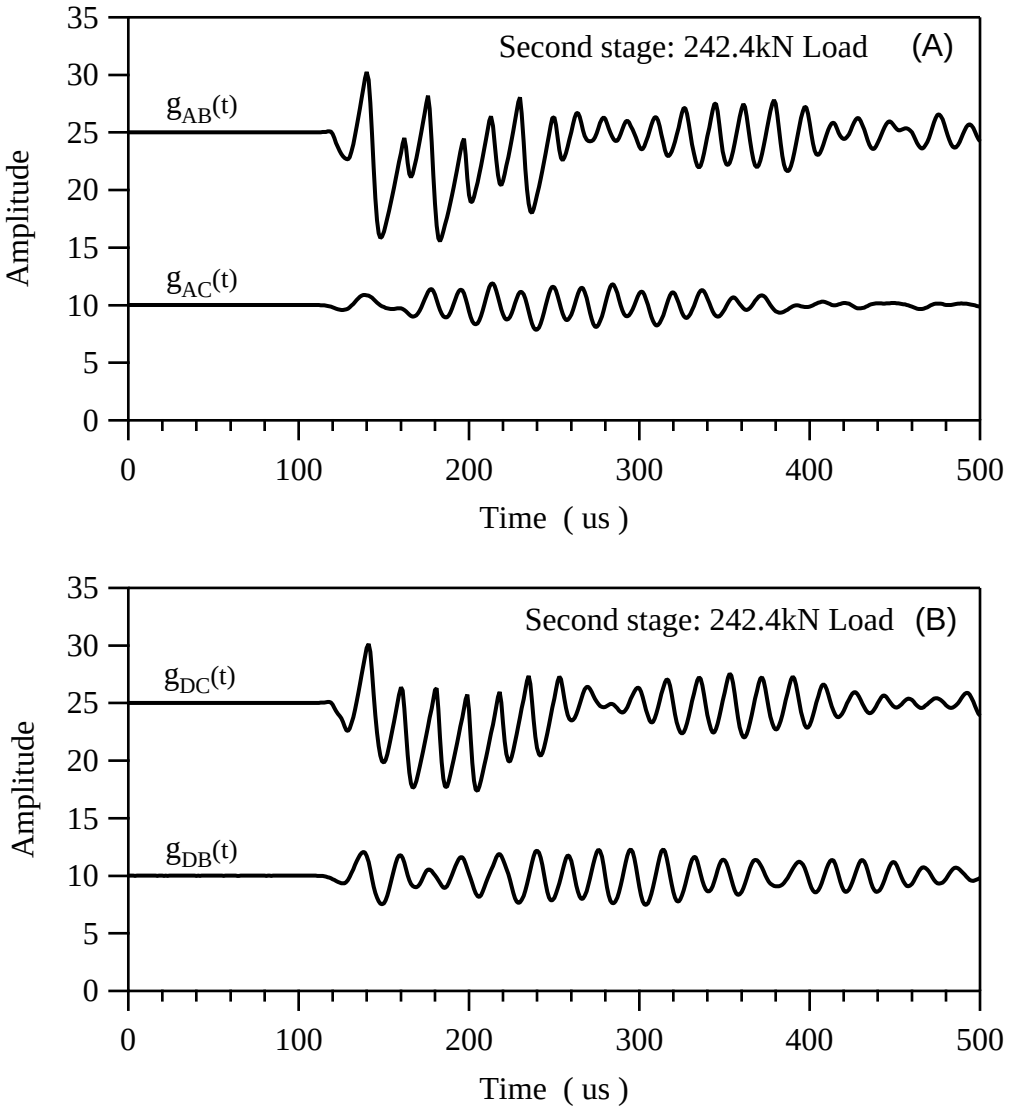

Figure 8.34: Time signals measured in-situ at the second stage, where the load is 242.4*kN*.

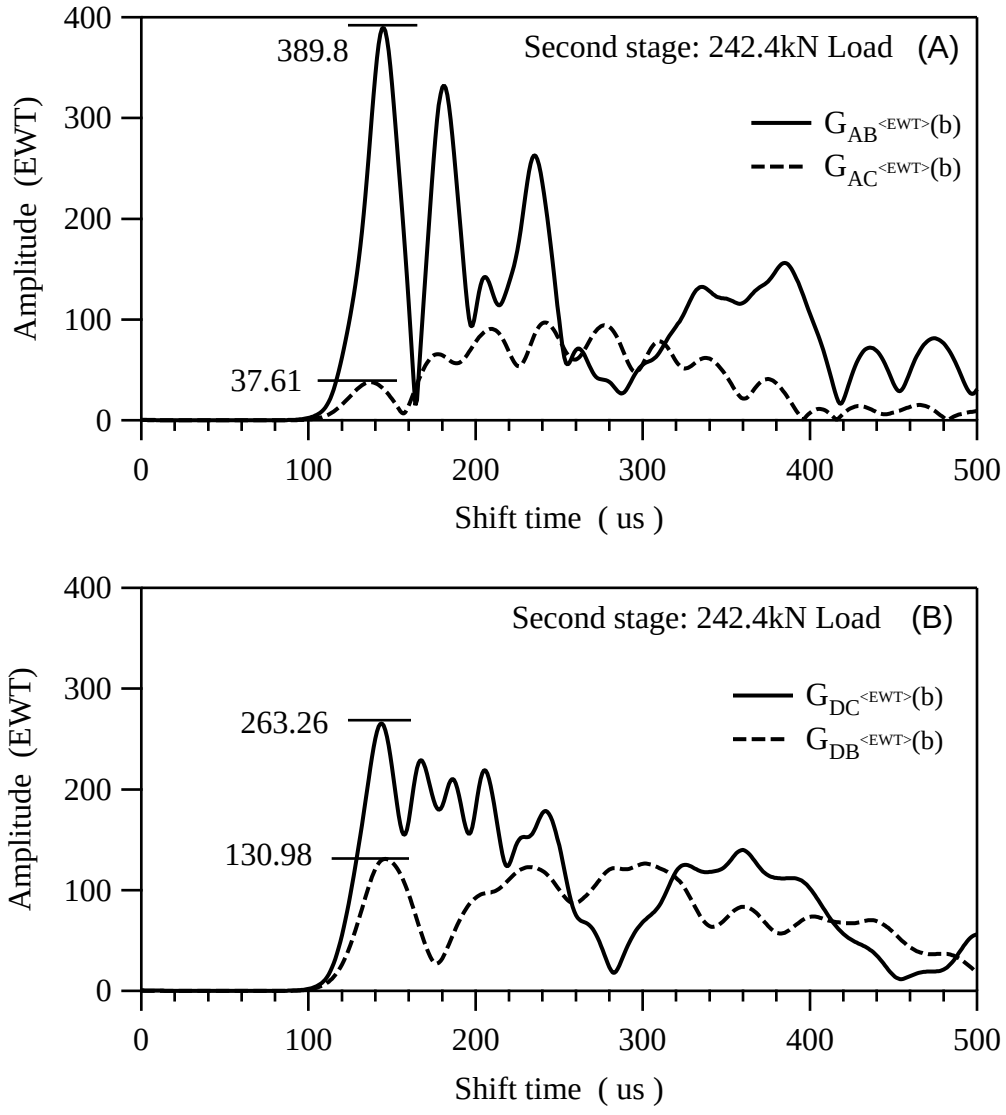

Figure 8.35: Amplitudes from the extended wavelet transforms for the second stage; the load = 242.4*kN*.

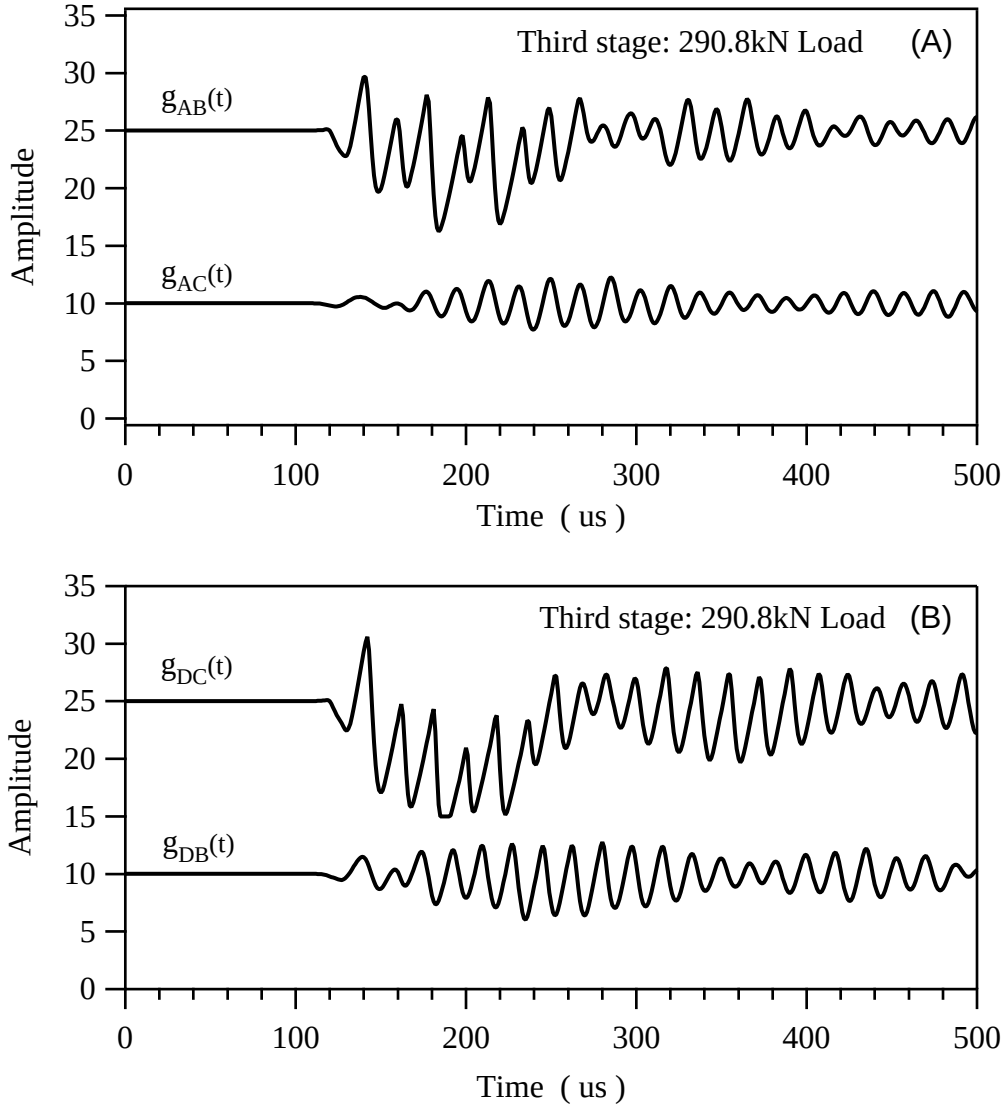

Figure 8.36: Time signals measured in-situ at the third stage; the load = 290.8*kN*.

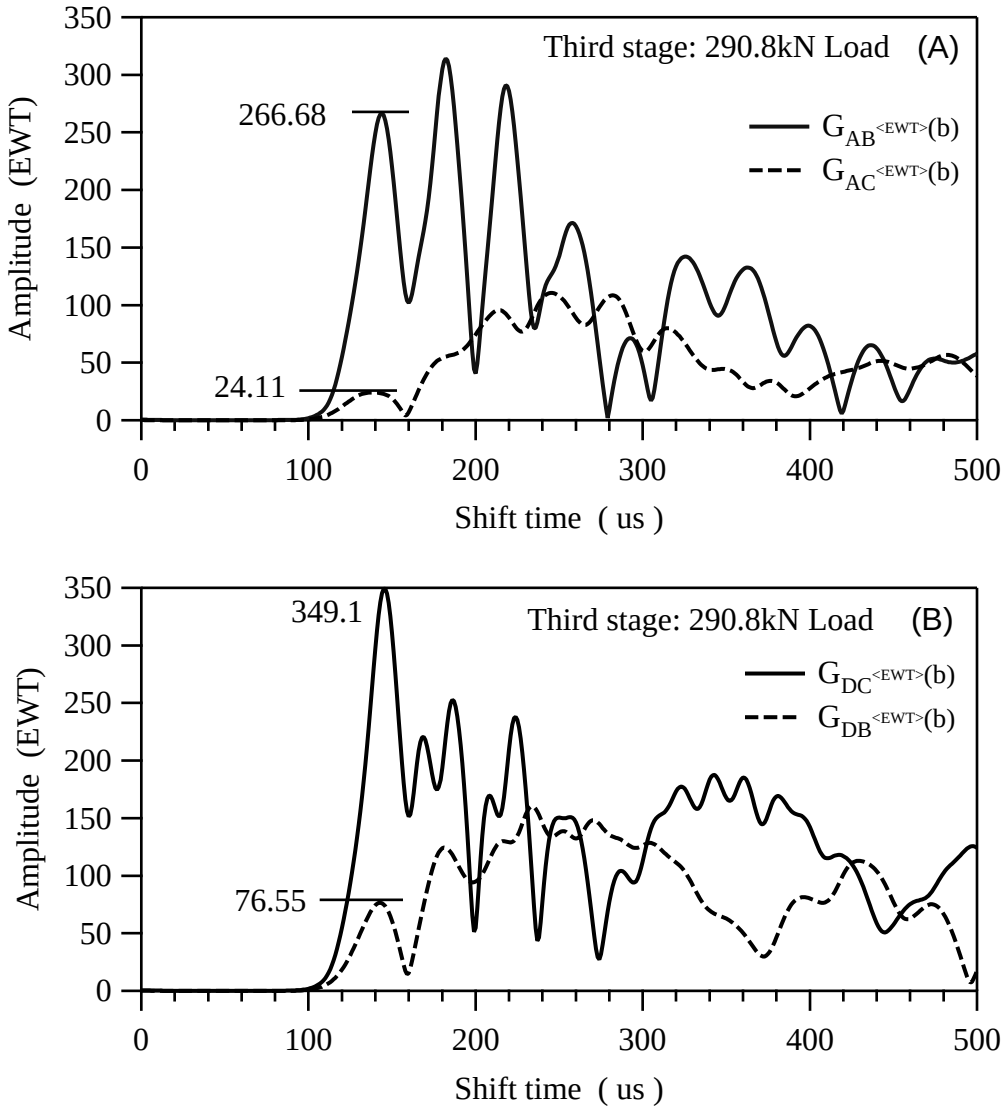

Figure 8.37: Amplitudes from the extended wavelet transform for the third stage; the load = 290.8*kN*.

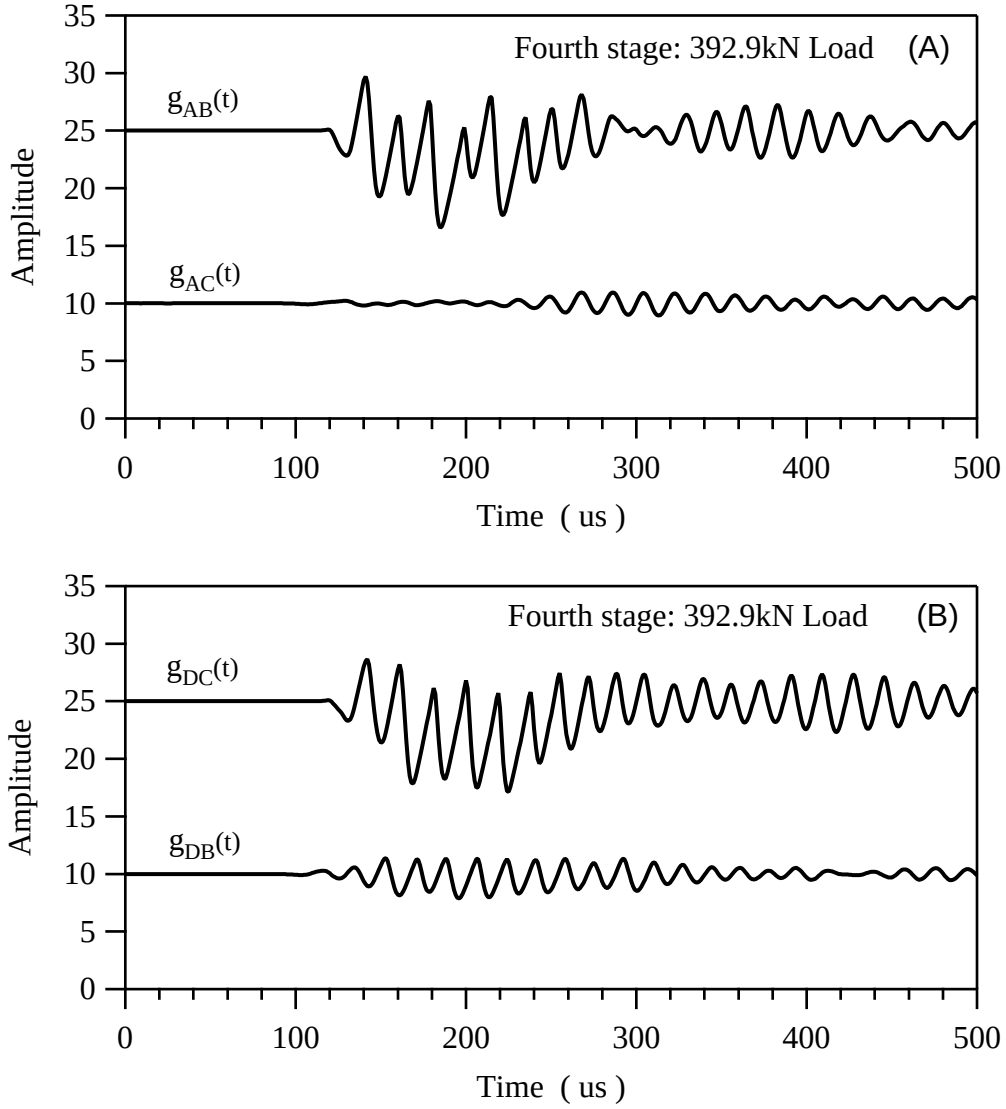

Figure 8.38: Time signals measured in-situ at the fourth stage; the load = 392.9*kN*.

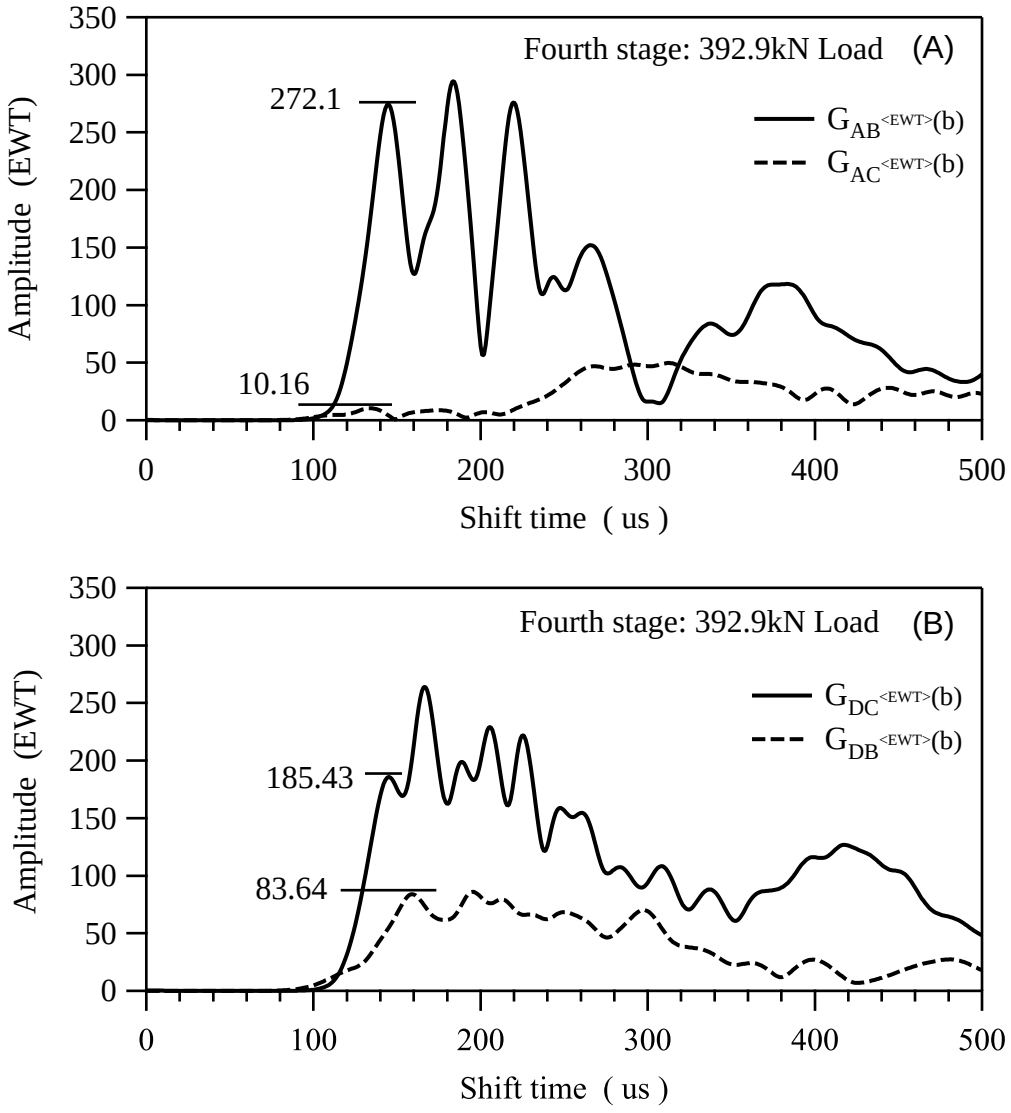

Figure 8.39: Amplitudes from the extended wavelet transform for the fourth stage; the load = 392.9*kN*.

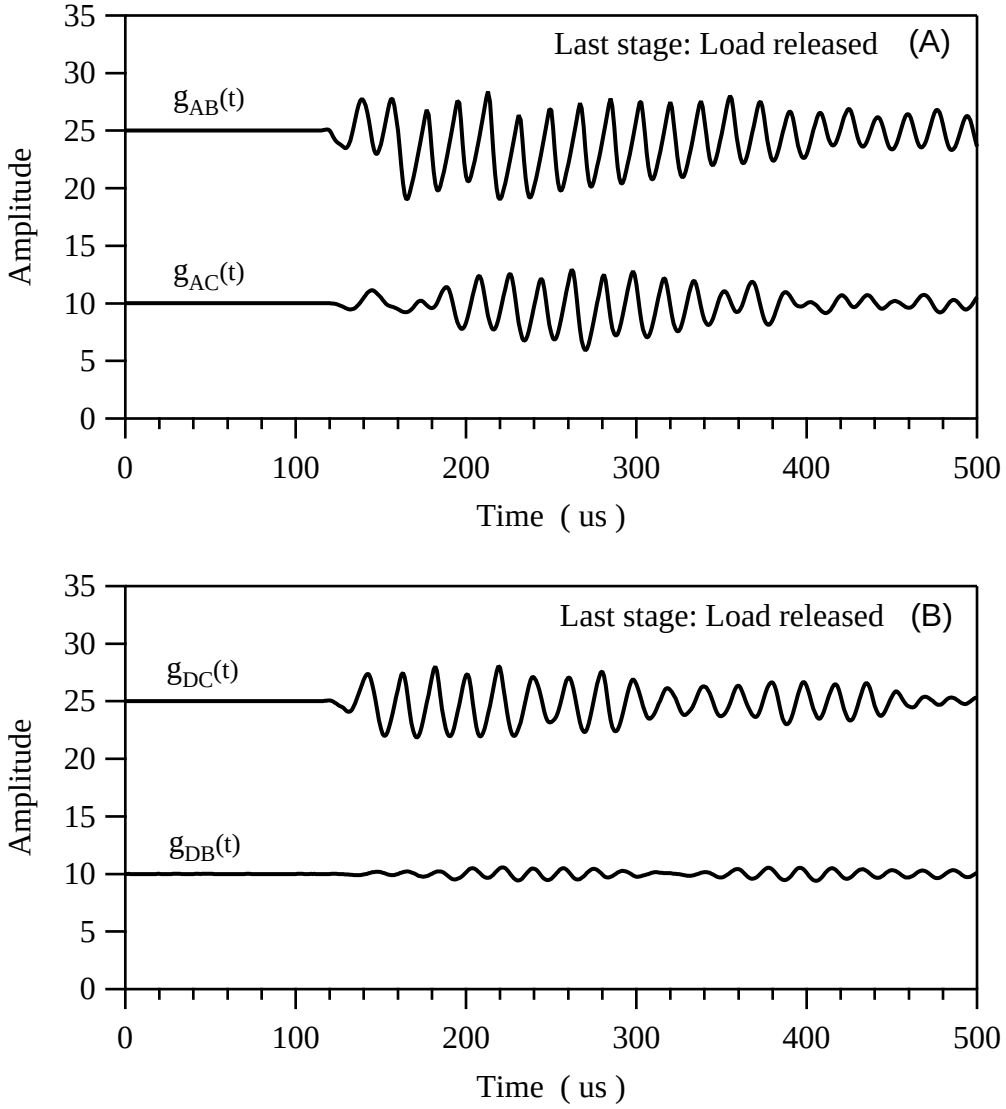

Figure 8.40: Time signals measured in-situ at the last stage; the load is released.

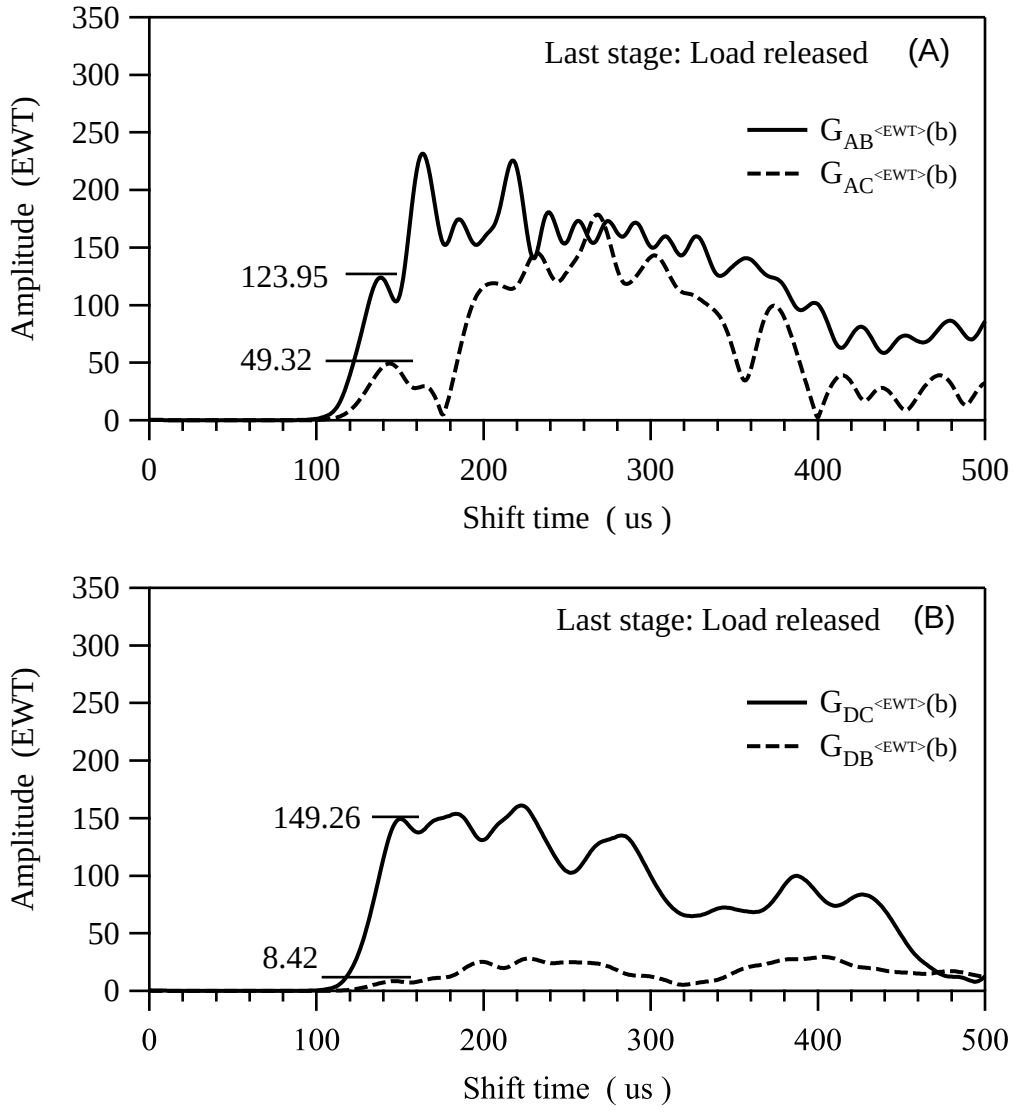

Figure 8.41: Amplitudes from the extended wavelet transform for the last stage; the load is released.

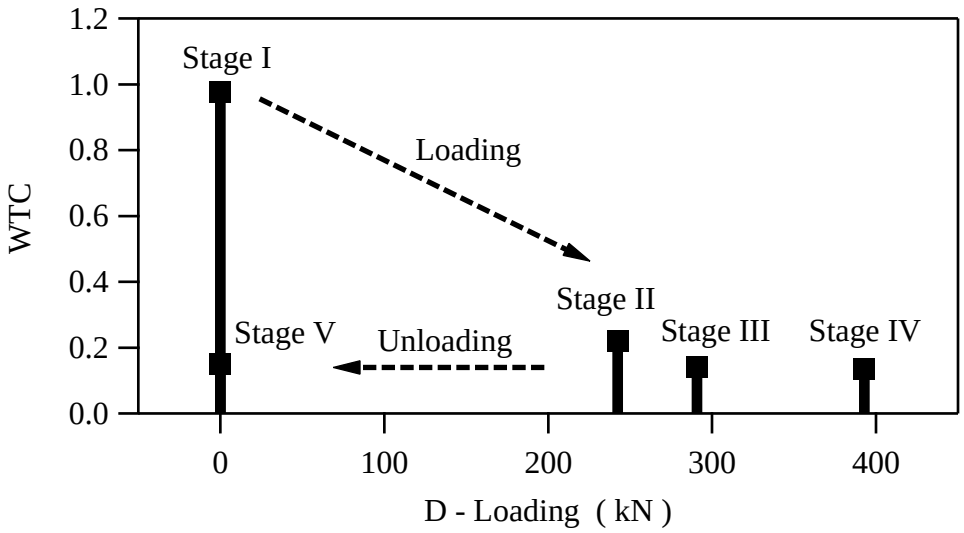

Figure 8.42: Experimental WTC at different D-loading stages.

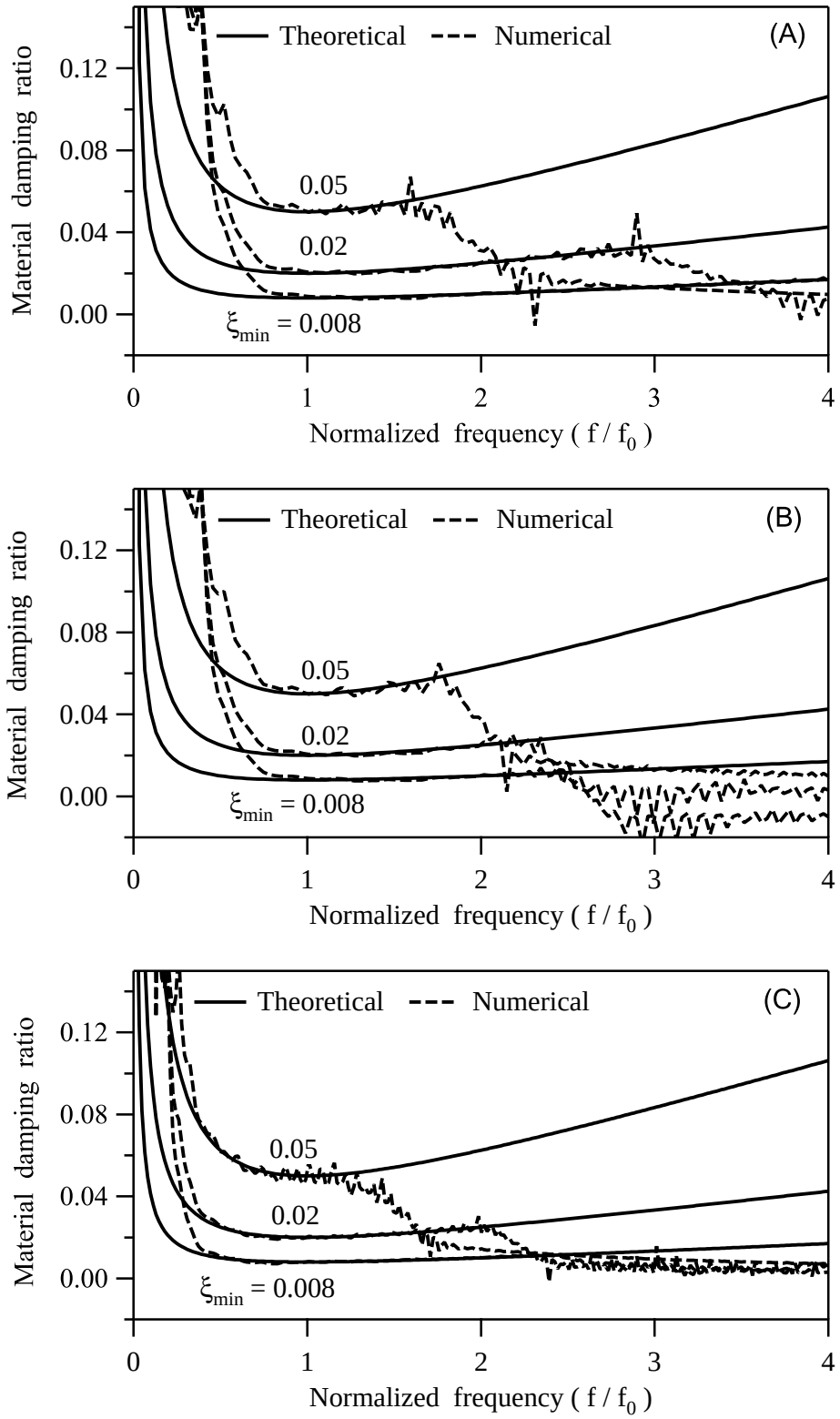

Figure 8.43: Material damping ratio from the Fourier transform vs. normalized frequency. (A) Lamb source ($f_0 = 50kHz$); (B) Morlet source ($f_0 = 50kHz$); (C) Morlet source ($f_0 = 100kHz$).

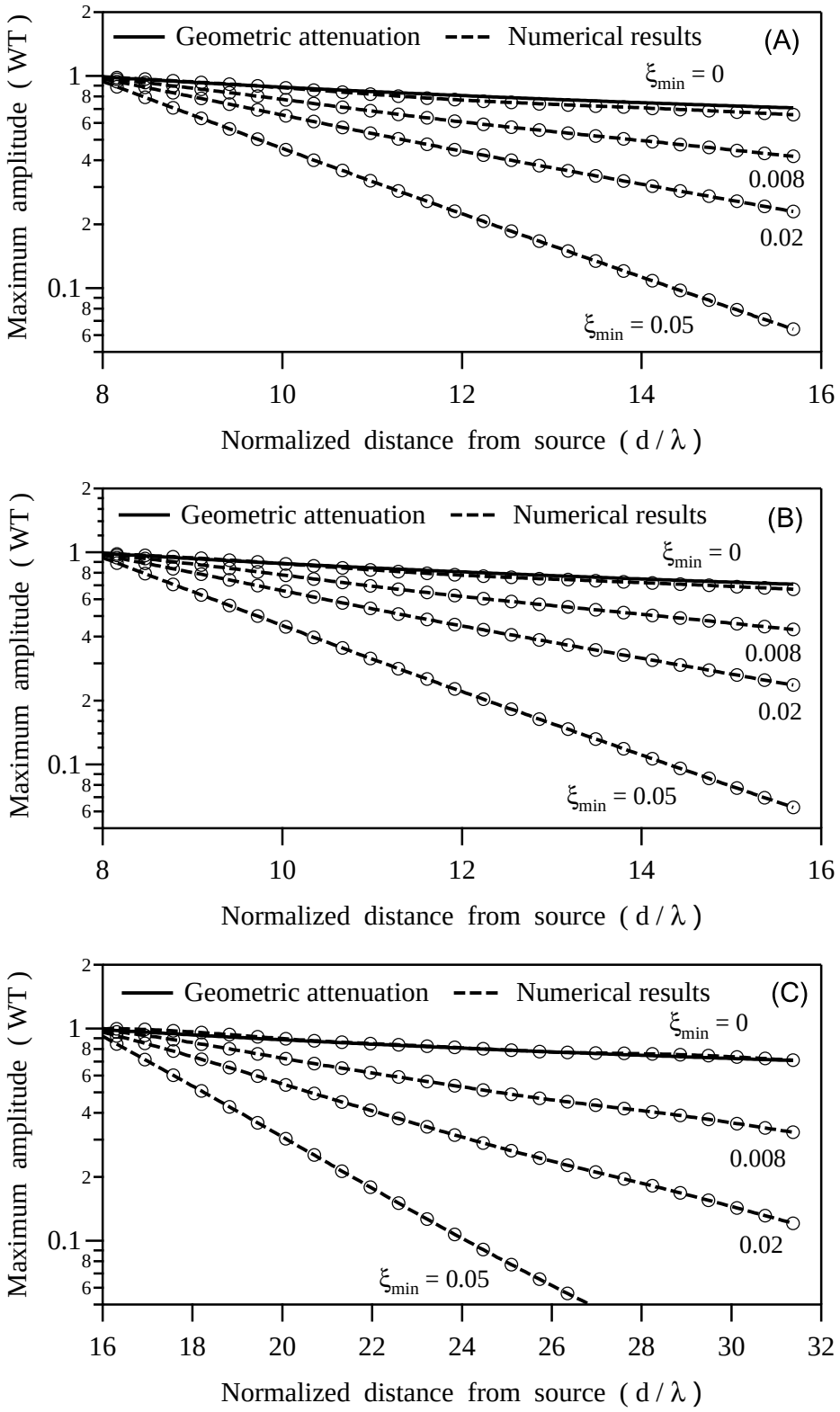

Figure 8.44: Logarithm of maximum amplitude from the wavelet transform vs. normalized distances. (A) Lamb source ($f_0 = 50kHz$, $\lambda = 51mm$); (B) Morlet source ($f_0 = 50kHz$, $\lambda = 51mm$); (C) Morlet source ($f_0 = 100kHz$, $\lambda = 26mm$).

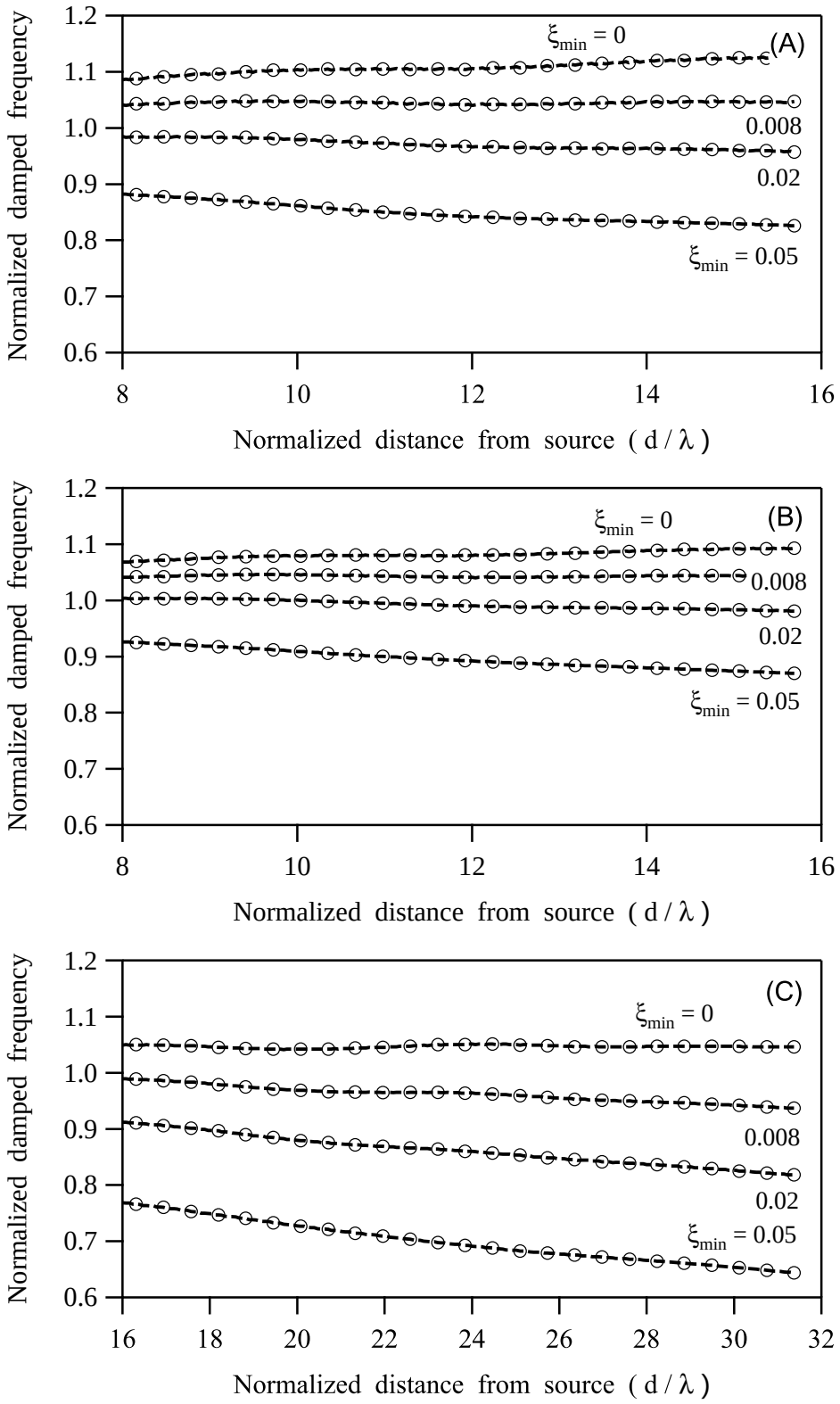

Figure 8.45: Normalized damped frequency (f/f_0) from the wavelet transform vs. normalized distances. (A) Lamb source ($f_0 = 50kHz$, $\lambda = 51mm$); (B) Morlet source ($f_0 = 50kHz$, $\lambda = 51mm$); (C) Morlet source ($f_0 = 100kHz$, $\lambda = 26mm$).

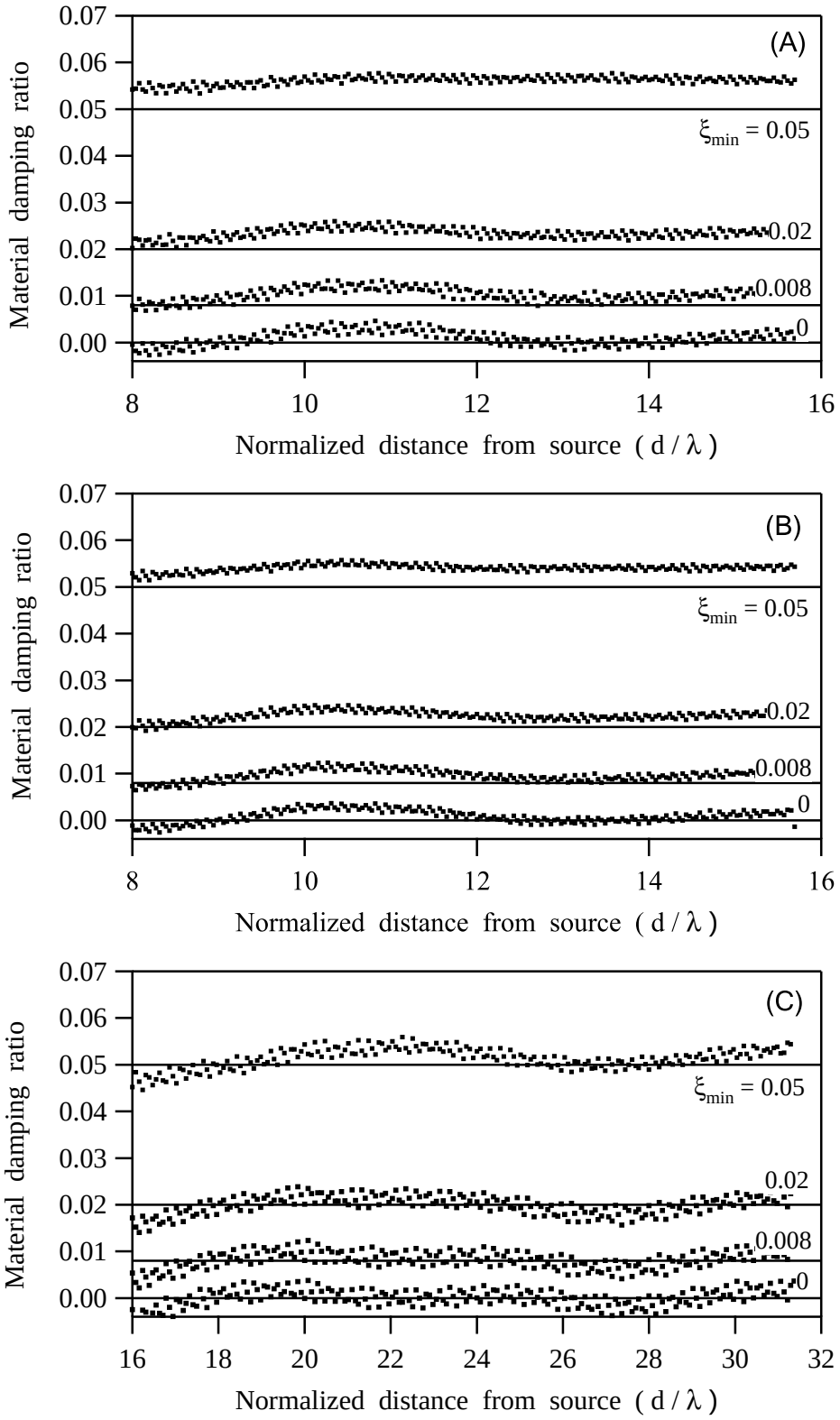

Figure 8.46: Material damping ratio from the wavelet transform vs. normalized distance. (A) Lamb source ($f_0 = 50kHz$, $\lambda = 51mm$); (B) Morlet source ($f_0 = 50kHz$, $\lambda = 51mm$); (C) Morlet source ($f_0 = 100kHz$, $\lambda = 26mm$).

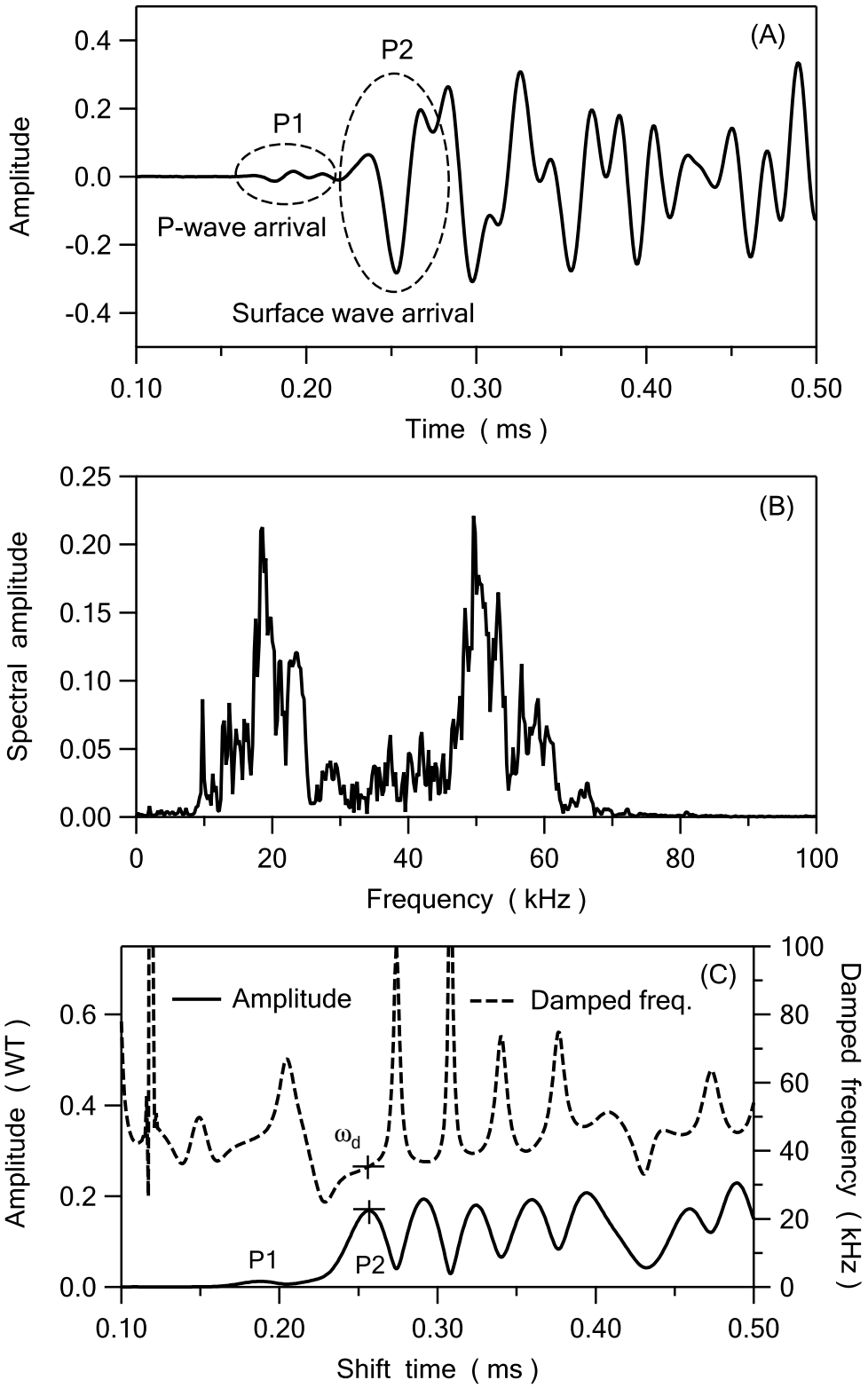

Figure 8.47: Laboratory results at the first receiver location (220*mm* from the source). (A) time signal; (B) spectral amplitude; (C) amplitude and damped frequency from the wavelet transform, $\omega_d = 35.56kHz$ at the first surface wave arrival.

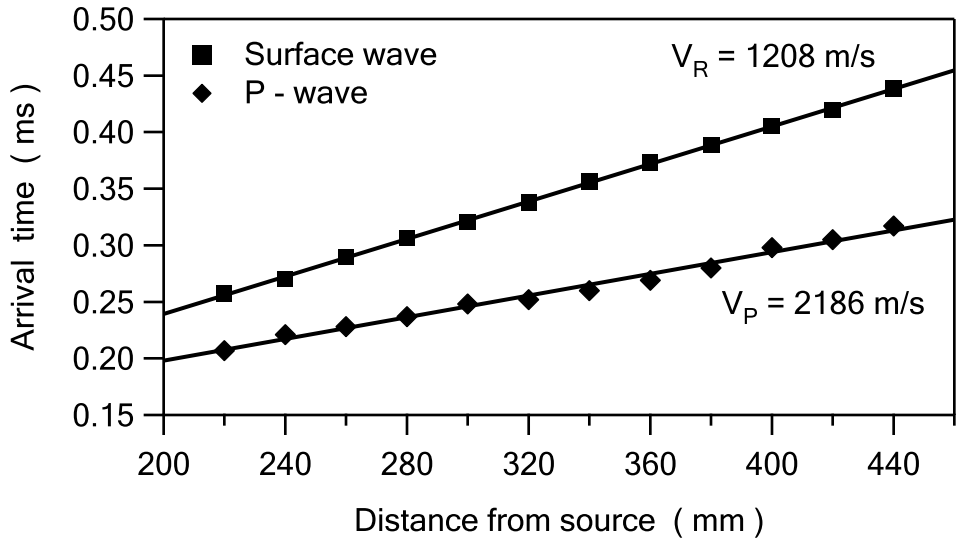

Figure 8.48: The arrival times of the first P-wave and the first surface wave at different receiver locations.

.

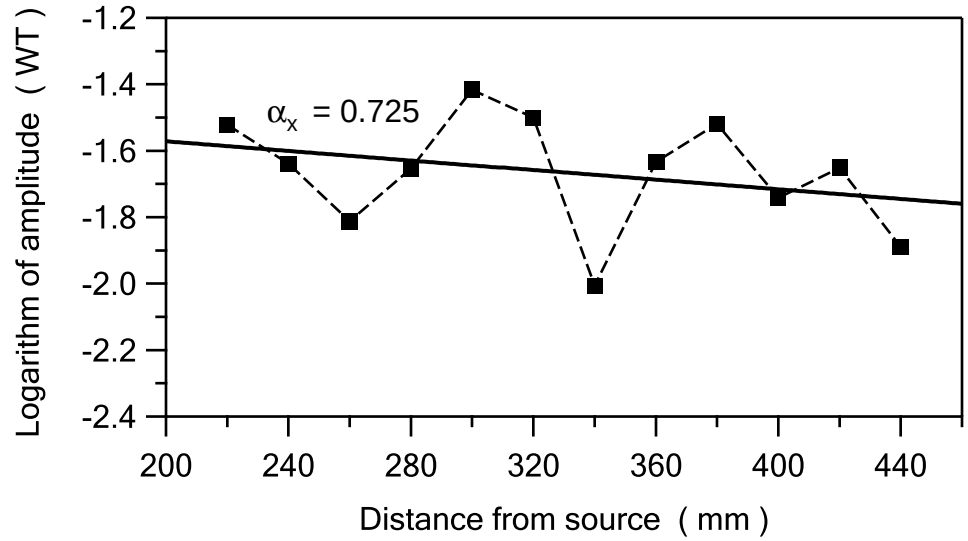

Figure 8.49: Logarithm of the maximum amplitudes from the wavelet transform vs. receiver location.

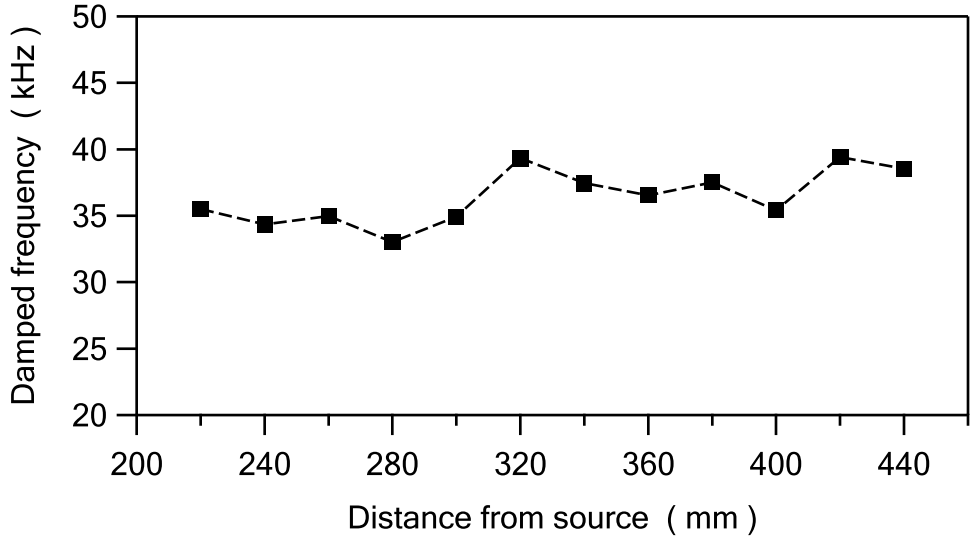

Figure 8.50: Damped frequency from the wavelet transform vs. receiver location.

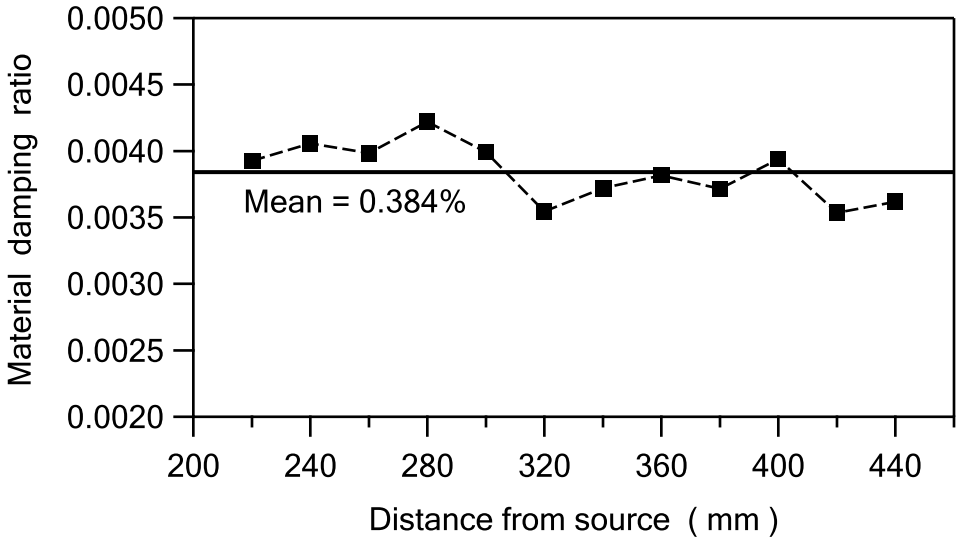

Figure 8.51: Laboratory measurement of material damping ratio on a sand box

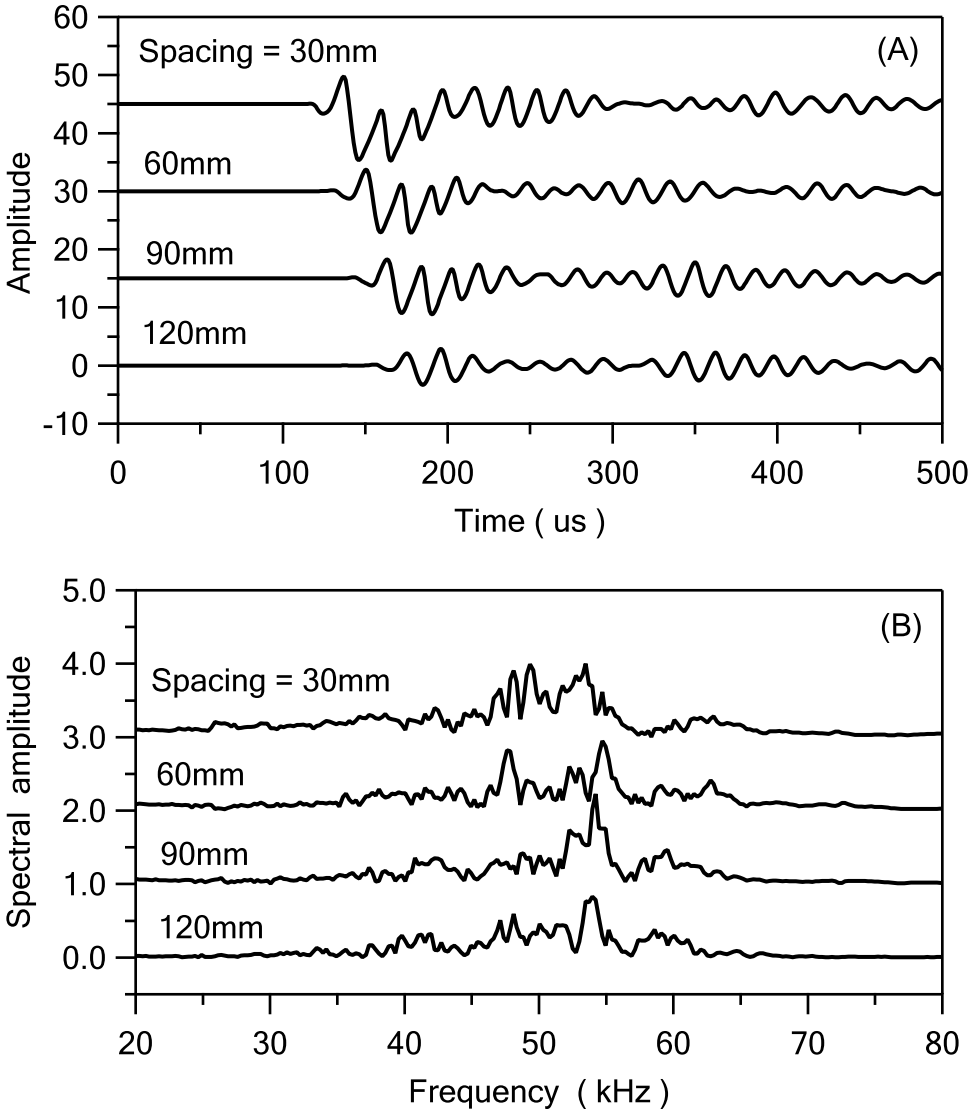

Figure 8.52: Time signals and the spectral amplitudes for different receiver locations.

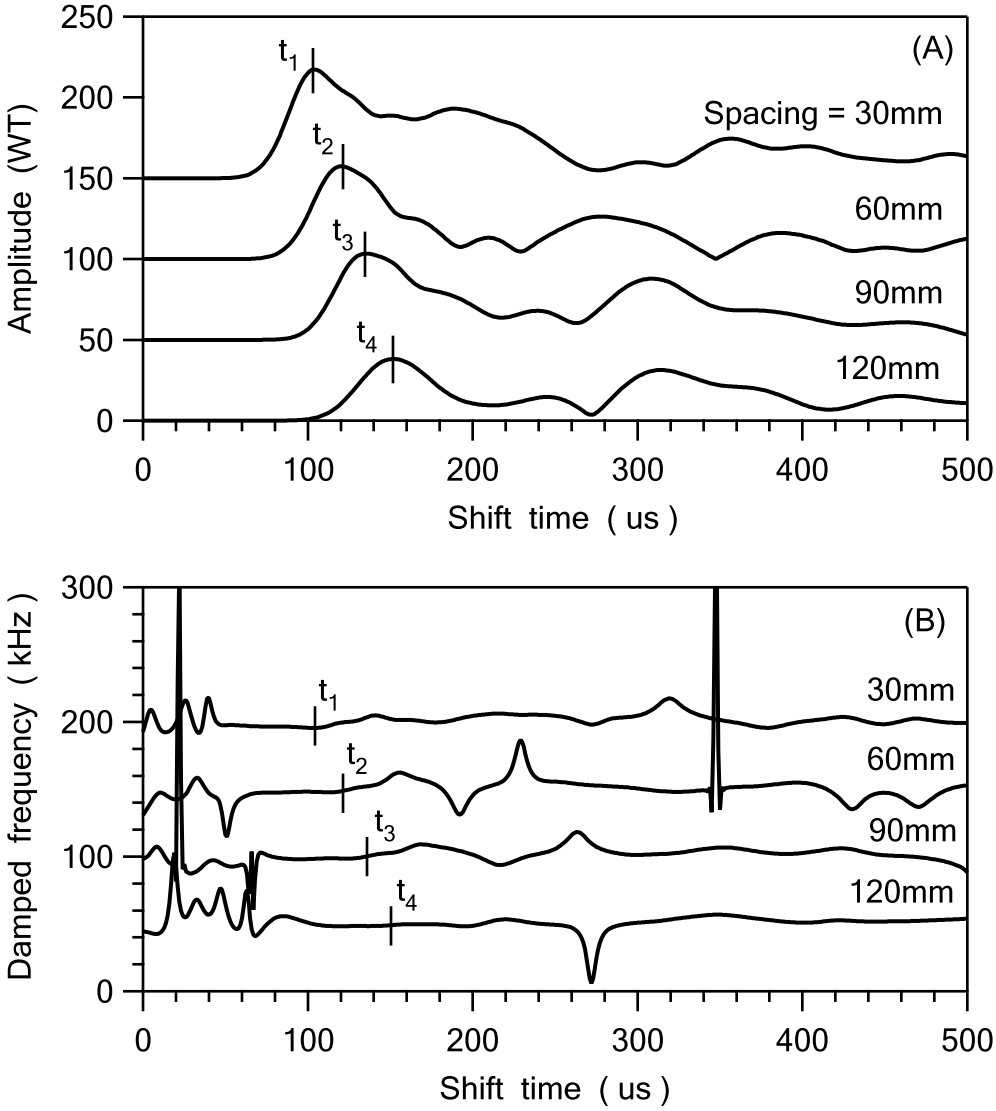

Figure 8.53: Laboratory results of the wavelet transform for different receiver locations. (A) amplitude vs. shift time; (A) damped frequency vs. shift time. $t_1 = 104\mu s$, $t_2 = 120\mu s$, $t_3 = 135\mu s$, and $t_4 = 152\mu s$.

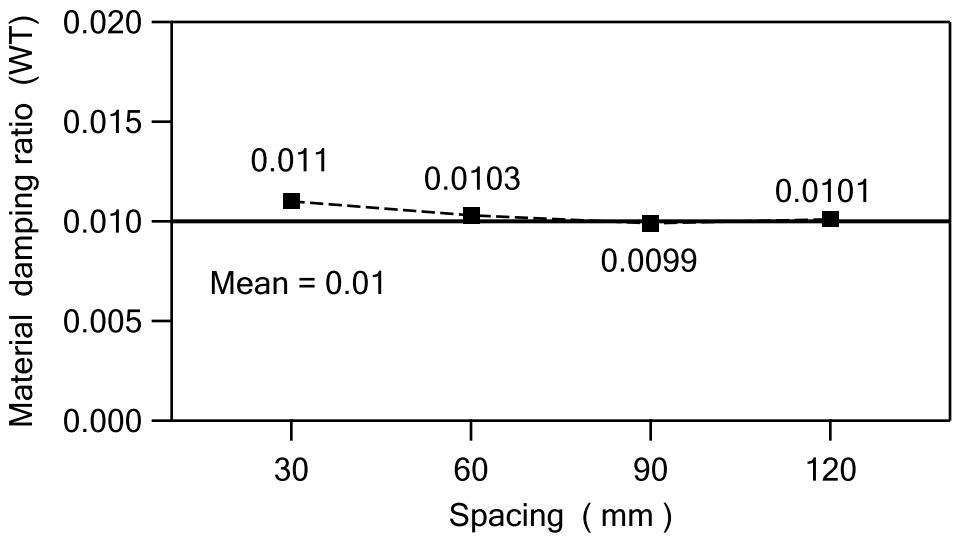

Figure 8.54: Laboratory measurement of material damping ratio on a concrete plate.

Chapter 9

Summary and conclusions

9.1 Depth evaluation of a surface-breaking crack

This research presents results from experimental and numerical tests performed on an $80mm$-thick concrete plate with well-defined notch, and experimental tests on cracked real concrete pipes. The WTC method is proposed for the depth evaluation of surface-breaking cracks in concrete. The new WTC experimental results using a $50kHz$ ultrasonic transmitter as a source show good potential for practical applications. Based on the same underlying physical principles, the central frequency of the source should be changed according to the plate thickness. The main conclusions are:

- A theoretical transfer function for Lamb modes is derived; it shows that the frequency components of propagating Lamb waves vary with distance because of the Lamb mode dispersion and higher Lamb mode participation. The numerical simulations support the theoretical results. Therefore, an equal spacing configuration is used for the WTC measurement.

- In the presence of a surface-breaking crack, the contour plots of the 2D Fourier transform of numerical results show incident, transmitted, and reflected Lamb modes. With a 2D filter, a single Lamb mode can be extracted. Because surface responses are dominated by fundamental Lamb modes for both the transmitted and reflected waves, they can be used for the depth evaluation of a surface-breaking crack. Fundamental Lamb modes behave similar to Rayleigh waves for high frequencies, where the wavelength is small relative to the plate thickness. The transmission ratio, which is calculated between the transmitted and incident fundamental Lamb mode S0 using the wavelet transform is related to the crack depth (d) for normalized depths smaller than $d/\lambda = 1/3$.

- An ultrasonic piezoelectric transmitter provides known frequency components in a high frequency range, and it is used on the surface of a medium as a source. The initial output force of an ultrasonic piezoelectric transmitter is modeled with a Morlet function. The generated ultrasonic pulse propagates in a medium, and the surface responses are analyzed with the wavelet transform using the Morlet function as a wavelet. An agreement of the numerical and experimental results supports the source modeling.

- The new WTC method is used to practically measure the depth of a notch in laboratory. The laboratory results show good agreement with the numerical results. The WTC is correlated with the crack depth in a sensitive depth range, which is determined by the central frequency of an ultrasonic piezoelectric transmitter.

Based on the tests performed on real concrete pipe specimens, the main conclusions are:

- There is no significant difference between a notch and a crack for the WTC measurement. The WTC can be used to measure crack depth.

- The WTC is significantly reduced in the presence of a crack, because the depth of a crack exceeds a sensitive depth range. However, the WTC still decreases as the crack depth increases.

- After the load is removed, the WTC shows that the crack depth is practically the same depth.

Numerical simulations are conducted for the four different cases:

- The numerical models are calibrated using Lamb's problem, theoretical geometric attenuation, and 2D Fourier transform. For the case presented in this research, the fundamental Lamb mode S0 is nearly non-dispersive at low frequencies in a small frequency bandwidth; this non-dispersive behavior is also used to calibrate the numerical models.

- Numerical study I: Rayleigh wave propagation in a half space. Rayleigh waves propagate as a non-dispersive mode at a constant velocity. The non-dispersive property of Rayleigh waves can be shown in time domain and frequency domain. Using 2D Fourier transform, Rayleigh waves are shown in the wave number-frequency domain as a single mode. Using an axisymmetric model, a half space is

simulated as a plate, which has a finite thickness and an artificial quiet boundary at bottom. The quiet boundary does not work perfectly; therefore, the thickness effect of a plate is studied, where a ratio of wavelength vs. plate thickness is important, and the thickness effect decreases as the thickness increases.

- Numerical study II: Rayleigh wave reflections in the presence of a surface-breaking crack. In the non-equal spacing configuration used in the FTC method, the incident and reflected waves are superimposed for locations before a crack; therefore, the effect of wave reflections depends on the distance from the crack. Amplification or constructive interference takes place at distances multiple of half the wavelength ($\lambda/2$); whereas, de-amplification or destructive interference takes place at distances multiple of half the wavelength plus one quarter of a wavelength ($\lambda/2+\lambda/4$).

- Numerical study III: Lamb wave propagation in a plate. Different Lamb modes can be generated in a plate, and they are analyzed using the 2D Fourier transform and wavelet transform. In the presence of a surface-breaking crack, the transmitted and reflected waves are dominated by the fundamental Lamb modes. The wave propagation of the fundamental Lamb modes is analyzed with the wavelet transform (WT); the WT transmission ratio from the fundamental Lamb modes is sensitive to the crack depth (d) in a normalized range from $d/\lambda = 0.1$ to $1/3$.

- Numerical study IV: validation of the experimental results. The WTC is measured in the laboratory tests on concrete plate specimens. To validate the experimental results, the numerical simulations using the plane-strain numerical models of the experimental specimen are conducted. The numerical and experimental results show good agreement for all the crack depths studied.

Further studies are recommended for the depth evaluation of a surface-breaking crack:

- Four parameters are important for the depth evaluation of a surface-breaking crack: the depth of a surface-breaking crack, the thickness of a plate, the central frequency and the frequency bandwidth of the source. Different values of these parameters can be used to study their effects on the depth evaluation of a surface-breaking crack.

- Instead of changing the depth of a surface-breaking crack, the central frequencies of the source can be varied. Therefore, for a certain depth of a crack, the variation of WTC vs. central frequency of an ultrasonic piezoelectric transmitter can be studied. This study requires the construction of customized transducers.

- Different source-receiver spacing should be used.
- The wall surface of a concrete pipe is curved; therefore, the surface wave propagation on a curved surface should be studied for different curvatures of pipe walls.
- Different types of a crack can be found in practice, for example different tip patterns and geometries of a crack; further studies related to this issue can be conducted.
- Homogeneous material is assumed in this study. However, heterogeneity in material that is randomly distributed at a micro-scale affects the wave propagation of high frequencies; further studies related to this issue can be conducted.

9.2 Measurement of material damping ratio

This research presents a new methodology for the measurement of material damping ratio using the wavelet transform and surface waves. A theoretical study, numerical simulations, and experimental tests are conducted to show the validity for this new methodology. Main conclusions are:

- In the new theoretical equation, material damping is given from the wavelet transform of propagating surface waves; with respect to distance, the derivatives of the maximum amplitude and phase spectrum from the wavelet transform give the spatial attenuation coefficient and damped frequency for a SDOF model, respectively.
- The calculated damping ratio represents an average damping for the frequency bandwidth determined by the source.
- In the numerical simulations, three sources are used, and four values of the minimum Rayleigh damping ratio are selected to represent different ranges of a material damping ratio. The material damping ratio calculated from the wavelet transform shows good agreement with the theoretical results, which are given by the theoretical Rayleigh damping ratio.
- Experimental results of the material damping ratio using the new methodology in a cemented sand box and a concrete plate agree with published results.

Further studies are recommended for the measurement of material damping ratio:

- For receiver locations that are near to the source, the geometric attenuation dominates; while, for receiver locations that are far from the source, wave reflections from boundaries become significant. Therefore, the study for the selection of receiver locations are important.
- Different central frequencies and frequency bandwidths of the source can be used.
- For a layered medium, low frequency components of surface waves propagate at a deep depth, and damping is affected by different materials. Therefore, the effects of different layer thicknesses on a global damping can be studied.

Bibliography

[1] Abraham, O., Leonard, C., Cote, P. and Piwakowski, B., Time frequency analysis of impact-echo signals: numerical modeling and experimental validation, Nov. - Dec., 2000, ACI Materials Journal, v97 n6, pp645-657.

[2] Achenbach, J. D., Komsky, I. N., Lee, Y. C. and Angel, Y. C., Self-calibrating ultrasonic technique for crack depth measurement, Journal of Nondestructive Evaluation, 1992, v11 n2, pp103-108.

[3] ACI Committee 228, Nondestructive test methods for evaluation of concrete in structures, ACI 228.2R - 98, June 1998.

[4] Addison, P. S., The illustrated wavelet transform handbook, Institute of Physics Publishing, Bristol and Philadelphia, USA, 2002.

[5] Angel, Y.C. and Achenbach, J. D., Reflection and transmission of obliquely incident Rayleigh waves by a surface breaking crack, Journal of the Acoustical Society of America, 1984, v75, pp313-318.

[6] Bath, M and Berkhout A. J., Mathematical Aspects of Seismology, Klaus Helbig and Sven Trietel, Geophysical, London, 1984.

[7] Bathe, K. J. and Wilson, E. L., Numerical Methods in Finite Element Analysis, Prentice-Hall, Englewood, Cliffs, NJ, 1976.

[8] Blitz, J. and Simpson, G., Ultrasonic method of non-destructive testing, Chapman & Hall, 1996.

[9] Brown, L. F., Design considerations for piezoelectric polymer ultrasound transducers, IEEE Transactions on Ultrasonic, Ferroelectrics and Frequency Control, Nov. 2000, v47, n6, pp1377-1396.

[10] Carino, N. J., Sansalone, M. and Hsu, N. N., Flaw detection in concrete by frequency spectrum analysis of impact echo waveforms, International Advances in Nondestructive Testing, 1986, 12th Edition, New York, pp1-20.

[11] Cartz, L., Non-destructive testing, Radiograph, Ultrasonic, Liquid penetrates, Magnetic particle, Eddy current, ASM International, USA, 1995.

[12] Caughey, T.K., Classical normal modes in damped linear systems, Journal of Applied Mechanics, 27, pp269-271, 1960.

[13] Chang, Young-Fo and Wang, Chung-Yue., A 3-D image detection method of a surface opening crack in concrete using ultrasonic transducer arrays, Journal of Nondestructive Evaluation, 1997, v16, n4, pp193-203.

[14] Chen, L., Zhu, J., Yan, X. and Song, C., On arrangement of source and receivers in SASW testing, Soil Dynamics and Earthquake Engineering, July 2004, v24, n5, pp389-396.

[15] Cho, Y. S. and Lin, F. B., Integrity analysis of signal and multiplayer thin cement mortar slab structure using the spectral analysis of surface wave NDT method, Construction and Building Materials, 2000, v14, pp387-395.

[16] Cho, Y. S., Non-destructive testing of high strength concrete using spectral analysis of surface waves, NDT & E International, June 2003, v36, n4, pp229-235.

[17] Cremer, L. and Heckl, M., Structure-Borne Sound. Springer-Verlag, New York, 1988.

[18] Deng, C. J., Schmerr, L. W. and Sedov, A., Modeling and measuring all the elements of an ultrasonic nondestructive evaluation system 1: modeling foundation, Research in Nondestructive Evaluation, 2002, v14 n3, pp141-176.

[19] Deng, C. J., Schmerr, L. W. and Sedov, A., Modeling and measuring all the elements of an ultrasonic nondestructive evaluation system 2: model based measurements, Research in Nondestructive Evaluation, 2002, v14, n4, pp177-201.

[20] EM350 lecture notes., Introduction to non-destructive evaluation engineering, Iowa State University, USA, 2005.

[21] Fitting, Dale W. and Adler, Laszlo, Ultrasonic spectral analysis for nondestructive evaluation, Plenum Press, New York and London, 1981.

[22] Graff, K. F., Wave Motion in Elastic Solids, New York, USA, 1991.

[23] Hayashi, T. and Kawashima, K., Single mode extraction from multiple modes of Lamb wave and its application to defect detection, JSME International Journal, 2003, Series A, v46, n4, pp620-626.

[24] Heisey, J. S., Stokoe, K. H., Hudson, W. R. and Meyer, A. H. Determination of in situ wave velocities from spectral analysis of surface waves, Research Report 256-2, Centre for Transportation Research, University of Texas at Austin, 277pp, 1982.

[25] Hevin, G., Abraham, O., Pedersen, H. A. and Campillo, M., Characterization of surface cracks with Rayleigh waves: a numerical model, NDT & E International, 1998, v31, n4, pp289-297.

[26] Hiltunen, D. R. and Woods, R. D., SASW and cross hole test results compared, Geotechnical Special Publication, 1988, pp279-289.

[27] Hunter, S. C., Energy absorbed by elastic waves during impact, Journal of the Mechanics and Physics of Solids, 1957, v5, pp162-171.

[28] Itasca, Fast Lagrangian Analysis of Continua Users Guide, Minnesota, USA, 2000.

[29] Kalinski, M. E., Stroke, K. H., Jirsa, J. O. and Roesset, J. M., Nondestructive identification of internally damaged areas of concrete beam using the spectral analysis of surface waves method, Transportation Research Record, 1994, n1458, pp14-19.

[30] Kausel, E., PUNCH: a computer program for the determination of the Green's functions in layered media, 2000.

[31] Khan, Z., Majid, A., Cascante, G., Hutchinson, D. J. and Pezeshkpour, P., Characterization of a cemented sand with the pulse-velocity method, Canadian Geotechnical Journal, 2006, v43, pp294-309.

[32] Krautkrämer, J. and Krautkrämer, H., Ultrasonic Testing of Materials, Springer-Verlag, 1990.

[33] Lamb, H., On waves in an elastic plate, Proceedings of the London Mathematical Society 21:85, 1889.

[34] Lamb, H., On the propagation of tremors over the surface of an elastic solid, Philosophical Transactions of the Royal Society of London, 1904, Series A203, pp1-42.

[35] Lardies, J, Identification of a dynamic model for an acoustic enclosure using the wavelet transform, Applied Acoustics 68, 2007, pp473-490.

[36] Lick, W. J., Difference equations from differential equations, Spring-Verlag, Berlin, Germany, 1989.

[37] Lin, Y. and Sansalone, M., Detecting flaws in concrete beams and columns using the impact-echo method, ACI Materials Journal, Jul. - Aug. 1992, v89 n4, pp396-405.

[38] Lin, Yiching and Su, Wenchi, Use of stress waves for determining the depth of surface-breaking cracks in concrete structures, ACI Materials Journal, Sep. - Oct. 1996, v93, pp494-505.

[39] Liu, M and Gorman, D. G., Formulation of Rayleigh damping and its extensions. Computers & Structures, 1995, v57, n2, pp277-285.

[40] Liu, P. L., Tsai, C. D. and Wu, T. T., Imagine of surface-breaking concrete cracks using transient elastic waves, NDT & E International, Oct. 1996, v29 n5, pp323-331.

[41] Miller, G. F. and Pursey, H., On the partition of energy between elastic waves in a semi-infinite solid, Proceeding of the Royal Society of London, 1955, Series A, v233, pp251-541.

[42] Morrison, N., Introduction to Fourier analysis, John Wiley & Sons Inc., 1994, pp563.

[44] Murigendrappa, S. M., Maiti, S. K. and Srirangarajan, H. R., Frequency-based experimental and theoretical identification of multiple cracks in straight pipes filled with fluid, NDT & E International 37, Sep. 2004, v37 n6, pp431-438.

[44] Murigendrappa, S. M., Maiti, S. K. and Srirangarajan, H. R., Experimental and theoretical study on cracks detection in pipes filled with fluid, Journal of Sound and Vibration, Mar. 2004, v270, n4-5, pp1013-1032.

[45] Naik, T. and Malhotra, M., Handbook on nondestructive testing of concrete, CRC Press, 1991.

[46] National Institute of Quality Supervision for Civil Structures (China), Nondestructive testing techniques for concrete structures (in Chinese), 1997.

[47] Ovanesova, A. V. and Suarez, L. E., Application of wavelet transforms to damage detection in frame structures, Engineering Structures 26(2004), pp39-49.

[48] Panametrics-NDT, Ultrasonic transducers technical notes, *www.olympusndt.com*, 2006.

[49] Park, S. E. and Shrout, T. R., Characteristics of relaxor-based piezoelectric single crystals for ultrasonic transducers, IEEE ultrasonics symposium proceedings, pp935-942, 1996.

[50] Popovics, J. S., Rose, J. L., Popovics, S., Newhouse, V. L., Lewin, P., and Bilgutay N., Approaches for the generation of stress waves in concrete, Experimental Mechanics, 1995, v35(1), pp36-41.

[51] Popovics, J. S., Song, W. J. and Achenbach, J. D., A study of surface wave attenuation measurement for application to pavement characterization, Proceedings of SPIE, 1998, pp300-308.

[52] Popovics, J. S., Song, W. J. and Achenbach, J. D., One-sided stress wave velocity measurement in concrete, ASCE Journal of Engineering mechanics, 1998, v124, pp1346-1353.

[53] Popovics, J. S., Song, W. J., Ghandehari, Masoud, Subramanian, K. V., Achenbach, J. D. and Shah, S. P., Application of surface wave transmission measurements for crack depth determination in concrete, ACI Materials Journal, 2000, v97, n2, pp127-135.

[54] Proctor, T. M. and Breckenridge, F. R., Source force waveforms: the use of a calibrated transducer in obtaining an accurate waveform of a source, Journal of Acoustic Emission, 1992, v10:3, pp43-48

[55] Pratt, D. and Sansalone, M., Impact-echo signal interpretation using artificial intelligence, ACI Materials Journal, Mar. - Apr. 1992, v89, n2, pp178-187.

[56] Qian, Shie, Time-frequency and wavelet transforms, Prentice-Hall Inc, 2002.

[57] Rayleigh, L., On the free vibrations of an infinite plate of homogeneous isotropic matter. Proceedings of the London Mathematical Society 20:225, 1888.

[58] Rayleigh, L., On waves propagated along the plane surface of an elastic solid, Proceedings of the London Mathematical Society, 1885, v17, pp4-11.

[59] Richart, F. E., Hall, J. R. and Woods, R. D., Vibrations of soils and foundations, Prentice-Hall Inc, 1970, 414pp.

[60] Rix, G. L., Bay, J. A. and Stroke II, K. H., Assessing in situ stiffness of curing Potland cement concrete with seismic tests, Transportation Research Record, 1990, n1284, pp8-15

[61] Robinson, E.A., Durrani, T.S. and Peardon, L.G., Geophysical signal processing, 1986.

[62] Sachse, W. and Pao, Y., On the determination of phase and group velocities of dispersive waves in solids, Journal of applied Physics, 1978, v49(8), pp4320-4327.

[63] Santamarina, J. C. and Fratta D., Introduction to Discrete Signals and Inverse Problems in Civil Engineering, ASCE press, Virginia, USA, 1998.

[64] Sansalone, M., Impact-Echo: the complete story, ACI Structural Journal, Nov. - Dec. 1997, v94, n6, pp777-786.

[65] Sansalone, M., Carino, N. J. and Hsu, N. J., Finite element study of transient wave propagation in plates, Journal of Research of the National Bureau of Standards, Jul. - Aug. 1987, v92, n4, pp267-278.

[66] Sansalone, M., Lin, J. M. and Streett, W. B., Determining the depth of surface-opening cracks using impact-generated stress waves and time-of-flight techniques, ACI Materials Journal, Mar. - Apr. 1998, v95, n2, pp168-177.

[67] Sansalone, M., Lin, J. M. and Streett, W. B., A procedure for determining P-wave speed in concrete for use in impact-echo testing using a direct P-wave speed measurement technique, ACI Materials Journal, Nov. - Dec. 1997, v94, n6, pp531-539.

[68] Sheu, J. C., Applications and limitations of the spectral-analysis-of-surface-waves method, Ph.D. Thesis, Department of Civil Engineering, University of Texas at Austin, 1987.

[69] Silk, M. G., The determination of crack penetration using ultrasonic surface waves, Ultrasonics, 1976, v38, pp290-297.

[70] Song, W. J., Popovics, J. S. and Achenbach, J. D., Crack depth determination in concrete slabs using wave propagation measurements, Proceedings of the Federal Aviation Administration Technology Transfer Conference, Atlantic City, NJ, USA, April, 1999.

[71] Song, W. J., Popovics, J. S., Aldrin, J. C. and Shah, S. P., Measurement of surface wave transmission coefficient across surface-breaking cracks and notches in concrete, Journal of Acoustical Society of America 113(2), Feb. 2003, pp717-725.

[72] Stark, H. G., Wavelets and signal processing, Springer, Berlin, Germany, 2005.

[73] Staszewski, WJ, Structural and mechanical damage detection using wavelets, The Shock and Vibration Digest, 1998, v30(6), pp457-472.

[74] Stokoe, K. H. and Nazarian S., Effectiveness of ground improvement from spectral analysis of surface waves, Proceedings of the European Conference on Soil Mechanics and Foundation Engineering, 1983, v1, pp91-94.

[75] Strikwerda, J. C., Finite difference scheme and partial differential equations, Wadsworth and Brooks, Pacific Grove, California, USA, 1989.

[76] Toksoz, M. N., Johnston, D. H. and Timur, A., Attenuation of seismic waves in dry and saturated rocks: I. Laboratory measurements. Geophysics, 1979, v 41, n4, pp681-690.

[77] Toutanji, H. A., Development of a new experimental approval for bridge deck evaluation, UTCA Report (01327), University of Alabama, USA, April, 2003.

[78] Viktorov, I. A., Rayleigh and Lamb waves, Plenum Press, New York, 1967.

[79] Virieux, J., P-SV wave propagation in heterogeneous media: Velocity-stress finite difference method, Geophysics 51, 1986.

[80] Wang, Y. H., Yan, W. M. and Lo, K. F., Damping-ratio measurements by the spectral-ratio method. Canadian Geotechnical Journal, 2006, v43, pp1180-1194.

[82] Wolf, J. P., Foundation Vibration Analysis Using Simple Physical Models, PTR Prentice Hall, 1994.

[82] Wolf, J. P. and Obernhulber, P., Free-field response from surface and inclined body waves, Transactions of the International Conference on Structural Mechanics in Reactor Technology, 1981, 14pp.

[83] Wong, Y. J., Paurobally, R. and Pan, J., Hybrid active and passive control of fan noise, Applied Acoustics, 2003, v64, n9, pp885-901.

[84] Yang, Yanjun, Cascante, Giovanni and Polak, Maria Anna, Numerical and experimental evaluation of the depth of surface-breaking cracks in concrete plates, Jounal of Nondestructive Evaluation, 2008, submitted.

[85] Yang, Yanjun, Cascante, Giovanni and Polak, Maria Anna, Depth detection of surface-breaking cracks in concrete plates using fundamental Lamb modes, NDT & E International, 2009, published (doi:10.1016/j.ndteint.2009.02.009).

[86] Yang, Yanjun, Cascante, Giovanni and Polak, Maria Anna, Material damping measurements using the wavelet transform of surface waves, Journal of Geotechnical and Geoenvironmental Engineering, ASCE, 2009, submitted.

[87] Yang, Yanjun, Polak, Maria Anna, and Cascante, Giovanni, Nondestructive evaluation of the depth of surface-breaking cracks in concrete pipes, Tunnelling and Underground Space Technology, 2009, submitted.

[88] Zerwer, A., Near surface fracture detection in structural elements: investigation using Rayleigh waves, Ph. D. Thesis, University of Waterloo, Ontario, Canada, 1999.

[89] Zerwer, A., Cascante, G. and Hutchinson, J., Parameter estimation in finite element simulations of Rayleigh waves, Journal of Geotechnical and Geoenvironmental Engineering, Mar. 2002, v128, n3, pp250-261.

[90] Zerwer, A., Polak, M. A. and Santamarina, J. C., Effects of surface cracks on Rayleigh wave propagation: an experimental study, Journal of Structural Engineering, Feb. 2002, v128, n2, pp240-248.

[91] Zerwer, A., Polak, M. A. and Santamarina, J. C., Wave Propagation in thin Plexiglas plates: Implications for Rayleigh waves, NDT & E International, 2000, v33, pp33-41.

[92] Zerwer, A., Polak, M. A. and Santamarina, J. C., Rayleigh wave propagation for the detection of near surface discontinuities: finite element study, Journal of Nondestructive Evaluation, June 2003, v22, n2, pp39-52.

[93] Zhong, S., Oyadiji, S. O. and Ding, K, Response-only method for damage detection of beam-like structures using high accuracy frequencies with auxiliary mass spatial probing. Journal of Sound and Vibration, 2008, v311, pp1075-1099.

[94] Zukas, J. A., Nicholas, T., Swift, H. F., etc., Impact dynamics, John Wiley & Sons, 1982.

Appendix

A1: Calculation of dispersion curves

Elastic constants

ORIGIN ≡ 1 $\quad$ $zero := 10^{-300}$

P-wave and S-wave velocity: $V_P := 4800$ $\quad$ $V_S := 2770$

Half the thickness of a plate: $h := \frac{0.08}{2}$ $\quad$ $h = 0.04$

Poission ratio: $fun(x) := \frac{V_S}{V_P} - \sqrt{\frac{1 - 2\cdot x}{2\cdot(1 - x)}}$ $\quad$ $\nu := root(fun(x), x, 0.1, 0.5)$ $\quad$ $\nu = 0.25035$

R-wave velocity: $V_R := \frac{0.87 + 1.12\cdot\nu}{1 + \nu}\cdot V_S$ $\quad$ $V_R = 2548.55356$

Mass density: $\rho := 2340$

Shear modulus: $G := V_S^2\cdot\rho$ $\quad$ $G = 1.79546 \times 10^{10}$

Young's modulus: $E := G\cdot 2(1 + \nu)$ $\quad$ $E = 4.48989 \times 10^{10}$

Constraint modulus: $M := \frac{1 - \nu}{(1 + \nu)\cdot(1 - 2\cdot\nu)}\cdot E$ $\quad$ $M = 5.39136 \times 10^{10}$

Bulk modulus: $K := \frac{E}{3\cdot(1 - 2\cdot\nu)}$ $\quad$ $K = 2.99742 \times 10^{10}$

P-wave velocity: $V_P = 4800$ $\quad$ $\sqrt{\frac{M}{\rho}} = 4800.00031$

S-wave velocity: $V_S = 2770$ $\quad$ $\sqrt{\frac{G}{\rho}} = 2770$

Elastic constants

Rayleigh - Lamb - Frequency Equations

$p(\omega, k) := \sqrt{\left(\frac{\omega}{V_P}\right)^2 - k^2}$ $\quad$ $q(\omega, k) := \sqrt{\left(\frac{\omega}{V_S}\right)^2 - k^2}$

For symmetric Lamb modes:

$$F_{sym}(\omega,k) := \infty \text{ on error } \frac{\tan(q(\omega,k)\cdot h)}{q(\omega,k)} + \frac{4\cdot k^2\cdot p(\omega,k)\cdot\tan(p(\omega,k)\cdot h)}{\left(q(\omega,k)^2 - k^2\right)^2}$$

For anti-symmetric Lamb modes:

$$F_{anti}(\omega,k) := \infty \text{ on error } q(\omega,k)\cdot\tan(q(\omega,k)\cdot h) + \frac{\left(q(\omega,k)^2 - k^2\right)^2\cdot\tan(p(\omega,k)\cdot h)}{4\cdot k^2\cdot p(\omega,k)}$$

Rayleigh - Lamb - Frequency Equations

Range for frequency and phase velocity

Numerical time increment: $\text{delta\_t} := 7.5\cdot 10^{-8}$

$\text{f\_inc} := \frac{1}{1024\cdot 10\cdot 4\text{delta\_t}}$ $\quad \text{f\_max} := 510\cdot 10^3$ $\quad \text{f\_inc} = 325.52083$

Point number in frequency: $\text{Nf} := \text{ceil}\left(\frac{\text{f\_max}}{\text{f\_inc}}\right)$ $\quad \text{Nf} = 1567$

Frequency range:

Increment: $\omega\_\text{inc} := 2\cdot\pi\cdot\text{f\_inc}$ **Start:** $\omega 0 := 2\cdot\pi\cdot\text{f\_inc}$ **End:** $\omega\_\text{max} := 2\cdot\pi\cdot\text{f\_max}$

Phase velocity range:

Increment: $\text{v\_inc} := 1.0$ **Start:** $\text{v0} := 10$ **End:** $\text{v\_max} := 10000$

Range for frequency and phase velocity

Symmetric Lamb modes

MX1 :=

row ← 1

ω ← ω0

while ω ≤ ω_max

  v ← v0

  $val \leftarrow F_{sym}\left(\omega, \frac{\omega}{v}\right)$

  sgn ← sign(val)

  v2 ← v + v_inc

  $val2 \leftarrow F_{sym}\left(\omega, \frac{\omega}{v2}\right)$

  sgn2 ← sign(val2)

  while v2 < v_max

    while v2 < v_max ∧ sgn·sgn2 ≥ 0

      v2 ← v2 + v_inc

      $val2 \leftarrow F_{sym}\left(\omega, \frac{\omega}{v2}\right)$

      sgn2 ← sign(val2)

    if v2 < v_max ∧ sgn·sgn2 < 0

      cond ← 1

      $cond \leftarrow 0 \quad \text{on error } root\left(F_{sym}(\omega, k), k, \frac{\omega}{v2}, \frac{\omega}{v}\right)$

      if cond = 1

        $M_{row,1} \leftarrow \frac{\omega}{2 \cdot \pi}$

        $M_{row,2} \leftarrow \frac{\omega}{root\left(F_{sym}(\omega, k), k, \frac{\omega}{v2}, \frac{\omega}{v}\right)}$

        row ← row + 1

      v ← v2

      val ← val2

      sgn ← sign(val2)

      v2 ← v + v_inc

      $val2 \leftarrow F_{sym}\left(\omega, \frac{\omega}{v2}\right)$

      sgn2 ← sign(val2)

  ω ← ω + ω_inc

M

$$MK1 := \left| \begin{array}{l} \text{for } i \in 1 .. \text{rows}(MX1) \\ \quad \left| \begin{array}{l} M_{i,1} \leftarrow MX1_{i,1} \\ M_{i,2} \leftarrow \dfrac{MX1_{i,1}}{MX1_{i,2}} \end{array} \right. \\ M \end{array} \right.$$

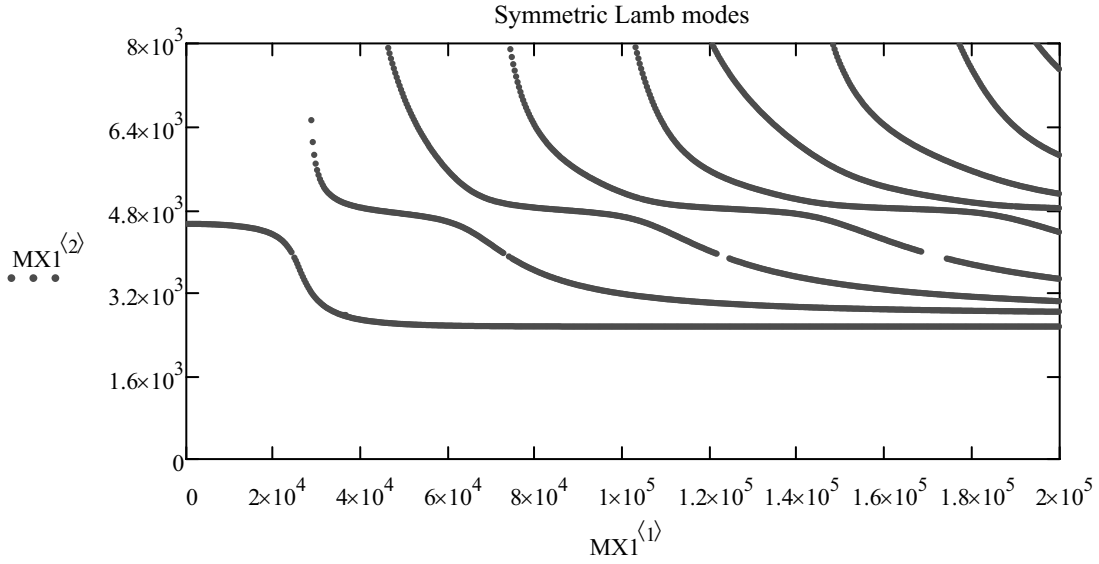

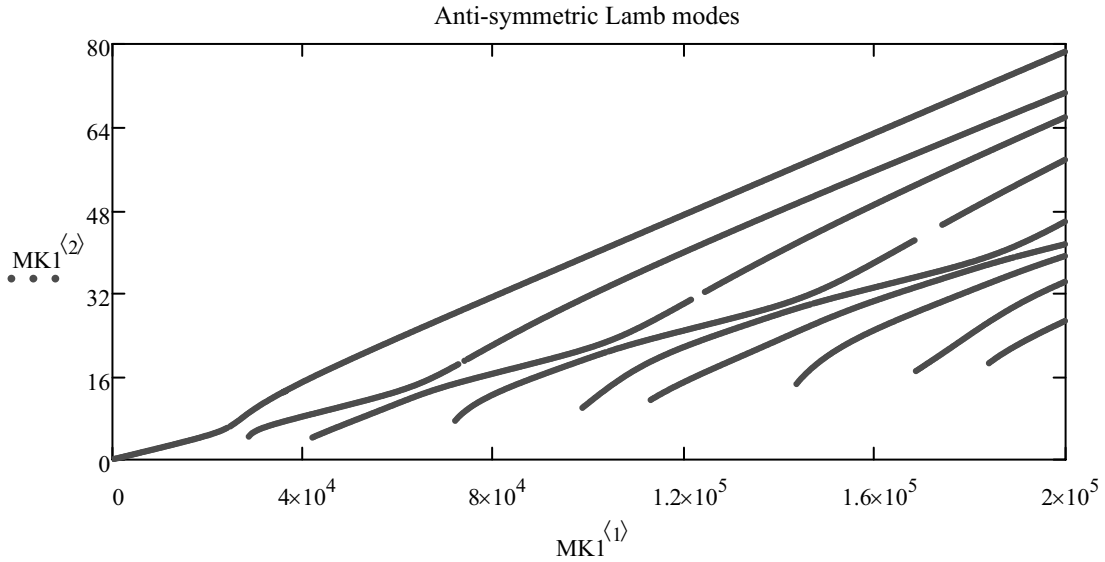

Symmetric Lamb modes

Anti-symmetric Lamb modes

```
MX2 := | row ← 1
       | ω ← ω0
       | while ω ≤ ω_max
       |     v ← v0
       |     val ← F_anti(ω, ω/v)
       |     sgn ← sign(val)
       |     v2 ← v + v_inc
       |     val2 ← F_anti(ω, ω/v2)
       |     sgn2 ← sign(val2)
       |     while v2 < v_max
       |         while v2 < v_max ∧ sgn·sgn2 ≥ 0
       |             v2 ← v2 + v_inc
       |             val2 ← F_anti(ω, ω/v2)
       |             sgn2 ← sign(val2)
       |         if v2 < v_max ∧ sgn·sgn2 < 0
       |             cond ← 1
       |             cond ← 0  on error root(F_anti(ω, k), k, ω/v2, ω/v)
       |             if cond = 1
       |                 M[row, 1] ← ω/(2·π)
       |                 M[row, 2] ← ω/root(F_anti(ω, k), k, ω/v2, ω/v)
       |                 row ← row + 1
       |             v ← v2
       |             val ← val2
       |             sgn ← sign(val2)
       |             v2 ← v + v_inc
       |             val2 ← F_anti(ω, ω/v2)
       |             sgn2 ← sign(val2)
       |     ω ← ω + ω_inc
       | M
```

$$MK2 := \left| \begin{array}{l} \text{for } i \in 1 .. \text{rows}(MX2) \\ \quad \left| \begin{array}{l} M_{i,1} \leftarrow MX2_{i,1} \\ M_{i,2} \leftarrow \dfrac{MX2_{i,1}}{MX2_{i,2}} \end{array} \right. \\ M \end{array} \right.$$

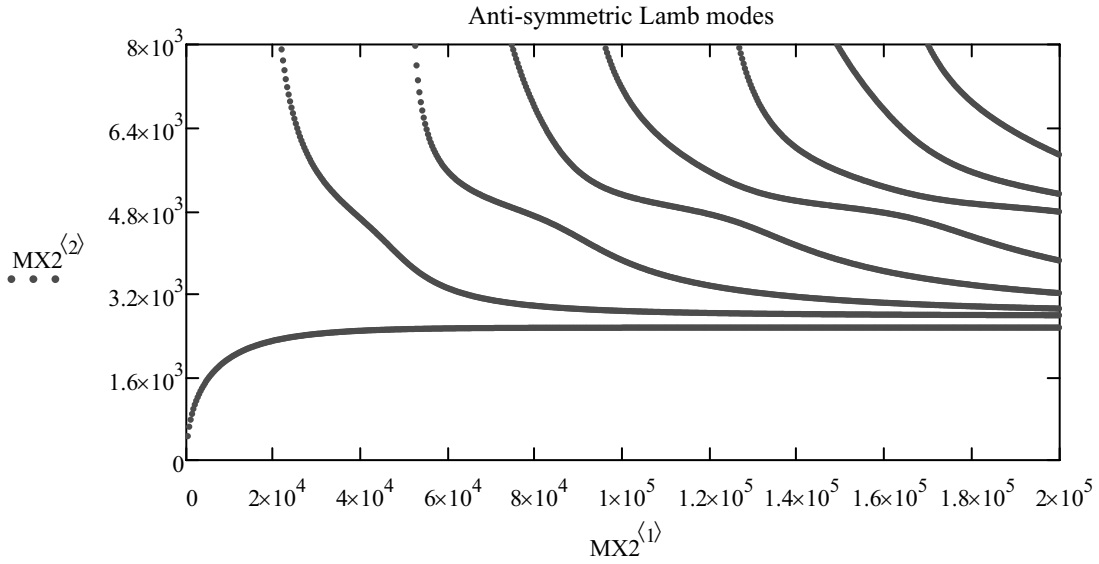

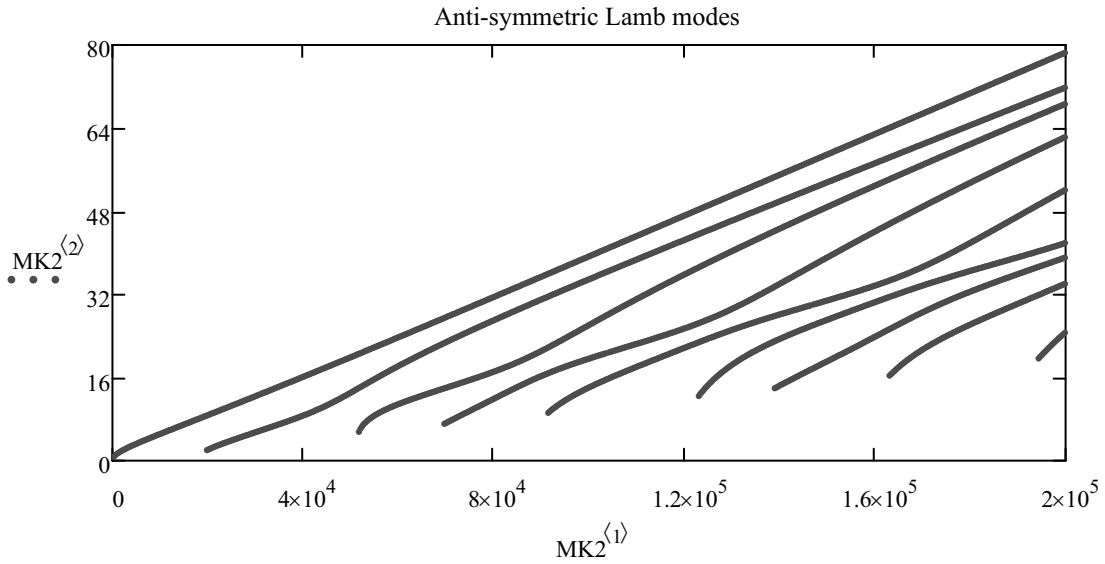

Anti-symmetric Lamb modes

A2: Calculation of material damping ratio

Parameters

ORIGIN = 0 **Rayleigh velocity:** $V_R := 1208$

$N := 4096$ $i := 0 .. N - 1$ $Nf := \frac{N}{2}$ $jf := 0 .. Nf$

Sampling rate: $\Delta t := 1 \cdot 10^{-6}$ $\Delta t = 1 \times 10^{-6}$ $t_i := i \cdot \Delta t$

Interval in frequency: $\Delta f := \frac{1}{t_{N-1} - t_0}$ $\Delta f = 244.2$ $f_{jf} := jf \cdot \Delta f$

Nyquist frequency: $f_{nqu} := \frac{1}{2 \cdot \Delta t}$ $f_{nqu} = 5 \times 10^5$

Central frequency of a Morlet function: $f_o := 50 \cdot 10^3$

Plate thickness: $h := 80 \cdot 10^{-3}$ **Source location:** $x_s := 0 \cdot 10^{-3}$

Receiver spacing: $\Delta x := 20 \cdot 10^{-3}$

Number of receivers: $Nx := 12$ $jx := 0 .. Nx - 1$

First receiver location: $x_o := 0.22$ **Receiver locations:** $x_{jx} := x_o + jx \cdot \Delta x$

Last receiver location: $x_{Nx-1} = 0.44$

Parameters

Load experimental data

```
M0_ch0 := READPRN(".\\miniature2\ASCII\220mm_1.txt")
M0_ch1 := READPRN(".\\miniature2\ASCII\240mm_1.txt")
M0_ch2 := READPRN(".\\miniature2\ASCII\260mm_1.txt")
M0_ch3 := READPRN(".\\miniature2\ASCII\280mm_1.txt")
M0_ch4 := READPRN(".\\miniature2\ASCII\300mm_1.txt")
M0_ch5 := READPRN(".\\miniature2\ASCII\320mm_1.txt")
M0_ch6 := READPRN(".\\miniature2\ASCII\340mm_1.txt")
M0_ch7 := READPRN(".\\miniature2\ASCII\360mm_1.txt")
M0_ch8 := READPRN(".\\miniature2\ASCII\380mm_1.txt")
M0_ch9 := READPRN(".\\miniature2\ASCII\400mm_1.txt")
M0_ch10 := READPRN(".\\miniature2\ASCII\420mm_1.txt")
```

M0_ch11 := READPRN(".\\miniature2\ASCII\440mm_1.txt")

$$
M1 := \left(\begin{array}{l}
\text{length} \leftarrow \text{rows}(M0\_ch0) \\
\text{for } jx \in 0 .. Nx - 1 \\
\quad \text{for } i \in 0 .. N - 1 \\
\quad\quad M_{i,jx} \leftarrow \begin{cases} M0\_ch0_{i,0} & \text{if } i < \text{length} \quad \text{if } jx = 0 \\ 0 & \text{otherwise} \end{cases} \\
\quad\quad M_{i,jx} \leftarrow \begin{cases} M0\_ch1_{i,0} & \text{if } i < \text{length} \quad \text{if } jx = 1 \\ 0 & \text{otherwise} \end{cases} \\
\quad\quad M_{i,jx} \leftarrow \begin{cases} M0\_ch2_{i,0} & \text{if } i < \text{length} \quad \text{if } jx = 2 \\ 0 & \text{otherwise} \end{cases} \\
\quad\quad M_{i,jx} \leftarrow \begin{cases} M0\_ch3_{i,0} & \text{if } i < \text{length} \quad \text{if } jx = 3 \\ 0 & \text{otherwise} \end{cases} \\
\quad\quad M_{i,jx} \leftarrow \begin{cases} M0\_ch4_{i,0} & \text{if } i < \text{length} \quad \text{if } jx = 4 \\ 0 & \text{otherwise} \end{cases} \\
\quad\quad M_{i,jx} \leftarrow \begin{cases} M0\_ch5_{i,0} & \text{if } i < \text{length} \quad \text{if } jx = 5 \\ 0 & \text{otherwise} \end{cases} \\
\quad\quad M_{i,jx} \leftarrow \begin{cases} M0\_ch6_{i,0} & \text{if } i < \text{length} \quad \text{if } jx = 6 \\ 0 & \text{otherwise} \end{cases} \\
\quad\quad M_{i,jx} \leftarrow \begin{cases} M0\_ch7_{i,0} & \text{if } i < \text{length} \quad \text{if } jx = 7 \\ 0 & \text{otherwise} \end{cases} \\
\quad\quad M_{i,jx} \leftarrow \begin{cases} M0\_ch8_{i,0} & \text{if } i < \text{length} \quad \text{if } jx = 8 \\ 0 & \text{otherwise} \end{cases} \\
\quad\quad M_{i,jx} \leftarrow \begin{cases} M0\_ch9_{i,0} & \text{if } i < \text{length} \quad \text{if } jx = 9 \\ 0 & \text{otherwise} \end{cases} \\
\quad\quad M_{i,jx} \leftarrow \begin{cases} M0\_ch10_{i,0} & \text{if } i < \text{length} \quad \text{if } jx = 10 \\ 0 & \text{otherwise} \end{cases} \\
\quad\quad M_{i,jx} \leftarrow \begin{cases} M0\_ch11_{i,0} & \text{if } i < \text{length} \quad \text{if } jx = 11 \\ 0 & \text{otherwise} \end{cases} \\
M
\end{array}\right)
$$

Load experimental data

Time traces and frequency responses

Cancel DC component: $M1^{\langle jx \rangle} := M1^{\langle jx \rangle} - \text{mean}\left(M1^{\langle jx \rangle}\right)$

Eliminate geometric attenuation: $M1_{i,jx} := \left(\frac{x_{jx}}{x_0}\right)^{0.5} \cdot M1_{i,jx}$

Fourier transforms: $FM1^{\langle jx \rangle} := \text{fft}\left(M1^{\langle jx \rangle}\right)$ $\quad max\_FM1 := \max\left(\overrightarrow{|FM1|}\right)$ $\quad FM1 := \frac{FM1}{max\_FM1}$

Time traces

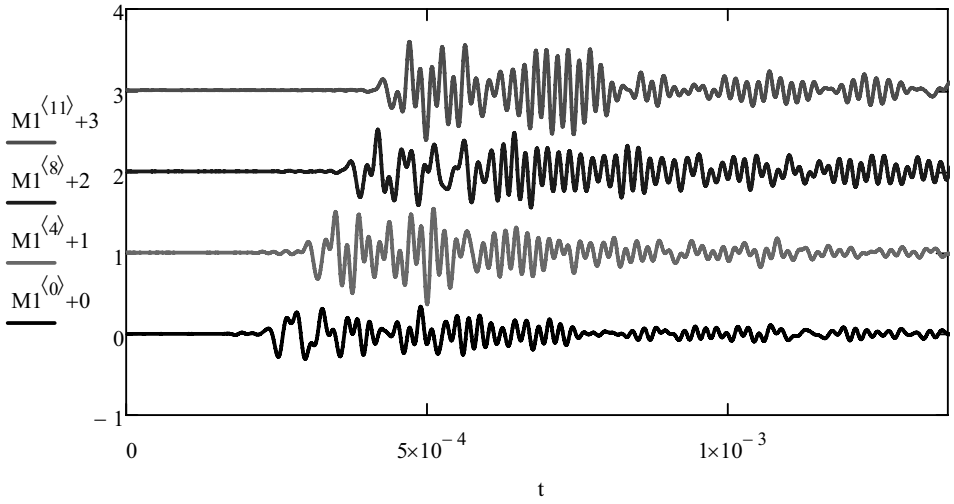

Frequency spectra

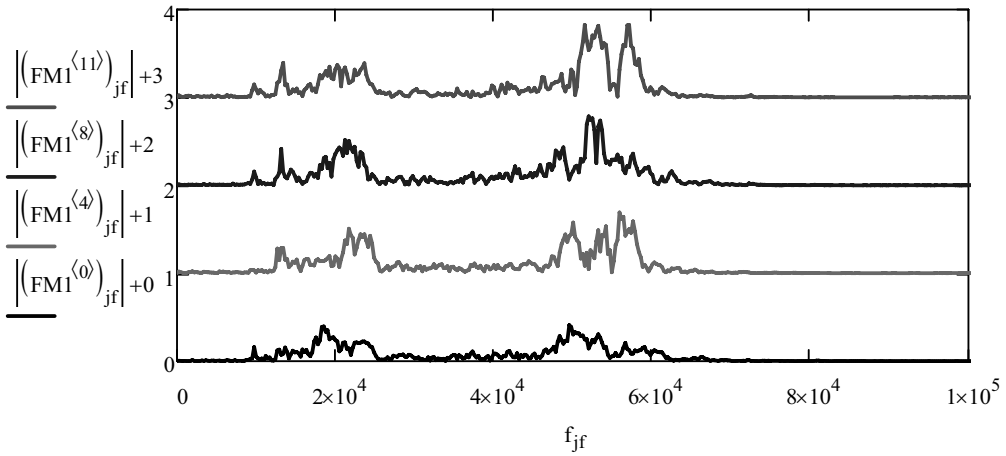

Time traces and frequency responses

Definition of the wavelet transform using a Morlet wavelet

Frequency: $f_o = 5 \times 10^4$ $\quad \omega_o := 2 \cdot \pi \cdot f_o$ $\quad \omega_o = 3.142 \times 10^5$

Time period: $T_o := \frac{1}{f_o}$ $T_o = 2 \times 10^{-5}$

Modulation parameter: $\tau := 1.12 \cdot 10^{-5}$

Shift time: $t_o := 2.0 \cdot T_o$ $t_o = 4 \times 10^{-5}$

Morlet wavelet and its Fourier transform:

$$\phi(t) := e^{j \cdot \omega_o \cdot t} \cdot e^{-\left(\frac{t}{\tau}\right)^2} \qquad U(f) := e^{-\left(\frac{\tau}{2}\right)^2 \left(2\pi \cdot f - \omega_o\right)^2}$$

Frequency bandwidth: $BW := 2 \frac{\sqrt{\ln(4)}}{\tau} \cdot \left(\frac{1}{2 \cdot \pi}\right)$ $BW = 3.346 \times 10^{4}$

Time signal

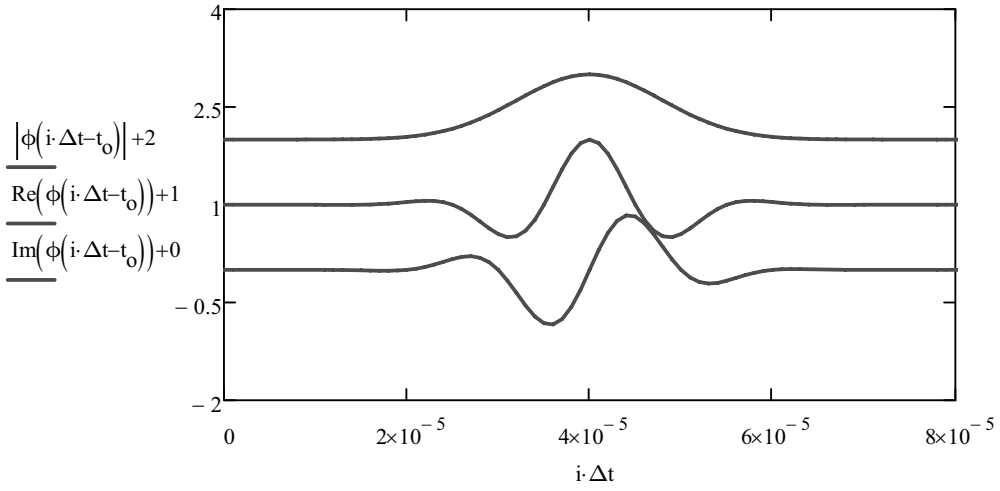

Frequency spectrum

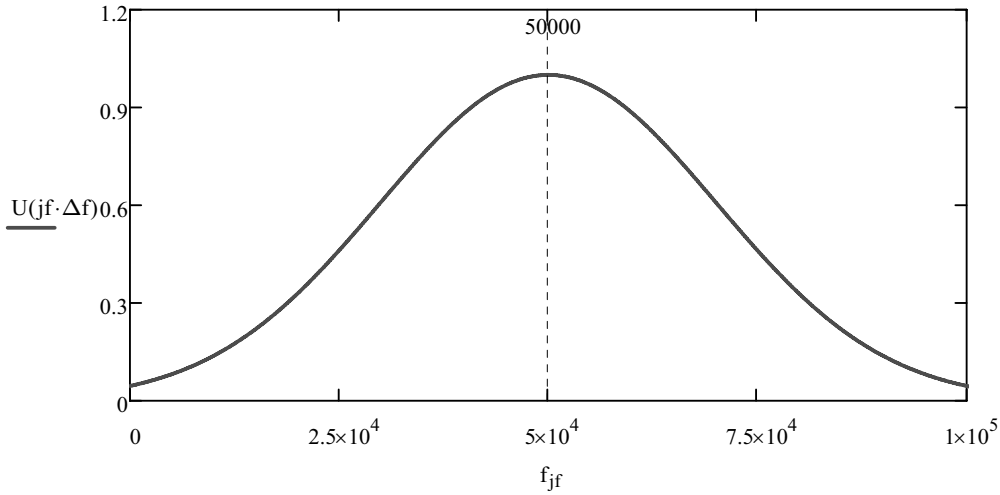

EQUATIONS FOR WAVELET TRANSFORM

In time: $WT_x(a,b)=\frac{1}{\sqrt{a}}\int_{-\infty}^{\infty} x(t)\,\varphi^*\left(\frac{t-b}{a}\right)dt$

In frequency : $WT_x(a,b)=\sqrt{a}\int_{-\infty}^{\infty} X(\omega)\,\Psi^*(a\omega)\,e^{j\omega b}d\omega$

Wavelet transform calculation in time:

$$WTT(a,b,data):=\frac{1}{\sqrt{a}}\sum_{i=0}^{N-1}\left(data_i\cdot\overline{\phi\left(\frac{i\cdot\Delta t-t_o-b}{a}\right)}\right)$$

Wavelet transform calculation in frequency:

$$WTF(a,b,data):=\sqrt{a}\sum_{i=0}^{N-1}\left[data_i\cdot\overline{U(a\cdot i\cdot\Delta f)}\cdot e^{j\cdot 2\cdot\pi\cdot(i\cdot\Delta f)\cdot b}\right]$$

Definition of the wavelet transform using a Morlet wavelet

Results of wavelet transform

Dilation parameter "a": $a:=1$ $Nw:=\frac{N}{4}$ $iw:=0..Nw-1$

Wavelet transform calculations:

$Mw1_{iw,jx}:=WTT\left(a,iw\cdot\Delta t,M1^{\langle jx\rangle}\right)$ $Mw\_am_{iw,jx}:=\left|Mw1_{iw,jx}\right|$

$max1:=max(Mw\_am)$ $max1=5.689$ $Mw\_am:=\frac{Mw\_am}{max1}$

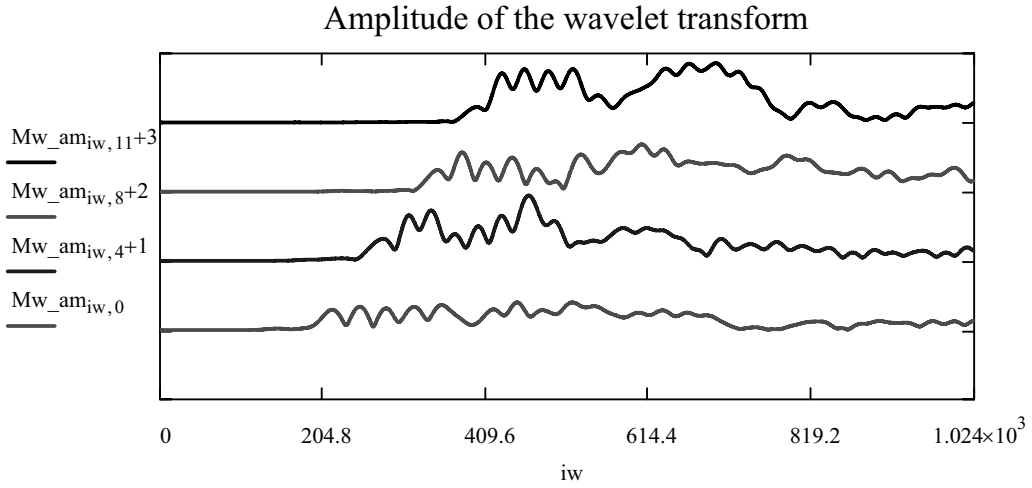

The first arrival times are selected:

$$\text{first\_T} := (217 \quad 230 \quad 250 \quad 266 \quad 281 \quad 298 \quad 316 \quad 333 \quad 349 \quad 365 \quad 380 \quad 398)$$

Corresponding amplitudes of the wavelet transform:

$$\text{first\_D} := \left| \begin{array}{l} \text{for } jx \in 0 .. Nx - 1 \\ \quad \left| \begin{array}{l} T \leftarrow \text{first\_T}^{T} \\ n \leftarrow T_{jx} \\ M_{jx} \leftarrow \text{Mw\_am}_{n,jx} \end{array} \right. \\ M^{T} \end{array} \right.$$

$$\text{max2} := \max\left(\overrightarrow{|\text{Mw1}|}\right) \qquad \text{Mw1} := \frac{\text{Mw1}}{\text{max2}}$$

$$D_{jx} := \left(\text{first\_D}^{T}\right)_{jx} \qquad \text{lnD}_{jx} := \ln\left(D_{jx}\right)$$

$$\text{Sp\_lnD} := \text{lspline}(x, \text{lnD}) \qquad \text{fit\_lnD}(u) := \text{interp}(\text{Sp\_lnD}, x, \text{lnD}, u)$$

$$\text{d\_fit\_lnD}(u) := \left(\frac{d^{1}}{du^{1}} \text{fit\_lnD}(u)\right)$$

$$\text{v\_fit\_lnD}_{jx} := \text{fit\_lnD}\left(x_{jx}\right) \qquad \text{slope}(x, \text{v\_fit\_lnD}) = -0.096 \qquad \text{line}(x, \text{v\_fit\_lnD}) = \begin{pmatrix} -1.311 \\ -0.096 \end{pmatrix}$$

$$\text{y\_fit\_lnD}(u) := \text{line}(x, \text{v\_fit\_lnD})_{1} \cdot u + \text{line}(x, \text{v\_fit\_lnD})_{0}$$

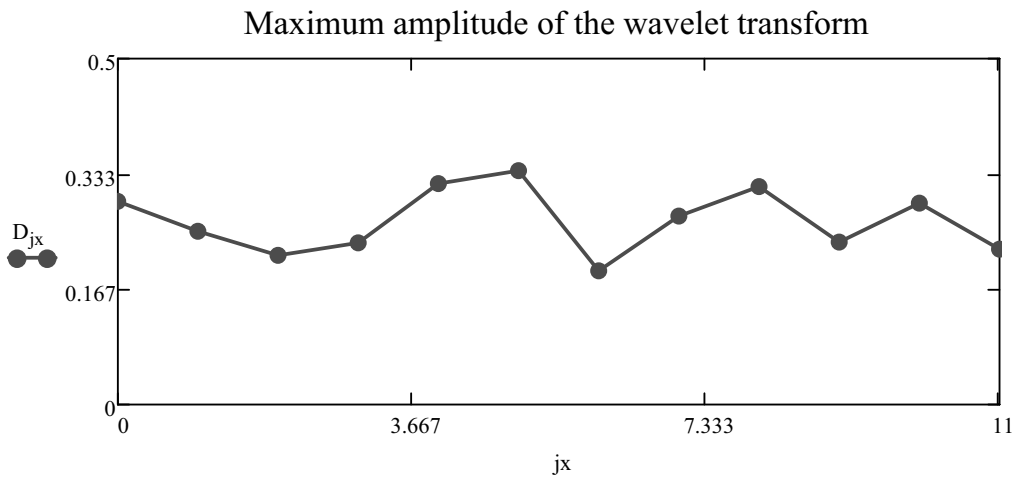

Logarithm of the maximum amplitude

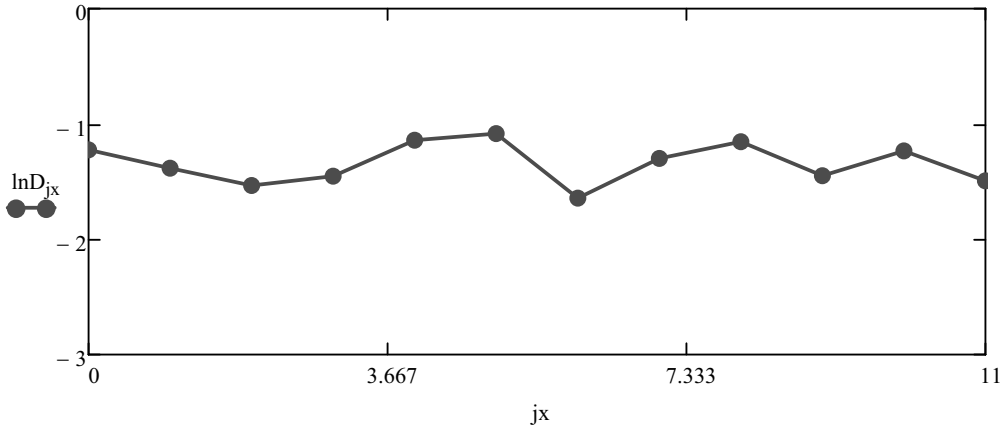

Derivative of the maximum amplitude

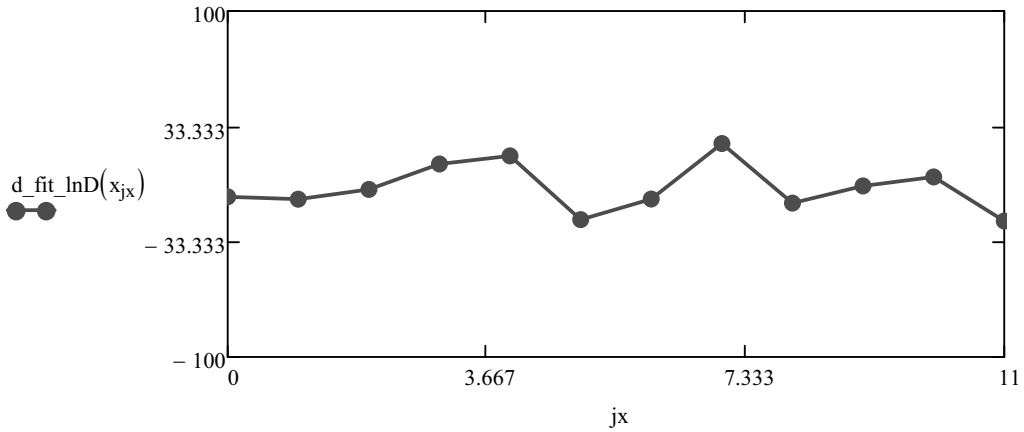

$Nx1 := 512$ $\quad jx1 := 0 .. Nx1 - 1$

$x1_{jx1} := \frac{jx1}{Nx1} \cdot x_{Nx-1}$ $\quad LnD1_{jx1} := fit\_lnD\left(x1_{jx1}\right)$

Phase of the wavelet transform: $\quad Mw\_ph_{iw,jx} := phasecor\left(phase\left(Mw1^{\langle jx \rangle}\right)\right)_{iw}$

$r0 := 5$ $\quad r1 := 10$ $\quad u1_{iw} := iw \cdot \Delta t$

$v0_{iw} := Mw\_ph_{iw,r0}$ $\quad Sp0 := cspline(u1, v0)$

$fit0(u) := interp(Sp0, u1, v0, u)$ $\quad d\_fit0(u) := \frac{1}{2\pi}\left(\frac{d}{du} fit0(u)\right)$

$v1_{iw} := Mw\_ph_{iw,r1}$ $\quad Sp1 := cspline(u1, v1)$

$fit1(u) := interp(Sp1, u1, v1, u)$ $\quad d\_fit1(u) := \frac{1}{2\pi}\left(\frac{d}{du} fit1(u)\right)$

Amplitude and phase

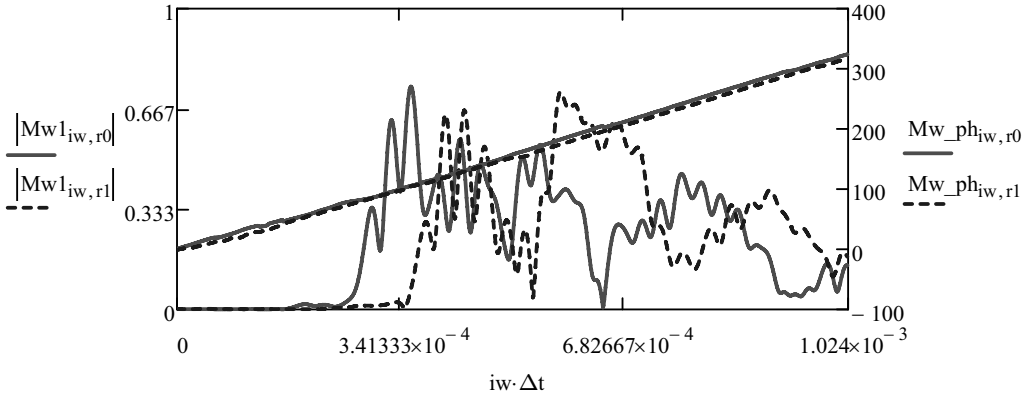

Amplitude and damped frequency

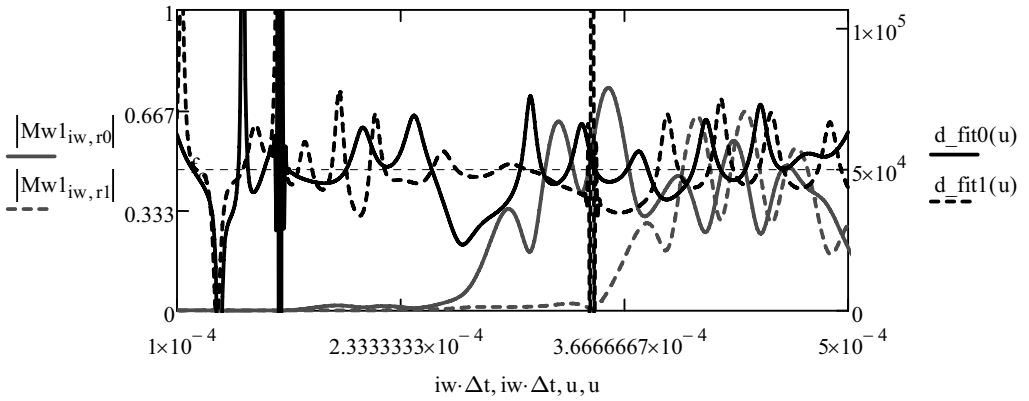

Time arrival:

$$arriv\_nm_{jx} := \left(first\_T^{T}\right)_{jx}$$

Damped frequency at the arrival time:

$$damped\_fq := \left| \begin{array}{l} \text{for } jx \in 0 .. Nx - 1 \\ \quad \text{for } iw \in 0 .. Nw - 1 \\ \quad\quad t_{iw} \leftarrow iw \cdot \Delta t \\ \quad\quad ph_{iw} \leftarrow phasecor\left(phase\left(Mw1^{\langle jx \rangle}\right)\right)_{iw} \\ \quad Sp \leftarrow cspline(t, ph) \\ \quad fit(u) \leftarrow interp(Sp, t, ph, u) \\ \quad d\_fit(u) \leftarrow \frac{1}{2\pi}\left(\frac{d}{du} fit(u)\right) \\ \quad u1 \leftarrow arriv\_nm_{jx} \cdot \Delta t \\ \quad M_{jx} \leftarrow d\_fit(u1) \\ M \end{array} \right.$$

$Sp\_damped\_fq := cspline(x, damped\_fq)$

$fit\_damped\_fq(u) := interp(Sp\_damped\_fq, x, damped\_fq, u)$

$line(x, damped\_fq) = \begin{pmatrix} 3.022 \times 10^4 \\ 1.876 \times 10^4 \end{pmatrix}$ $slope(x, damped\_fq) = 1.876 \times 10^4$

$y\_damped\_fq(u) := line(x, damped\_fq)_1 \cdot u + line(x, damped\_fq)_0$

$damped\_fq1_{jx} := fit\_damped\_fq(x_{jx})$

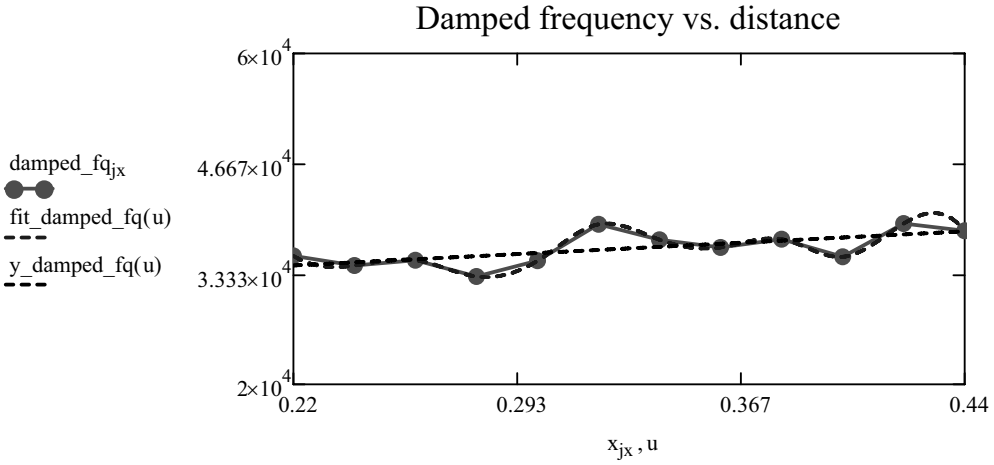

Results of wavelet transform

Material damping ratio calculations

$lnA_{jx} := ln\left(\frac{D_{jx}}{U(fit\_damped\_fq(x_{jx}))}\right)$ $y\_damped\_fq(x_{r1}) = 3.81 \times 10^4$

$Sp\_lnA := cspline(x, lnA)$ $fit\_lnA(u) := interp(Sp\_lnA, x, lnA, u)$

$d\_fit\_lnA(u) := \left(\frac{d^1}{du^1} fit\_lnA(u)\right)$

$v\_fit\_lnA_{jx} := fit\_lnA(x_{jx})$ $slope(x, v\_fit\_lnA) = -0.725$

$y\_fit\_lnA(u) := line(x, v\_fit\_lnA)_1 \cdot u + line(x, v\_fit\_lnA)_0$

$\alpha_x := -\text{slope}(x, v\_fit\_lnA)$ $\alpha_x = 0.725$

$$\text{fit\_damping}(u) := \frac{\alpha_x}{2 \cdot \pi \cdot \text{fit\_damped\_fq}(u)} \cdot V_R$$

$\text{damping}_{jx} := \text{fit\_damping}\left(x_{jx}\right)$

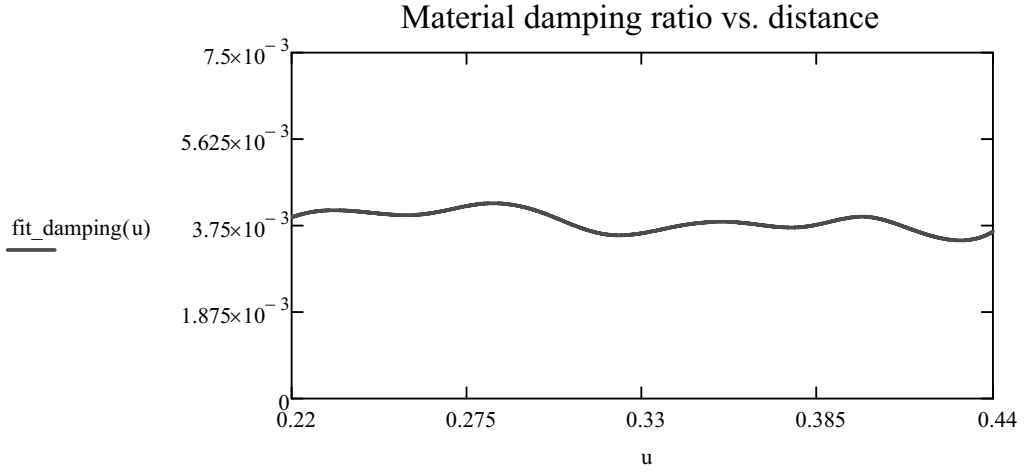

$$\text{mean\_damping} := \left| \begin{array}{l} \text{sum} \leftarrow 0 \\ \text{for } jx \in 0 .. Nx - 1 \\ \quad \text{sum} \leftarrow \text{sum} + \text{fit\_damping}\left(x_{jx}\right) \\ \text{sum} \leftarrow \dfrac{\text{sum}}{Nx} \\ \text{sum} \end{array} \right.$$

$\text{mean\_damping} = 3.839 \times 10^{-3}$

Material damping ratio calculations

A3: Numerical calibration of Lamb waves in a plate

```
NEW

config dynamic ;Plain_strain by default


DEF setup

 ;Plate dimension: 1200mm x 80mm
 ;Grid numbers: 4800 x 320, delta_x = 0.25mm

  xn = 4800 ;grid number
  yn = 320

  xn1 = xn + 1 ;node number
  yn1 = yn + 1


  ;Points for the velocity source applied to the left boundary
  tm1 = 20000

  ;Total numbers of points in the Lamb mode file
  tot1 = tm1 * yn1



 ;Actual size of the plate
  xsz = 1.2   ;1200mm
  ysz = -0.08 ;80mm

 ;Dynamic time increment
  delta_t = 7.5e-9


 ;Reset history numbering
  command

     history reset

  end_command

END ;setup



setup

grid xn, yn

gen 0, ysz  0, 0  xsz, 0  xsz, ysz

model elastic

;Material properties
 prop dens = 2340 bulk = 3.0e10 shear = 1.8e10


SET gravity 0.0
```

```
;Fixed nodes
 fix x y i = xn1 j = 1
 fix x y i = xn1 j = yn1


DEF input_sourc ;Create tables for the source

   string aa1
   array aa1(tot1)

   float aa2
   array aa2(tot1)

  ;Read Lamb mode shape of the horizontal velocity
   status = open ('c:\FLAC\LAMB\PRNs\S0U_10k.prn', 0, 1)
   status = read(aa1, tot1)
   status = close

   loop n (1, tot1)
        aa2(n) = parse(aa1(n), 1) ;Convert string to float number
   end_loop

   loop n (1, yn1)
        loop n1 (1, tm1)

           ntab = n ;horizontal source

           xtable(ntab, n1) = n1 * delta_t

           ytable(ntab, n1) = aa2((n-1)*tm1 + n1)

        end_loop
   end_loop


  ;Read Lamb mode shape of the vertical velocity
   status = open ('c:\flac\lamb\PRNs\s0w_10k.prn', 0, 1)
   status = read(aa1, tot1)
   status = close

   loop n (1, tot1)
        aa2(n) = parse(aa1(n), 1) ;Convert string to float number
   end_loop

   loop n (1, yn1)
        loop n1 (1, tm1)

           ntab = yn1 + n ;Vertical source

           xtable(ntab, n1) = n1 * delta_t

           ytable(ntab, n1) = aa2((n-1)*tm1 + n1)

        end_loop
   end_loop

 END ;input_sourc


 input_sourc
```

```
 DEF apply_sourc

   Fb = 1 ;Amplitude

   loop n (1, yn1)

     ntab1 = n

     ntab2 = yn1 + n

     command
       apply xvel Fb hist tab ntab1 i = 1 j = n

       apply yvel Fb hist tab ntab2 i = 1 j = n
     end_command

  end_loop

 END ;apply_sourc



;Define a Morlet source, refering to MathCAD file 'Gen_sourc'
 DEF Mor_func

   ;dytime = stepno * dydt


   f_o = 10.0e3 ;Central frequency of a Morlet function
   sigma_o = 6.25e-9

   t_o = 2.5e-4 ;time shift
   dua = 5.0e-4 ;time duration (2*t_o)


   t1 = dytime ;current time
   t2 = t1 - t_o

   if t1 < dua

      Mor_func = cos(2*pi*f_o*t2) * exp(-(t2^2 / sigma_o))

   else

      Mor_func = 0

   end_if

 END ;Mor_func



 DEF init_model

   command

     set dydt = delta_t
     set dytime = 0
     history nstep = 10

    ;history 10000 Mor_func
     history 10001 unbal
     history 10002 dytime
```

```
  end_command


 ;Shot Number
  movieshots = 1

 ;Step Number for each shot
  moviesteps = 40000 ;moviesteps / nstep = 4000

END ;init_model



DEF hor_rece ;Place receivers in horizontal direction

 ;Receiver locations (400mm - 800mm)
  r0 = 1600 ;1600 x 0.25mm = 400mm

 ;Number of receivers (horizontal direction)
  h_num = 201

 ;Receiver increment
  inc = 8 ;8 x 0.25mm = 2mm


  loop n (1, h_num)

     r = r0 + (n-1)*inc

     command
       ;X displacement
        history xacc i = r j = yn1 ;History at surface

       ;Y displacement
        history yacc i = r j = yn1

     endcommand
  end_loop

END ;hor_rece



DEF ver_rece ;Place receivers in vertical direction

 ;First receiver location
  r0 = yn1 ;at surface

 ;Number of receivers (vertical direction)
  v_num = 41

 ;Receiver increment
  inc = 8 ;8 x 0.25mm = 2mm


  loop n (1, v_num)
     r = r0 - (n-1)*inc

     command
       ;X-velocity
        history xacc i = 1 j = r ;Hist at left end

       ;Y-velocity
        history yacc i = 1 j = r
```

```
     endcommand
  end_loop

END ;ver_rece


DEF save_hx ;X_displacment (horizontal direction)

  loop n (1, h_num)

    m = (n-1)*2 + 1

    command
      history write m ;Writing hx_disp
    end_command

  end_loop

END ;save_hx


DEF save_hy ;Y_displacment (horizontal direction)

 loop n (1, h_num)

    m = (n-1)*2 + 2

    command
      history write m ;Writing hy_disp
    end_command

  end_loop

END ;save_hy




DEF save_vx ;X_displacment (vertical direction)

  loop n (1, v_num)

    m = 4*h_num + (n-1)*2 + 1

    command
      history write m ;Writing vx_disp
    end_command

  end_loop

END ;save_vx


DEF save_vy

  loop n (1, v_num) ;Y_displacment (vertical direction)

    m = 4*h_num + (n-1)*2 + 2

    command
```

```
      history write m ;Writing vy_disp
    end_command

  end_loop

END ;save_vy



DEF save_sour

  command
    history write 10000 ;Writing source
  end_command

END ;save_sour


DEF save_unbal

  command
    history write 10001 ;Writing un_balanced force
  end_command

END ;save_unbal




DEF run_model

  init_model

  hor_rece ;Place horizontal receivers

  ver_rece ;Place vertical receivers

  apply_sourc


  command
    ;for movie view
    ;window 0.575 0.625 -0.10 0.05
  end_command


  loop n (1, movieshots)
    command
    step moviesteps
   ;plot bou red vel yel max=0.6e-5 apply green
    end_command
  end_loop

END ;### End of Functions



 ;save c:\FLAC\LAMB\dum_1.sav

 ;movie on file c:\FLAC\LAMB\LM_1.dcx


 run_model
```

```
set hisfile c:\FLAC\LAMB\data\166hx.his
save_hx

set hisfile c:\FLAC\LAMB\data\166hy.his
save_hy

set hisfile c:\FLAC\LAMB\data\166vx.his
save_vx

set hisfile c:\FLAC\LAMB\data\166vy.his
save_vy

;set hisfile c:\FLAC\LAMB\data\166sour.his
;save_sour

set hisfile c:\FLAC\LAMB\data\unbal.his
save_unbal
```